Centre of Excellence for the Application of Superconducting and Plasma Technologies in Power Engineering

Institute of Electrical Engineering & Electrotechnologies
Lublin University of Technology

Proceedings

of

the 6th International Conference

ELMECO-6

ELECTROMAGNETIC DEVICES AND PROCESSES IN ENVIRONMENT PROTECTION

joint with

9th Seminar "Applications of Superconductors"

AoS-9

June 24 – 27, 2008

Nałęczów, Poland

Centre of Excellence for the Application
of Superconducting and Plasma Technologies
in Power Engineering

Institute of Electrical Engineering & Electrotechnologies
Lublin University of Technology

Proceedings

of

the 6th International Conference

ELMECO-6

ELECTROMAGNETIC DEVICES AND PROCESSES
IN ENVIRONMENT PROTECTION

joint with

9th Seminar “Applications of Superconductors"

AoS-9

June 24 – 27, 2008

Nałęczów, Poland

Institute of Electrical Engineering and Electrotechnologies
Lublin University of Technology
38a Nadbystrzycka St. 20-618 Lublin

Tel./fax: 48 81 53 84 289, 48 81 53 84 643
E-mail: we.ipee@pollub.pl
http://ipee.pollub.pl/elmeco_aos

6th International Conference

ELMECO-6

ELECTROMAGNETIC DEVICES AND PROCESSES IN ENVIRONMENT PROTECTION

joint with

9th Seminar "Applications of Superconductors"

AoS-9

June 24 – 27, 2008
Nałęczów, Poland

Organized by:

Centre of Excellence for the Application of Superconducting and Plasma Technologies in Power Engineering
Institute of Electrical Engineering and Electrotechnologies
Lublin University of Technology

Conference venue:
Conference Centre ENERGETYK
10 Paderewskiego St., 24 - 140 Nałęczów
tel. (48-81) 50 14 604

Scientific Committee

Kazimierz Adamiak	(University of Western Ontario, Canada)
Krystyna Cedzyńska	(Technical University of Łódź, Poland)
Antoni Cieśla	(AGH University of Science and Technology, Cracow, Poland)
Marian Ciszek	(Polish Academy of Science, Wrocław, Poland)
Vladimir Datskov	(Joint Institute for Nuclear Research, Dubna, Russia)
Gordon B. Donaldson	(University of Strathclyde, Glasgow, UK)
Kenji Ebihara	(Kumamoto University, Japan)
Bartek A. Głowacki	(University of Cambridge, UK)
Bogusław Grzesik	(Silesian University of Technology, Gliwice, Poland)
Jan Janca	(Technical University of Brno, Czech Republic)
Tadeusz Janowski	(Lublin University of Technology, Poland)
Ulrich Kogelschatz	(ABB, Switzerland)
Zbigniew Kołaciński	(Technical University of Łódź, Poland)
Jan Leszczyński	(Technical University of Łódź, Poland)
Bolesław Mazurek	(Electrotechnical Institute, Wrocław, Poland)
Jerzy Mizeraczyk	(Institute of Fluid Flow Machinery, PAS, Gdańsk, Poland)
Anthony J. Moses	(Wolfson Centre for Magnetics Techn., Cardiff Univ., UK)
Andrzej Nafalski	(University of South Australia, Adelaida)
Ryszard Pałka	(Szczecin University of Technology, Poland)
Krzysztof Schmidt-Szałowski	(Warsaw University of Technology, Poland)
Andrzej Siemko	(CERN, Geneva, Switzerland)
Jacek Sosnowski	(Electrotechnical Institute, Warsaw, Poland)
Petro G. Stakhiv	(Technical University of Lviv, Ukraine)
Henryka D. Stryczewska	(Lublin University of Technology, Poland)
Bronisław Susła	(Poznań University of Technology, Poland)
Jan Sykulski	(University of Southampton, UK)
Andrzej Wac-Włodarczyk	(Lublin University of Technology, Poland)
Hans Erich Wagner	(Ernst-Moritz-Arndt-University, Greifswald, Germany)
Chobei Yamabe	(Saga University, Japan)
Sotoshi Yamada	(Kanazawa University, Japan)
Kazimierz Zakrzewski	(Technical University of Łódź, Poland)
Andrzej Zaleski	(Polish Academy of Science, Wrocław, Poland

Organizing Committee

Tadeusz Janowski - **Chairman**
Henryka Danuta Stryczewska
Andrzej Wac-Włodarczyk
Paweł Surdacki
Sławomir Kozak
Beata Kondratowicz-Kucewicz
Agata Troncewicz-Świtek
Renata Jaroszyńska - **Secretary**

ISBN: 978-83-61301-20-2

The proceedings have been published based on papers delivered by authors

CONTENTS

ORAL SESSION OS-1

ORAL SESSION OS-2

ORAL SESSION OS-3

ORAL SESSION OS-4

POSTER SESSION PS-1

POSTER SESSION PS-2

Conference **ELMECO-6**
ELECTROMAGNETIC DEVICES AND PROCESSES IN ENVIRONMENT PROTECTION
joint with
9th Seminar APPLICATIONS OF SUPERCONDUCTORS **AoS-9**
June 24 – 27, 2008 Nałęczów, Poland

PLASMA TREATMENT OF SPENT CHEMICALS

Zbigniew KOLACINSKI[1], Lukasz SZYMANSKI[2], Witold SROCZYNSKI[1], Zbigniew MUSZCZYNKO[1]

Technical University of Lodz (1), Academy of Humanities and Economics in Lodz (2)

***Abstract**. The aim of the paper is to study a stream rate and quantity of organic fluid waste production by an average analytic chemical laboratory, to find out the required conditions of its thermal treatment and to demonstrate a concept of compact device PDUCR)Plasma Destructor of Used Chemical Reagents) able do utilize from one to a few kilograms of reagent per hour.*
***Streszczenie.** Celem tego artykułu jest przeanalizowanie wytwarzanych ilości organicznych odczynników ciekłaych przez średniej wielkości laboratiorium analityczne w celu znalezienia wymaganych warunków termicznego rozkładu oraz przedstawienie kompaktowego urządzenia PUOC (Plazmowy Utylizator Odczynników Chemicznych) zdolnego do utylizacji od jednego do kilku kilogramów odczynnika na godzinę.*

Keywords: Plasma treatment, thermal destruction, fluid waste, spent chemicals

Słowa kluczowe: Plazmowa utylizacja, rozkład termiczny, odpady ciekłe, zużyte chemikalia

Introduction

In a chemical analytic laboratory practice small amounts of diverse reagents, mostly liquid organic substances are used for many purposes such as chromatography. They are the chlorinated solvents, solvents from the group of alcohols, esters, and aliphatic or aromatic hydrocarbons. Annually particular analytic laboratory have been using from several to a dozen of tones of those reagents, which as containing some dirt must be qualified as the waste. Small daily production rate of those wastes (rating from several to some tens of kilograms) must be collected and temporary stored before transportation to a place of utilization. The cost of building and exploitation fulfilling the suitable requirements of store-house is in this process the financial largest burden.
The avoidance of stockpiling and transportation of those waste is the economic challenge in the procedure of utilization of the used reagents. So far any device able to utilize those wastes "in situ" where they are produced had not been offered. Such device had to be placed in/or close to the laboratory and may be working in measure of the need (batch mode) on principle how the office document shredder.

Quantitative and parametric analysis the of the chemical reagents waste stream

The quantitative and parametric analysis has been done by the review of accessible literature as well as inquiries of representative laboratories in a wide range of industries, including cosmetic industry, industry of paints and varnishes as well as chemical and pharmaceutical industry. The most credible and reliable data were got from 27 chemical profile faculties of Polish universities [1]. Estimated for the whole country quantity of chemical wastes generated in the university laboratories can reach 100 tones annually in which organic solvents participate in 36%.
The traditional thermal utilization (incineration) of this group of wastes is very difficult because of chlorine content in the waste that cause the possible formation of furans and dioxins. It can be successfully performed with the use of thermal plasma which can be generated in oxygen free atmosphere.

Chemical reagents thermal destruction

To find the most effective conditions for these waste destruction in the thermal plasma, the thermochemical calculations have been done before the PDUCR designing and employing it in the experiment. To optimize the conditions of the reaction we have calculated the decomposition of solvents within the range of temperatures from 400 to 2400K using the CHEMSAGE program based on the minimization of Gibb's free energy [2].
The example of calculation results is shown in the Fig. 1.

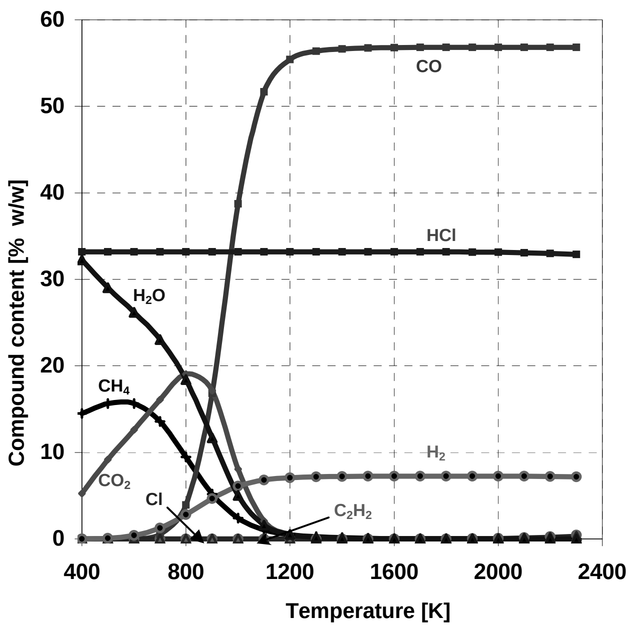

Fig. 1. Gas compounds ratio at decomposition process of methanol-carbon tetrachloride mixture (66%/34% w/w)

We can see here 33 weight % of hydrochloride that must be converted into salt before hydrogen and carbon monoxide burning. In fact, chlorine amount in the utilizated waste does not exceed a few percent so performed calculations had sufficient "safety margin".

PDUCR (Plasma Destructor of Used Chemical Reagents) concept

In Fig. 2 the scheme of device PDUCR and required installation are presented.

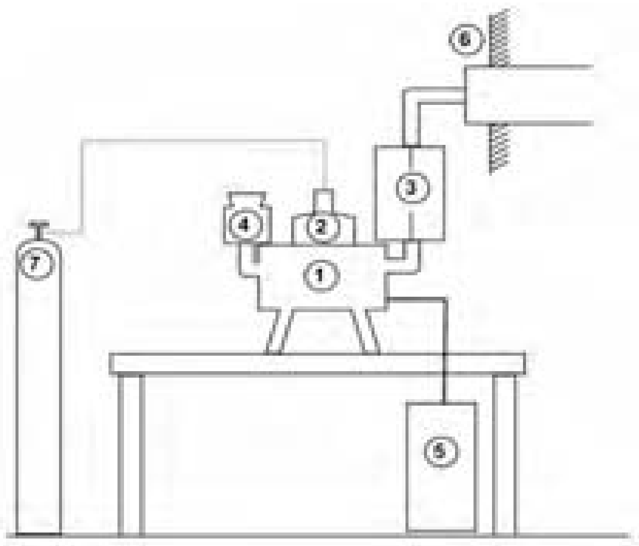

Fig. 2. PDUCR: 1- plasma reactor; 2- adjustment actuator; 3- chlorine absorber and catalytic oxidiser; 4- waste container; 5 - control unit; 6- fan; 7 – inert gas bottle [3].

The deciding factor verifying the usefulness of the constructed device for the process of chemical reagents utilization was a comparison of the parameters of gas with acceptable emission values specified by legal regulations. The chart below shows that the constructed device complies with legal requirements established by Polish law.

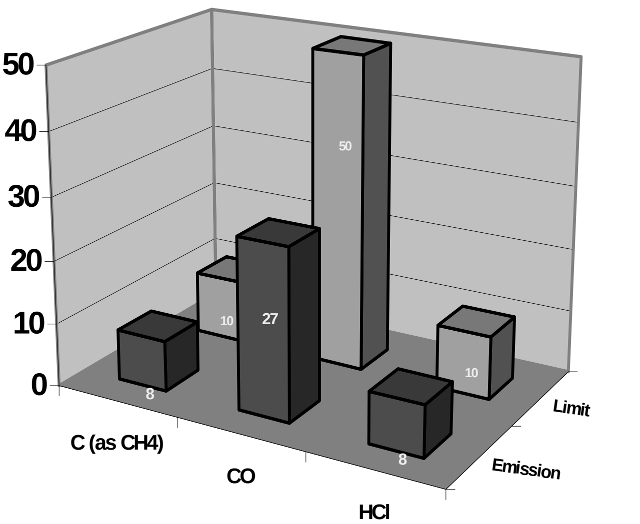

Fig. 3. Comparison of the gas parameters emitted from PDCUR with polish law regulations

The view of constructed device is shown in Fig. 4. The great advantage of presented plant is very compact construction and possible mobility of constructed device.

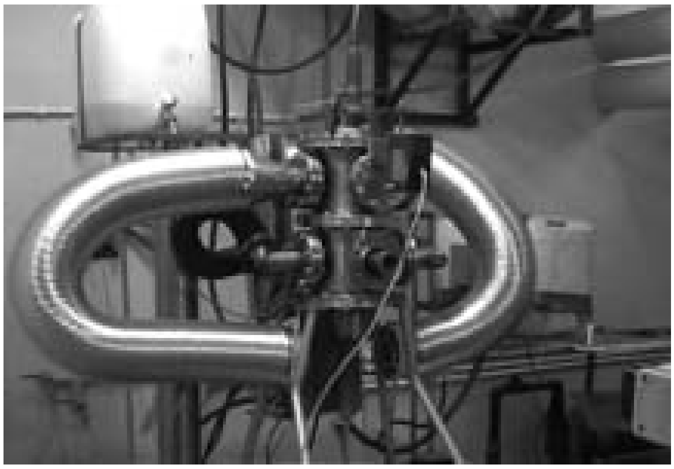

Fig. 4. General view of ready-made PDUCR.

Conclusion

PDUCR is dedicated to utilization of spent reagents in place of their formation. Such solution allows to avoid of stockpiling and transportation of those waste before utilization of spent reagents. PDUCR is able to utilize those wastes “in situ” where they are produced. It can be placed in/or close to the laboratory and may be working in measure of the need (batch mode) on principle how the office document shredder.

Acknowledgments

The scientific work has been financed by Polish Minister of Science and Higher Education, executed within the framework of the Multi-Year Program entitled "Development of innovativeness systems of manufacturing and maintenance 2004-2008".

REFERENCES

[1] (2000) Informacja o pracach nad systemem zarządzania chemikaliami w polskich uczelniach. „Opracowanie sposobu oraz systemu organizacyjnego gospodarowania substancjami chemicznymi na wydziałach chemicznych i pokrewnych szkół wyższych oraz koncepcji technologicznej neutralizacji oraz utylizacji odpadów z laboratoriów chemicznych”, Wydział Chemiczny Politechniki Śląskiej

[2] Cedzyńska K., Kołaciński Z. (2004). Plasma Destruction of Toxic Chloroorganic Wastes Towards Zero Residues. *Journal of Advanced Oxidation Technologies*. ISSN 1203-8407. Science & Technology Network, Inc. Vol. 7, No. 1

[3] Kołaciński Z., Sroczyński W., Muszczynko Z. et al. (2006). Plasma Treatment of Spent Chemical Reagents. *Maintenance Problems* 4/2006. ISSN 1232-9312. NRI Radom

Authors: prof. dr hab. inż. Zbigniew Kołaciński, Politechnika Łódzka, Katedra Aparatów Elektrycznych, ul. Stefanowskiego 18/22, 90-924 Łódź, E-mail: zbigniew@p.lodz.pl; dr inż. Witold Sroczyński, Politechnika Łódzka, Instytut Podstaw Chemii Żywności, ul. Stefanowskiego 4/10, 90-924 Łódź, E-mail: sroka@snack.p.lodz.pl; dr inż. Łukasz Szymański, Wyższa Szkoła Humanistyczno-Ekonomiczna, ul. Rewolucji 1905 r. 64, 90-222 Łódź E-mail: lusyma@p.lodz.pl; mgr inż. Zbigniew Muszczynko Politechnika Łódzka, Katedra Aparatów Elektrycznych, ul. Stefanowskiego 18/22, 90-924 Łódź, E-mail: zibim79@o2.pl

APPLICATION OF GASEOUS OZONE TO AGRICULTURAL SOIL STERILIZATION

Kenji EBIHARA[1], Shinji SUGIMOTO[2], Tomoaki IKEGAMI[3], Fumiaki MITSUGI[3] , Henryka.D.STRYCZEWSKA[4]

[1]Dojindo Laboratories,Tabaru 2025-5,Kamimashiki,Kumamoto 861-2202,Japan

[2]Dojinglocal Co.,Tabaru 2081-25, Kamimashiki,Kumamoto 861-2201,Japan

[3]Graduate School of Science and Technology, Kumamoto University, 2-39-1 Kurokami 860-8555,Japan

[4]Faculty of Electrical Engineering and Computer Science, Lublin University of Technology,

Nadbystrzycka Street,38A,20-618 Lublin, Poland

Abstract *The gaseous ozone sterilization system has been developed for agricultural soil treatment which is environmentally friendly technique alternative to chemical fumigation. High dense ozone suitable to the sterilization was generated using pulsed high frequency dielectric barrier discharges. The effect of ozone treatment on soil properties and plant growth was studied.*

Keywords: ozone, sterilization, dielectric barrier discharge, high frequency, plant growth

Introduction

Ozone possessing strong oxidative and germicidal properties has a very short half-life time of minutes or less in soil and decomposes into simple diatomic oxygen. The ozone is known to be potent bactericide and virucide. Therefore the on-site gas-phase ozone process of agricultural sterilization can provide a promising alternative to traditional chemical or thermal (heat) treatment. Numerous methods including autoclaving (moist heat), dry heat and microwaves have been attempted as alternatives to chemical fumigation.

We have developed the gaseous ozone sterilization system for the agricultural soil and studied the effect on the soil properties and the plant growth [1-6]. The dielectric barrier discharge operated using pulsed high frequency generators which were connected to the screw type electrodes was found to generate high dense ozone of about 100g/m^3. The critical sterilization conditions of the agricultural soil were also investigated in the incubator and the agricultural green house [5,6]. The experimental works showed that the sterilization is controlled by mostly three parameters; ozone concentration, dosage and ozone diffusion (penetration) length in the soil. We found that threshold conditions for our system are the ozone concentration of 20 g/m^3, the ozone dosage of 12mgO$_3$/g(soil) and the diffusion length of 80mm(radius). We also studied soil properties when the ozone was injected into the agricultural soil. The in-situ measurements of the pH and the electrical conductivity with the soil temperature showed that the rapid decrease of the pH and the gradual increase in the electrical conductivity appear during ozone treatment process. It is interesting that the soil temperature simultaneously attains to a maximum temperature near 70℃ in about 20min. The plant growth experiments of several vegetables in the incubator and the green house showed that the growth for most of vegetables are suppressed by the ozone treatment and that the growth for some vegetables are enhanced.

In this paper we present recent progress in agricultural soil sterilization using high dense ozone.

Experimental

The dielectric barrier discharge was used to produce high dense ozone having the ability of sterilization of bacteria, virus and nematodes in the soil. A pulsed electric power was generated by the high frequency oscillator which operates at the continuous mode and the interval mode (frequency range:1kHz-30kHz, pulse rise time:5μs, Vp-p:15kV, 4kW, PHF-4K,HAIDEN). The dielectric barrier discharge was produced between a screw-type cylindrical electrode (outer dia. 10mm) and the gold electrode coated on the quartz tube (inner dia.12mm). The electrode of axial length of 250mm was water-cooled in order to suppress the dissociation of ozone. The multi-channel electrode system consisting of the 10 electrodes elements can supply a large volume of high dense ozone. Oxygen gas was introduced to the electrodes at various flow rates. High dense ozone in gas phase (over 20g/m^3) was directly injected into the agricultural soil (Kuroboku) at a depth of about 70mm.

The in-situ measurement of the pH and the electrical conductivity (EC) of the ozone treated soil was carried out. The pH and the EC of the soil were measured by pH/Nitricion/ pH and pF/EC meters (PRN-41 and PFC-42, Fujiwara Scientific Co.,LTD) while the ozone was supplied.

In the case of ozone sterilization experiment in the green house, the Kuroboku soil was filled in the drain bed container (1200X900X500mm) and ,then, high dense ozone was injected into the soil at a half area of the drain bed.

Results and Discussion

Fig.1 shows voltage and current wave forms of pulsed high frequency generator (A) and the dielectric barrier discharge (B). We can notice the phase difference between voltage and current. The distorted current wave has short pulsed currents which indicate appearance of microdischarges. The pulsed decaying discharge current contributes to decrease the dielectric heating loss of the quartz tube. Fig.2 shows the ozone generation efficiency as a function of ozone concentration. Here we supplied ozone of 8 liter/min to 4 electrodes connected in parallel. The dense ozone with the flow rate of $0.6gO_3$/min at $68g/m_3$ can be injected into the soil.

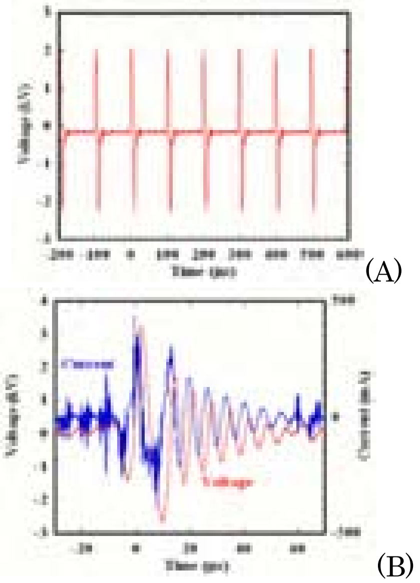

Fig.1 Pulsed high frequency voltage(A) and dielectric barrier discharge(B).

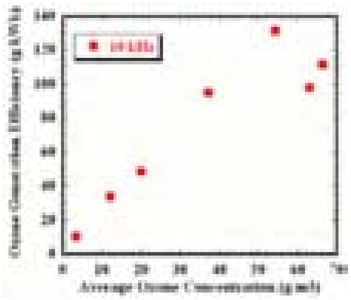

Fig.2 Ozone generation efficiency vs. ozone concentration for four parallel electrodes. The flow rate for each electrode was 2L/min and total rate was 8L/min.

The agricultural soil properties during ozone treatment is shown in Fig.3. The EC initially decreases rapidly and has a minimum value at 18min. After initial phase, the conductivity gradually increases to attain the saturated value of 70mS/m. The soil temperature also shows a maximum temperature of 60℃ and drops to the temperature around 30℃ after 2 hours. Most of the pathogenic bacteria are killed over 70℃. The bacteria growth is expected to slow down around 60℃.

We have observed the effect of the ozone treatment on the plant growth for several vegetables. Oxidization, sterilization and chemical adsorption in the agricultural soil are expected and reflect on the plan growth. Ozone interferes with the metabolism of bacterium cells. A sufficient amount of ozone breaks through the cell membrane leading to the destruction of the bacteria in the soil.

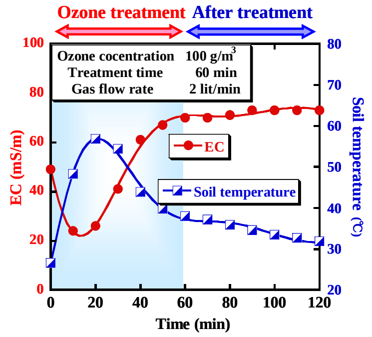

Fig.3 Time development of EC and soil temperature during ozone treatment.

Our experiments for vegetables growth showed that the ozone treatment at $100gO_3/m^3$ for 60min suppresses the plant growth for lettuce and Chinese cabbage and, contrarily, enhances the growth for spinach.

Conclusions

High dense ozone sufficient for agricultural soil sterilization was produced using pulsed high frequency power source. The soil during the ozone treatment showed remarkable change of electrical conductivity and temperature. The ozone treatment gave different effects on vegetable growth.

Acknowledgment

The authors would like to express the gratitude to Y.Gyoutoku and Dr.T.Sakai for their collaboration and valuable discussions and M.Takayama for his technical support.

This work has been supported by Research Project for Utilizing Advanced Technologies in Agriculture, Forestry and Fisheries(the Ministry of Agriculture, Forest and Fisheries), and the Strategic Research Promotion Program of Information Technology of the Ministry of Internal Affairs and Communications.

REFERENCES

[1] Ebihara,E.,Takayama,M.,Ikegami,T.,Ogata,K.,Stryczewska,H. D., Gyoutoku,Y., and Sakai,T. ,Development of agricultural soil sterilization using ozone generated by high frequency dielectric barrier discharge, J.Adv. Oxid. Technol. Vol.9, No.2, pp.170-173,2006

[2] Takayama, M., Ebihara,E., Stryczewska,H.D., Ikegami,T., Gyoutoku,Y., Kubo,K., Tachibana,M. ,Thin Solid Films, 506-507, pp.396-399,2005

[3] Ebihara,K., Takayama,M., Ikegami,T., Stryczewska,H.D., Gyoutoku,Y., Yokoyama,T., Gunjikake,N., Tachibana,M., Sakai,T., Proceedings of 17th International Symposium on Plasma Chemistry, Toronto, Canada,August 7th-12th,CD(1201).,2005

[4] Ebihara,K.,Takayama,M.,Ikegami,T.,Ogata,K. ,Stryczewska,H. D., Gyoutoku,Y.,Sakai,T., Development of agricultural soil sterilization using ozone generated by high frequency dielectric barrier discharge, 5th International Conference **ELMECO** and Workshop, Naleczow, Poland(September 4-7,2005) pp.14,2005

[5] Ebihara,K., Takayama,M., Strycewska,H.D., Ikegami,T., Gyoutoku,Y., Tachibana,M., Wide range concentration control of dielectric barrier discharge generated ozone for soil sterilization,

[6] IEEJ Transaction (inJapanese), 125, No.10, pp.963-969,2006.

[7] Ebihara, K., Agricultural soil sterilization using high concentration ozone generated by pulsed high frequency barrier discharges, The Workshop on the Applications of Plasma to Green Environmental Technology ,Taoyuan, Taiwan, December 11-12,2006:Proceedings, pp.86-90,2006.

Corresponding Author *: Professor K.Ebihara, Dojindo Laboratories and Kumamoto University, E-mail:k-shrimp@road.ocn.ne.jp*

Conference **ELMECO-6**
ELECTROMAGNETIC DEVICES AND PROCESSES IN ENVIRONMENT PROTECTION
joint with
9th Seminar APPLICATIONS OF SUPERCONDUCTORS **AoS-9**
June 24 – 27, 2008 Nałęczów, Poland

FEM AND LABORATORY TESTS OF HTS TRANSFORMER WITH IMPROVED UTILIZATION OF SUPERCONDUCTING WIRE

Bogusław GRZESIK, Mariusz STĘPIEŃ, Sebastian KROSNY

Silesian University of Technology

***Abstract**. The paper describes results of FEM analysis and laboratory tests of HTS transformer with modified shape of windings. The shape of transformer windings, called as helical one, improves HTS wire utilisation due to magnetic flux decreasing. The transformer has 1:1 turn-to-turn ratio and amorphous magnetic core immersed in LN2. It operates at 50 Hz. Components of magnetic flux density, determined by 3D FEM analysis, are investigated in the paper. Also some aspects of laboratory tests are described.*

***Streszczenie.** W artykule opisano wyniki analizy MES i testów laboratoryjnych transformatora HTS o zmodyfikowanym kształcie uzwojeń. Kształt, zwany heliakalnym, poprawia wykorzystanie prądowe przewodów HTS poprzez obniżenie składowych indukcji. Transformator ma przekładnię zwojową 1:1 i rdzeń amorficzny zanurzony w ciekłym azocie. Częstotliwość znamionowa wynosi 50 Hz. Rozkład składowych indukcji uzyskany w wyniku analizy MES 3D jest analizowany w artykule. Omówiono także pewne aspekty badań laboratoryjnych.*

Keywords: Transformer HTS, improved utilization of HTS wire, amorphous core, 3D FEM analysis.
Słowa kluczowe: Transformator HTS, podwyższone wykorzystanie przewodu HTS, rdzeń amorficzny, analiza MES 3D.

Introduction

Till today HTS power transformers are constructed as conventional structure. It means that transformer has solenoidal windings coaxially arranged and magnetic core with two or three columns. Additionally many of known transformers have magnetic core thermally insulated. Ends of solenoidal or cylindrical windings produce not homogenous distribution of magnetic field which influences on critical current in HTS wire. Because of serial connection of wire in each winding critical current decreased at ends of winding is decrease in whole winding. The second feature – thermal insulation between windings and magnetic core decreases coupling between windings and increases leakage flux in transformer. Presented here transformer is considerably different. It has windings helical in shape and magnetic core immersed in liquid nitrogen.

Consideration in the paper shows that this design allows critical current higher than previously presented, and power properties of transformer are the same or better while magnetic core is immersed in LN2.

Description of the transformer

The design of the transformer is presented in Fig. 1 and Fig. 2. Windings are wounded on toroidal support. Each of wire has helical shape. Additionally each of windings has the same length and shape. Amorphous magnetic core is deposited outside coaxially to windings.

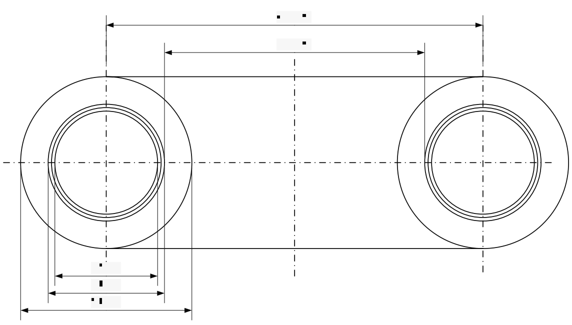

Fig.1. Dimensions of the transformer

Fig.2. Model of the helical HTS transformer

The transformer operates at 50 Hz whole immersed in LN2. posited outside coaxially to windings. The constructional materials are BiSCCO 2223 wire with critical current 146 A and amorphous magnetic material Metglas 2605SA1 characterized by relative permeability above μ_r=20000 and specific power losses P_V=0,81 W/kg at 50 Hz and 1.2 T.

Power properties of the transformer

The transformer is designed as experimental device characterized by improved utilisation of critical current in windings. Because of single layer windings transformer presents relatively small power properties. There are (obtained by FEM analysis): nominal output power S_N=0,98 kVA, rated voltage $U1_N$=23 V and maximum efficiency hmax=99,6% (excluding losses of cooling system). The properties were obtained at turn-to-turn ratio 1:1, number of turns in each winding 31, critical current 120 A and maximum flux density in magnetic core 1.2 T.

The power losses in transformer are very low. The highest power losses are generated in magnetic core. They are near 78% of total power losses. The highest power losses in windings are hysteresis losses (approx. 19%). The rest sources of losses are lower than 3% of total losses.

Flux density in helically shaped windings

The idea of the transformer is improved utilization of HTS wire due to shape of magnetic field in the wire region. The highest values of critical current are obtained at magnetic flux density parallel to HTS wire. In typical transformer windings magnetic flux density is parallel to wire only in middle part of the windings. Presented here design produces magnetic field similar to single toroidal ring wire with diameter equal to diameter of cross-section of winding. The magnetic field and current density were tested using 3D FEM model. The windings model is depicted in Fig. 3. It shows 60 degrees sector of 8 turn windings and additionally single wire with marked part of wire.

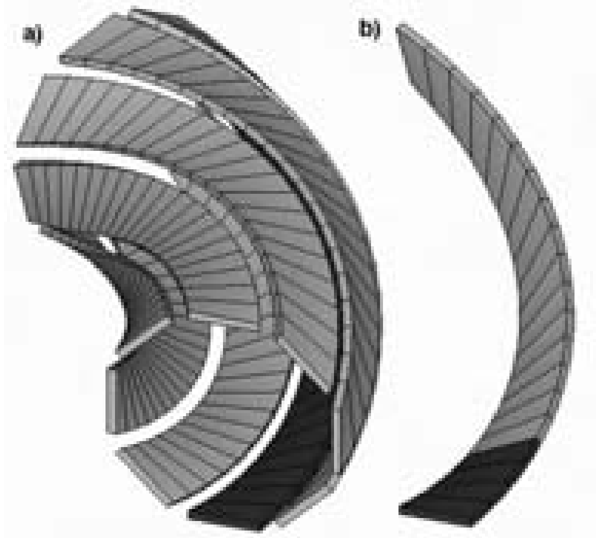

Fig.3. 3D model of transformer windings, a) sector of windings with marked single wire, b) single wire with marked part of wire

The magnetic flux density is in circular shape and it reach deformation in between windings. The flux density distribution is depicted in Fig. 4. The deformation of flux density decreases with distance between windings.

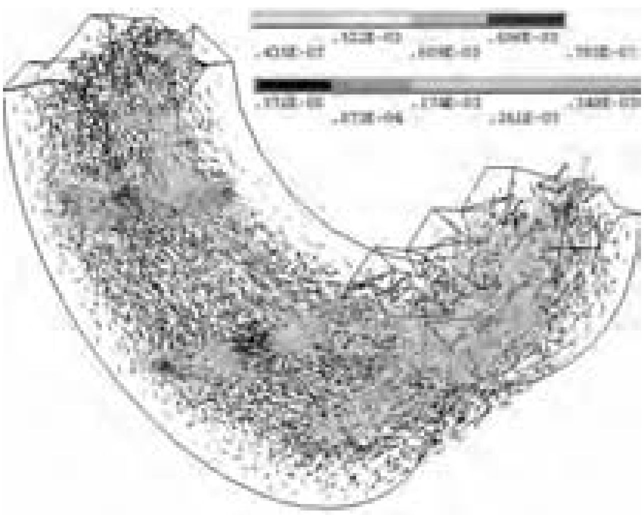

Fig.4. Flux density distribution in windings region (12 degrees region depicted)

Small values of flux density influences very slightly on critical current in single wire. Because of filament structure of HTS wire the most outside part of wire is only silver support of wire. Current and flux density inside of wire are homogenous and parallel to wire surface. The distribution of these quantities is depicted in Fig. 5.

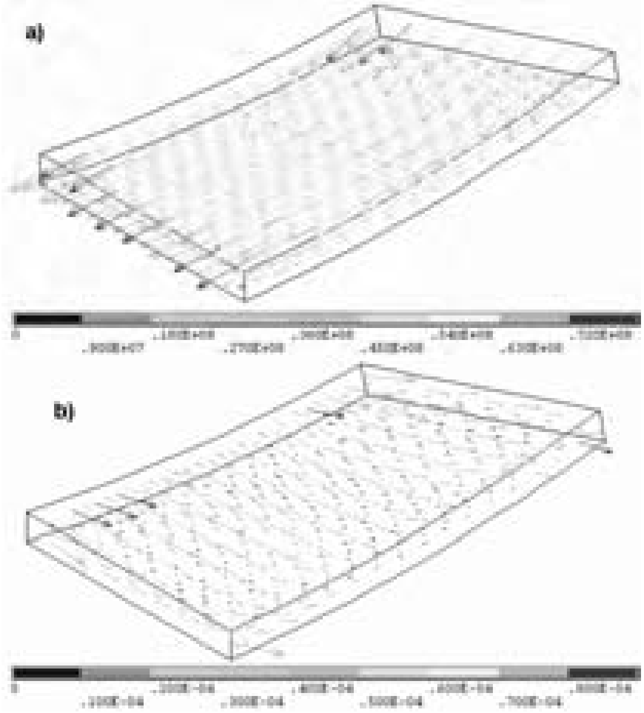

Fig.5. Current density (a) and flux density (b) in HTS wire (part of wire marked in Fig 3b)

Calculated values of flux density components shows that parallel component (Bx) is more than ten times greater than By and Bz components. It is main advantage of presented transformer.

Laboratory tests

The most important disadvantage of transformer is shaping of windings due to very small flexibility of HTS wire. Laboratory tests done for his transformer were focused on influence of shape curvature on critical current of transformer. It shows that proposed diameter of transformer (300 mm) allows shaping of transformer windings without decreasing of critical current.

Conclusions

The following conclusions can be drawn after the work: i) the idea of the transformer is way to improve critical current of the transformer, ii) the transformer shows good power properties – efficiency 99,6% but only single layer design was tested (output power below 1kVA), iii) flux density calculated by FEM shows parallel component ten times greater than the other one, iv) because of HTS wire flexibility the windings shaping is important difficulties.

REFERENCES

[1] Grzesik B., Janowski T., Stępień M., HTS Toroidal Helical Transformer, ak pisać tekst do Przeglądu, *Journal of Physics: Conference Series*, Article no. 012311 Vol. 97

[2] Friedman A. et al., HT-SMES operating at liquid nitrogen temperatures for electric power quality improvement demonstrating, *IEEE Trans. Appl. Superconductivity.* Vol 13 Issue 2 pp 1875 - 1878

***Authors**: dr hab. inż. Bogusław Grzesik, prof. Politechniki Śląskiej, dr inż. Mariusz Stępień, mgr inż. Sebastian Krosny, Politechnika Śląska, Katedra Energoelektroniki, Napędu Elektrycznego i Robotyki, ul. B. Krzywoustego 2, 44-100 Gliwice. E-mail: Boguslaw.Grzesik@polsl.pl, Mariusz.Stepien@polsl.pl, Sebastian.Krosny@polsl.pl*

Conference **ELMECO-6**
ELECTROMAGNETIC DEVICES AND PROCESSES IN ENVIRONMENT PROTECTION
joint with
9th Seminar APPLICATIONS OF SUPERCONDUCTORS **AoS-9**
June 24 – 27, 2008 Nałęczów, Poland

CHARACTERISTICS OF NEW MAGNETIC MATERIALS IN LN2 FOR HTS TRANSFORMERS

Mariusz STĘPIEŃ, Bogusław GRZESIK

Silesian University of Technology, Gliwice, Poland

Abstract*. The paper describes characteristics of three magnetic materials, amorphous and nanocristalline, measured at LN2 temperature and at room temperature. Proposed application of tested materials are HTS transformers with warm magnetic cores. Characteristics are measured at 50 Hz using Remacomp® meter and at higher frequencies - > 100 kHz using Class DE inverter. Results shows good properties of presented materials for proposed application.*

Streszczenie. *W artykule opisano charakterystyki trzech amorficznych i nanokrystalicznych materiałów magnetycznych zmierzone w temperaturze LN2 oraz w temperaturze pokojowej. Proponowanym zastosowaniem są transformatory HTS z rdzeniem pracującym w temperaturze otoczenia. Charakterystyki zmierzono przy 50 Hz przyrządem Remacomp® oraz przy wyższych częstotliwościach - > 100 kHz z zasilaniem z falownika klasy DE. Wyniki potwierdzają dobre właściwości badanych materiałów do proponowanego zastosowania.*

Keywords: magnetic materials, hysteresis losses, operation at LN2, HTS transformers.
Słowa kluczowe: materiały magnetyczne, straty histerezowe, praca w ciekłym azocie, transformatory HTS.

Introduction

New way to increasing power density delivered by transformers is substituting of traditional transformer by HTS transformers [1], [2], [3]. Power density in HTS transformers is near double increased in comparison to traditional transformer [4]. Unfortunately power losses in HTS transformer strongly depend on properties of magnetic material. Very promising are new materials, amorphous and nanocrystalline. It shows power losses few times lower than traditional transformer strip. Additional advantage are relatively small power losses generated at LN2 temperature. It allows operation of magnetic material at LN2. Although power losses in core are slightly higher, coupling of windings and windings and core are better the overall properties of transformer are acceptable [5].

This paper examines properties of three different materials: amorphous $FeCo_{40}$ and Pyropherm and nanocrystalline Finemet®. B-H curves are presented at 50 kHz and 100 kHz at LN2 and room temperature.

Basic properties of magnetic materials

Basic properties of mentioned materials were obtained using Remacomp 100® [6] and inverter of Class DE.

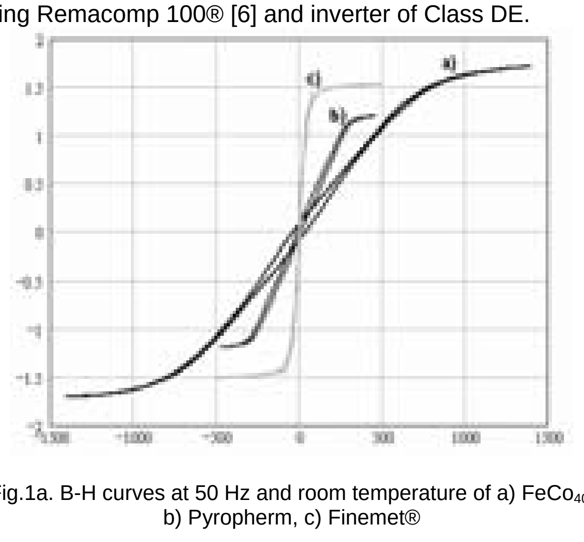

Fig.1a. B-H curves at 50 Hz and room temperature of a) $FeCo_{40}$, b) Pyropherm, c) Finemet®

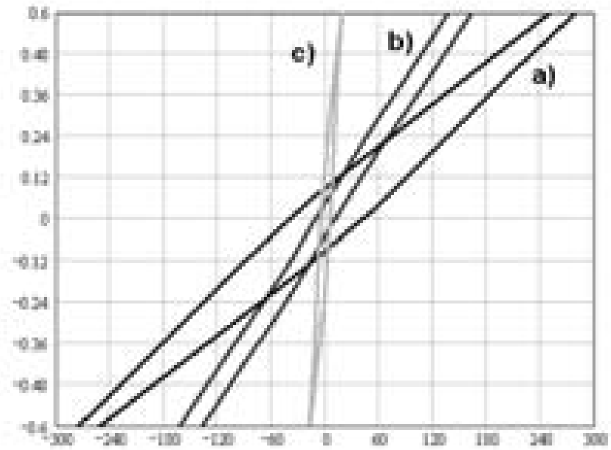

Fig.1b. B-H curves at 50 Hz and room temperature of a) $FeCo_{40}$, b) Pyropherm, c) Finemet®

Table 1. The parameters of the magnetic materials

Magnetic material	P, W/kg @ 293 K	P, W/kg @ 77 K	Sample ID
ET114-27 (FeSi 0.27mm, <0,08%C; 2,8-4,2Si)	1.14 (1.7 T)	3.36 (1.3 T)	1Fe
FeCo40 (amorph.) (IMN-Gliwice)	0.3 (1.12 T)	0.36 (1.2 T)	167/07/R
Pyroperm (amorph.) (IMN-Gliwice)	0.2 (1.6 T)	0.71 (1.6 T)	192/07/R
$Fe_{78,8}Nb_{2,6}Cu_{0,6}Si_9B_9$ [Finemet] (IMN-Gliwice)	0.12 (1.5 T)	0.2 (1.5 T)	198/07/R
27QG110 (FeSi) 0.27mm (u=10000)	0.59 (1.7 T)	0.71 (1.3 T)	1)
SA1 (amorphous) (0.27mm	0.15	0.20	1)

Measurements at 50 Hz were carried out with Rmacomp 100® while for measurement at higher frequencies Class DE current inverter was used – Fig. 2.

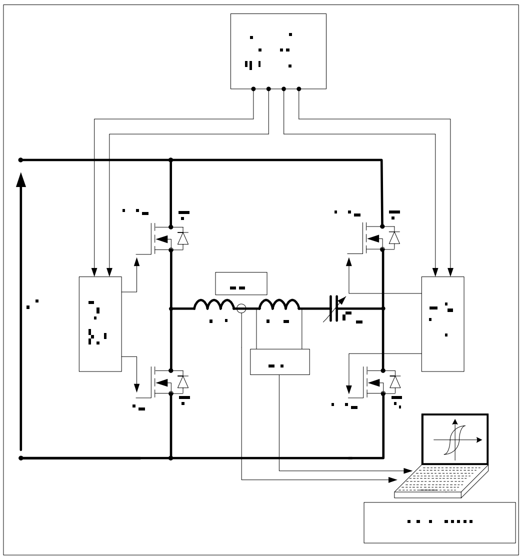

Fig.2. Laboratory set-up for measuring B-H curves at higher frequencies

Properties of magnetic materials at high frequencies

Power losses in magnetic materials increase strongly with frequency. B-H curves of materials tested at 100 kHz are given in Fig. 3 and Fig. 4 for room temperature and LN2.

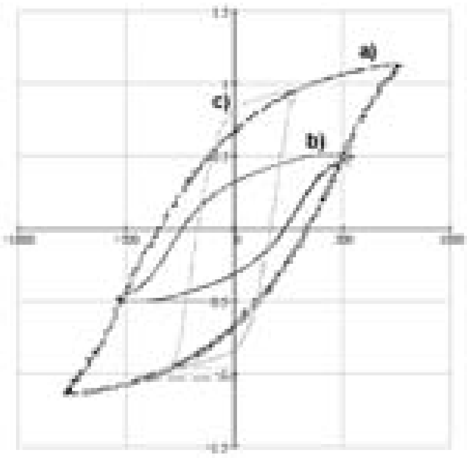

Fig.3. B-H curves at 100 kHz and room temperature of $FeCo_{40}$, Pyropherm and Finemet®

Results presented at 50 Hz have been confirmed at 100 kHz. FeCo40 shows the highest saturation field but also the highest power losses. Pyropherm has very low saturation level. Finemed@ is still the best material – with

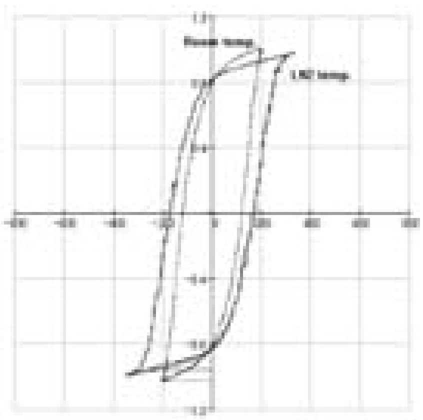

Fig.4. B-H curves of Finemet® at 100 kHz and at room (dotted) and LN2 (solid) temperature

slightly lower saturation field than $FeCo_{40}$ and the lowest power losses. Next important result are power losses at LN2. Fig. 5. depicts power losses of Finemet at room and LN2 temperature.

Measured B-H curve shows slightly higher power losses and lower saturation field at LN2. Power losses of tested materials at room temperature (RT) and LN2 temperature are gathered in Table 1 and Table 2

Table 2. Specific power losses of magnetic material at 100 kHz

$FeCo_{40}$		Pyropherm		Finemet®	
RT	LN2	RT	LN2	RT	LN2
kW/kg					
7,9	11,5	23,9	30,6	8,3	9,4

In order to have data concerning HTS Toroidal Helical Transformer [5] FEM calculations were carried out resulting in the following: ΔP_{total}=4.5W, where 3.5W (78%) in core, 0.78W (19%) hysteresis losses in HTS wire and 0.15W (3%) other losses.

Conclusions

Presented in this paper properties of new, amorphous and nanocrystalline materials confirms usability of these materials for HTS transformer with cold (LN2) magnetic core operating at 50Hz. The best properties were observed for Finemet® material. One concern is only about mechanical properties of this material. Tests in LN2 shows small increasing of power losses in material and small decreasing of saturation field. The important advantage of cold core is good coupling of windings with core due to removing thermal insulations which has been inserted in between windings and magnetic core.

REFERENCES

[1] Sykulski J.K (1999).: High Temperature Superconcucting Demonstrator Transformer: Design Considerations and First Test Results, IEEE Transactions on Magnetics, Vol 35, No 5, September 1999, pp. 3559-3561.

[2] Sykulski J. (2004): Superconduction Transformers, Advanced Research Workshop on Modern Transformers, ARWtr 2004, 28-30 October 2004, Vigo, Spain.

[3] Wang Y. et al. (2004): A single phase model of 9 kVA high-temperature superconducting power transformer, , Institute of Physics Publishing (People Republic of China): Superconductr Science and Technology 17 (2004) 1014-1017.

[4] Tixador P., HTS transformers and SMES, *KIT Summer School on Superconductivity,* Karlsruhe 2007

[5] Grzesik B., Janowski T., Stępień M., HTS Toroidal Helical Transformer, *Journal of Physics: Conference Series,* Article no. 012311 Vol. 97, 2008.

[6] MPS, Magnet-PHYSIK Dr. Steingroever GmbH, Cologne, Germany, **http://www.magnet-physics.com/company.html**

***Authors**: dr inż. Mariusz Stępień, dr hab. inż. Bogusław Grzesik, Politechnika Śląska, Katedra Energoelektroniki, Napędu Elektrycznego i Robotyki, ul. B. Krzywoustego 2, 44-100 Gliwice. E-mail: mariusz.stepien@polsl.pl, bogusław.grzesik@polsl.pl*

Conference **ELMECO-6**
ELECTROMAGNETIC DEVICES AND PROCESSES IN ENVIRONMENT PROTECTION
joint with
9th Seminar APPLICATIONS OF SUPERCONDUCTORS **AoS-9**
June 24 – 27, 2008 Nałęczów, Poland

INVESTIGATIONS OF THE DBD REACTOR WITH METAL MESH ELECTRODES AND GLASS WOOL DIELECTRIC

Ernest GNAPOWSKi

Institute of Electrical Engineering and Electrotechnologies

Streszczenie. *Badano model reaktora plazmowego z wyładowaniami barierowymi jako źródło nietermicznej plazmy do zastosowań w procesach dezynfekcji, sterylizacji, obróbki gazów, a także do zastosowań rolniczych i biotechnologicznych. Reaktor składa się z elektrod siatkowych między którymi umieszczono dielektryk porowaty w formie waty szklanej.* ***(Badania eksperymentalne reaktora z wyładowaniami barierowymi w obecności elektrod siatkowych i dielektryka porowatego).***
Abstract*. Compact plasma reactor with atmospheric pressure discharges generated in dielectric barrier (DB) configuration as a source of active species for the purpose of disinfection, sterilization, polluted gas treatment, VOC elimination and especially in biotechnological and agriculture applications, is proposed and investigated in this paper. Reactor consists of mesh electrodes and located between them porous dielectric.*

Słowa kluczowe: wyładowana dielektryczne barierowe, generacja ozonu, nietermiczna plazma, elektrody siatkowe.
Keywords: ozone, non-thermal plasma, glass-wool packing, atmospheric pressure glow discharges (APGD).

Introduction

Investigations on the improvement of dielectric barrier discharge plasma reactor's efficiency are carried out for a long time in many research centers. They are focused on application of new electrodes' configurations, dielectric materials, reactor's geometries and electric power supply systems [1],[2], [3], [4].

Novel configurations of glow atmospheric pressure discharges, so called spatially confined discharges, in narrow channels, porous or micro-hollow structures with the presence of perforated or fibrous packing and capillary electrodes have recently been investigated intensively as a promising source of electrons and free radicals chemistry without the flow gas heating [5], [6], [7].

In the configuration of ozone generator, proposed in the paper, the combination of volume dielectric barrier discharges, atmospheric pressure glow discharges in narrow channels of mesh electrode and fibrous dielectric as well as surface discharges on the glass fibers of the wool dielectric and back–corona discharges are expected to occur.

Presented in the paper preliminary investigations of DBD reactor with metal mesh electrode and glass wool dielectric confirm possibility to generate atmospheric pressure discharges with quite high intensity and at relatively low value of supply voltage of mains frequency that could be the source of energetic electrons and free radicals. Presence of the wool glass packing in the discharge gap causes an increase of power delivered to the discharge zone and the discharges intensity.

Experimental reactor

Characteristics of the discharge are measured in the developed model of the reactor, that allows varying the electrode distance and the thickness of dielectric layer.

In the investigated configuration the air or oxygen was flowing through fine mesh metal electrode (#400).The second mesh electrode was covered by polyamide insulating foil. Between electrodes, in the discharge gap, the glass wool dielectric has been inserted. The electrodes diameter is 5 cm and the gap distance can be regulated from 1-10 mm. The transparent Teflon's reactor housing made the observation of discharges possible (Figure 1).
An experimental system consisted of 50 Hz, 230/10000 V transformer with regulated by autotransformer voltage, gas flow meter (EL-FLOW F-202AV-AAD-44-V) and its controller (E-7400-10-01-01-AAA) as well as ozone monitor BMT 961TC. The applied voltage, discharge current and their courses were measured by a high voltage probe (P6015A) with oscilloscope Tektronix TDS 380, 400MHz, and 2GS/s.

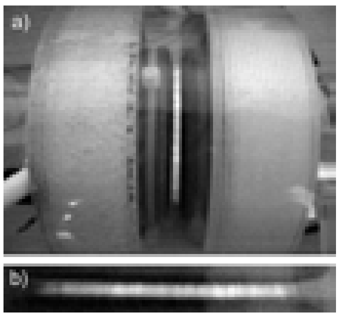

Fig. 1. Picture of the reactor (a) and gap with the discharge (b); gap lenght - 4 mm, gas flow rate 0.5 l/min, air.

The electrical power to the discharge was measured by the voltage-charge Lissajous's figures - signal proportional to the charge was taken from 0.51μF capacitor connected in series with reactor. Conditions of the experiments are gathered in Table 1.

Table 1. Experimental conditions

Parameter	Setting used
Electrode diameter, mm	50
Discharge gap, mm	1 – 5
Dielectric thickness, mm	0.025, 0.05, 0.075
Flow rate, L·min^{-1}	0.5 – 2
Gas pressure, atm	1
Material gas	Synthetic air
Supply voltage value and frequency	0 – 10 kV, 50 Hz

Results and discussion

Discharges in the configuration with dielectric barrier usually consists of a great number of more or less uniformly distributed filaments in parallel, while atmospheric pressure glow discharges (APGD) are characterized by single current pulse per half period of the AC supply voltage [5], [7], [8].
At some conditions, in the same electrode configuration with dielectric barrier, two kinds of discharges can be generated and sometimes they are called as type 1 and type 2 discharges [5]. To stabilize and make the atmospheric pressure glow discharges homogenous the three basic conditions should be satisfied: (i) the presence of solid dielectric material between discharge electrodes, (ii) the suitable kinds of dilution gases passing the discharge gap, (iii) the power supply frequency over 1 kHz [6], [8]. It is relatively easy to generate APGD in such gases like helium, neon and their mixtures, even at 50/60Hz mains frequency of power supply voltage, but in the case of air, nitrogen or argon transition the glow into filamentary discharge is usually observed. Not only the kind of gas but also the mesh electrodes' presence facilitates generation the APGD and makes discharges more homogenous [7]. As investigations in [9] show, the discharge energy at the presence of mesh electrode is higher than for flat one and the stability of the discharge for fine mesh is much better. Also, the fibrous dielectric can play similar roles to mesh electrode.

The discharge observed in the investigated reactor (Figure 1) homogenously fill up the gap. The surface discharges have been additionally observed in the presence of the glass wool packing. The discharge is more homogenously distributed in lesser gap. For gaps longer than 5 mm, the sparks have started to occur on the electrodes' edges, where electric field is not uniformly distributed. Voltage and current waveforms of the discharge are presented in Figure 2 and the Lissajous figures for the reactor with and without glass wool packing are shown in the Figure 3.

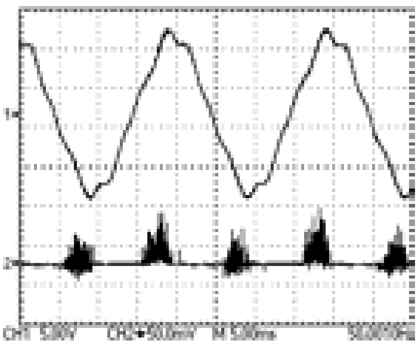

Fig. 2. Waveform of voltage and current of the discharge in the reactor with glass wool packing in air, gap lenght – 3 mm, flow rate-1l/min.

Figure 2 shows that the polarity of supply voltage influences the positive and negative half cycles of current's course. That could be explained by different affect of the negative and positive charges on the fibers of the glass wool dielectric packing. The presence of glass wool packing in the discharge gap cause not only the increase of discharge intensity but also increase of power delivered to the discharge, as it can be seen in Figure 5, what is more, it is confirmed by bigger surface of the Lissajous figure. In the paper [9] the bigger surface of the Lissajous figure is also explained by the influence of resistive losses that occur due to partial discharges at the fine mesh electrode.

Discharge power per unit electrode surface calculated from Lissajous figures is equal to 3500 W/m3 in the reactor with glass wool packing in comparison to 3000 W/m3 for reactor operating without glass wool packing at the same conditions.
The ozone concentration not only depends on the value of supply voltage and gas flow rate as it was expected, but also on the gap length and presence of glass wool dielectric in the discharge gap.

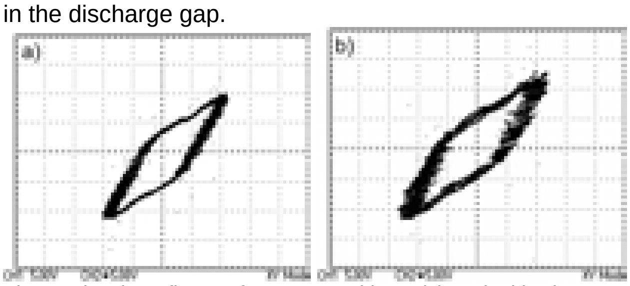

Fig. 3. Lissajous figures for reactor without (a) and with glass wool packing (b) for air at the same conditions of gas flow rate and electrode distance (0,5l/min, gap - 2 mm, 50 Hz, 0,51μF series capacitance).

The presence of the glass wool barrier would facilitate the occurrence of the so called back-corona discharges that influence the overall discharge intensity and can be effective for decomposition of gaseous pollutants, like VOC, hydrocarbons or nitrogen oxides.

Conclusion

The main purpose of the investigation presented in the paper was to check a configuration of ozone generator being the combination of the DBD's reactor with the porous or fibrous dielectric packing and with mesh electrodes, in which the plasma gas is flowing perpendicularly through the mesh and dielectric. First results show that both presence of mesh electrodes and glass wool packing influence the intensity of the discharge that occurs at lower value of supply voltage in comparison to traditional DBD's or surface discharge electrodes' arrangement. Courses of current and Lissajous figures confirm the role of mesh electrodes and fibrous dielectric on the discharge behaviour, which is the source of non-thermal plasma being the mixture of volume dielectric barrier discharge plasma, the surface one and micro-plasmas in the mesh holes and micro-channels of the fibrous dielectric glass wool packing.
Further investigations should be performed to test out the impact of mesh's dimension, gas composition as well as the type of porous material as a packing dielectric on the discharge intensity, ozone concentration, energetic effectiveness of its production and gaseous pollutants destruction efficiency.

REFERENCES

[1] I. Pollo, *J. Adv. Oxid. Technol.* Vol. 7, No.1, 2004
[2] K. H. Becker, U. Kogelschatz, K. H. Schoenbach and R. J. Barker (Eds.): Non-equilibrium Air Plasmas at Atmospheric Pressure, Taylor &Francis, CRC Press, 2004
[3] H. Stryczewska, et all, Non-thermal Plasma Based Technology for Soil Treatment, *Plasma Process.Polym,* 2005, 2, 238
[4] U. Kogelschatz, *Transaction of the Institute of Fluid Flow Machinery,* No. 119, 2007, 55
[5] L. Hulka, G. J. Pietsch, *Plasma Process.Polym,* 2005, 2, 222
[6] A. Bogaerts et al, *Spectrochimica Acta,* Part B 57, 2002, 609
[7] S. Okazaki, M. Kogoma et al., *J. Phys.D:* Appl. Physics, 1994, 1985
[8] Gherardi N, Gouda G, Gat E, Ricard A, and Massines A, Plasma Sources Sci. Technol. vol. 9, 2000, 340
[9] J. Tepper, P. Li and M. Lindmayer, Proc. Of XIV Intern. Conference on Gas Discharges and their Applications, Liverpool, 01.-06. Sept. 2002

***Authors**:* Ernest Gnapowski, Henryka Danuta Stryczewska, Institute of Electrical Engineering and Electrotechnologies, Faculty of Electrical Engineering and Computer Science, Lublin University of Technology, 20-618 Lublin, Nadbystrzycka Street 38A, Poland, fax. No +48 81 5384289

Conference **ELMECO-6**
ELECTROMAGNETIC DEVICES AND PROCESSES IN ENVIRONMENT PROTECTION
joint with
9th Seminar APPLICATIONS OF SUPERCONDUCTORS **AoS-9**
June 24 – 27, 2008 Nałęczów, Poland

COAXIAL MICROPLASMA SOURCE

Łukasz KROPLEWSKI[1], Paweł ŻOCHOWSKI[1], Mariusz JASIŃSKI[1], Mirosław DORS[1], Zenon ZAKRZEWSKI[1], Jerzy MIZERACZYK[1,2]

The Szewalski Institute of Fluid Flow Machinery (1), Gdynia Maritime University (2)

***Abstract**. In this paper the results of an experimental investigation of a microwave sustained discharge in argon at atmospheric pressure are given. The coaxial based plasma torch operated at frequency of 2.45 GHz for gas flow rates of 0.7, 1.5 and 3 l/min. Measurements of the absorbed versus reflected power as well as the electromagnetic field and the anti-bacteria UVB radiation close to the discharge were conducted. The obtained results are an/come as an effect of a preliminary investigation that yielded interesting focal points and indicated several areas for improving the design as well as the performance of the micro-plasma source being examined.*

Keywords: microwaves, microwave plasma, microplasma.
Słowa kluczowe: mikrofale, plazma mikrofalowa, mikroplazma.

Introduction

Nowadays, there is a growing interest in atmospheric pressure microwave microplasma sources (MMSs) [1-8]. They are needed for gas cleaning, microwelding, surface modification, light sources, and atomic spectroscopy system. They can be also used in the biomedical applications such as sterilization of medical instruments, high-precision surgery, cells treatment and deactivation of bacteria and viruses [1-8].

We present a new MMS based on a coaxial line. The main advantage of the presented MMS is its simplicity and low cost. Our first model of MMS was described in [9]. Here we present its advanced version.

Experimental set-up

The scheme of the experimental setup is shown in Figure 1. It consists of a microwave magnetron generator (2.45 GHz), microwave power measuring system (directional coupler, power meters with thermistor mounts), gas flow control system (Mass flow controller) and microwave microplasma source (MMS). The whole arrangement was connected via coaxial cable (50 Ω).

The absorbed microwave power P_A, i.e. microwave power delivered to the discharge was calculated as P_I - P_R, where P_I and P_R are the incident and reflected microwave powers, respectively. The incident and reflected microwave powers P_I and P_R were directly measured using directional coupler equipped with bolometric heads and HP power meters (Fig. 1).

In this investigation argon at atmospheric pressure was used as a working gas. The argon flow rates varied from 1 to 20 l/min. The microwave power was from 10 to 80 W.

The structure of the presented MMS is based on the transmission coaxial line. The sketch of the MMS is shown in Fig. 2.

Electromagnetic field and UV-B emission from plasma region were measured using ETS-Lindgren™ Model 1600 Microwave Survey Meter and UVB-20 Sonopan meter, respectively.

Results

As can bee seen in Fig. 3, shape of microplasma generated using our MMS depends mainly on the argon flow rate, whereas power delivered to the discharge has no effect. The height of the microplasma increase with argon flow rate. At the argon flow rate of 3.0 l/min microplasma tends to split into two filaments.

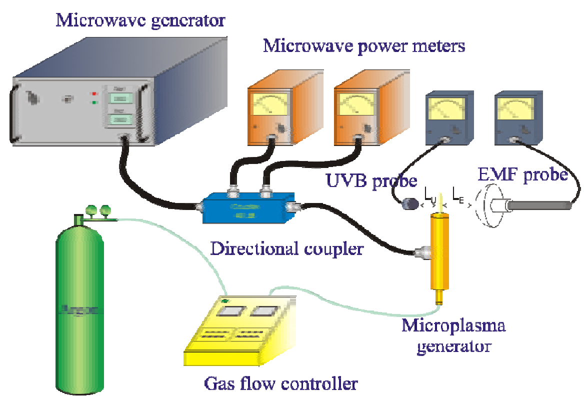

Fig.1.Experimental set-up.

Influence of the incident microwave power P_I on the reflection coefficient P_R/P_I for different argon flow rates Q is shown in Fig. 4. We can see that at low incident power and high argon flow rate the reflection coefficient is relatively high. It decrease when increasing incident power and argon flow rate. In all cases there can be observed a volatile behaviour around 80 W of incident power. This fact is due to the microwave generator shifting from pulse mode to a continuous work mode.

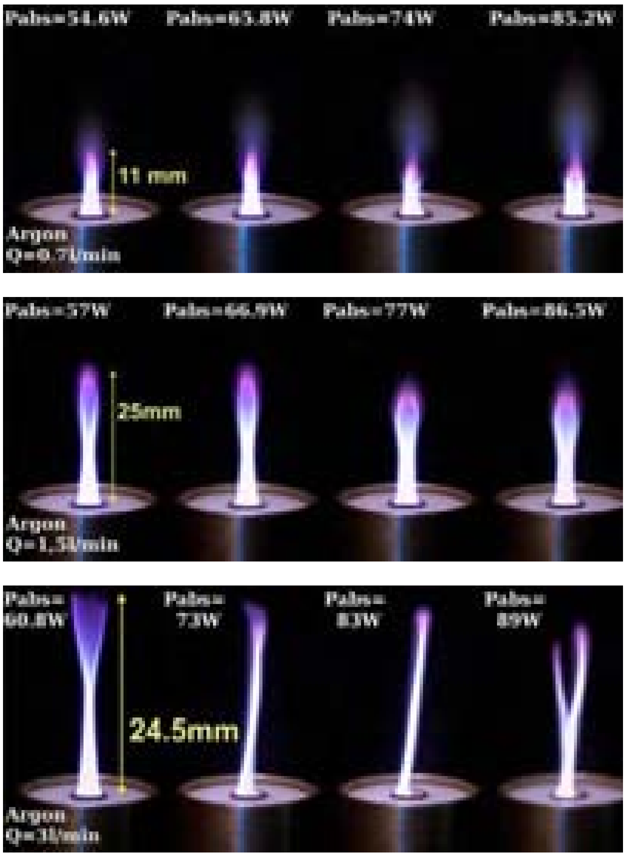

Fig. 3. Microplasma shapes for argon flow of 0.7 l/min, 1.5 l/min and 3.0 l/min.

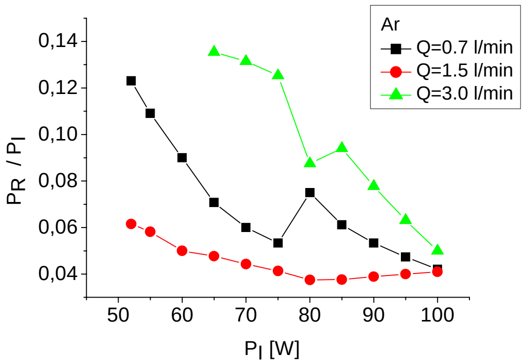

Fig.4. The reflection coefficient P_R/P_I versus incident microwave power for different argon flow rates Q.

Similar effect of change from pulse to continuous mode of work is seen in electromagnetic field measured 11 cm from the plasma region (Fig. 5) and in results of UV-B measurements carried out 7 cm from the plasma region (Fig. 6).

It is known, that sensitive of bacteria to UV-B radiation depends on their kind and radiation time. For example, *Escherichia coli,* which is typical bacteria in epidemiological studies, is killed in 90% after absorbing 30 J/m^2 of UV-B. Taking into account results presented in Fig. 6, one can calculate that *E. coli* is killed in 90% after 750 s of radiation using our microplasma generated at argon flow rate of 3.0 l/min and absorbed power of 96 W when placed 7 cm from bacteria contaminated material.

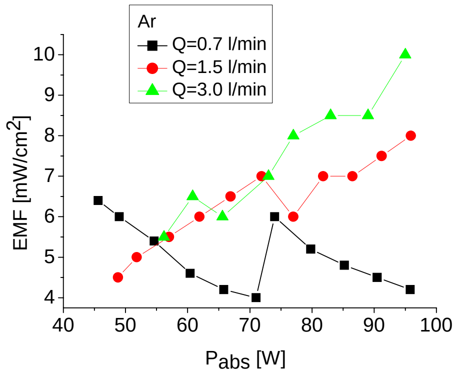

Fig.5. Electromagnetic field measurement versus the absorbed microwave power P_{abs} for different argon flow rates. Probe was located 11 cm from the plasma region.

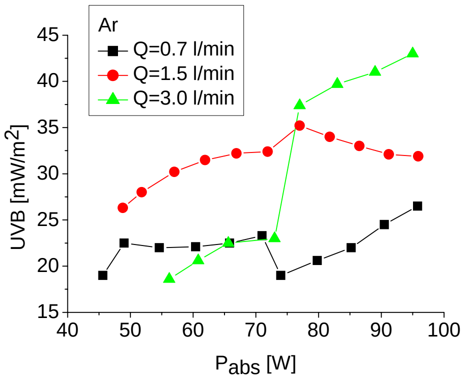

Fig.6. Anti-bacteria UVB radiation from the microplasma versus the absorbed microwave power P_{abs} for different argon flow rates. Probe was located 7 cm from the plasma region.

Conclusions

The simplicity of the MMS, operation stability and parameters of the microplasma allows the conclusion that the presented MMS can find practical applications in various fields, including material disinfection.

This research was supported by the Ministry of Science and Higher Education (MNiSW) under the programme 0895/B/T02/2007/33.

REFERENCES

[1] Kim J., Terashima K., *Proc. APSPT-4, (*2005) 324
[2] Yoshiki H., *Jpn. J. Appl. Phys.*, 45 (2006) 5618
[3] Iza F., Hopwood J.: *Plasma Sources Sci. Technol.*, 14 (2005) 397
[4] Kikuchi T., Hasegawa Y., Shirai H., *J. Phys. D: Appl. Phys.*, 37 (2004) 1537
[5] Stonies R., Schermer S., Voges E., Broekaert J.A.C., *Plasma Sources Sci. Technol.*, 13 (2004) 604
[6] Bilgic A.M., Engel U., Voges E., Kuckelheim M., Broekaert J.A.C., *Plasma Sources Sci. Technol.,* 9 (2000) 1
[7] Stalder K.R., McMillen D.F., Woloszko J., *J. Phys. D: Appl. Phys.*, 38 (2005) 1728
[8] Sladek R.E.J., Stoffels E., *J. Phys. D: Appl. Phys.*, 38 (2005) 1716
[9] Goch M., Jasiński M., Zakrzewski Z., Mizeraczyk J., *Czech. J. Phys.*, 56 (2006) 795

Conference **ELMECO-6**
ELECTROMAGNETIC DEVICES AND PROCESSES IN ENVIRONMENT PROTECTION
joint with
9th Seminar APPLICATIONS OF SUPERCONDUCTORS **AoS-9**
June 24 – 27, 2008 Nałęczów, Poland

TRANSVERSAL GAS DISCHARGES IN PLASMA LIQUID SYSTEMS AND ITS APPLICATIONS FOR ENVIRONMENTAL PROTECTION

Valeriy Chernyak[1], Sergej Olszewski[1], Iryna Prysiazhnevych[1], Vitalij Yukhymenko[1], Vadym Naumov[1], Dmitry Levko[2], Anatolij Shchedrin[2], Andriy Rybatsev[2], Valentina Demchina[3], Vladimir Kudryavtsev[3]

Kyiv National Taras Shevchenko University (1), Institute of Physics, National Academy of Sciences of Ukraine (2), Gas Institute, National Academy of Sciences of Ukraine (3)

***Abstract**. Results of the researching of plasma-liquid systems based on transversal discharges at atmospheric pressure for different ecological applications (such as: reforming of liquid hydrocarbons (biofuels) for obtaining hydrogen enriched combustible gases and for the destruction of toxic hydrocarbons in aqueous solutions) are presented in this work.*

Keywords: Electric discharge, non-equilibrium plasma chemistry, plasma-assisted fuel reforming, water clearing.

Introduction

Plasma-liquid systems (PLS) with transversal discharges were used for nanoparticles generation [1], plastic gasification [2], etc. One of the interesting applications of these devices for ecological purpose are reforming of liquid hydrocarbons (biofuels) for obtaining hydrogen enriched combustible gases and destruction of toxic hydrocarbons in aqueous solutions. Using of hydrogen enriched fuel mixtures leads to more complete and controllable combustion of fuels and reduces harmful emissions, such as NO_x and SO_x. The possibility of direct destruction of compound molecular structures in water by using such PLS enables to use these devices for water cleaning from highly active organic polutants [3].

PLS with transversal discharges are systems based on secondary discharge supported by plasma of transverse arc [4] and the discharge in gas channel, which is created by the gas flow (or by two counter flows) immersed into the liquid [5].

Inputting of the additional ionization source (transversal arc) appreciably inhibits development of overheated instability in plasma of the secondary discharge. It leads to increasing of the area of plasma-liquid contact. Besides using of the secondary discharge enables to control energy of charged particles bombarding liquid surface in wide range [6]. The large ratio of surface of plasma-liquid contact to the plasma volume and the process of effective ejection particles from plasma into the liquid by transversal gas flow are typical of discharges in gas channel with liquid wall.

Experemental Setups

Experiments were done with a PLS reactors with secondary discharge of the static type (Fig. 1.a) and of the dynamic type and reactors of the DGCLW type with one (Fig. 1.c) and two (Fig. 1.d) counter gas streams flooded in a fluid. Its consists of the cooper rod electrodes (1), plasma colomn (2), liquid (3), electrode in liquid (4), quarts tubes (5).

The plasma was diagnosed by the UV-NIR optical emission spectroscopy using the SPECAIR [7]. The component content of output gas products after the processing in the reactor was analyzed by the mass-spectrometry using a monopole - mass-spectrometer MX 7301 and by the gas chromatography using a gas chromatograph 6890 N Agilent with the thermal conductivity detectors. The spectrophotometry was used for study of a liquid after plasma treatment.

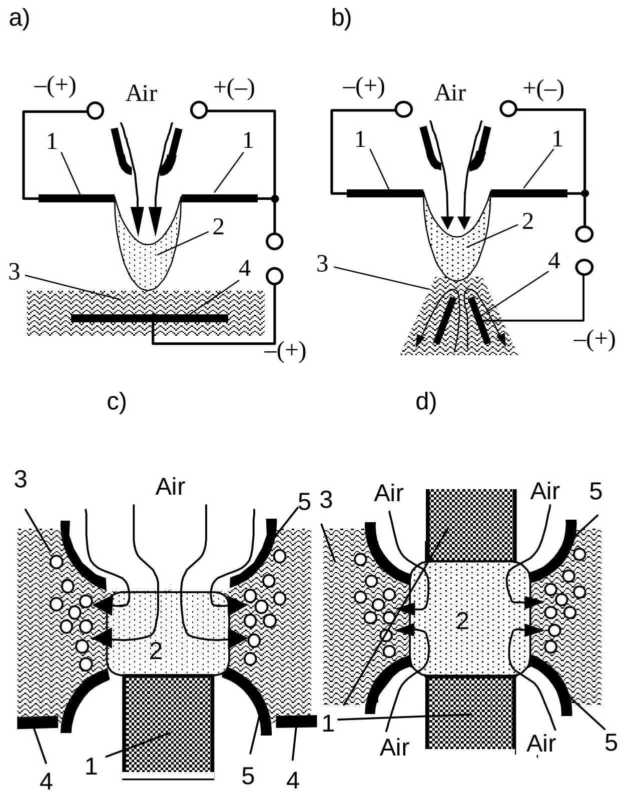

Fig. 1. Experimental setups.

Numerical modeling

In numerical modeling, the composition and concentrations of gas-phase species produced in the PLS reactor in the DGCLW discharge were calculated using a system of kinetic equations for kinetically valuable components of air-ethanol-water plasma and the Boltzmann equation for electron energy distribution function similarly to the 1D fluid (volume averaged) model used in [27] and modified by taking into account specific cross sections and rate constants for plasma-chemical reactions in the ethanol-water system according to recent recommendations of NIST [28]. In calculations it is assumed that (i) electric power introduced into the discharge is immediately averaged in plasma volume, (ii) internal electric field in the discharge does not vary in space and time, and (iii) during the pass of air through the discharge into the reactor its content is totally refreshed and its flow rate in the reactor volume is the same as in the discharge gap (see Fig. 2). The full kinetic mechanism includes 59 components (C_2H_5OH, N_2, O_2, H_2O, H_2, CO, etc), 76 electron-molecular processes, and 364 chemical reactions (for details see Web-site http://www.iop.kiev.ua/~plasmachemgroup).

Basic Results

Plasma reforming of ethanol:

- The dynamic plasma-liquid system with the electric discharge in a gas channel with liquid wall formed by a submerged air flow in liquid ethanol is quite efficient in plasma-chemical reforming of ethanol into syngas due to formation of chemically active agents in sufficient amount.
- The main stable gas-phase output components produced from ethanol in the plasma-chemical reactor are H_2, CO, CH_4, and C_2H_4.
- The composition content of output products and power inputs on the ethanol conversion in the electric discharge depends on the gas that forms the plasma and on the ethanol-water ratio in the mixture.
- The H_2 yield increases with increasing discharge power and reaches maximum if ethanol and water in the solution are in equal amounts.
- The minimal value of power inputs in investigated discharge modes is ~ 2.3 kWh/m^3 at the power of output syngas ~ 4.1 kWh/m^3.
- The kinetic plasma-chemical modeling is in a fairly good agreement (at least, for main syngas components, H_2 and CO and main components of plasma emission spectra C, C_2, CN, OH) with experimental data predicting a non-thermal plasma-chemical mechanism of the ethanol conversion in the investigated plasma-liquid system.

Plasma treatment of distilled water:

- The dynamic plasma-liquid reactor based on DGCLW makes essentially less nitrogen containing oxidizers, in comparison with the similar systems based on the secondary discharge.
- Use of supplied to a liquid of negative electric potential more effectively for generation of oxidizers than use of supplied of positive.
- The production efficiency of peroxide of hydrogen is more at use of air, than without it.
- The generation of nitric acid is the greatest in a mode without any gas.
- The current-voltage characteristic of DGCLW is unstable in time and will melt asymmetrical owing to generation of oxidizers in a solution.
- The kinetic plasma-chemical modeling is in a fairly good agreement (at least, for main components of plasma emission spectra N_2, NH, OH) with experimental data.
-

Plasma treatment of phenol solution:

- The flowing plasma-liquid system with electric discharge in a gas channel with liquid wall which is formed by a submerged gas flow in liquid is very effective in destruction of phenol in water due to the formation of chemically active oxidants in sufficient amount.
- The efficiency of destruction of phenol increases with increasing of the time of plasma-chemical processing in the reactor.
- The negative polarity of "liquid" electrode in discharge is more effective for plasma-chemical processing than the positive polarity.
- Plasma-treated solutions are chemically unstable in time and the time of their stabilization is longer than in other plasma-liquid systems.
- Final products of destruction in stabilized solutions qualitatively differ from products in other plasma-liquid systems.

REFERENCES

1. Chernyak V., Naumov V., Yukhymenko V., Zrazhevskij V., Prisyazhnevich I. The synthesis of nano-particles in plasma - liquid systems // Electronic Proc. 17th International Symposium on Plasma Chemistry (ISPC17), Toronto (Canada), August 7-12th, 2005. (3 pages).
2. Chernyak V., Naumov V., Trokhymchuk A., Prisyazhnevich I., Yukhymenko V., Babich I., Slyusarenko Yu. Transverse arc in gas and its application // Proc. XVIth Symposium on physics of switching arc, Vol. II: invited papers, Brno, Czech Republic, September 5-9, 2005.- pp. 223-231.
3. Chernyak V.Ya. Non-equilibrium plasmachemical destruction of toxic agents // NBC International.-2003.-№ 4.-P.55-56.
4. Chernyak V.Ya., Yukhymenko V.V., Babich I.L., Zrazhevskyy V.A., Tarasova Ya.B., Slyusarenko Y.I., Woewoda Yu.V., Chaban Yu.A., Trokhymchuk A.K. Destruction of chlorine-containing organic agents in a system plasma-liquid // Problems of Atomic Science and Technology. Series: Plasma Physics(10). 2005, № 1.-P.172-174.
5. Veremii Yu., Chernyak V., Trokhymchuk A., Kondratyuk Ya., Zrazhevskij V. Physicochemical properties of a plasma-liquid systems with an electric discharges in gas chanel with liquid wall //Ukr. J. Phys. 2006. V.51, N8.-P.769-774.
6. Prysiazhnevych I.V., Chernyak V.Ya., Safonov E.K. Optical and probe diagnostics of plasma-liquid systems with secondary discharge // Problems of Atomic Science and Technology. 2007.-№ 1. Series: Plasma Physics (13), P. 212-215.
7. *URL*: www.specair-radiation.net

***Authors**: prof. Valeriy Chernyak, Kyiv National Taras Shevchenko University, st. Prospect Glushkova 5/2, 03123 Kyiv, Ukraine. E-mail: chern@univ.kiev.ua; chernyak_v@ukr.net.*

PLASMA PROPERTIES OF TRANSVERSE ARC AT ATMOSPHERIC PRESSURE

Iryna Prysiazhnevych, Valeriy Chernyak, Sergej Olszewski, Vitaliy Yukhymenko

Kyiv National Taras Shevchenko University

***Abstract**. Plasma properties of the electric arc in the transversal blowing airflow at atmospheric pressure were investigated. Optical emission spectroscopy was used for diagnostics of this discharge. Method for determining of relative concentrations of emitted compounds in plasma by using SPECAIR program was suggested. It was shown that plasma of the transverse arc is nonthermal and its character is changing along the gas flow.*

Keywords: nonequilibrium plasma, transverse arc, population distribution temperatures (electronic, vibrational, rotational temperatures)

Introduction

It is well known that for solving a lot of different applied tasks plasmachemistry needs the sources of nonequilibrium atmospheric pressure plasmas with controllable level of nonisothermality. The most interesting from this point of view are dynamic plasma systems with transversal gas flows of atmospheric pressure: gliding arc *GA* [1,2], gliding arc in tornado *GAT* [3,4], transverse DC glow discharge [5], arc discharge in the transversal blowing gas flow (transverse arc *TA*) [6,7]. A transversal gas ventilation of the discharge increases efficiency of heat- and mass-exchange between plasma and environment. It is possible to influence on the plasma properties due to the choosing gas flow rate and discharge parameters (current, voltage). The results of researching of plasma properties of the transverse arc in airflow at atmospheric pressure are presented in this work.

Experimental setup

Arc in the transverse blowing gas flow differs from the non-stationary *GA* of Czernichowski type [1,2] by the fixed arc length. It has also a convective cooling of the plasma column by the airflow but without conductive heat losses at walls since it is a free arc jet. The scheme of the *TA* discharge in gas flow is shown on Fig. 1.

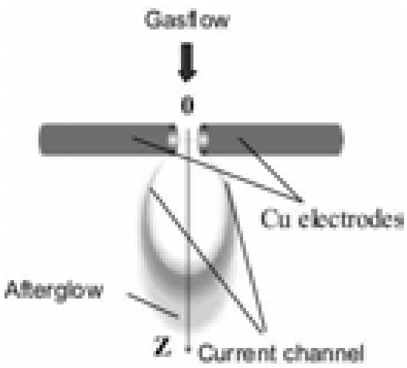

Fig.1. Experimental sketch of the transverse arc

The atmospheric airflow was directed from the nozzle across two horizontal opposite electrodes and formed a bright crescent-shaped electric arc. The rod copper electrodes with diameter *d*=6 mm and nominal gap between them δ ≈1.5 mm were used. Axially symmetrical nozzle, with inner diameter ∅=1 mm made from stainless steel was maintained vertically perpendicular to the electrode axis at the length *L* = 20 mm and centered strictly between the electrodes. The arc discharge was powered by the DC source at the ballast resistance R = 2 kΩ in the circuit. To regulate the airflow rate *G* a standard dry air system supplied with the flow meters was used. There was enough high gas-dynamic pressure in the flow to blow out the electric arc downstream. The gas flow rates *G*=0-110 cm^3/s and discharge current I_d (330-660 mA) were kept constant.

Diagnostics of plasma parameters was made by optical emission spectroscopy (OES). Computer operated CCD-based spectrometer SL40-2-3648USB with spectral resolution ~ 0,73 nm was used for spectra registration in the range of 210-1100 nm.

Temperatures, which correspond to the population distribution of the excited electronic states of atoms (electronic temperature T^*_e), vibration and rotational levels of molecules (vibration T^*_v and rotation T^*_r temperatures) in investigated plasmas, were determined.

Methodology

Determination of mole fractions of the emitted compounds of nonequilibrium plasma at atmospheric pressure in the case of weakly known composition of plasmaforming gas is very interesting and actual problem. Method of evaluation of relative concentration of neutral and ionic components in generated plasma by using SPECAIR [8] was suggested in this work.

SPECAIR code allows modeling the absolute intensity of spectral radiation emitted by gases and plasmas of various compositions (*N, O, C, NO*, N_2, N_2^+, *OH, NH*, C_2, *CN, CO*) in the wide spectral range for different pressures Traditionally SPECAIR uses database of an initial LTE species distribution in air at various temperatures (translation T_{trans}, electronic T^*_e, vibrational T^*_v and rotational T^*_r) in the range T=1000-14000 K.

So far as using known methods of working with SPECAIR for determining relative concentrations of radiating species [9] is not possible in the case of weakly known compound of plasmaforming gas, we suggested to use the following procedure.

At the first stage the identification of emission spectra was made and T^*_v and T^*_r temperatures were determined by fitting experimental spectrum of the 2nd positive system of N_2 with results of SPECAIR simulation. Electronic temperature T^*_e was evaluated from the best fit of the relative intensities of N_2 (C-B) and *NO* (A-X) in experimental spectrum with simulated one (after having T^*_v and T^*_r already determined) [9]. At the next step the intensity (signal) of each radiating species $S(A_i)$ was determine from experimental spectrum and corresponding to them wavelengths λ_i. were fixed. It is better to carry out this procedure of signal determination in the range free from overlapping spectral bands and lines. After that we simulated emission spectrum of each radiating compound by using SPECAIR at previously determined T^*_e, T^*_v, T^*_r temperatures under "mole fraction" database off. The intensities of calculated spectrum $N(A_i)$ at wavelength (where the corresponding experimental signals $S(A_i)$ were estimated) were determined. Then the concentration ratio of two radiating species A_1 and A_2 can be evaluated by following formula:

(1) $$\frac{[A_1]}{[A_2]} = \frac{S(A_1)\cdot N(A_2)}{S(A_2)\cdot N(A_1)}$$

That makes possible to determine relative concentration of each component in the investigated plasma:

(2) $$[A_1]^* = \frac{[A_1]}{\sum_i [A_i]}$$

Results

Emission of N_2 2nd positive system ($C^3\Pi_u$ -$B^3\Pi_g$), of N^+_2 1st negative system ($B^2\Sigma^+_u$-$X^2\Sigma^+_g$), of *NH* ($A^3\Pi^+$-$X^3\Sigma^-$), *NO* γ system ($A^2\Sigma^+$-$X^2\Pi$), weak *OH* bands ($A^2\Sigma^+$-$X^2\Pi$), *O* lines (λ=777.2; 844.6; 926.6 nm), *Cu* lines (material of electrodes) (λ=324.75; 327.4; 465.1; 510.5; 515.3; 521.8; 578.2 nm) was observed in plasma of the transverse arc in air.

Result of fitting of experimental spectrum of the transverse arc plasma with spectrum modeled by SPECAIR is presented on **Fig.2.**

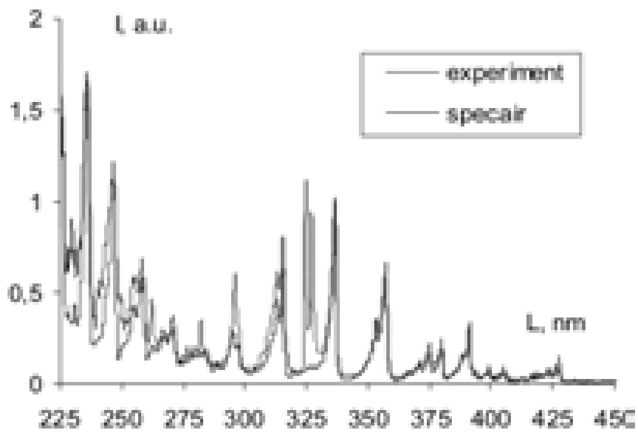

Fig. 2. Emission spectrum of transverse arc air plasma at atmospheric pressure (G=75 cm³/s Is=480 mA at the distance z=1,6 mm from electrode axis) and spectrum simulated by SPECAIR at T^*_e=4600 K, T^*_v=4200 K, T^*_r=2200 K.

From Fig.2 can be seen that a good fit was obtained. Discrepancy between spectra in the region of 325 nm can be deal with presence of Cu lines (λ=324,75 and 327,4 nm) and not identified bands (at λ=282,5 and λ=296 nm), which were not taking into account by SPECAIR calculations.

T^*_e was determined from Boltzmann plot by using intensities of oxygen spectral lines. T^*_v and T^*_r temperatures were estimated from 2nd positive system of nitrogen by fitting the experimental spectra with the simulated ones. Temperature distribution in plasma of transverse arc along gas flow z is shown on Fig. 3.

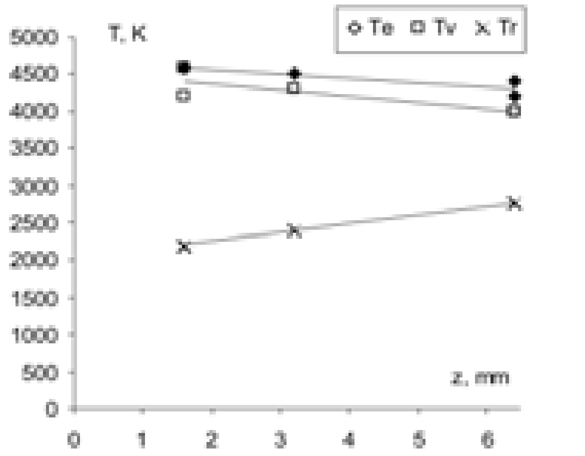

Fig. 3. Temperature distributions along air flow z (z=0 – point at electrode axis) in plasma of transverse arc at atmospheric pressure (G=75 cm³/s Is=480 mA).

Conclusions

1. Transverse arc generates nonthermal plasma with noticeable increasing of rotational temperature along the gas flow.
2. The relative concentrations of radiating plasma species (*N_2, N_2^+, NO, OH, NH*) in transverse arc were estimated by using SPECAIR. It was shown that relative concentration of [*NO*] evaluated from experimental spectra is significantly lower then data in SPECAIR database for pure air at the same temperatures.

This work was supported by the U.S. EOARD and the Science & Technology Center in Ukraine (project P354).

REFERENCES

[1] A. Czernichowski, *J. Pure & Appl. Chem.,* 66 (1994), No. 6, 1301-1310

[2] O. Mutaf-Yardimci, A.V. Saveliev, A.A. Fridman, *J. Appl. Phys.*, 87 (2000), No 4, 1632-1641

[3] C. S. Karla, I. Matveev, A. Gutsol, A. Fridman, *Elec. proc. of 2004 Technical Meeting, Central States Section,* (2004) 21-23 March 2004, Texas, A34.pdf

[5] Z. Machala, Ch. Laux, C. H. Kruger, *IEEE Trans. Plasma Sci.* 33 (2005), No 2, 320-321

[6] V. Chernyak, L. Kernazhitsky, V. Naumov, *et al J. Mol. Struc.* 744-747 (2005), 871-875

[7] I. V. Prysiazhnevych, V. Ya. Chernyak, V. V. Yukhymenko, *et al Ukr. J. Phys.*, 52 (2007)., № 11, 1061-1967

[8] SPECAIR Version 2.1. Available: http://www.specair-radiation.net

[9] Z. Machala, M. Janda, K. Hensel, *et al J. Mol. Spectr.* 243 (2007), 194-201

Authors: *Prof., Dr. Sci. Valeriy Chernyak National Taras Shevchenko University, Prospect Glushkova 2/5, Kyiv 03022, Ukraine, E-mail: chernyak_v@ukr.net; ing. Iryna Prysiazhnevych E-mail: priv@ukr.net*

MODELLING OF A MAGNETIC CURRENT LIMITER FOR RELIABLE OPERATION

G. S. Malhi[1] and S. C. Mukhopadhyay[1], A. Nafalski[2]
Massey University, New Zealand (1), University of South Australia, Australia (2)

Abstract. *The analysis of the magnetic field in the cores of a magnetic current limiter used to limit fault currents in power systems is presented in the paper. Finite element method was used to analyse different operational conditions of the limiter. In addition, the thermal analysis was applied, and both were used to determine the critical conditions of the limiter's reliable operation.*

Streszczenie. *W artykule przedstawiono analizę pola magnetycznego w rdzeniach magnetycznego ogranicznika prądu używanego do ograniczania prądów zwarciowych w układach elektroenergetycznych. Dodatkowo przeprowadzono analizę termiczna układu i wyniki obu analiz były użyte do określenia krytycznych warunków pracy ogranicznika, w celu uniknięcia jego uszkodzenia w warunkach zwarciowych.*

Keywords: magnetic current limiter, electromagnetic modelling, fault conditions.
Słowa kluczowe: magnetyczny ogranicznik pradu, modelowanie elektromagnetyczne, warunki zwarciowe.

Introduction

The frequency of fault occurrence in electrical power networks has increased considerably due to the interconnection of grids. During faults large currents are generated that by thermal or mechanical mechanisms may damage the network components. A magnetic current limiter (MCL) [1] that can be used for limiting fault currents consists of two saturable cores with sandwiched permanent magnets as shown in Fig. 1. The permanent magnets are used to saturate the core under normal operating conditions when the current is low and consequently the effective impedance of MCL is low. When large fault currents flow through the windings, the impedance of the MCL increases significantly in order to limit the current's value. A considerable amount of power is produced in MCL during a fault that leads to the temperature rise that may damage the limiter permanently. In order to protect the limiter from the damage, the thorough knowledge of the temperature distribution is required.

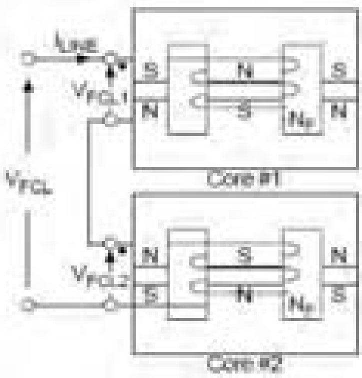

Fig. 1 Basic structure of the MCL

Field modelling

The finite element software package FEMLAB by COMSOL [2] was used for analysing the flux distribution of the MCL under normal and fault conditions. Fig. 2 shows the two dimensional geometry model of one-half of one core of the current limiter used for the field model. The model was solved after providing all necessary excitation and boundary conditions. Fig. 3 shows results of flux distribution for one core of the MCL when there is no current in the coil. The permanent magnets drive the core into the saturation region.

Under normal condition the current in one-half of the limiter aids the flux in one core but opposes the flux in the other core. The core has been modeled both for large values of positive as well as negative currents. While the current is positive and large in magnitude, the main difference is the magnitude of flux density inside the core. The flux density increases to a large value and the core is driven into strong saturation. Fig. 4 shows the flux distribution when large positive current flows in the windings. When current increases to a very high negative value (during a fault) the magnetic flux density decreases and the core comes out of the saturation. The flux distribution under this condition is shown in Fig. 5.

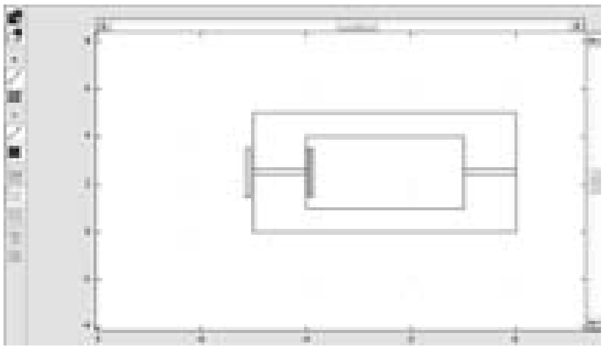

Fig. 2 2-D Geometry of MCL

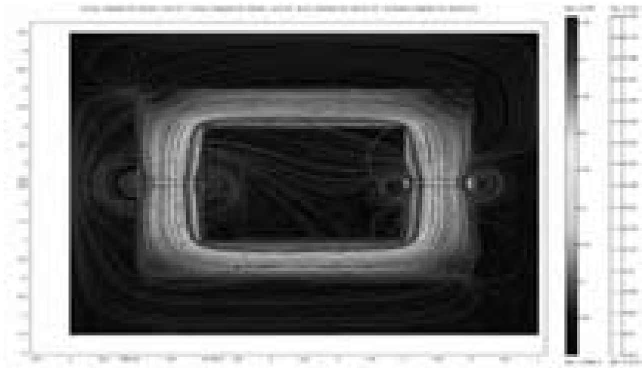

Fig. 3 Field distribution in MCL core with no current

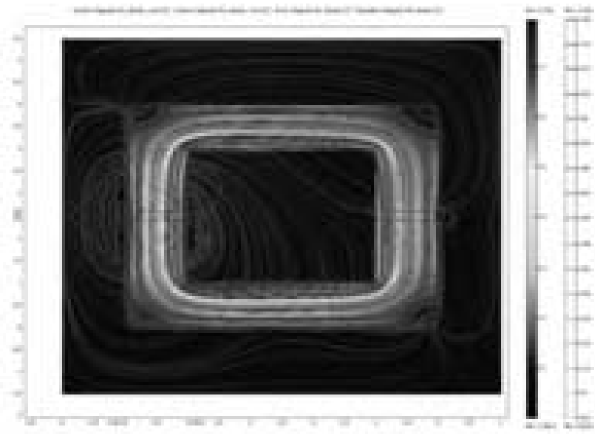

Fig. 4 Field distribution in MCL core with very large positive current

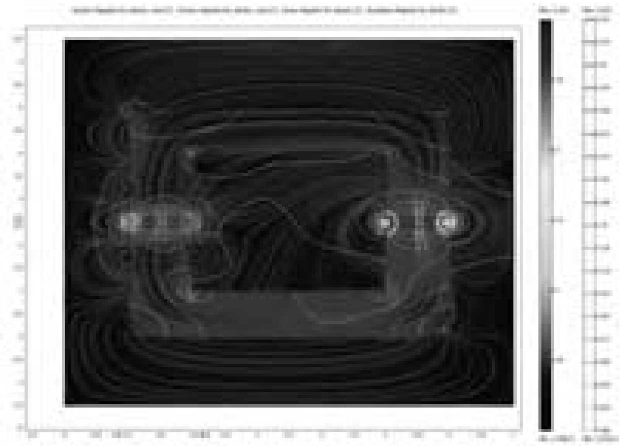

Fig. 5 Field distribution in MCL core with very large negative current

The flux density in the center of the core was evaluated as a function of the line current (Table 1). It can be seen that the large positive current forces the core to operate in saturation while the core comes out of saturation when the large negative current flows in the windings.

Table 1: Variation of magnetic flux density (T) vs current (A)

No.	Current (A)	Magnetic Flux Density (T)
1	0	0.459
2	10	0.493
3	40	0.596
4	-10	0.425
5	-50	0.278

The same model was analysed for thermal conditions. Fig 6 shows the temperature distribution results of the core in given operating conditions. The thermal analysis can be done both for steady state as well as for transient conditions. The steady state analysis is important to know the final temperature rise. Fig 7 shows the variation of final steady state temperature as a function of current. When the system operates at fault condition the final temperature can be too high and can destroy the MCL. Under the fault condition the MCL may not be allowed to operate continuously for reliable and safe operation. The allowed temperature rise for the MCL should be used as a parameter to decide about the safe time of operation. The time of a fault should be less than the time for reliable operation of the MCL. The time of allowable operation can be derived from the thermal analysis of the MCL.

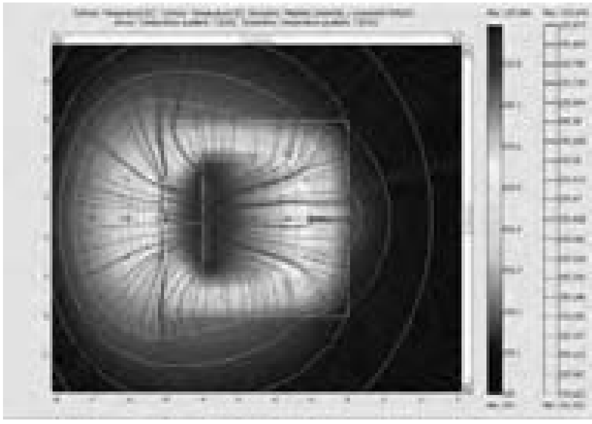

Fig. 6 Temperature distribution in one core of MCL

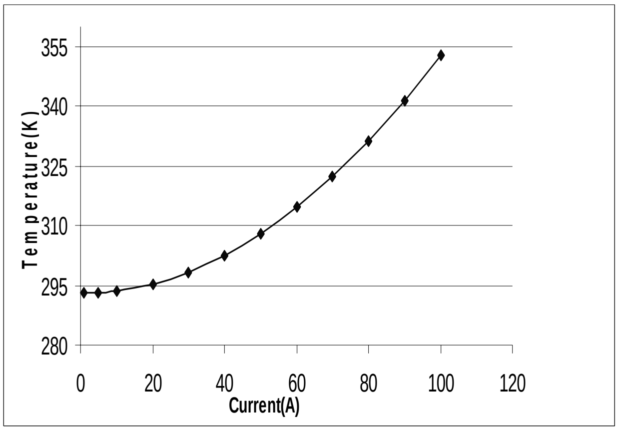

Fig.7 Temperature versus current in steady state

Conclusions

The analysis of electromagnetic field distribution of a magnetic current limiter using finite element software is presented in the paper together with the thermal analysis of the model. The analysis will be useful to restrict the operation of the limiter in order to avoid its damage during transient fault conditions. Transient analysis helps the designer in selecting the design parameters as well as to secure a safe and reliable operation of the limiter.

REFERENCES

[1] Mukhopadhyay, S. C., Iwahara, M. S. Yamada and Dawson, F. P., Analysis, design and experimental results for a passive current limiting device, *IEE Proceedings on Electric Power Applications*, 146 (1999), No. 3, 309-31.

[2] COMSOL, Multiphysics, www.comsol.com (2006).

Authors: *Mr. G. S. Malhi, Massey University, Palmerston North, New Zealand, E-mail: G.S.Malhi@massey.ac.nz, A/Prof. PhD D.Eng. S. C. Mukhopadhyay, Massey University, Palmerston North, New Zealand, E-mail: S.C.Mukhopadhyay@massey.ac.nz, Prof. PhD, DSc A. Nafalski, University of South Australia, Mawson Lakes 5095, Australia, E-mail: Andrew.Nafalski@unisa.edu.au*

Conference **ELMECO-6**
ELECTROMAGNETIC DEVICES AND PROCESSES IN ENVIRONMENT PROTECTION
joint with
9th Seminar APPLICATIONS OF SUPERCONDUCTORS **AoS-9**
June 24 – 27, 2008 Nałęczów, Poland

OZONE GENERATION CHARACTERISTICS OF OZONIZER WITH THE ROTATING TYPE ELECTRODE

Sebastian GNAPOWSKI, Chobei YAMABE and Satoshi IHARA

Saga University, Department of Electrical and Electronic Engineering, 1 Honjo-machi, Saga 840-8502, Japan

Abstract. An ozonizer using a rotating electrode was used to improve the ozone production characteristics. The ozone concentration increased up to maximum about two times lager compared with the case of no rotation. The input power increased with the rotating speed and discharge area grew up too. The reasons came from the increase of discharge length of canals during the rotation of electrode. During the experiments three types rotation electrode: different material (i.e. brass, copper and coaled gold) was used.

Keywords: rotating electrode, discharge canal, input power, ozone generation

Introduction

Many scientists have tried to increase the ozone production efficiency and the ozone has been applied to improve the human environment such as keeping higher quality of water and air [1-2].
The important parameters such as the dielectric constant, its thickness, gap distance and surface condition of electrode influence on the efficiency of ozone production. Another parameters such as the configuration of electrodes, the applied voltage waveform and the cooling system for the discharge region so on also have been studied. A different way for increasing ozone concentration using the rotating electrode was studied [3]. Previous reported papers described only the changing of ozone concentration with the experimental parameters. The important question is why the operation with rotating electrode increases the ozone concentration. What phenomena decide the increasing of the ozone concentration? In this paper, we described the characteristics of the dielectric barrier discharge (DBD) type ozonizer using a rotating type of electrode and we tried to study experimentally at first about phenomena during the rotation.

Experimental apparatus and procedure

An experimental set-up consisting of a discharge reactor and electrical circuit is shown in Fig.1. The rotating electrode was made from brass, coated gold, copper and the high voltage was applied on it. The speed of the rotating electrode was varied from 0 to 800 rpm by a variable speed motor. The dielectric barrier covered by a mesh electrode was glass tube and its thickness was 1.2 mm. The outer mesh electrode made from copper wires with diameter of 0.1 mm was grounded. The size of the copper mesh electrode was 0.2 mm square. The 99.5 % oxygen gas regulated by the digital mass flow controller was fed and the gas flow rate was in the range from 0.5 l/min to 2 l/min.

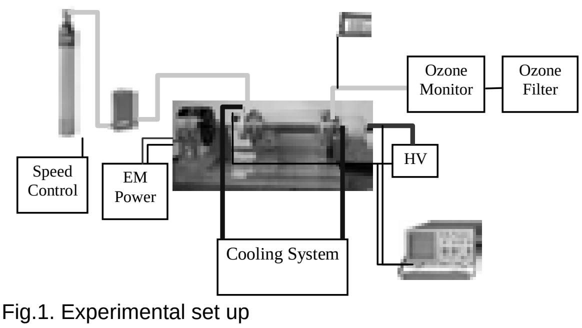

Fig.1. Experimental set up

Both the applied voltage and its frequency were set to be 9-10 kV and about 12 kHz.

The discharge gap distance was 1.1 mm and the discharge length along the reactor was 100 mm. The gas temperature at the outlet of the ozonizer was measured during the experiments. The measured data was saved every day in a computer. All experiments were carried out at atmospheric pressure in oxygen at around room temperature (15 ~ 35 ºC). The current and voltage signals were processed by a digitizing oscilloscope Tektronix TDS 520A and the voltage at the reactor was measured by a high voltage probe Tektronix P6015A. The ozone concentration was measured by the Ozone Monitor Type EG2001, measured range 0-200 [g/Nm^3]. The cooling system is very important because the temperature increase decomposes the produced ozone.

Results and discussion

The ozone concentration was improved with the case of rotation. During experiments we observed increasing of the input power with the rotating speed. The discharge area became bigger and the ozone concentration increased in spite of increasing the temperature when the rotating speed was changed from 0 rpm to 800 rpm. The temperature increased faster during the experiments operated at 800 rpm. During increasing of the rotation speed, light emission became more intensive because the discharge canals changed the position faster and as shown in Figs. 3 (a) and (b) the difference of light emission was observed. We can see the difference of the ozone concentration (g/Nm^3) as shown in Fig. 2 when the rotating speeds were changed. In this case, the applied voltage was set to be 10 kV (peak – to – peak). During the experiments the ozone concentration without rotation was about 17 g/Nm^3 at 1 l/min when brass rotating electrode was used. With same parameters the ozone concentration with copper rotating electrode was 18 g/Nm^3.

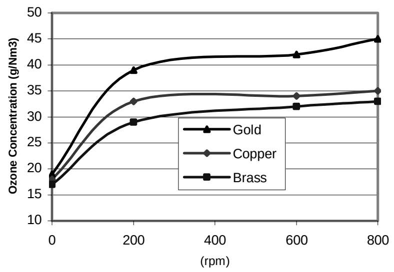

Fig.2. Ozone concentration vs. rotating speed

The highest ozone concentration without rotation we observed during experiments with a coated gold rotating electrode was about 19 g/Nm^3. When the rotating speed was 200 rpm the ozone concentration was improved about 14 g/Nm^3 more compared with no rotation (copper electrode) and 12 g/Nm^3 (brass rotatimg electrode). The gold coated rotating electrode worked the best compared with other, the ozone concentration increase 20 g/Nm^3. While rotating speed increased up to 600 rpm, the ozone concentration increased up to 3 g/Nm^3 compared to that with 200 rpm (coated gold and brass electrode) and only 1 g/Nm^3 the copper electrode. During the experiments with 800 rpm the ozone concentration was about 45 g/Nm^3 (coated gold rotating electrode), it was about 2.4 times larger compared with no rotation. The ozone concentration increases about twice compared with no rotation (brass rotating electrode) and was 2.2 times lager when copper rotating electrode was used. The best worked coated gold rotation electrode because surface electrode was kept same condition, other rotation electrode was oxidize during experiments and condition was changed.

When the rotating speed increases, the input power increases with rotating speed. The increase of the rotating speed changes the input power which is increased with rotating speed. During this experiments the gas flow rate was 0.5 l/min and the applied voltage was constant to be 10 kV (peak – to – peak). The area of the Lissajous figures was changed with rotating speed. According to the Lissajous figure we can estimate the input power to be 4.59 W (0 rpm), 5.5 W (200 rpm), 6.56 W (600 rpm) and 6.73 W (800 rpm). The increase of about 20 % at the rotating speed of 200 rpm and about 47 % increase at 800 rpm were confirmed. In the next time we changed the mesh copper electrode to spring wire electrode (wire diameter of 1.6 mm and pitch of 5 mm) we also changed gas supply from oxygen to nitrogen. We could observe and took nice (clear) photographs for single discharge canal. The discharge length of canals observed visually becomes longer with the rotating speed. These circumstances are shown in Figs. 3 (a) and (b). It was found that both the input power and discharge area became large because the discharge canals became long due to the rotating electrode. The discharge canal looks like arc. Figures 3 (a) and (b) show the different situation of discharge (i.e. difference length of canals) between without rotation and with rotation (200 rpm). Figure 3 (a) shows the discharge canal without rotation. The canal was straight and this length was same as gap distance of 1.1 mm. The discharge canal became longer with rotation as shows in Fig. 3 (b) at rotating speed of 200 rpm. Discharge canal became longer about 10 %.

Fig.3 (a) Discharge canal without rotation (unit: mm)

Fig.3 (b) Discharge canal with rotation at 200 rpm (unit: mm)

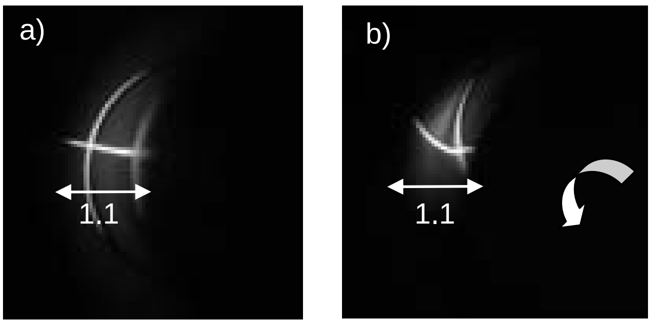

During the experiments, the discharge density and ozone concentration grew up. When the discharge canals became longest during the rotation, it will be possible to generate more collisions and more ozone concentration which will also be expected to lead higher efficiency of ozone generation.

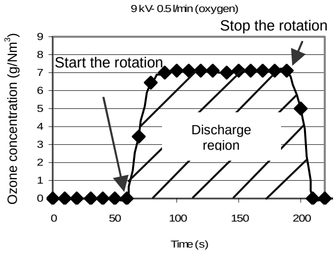

Fig.4. Variation of ozone concentration for different rotation mode

Figure 4 shows another different phenomena during the rotation of electrode. In this case, the gas flow was 0.5 l/min and the applied voltage of 9 kV (peak – to – peak) and the frequency of about 12 kHz were used. Without rotation we can't observe the discharge and the ozone concentration was zero. When the rotating speed was increased up to 200 rpm the discharge current including small discharge pulse was observed and the ozone concentration of about 7 g/Nm^3 was measured. This experimental results show that the rotation of electrode decreases the discharge onset voltage and the discharge starts at the lower voltage. Unfortunately we don't have good idea to explain about this phenomena yet although the discharge current is measured by the current pick up coil to confirm the start of discharge.

Conclusions

1. Both the discharge power and the ozone concentration were improved by using rotating electrode. In case of rotating electrode used for the ozonizer, difference phenomena such as the increasing of discharge area was observed compared with no rotation.
2. The ozone concentration increased about two times lager with rotating electrode.
3. The produced ozone increased with the rotating electrode speed and the efficiency of ozone production was improved about 30% with rotation.
4. The rotation of electrode decreased the discharge onset voltage.

Acknowledgement

A part of this work was supported by a Grant-in-Aid for Scientific Research of the Ministry of Education, Science, Sports and Culture, Japan.

REFERENCES

[1] K. Takatsu, T. Fujishima, T. Yamashita, H. Matsuo, T. Ikegami, K. Ebihara, Ozone Generation Characteristics of Compact Ozonizer with Screw Type Electrode 13th Asian Conference on Electrical Discharge, Hokkaido, University, Sapporo, Japan (2006) 1-4

[2] Murai A. and Nakajima T. "Ozone Generating Method Using a Catalysis Electrode in Barrier Discharge", 10th Interational Symposium on High Pressure Low Temperature Plasma Chemistry, Saga (2006), Japan 152-156

[3] Sebastian Gnapowski, Chobei Yamabe and Satoshi Ihara, "Ozone Generation Characteristics of Ozonizer with the Rotating Type Electrode" Japan-Korea Joint Symposium on Electrical Discharge and High Voltage Engineering, Tokyo (2007), 399-402

***Authors**: Sebastian Gnapowski, Saga University*, Department of Electrical and Electronic Engineering, *1 Honjo-machi, Saga, 840-8502, Japan, e*-mail: sgnapowski@wp.pl,
Chobei Yamabe, Saga University, Department of Electrical and Electronic Engineering, *1 Honjo-machi, Saga, 840-8502, Japan, e*-mail: yamabec@cc.saga-u.ac.jp,
Satoshi Ihara, Saga University, Department of Electrical and Electronic Engineering, *1 Honjo-machi, Saga, 840-8502, Japan, e-mail: iharas@cc.saga-u.ac.jp*

Conference **ELMECO-6**
ELECTROMAGNETIC DEVICES AND PROCESSES IN ENVIRONMENT PROTECTION
joint with
9th Seminar APPLICATIONS OF SUPERCONDUCTORS **AoS-9**
June 24 – 27, 2008 Nałęczów, Poland

PRESSURE DROP MEASUREMENTS IN CABLE IN CONDUIT CONDUCTORS (CICCs) FOR AN EXTENDED RANGE OF REYNOLDS NUMBER

Monika LEWANDOWSKA[1], Maurizio BAGNASCO[2]

Szczecin University of Technology (1), EPFL-CRPP, 5232 Villigen PSI, Switzerland (2)

***Abstract**. The experimental investigation of hydraulic resistance of flow in single channel CICCs for an extended range of Reynolds number (40-40000) has been performed at CRPP using water at room temperature and cryogenic helium. The experimental results are compared with the correlation resulting from the porous medium analogy model.*

***Streszczenie.** W pracy zaprezentowano wyniki pomiarów spadków ciśnienia w kablach nadprzewodnikowych typu CICC. Pomiary przeprowadzone zostały w bardzo szerokim zakresie liczby Reynoldsa (40-40000) przy użyciu wody oraz kriogenicznego helu. Wyniki pomiarów porównano z korelacją wynikającą z modelu, w którym obszar wiązki kabla traktowany jest jako ośrodek porowaty.*

Keywords: CICC, pressure drop, friction factor, porous media
Słowa kluczowe: kabel typu CICC, spadki ciśnienia, wsp.tarcia, media porowate

Introduction

All coils designed for ITER magnet system are made of Cable in Conduit Conductors (CICCs) cooled with forced flow of supercritical helium [1]. CICCs consist of a bundle of superconducting strands cabled in various configurations and size, depending on the desired current carrying capacity, which are enclosed in a leak tight pipe (the jacket). In some CICCs (e.g. ITER TF, PF and CS conductors) a low hydraulic resistance central channel, delimited by a spiral from the annular bundle region, has been added.

During normal operation of superconducting magnets heat coming from various internal and external sources is dissipated into the system. These heat loads have to be removed from a magnet to maintain its superconducting properties. Heat removal capability of a specific CICC design and the coolant pumping costs depend on the viscous pressure losses in the conductor. Assessment of pressure drop requires reliable correlations for the friction factors in each flow region of a CICC.

In the present work we concentrate on the bundle friction factor, for which various correlations have been proposed in literature, e.g. [2-4], in the form $f = f(\mathrm{Re},\varphi)$ or $f=f(\mathrm{Re})$ where Re is the Reynolds number and $\varphi = A_{fluid}/A_{total}$ is the void fraction (porosity). The void fraction is one of the main design parameters in a CICC, which governs its hydraulic resistance and ensures its mechanically stable configuration. In the presently designed and used CICCs the void fraction is around 0.34-0.40. Recently, however, because of the transverse load degradation of Nb_3Sn strands observed in ITER CICCs [5], reduction of the void fraction in the ITER TF coil conductor to the range of 0.28-0.30 has been decided to improve the conductor performance under electromagnetic forces. The impact of such a low void fraction on hydraulic resistance of flow in CICCs should be assessed.

Most of correlations for bundle friction factor in the literature have been obtained by ad hoc modifications of the known correlations for the pipe flow and by fitting to the data measured for specific conductors, yet their predictive capability is not satisfactory. Another approach to correlate the bundle friction factor, in which the bundle is treated as a porous medium was proposed in [6,7]. This method seems to be very promising since we can use the established theory. A few correlations for the friction factor in porous media have been proposed in the literature [7]. The most frequently used is that resulting from Darcy-Forchheimer equation, which can be written in the form

(1) $$f = 2D_h^2 \varphi K^{-1}/\mathrm{Re} + 2D_h \varphi^2 C_F K^{-1/2}$$

where K is the permeability and C_F is the drag coefficient that characterize a specific porous medium.

The systematic experimental investigations of the bundle friction factor were conducted at EPFL-CRPP in 2007 [8,9]. In these experiments CICCs with different void fraction and cabling pattern were tested. For each CICC the void fraction was measured and the friction factor as a function of Re was determined from the measurements of pressure drop and mass flow rate, using water at room temperature. It was shown, that porous medium model provides excellent fits to these experimental data. However, in these experiments Reynolds numbers below the ITER CICCs operating point range, which is of the order 10^3, were reached.

In this paper we report the results of new measurements of hydraulic resistance of flow in CICCs with low void fraction which were performed using two different fluids: water at room temperature and cryogenic helium. Thus, we obtained the data in a very wide range of Re (40-40000). The main aim of the present study is to verify if (i) the data obtained using different fluids are consistent (ii) the porous medium model works satisfactory in the extended range of Re (iii) the results obtained for lower Reynolds numbers may be safely extrapolated towards the ITER CICC operating point.

CICC samples and experimental set-up

Three square, single channel CICC's with almost the same dimensions, number of strands and cabling pattern, but different twist pitch lengths, referred to as PITSAM 2, PITSAM 5 LTP and PITSAM 5 STP, were used for the pressure drop tests. The most relevant conductor data are compiled in Table 1.

Table 1. Geometric parameters of the PITSAM samples

Description	PITSAM 2	PITSAM 5 LTP	PITSAM 5 STP
Outer conductor dimensions (mm)	12.58 x 12.50	12.61 x 12.53	12.69 x 12.57
Jacket thickness (mm)	1.75	1.75	1.75
Outer corner radius (mm)	1.9	1.9	1.9
Number of strands	108	108	108
Strand diameter (mm)	0.81	0.81	0.81
Mean twist pitch angle	0.974	0.977	0.972
Void fraction (calculated)	0.298	0.305	0.314
Sample length in test with water (m)	0.200	0.200	0.200
Sample length in test with helium (m)	2.000	2.000	2.000

The detailed description of the experimental set-up used for the pressure drop measurements with water, as well as the information about the sensors accuracy, signal treatment and raw data processing was presented in [8].

The tests using cryogenic helium were performed on the SULTAN facility [10]. The measurements were done by increasing the mass flow rate from 0 to 8 g/s in approximately equal increment steps. Each step lasted approximately 2 minutes in order to allow the helium flow to stabilize along the sample. To obtain each of data points we use the average values of the results at the end of each increase step, where all signals are stable. The absolute pressure and temperature in the middle of the sample are used to calculate helium properties.

Results

The dimensionless analysis of experimental results is performed in terms of Reynolds number and longitudinal bundle friction factor which are calculated as follows

(2) $$\mathrm{Re} = \rho v D_h / \mu = (\dot{m} D_h)/(\mu A_{fluid})$$

(3) $$f = -2D_h/(\rho v^2) \cdot dp/dx = (2D_h \rho A_{fluid}^2 \Delta p)/(\dot{m} L)$$

The exemplary results in dimensionless form are presented in Fig. 1 together with the Darcy-Forchheimer correlation (Eq.1). The error bars computed as a combined uncertainty are also indicated.

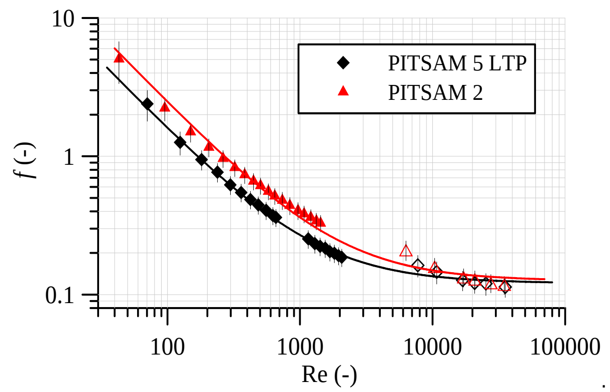

Fig.1. Friction factor as a function of Reynolds number for PITSAM samples and the fits resulting from Darcy-Forchheimer correlation. The data measured with water are indicated by filled symbols.

The values of permeability K and drag coefficient C_F for each conductor, computed by least square fitting taking into account error bars, are summarized in Table 2. It is seen that for PITSAM 5 LTP sample K and C_F best fitting the data measured with water only are close to the values obtained by fitting to the whole datasets. However, this is not the case for PITSAM 5 STP and PITSAM 2.

Table 2. Comparison of permeability K and drag coefficient C_F best fitting (a) the whole dataset (b) the data measured with water only. Friction factor values at Re = 2000 calculated from both fits are also presented.

Set	Parameter	PITSAM 2	PITSAM 5 LTP	PITSAM 5 STP
a	K x 10^9 (m^2)	0.600	0.959	0.905
	C_F (-)	0.036	0.040	0.037
	f (-)	0.244	0.195	0.207
b	K x 10^9 (m^2)	0.707	0.949	1.084
	C_F (-)	0.061	0.040	0.060
	f (-)	0.299	0.193	0.252

For each of the samples, data measured with different fluids are consistent. Porous medium analogy model provides satisfactory fits to experimental data over the whole range of Reynolds number. The results obtained using porous medium model for lower Re may be cautiously extrapolated towards the ITER relevant range with the relative uncertainty of the order of 25%.

Acknowledgements

The authors are indebt to Felix Stähli for the pressure drop measurements. The technical support of PSI is greatly acknowledged

This work, supported by the European Communities under the contracts of Association between EURATOM /SWISS and between EURATOM/IPPLM, was carried out within the framework of the EFDA. The views and opinions expressed herein do not necessarily reflect those of the European Commission.

REFERENCES

[1] ITER Design Description Document. Magnet. Section 1: Engineering Description, ITER_D_22HV5L v.2.2 (2006)
[2] Katheder H., Optimum thermohydraulic operation regime for cable in conduit superconductors. *Cryogenics*, 34 (1994), 595–5988 [ICEC supplement]
[3] Nicollet S., Cloez H., Duchateau J.-L., Serries J.P., Hydraulics of the ITER Toroidal Field model coil cable-in-conduit conductors. Proceedings of the 20th Symposium on Fusion Technology (1998), 771-774
[4] Takahashi Y., Tada E., Okuno K., Tsuji H., Ando T., Hiyama T., Koizumi K., Nishi M., Nakajima H., Yoshida K., Kato T., Kawano K., Oshikiri M., Hattori Y., Takahashi R., Kamiya S., Shimamoto S., Experimental results of JF-15 forced-cooled superconducting test loop. Proceedings of the 10th International Cryogenic Engineering Conference (1984), 87-90
[5] Bruzzone P., Wesche R., Stepanov B., The Voltage/Current Characteristic (n Index) of the Cable-in-Conduit Conductors for Fusion. *IEEE Trans. Appl. Supercon.*, 13 (2003), 1452-1455
[6] Long A.E., Transverse heat transfer in a cable-in-conduit conductor with central cooling channel. Master Thesis, MIT (1995)
[7] Bottura L., Marinucci C., A Porous Medium Analogy for the Helium Flow in CICC. Accepted for publication in *International Journal of Heat and Mass Transfer.*
[8] Bagnasco M., Bottura L., Bruzzone P., Lewandowska M., Marinucci C., Stähli F., Pressure drop of Cable-In-Conduit Conductors with different void fraction. *Adv. Cryo. Eng.*, 53 (2008), 1317-1324
[9] Bagnasco M., Lewandowska M., Pressure drop measurements in Cable-in-Conduit Conductors (CICC) with different layouts. To be presented at ICEC/ICMC 2008
[10] User specification for Conductor Samples to be Tested in the SULTAN Facility. EPFL-CRPP Report LRP 723/02 (2002)

***Authors**: dr inż. Monika Lewandowska, Politechnika Szczecińska, Instytut Fizyki, Al. Piastów 48, 70-310 Szczecin, E-mail: monika.lewandowska@ps.pl; Dr. Maurizio Bagnasco, EPFL - CRPP - Fusion Technology, Applied Superconductivity, WMHA/C33, CH 5232 - Villigen PSI, Switzerland, E-mail: maurizio.bagnasco@psi.ch*

Conference **ELMECO-6**
ELECTROMAGNETIC DEVICES AND PROCESSES IN ENVIRONMENT PROTECTION
joint with
9th Seminar APPLICATIONS OF SUPERCONDUCTORS **AoS-9**
June 24 – 27, 2008 Nałęczów, Poland

INFLUENCE OF MAGNETIC MATERIALS ON TRANSPORT PROPERTIES OF APPLIED SUPERCONDUCTORS

Bartek A GŁOWACKI[1], Milan MAJOROS[2], Archie M CAMPBELL[1]

University of Cambridge (1), The Ohio State University (2)

***Abstract**. Magnetic materials can help to improve the performance of practical superconductors on the macro/micro scale as magnetic diverters and also on the nanoscale as effective pinning centres. It was established by numerical modelling that magnetic shielding of the superconducting filaments reduces AC losses in self-field conditions due to decoupling of the filaments and, at the same time, it increases the critical current of the composite*

***Streszczenie.** Magnetyczne materiały umożlowiają polepszene wlasności naprzewodzących praktycznych nadprzewodników w skali makro jako magnetyczne osłony jak również w skali nano jako efektywne centra zaczepiania strumienia magnetycznego. Udowodniono przy użyciu modelowania numerycznego, że magnetyczne ekranowanie nadprzewordzących włókien redukuje zmiennoprądowe straty w wyniku magnetycznego rozłączenia włókien jak rownież powduje wzrost prądu krytycznego przewodu.*

Keywords: superconducting conductors, magnetism, ac losses, flux pinning
Słowa kluczowe: nadprzewodzace przewody, magnetyzm, straty zmiennopradowe, kotwiczenie strumienia magnetycznego

Introduction

In this article we will discuss the aspects of the influence of the ferromagnetic materials on the properties of the practical $YBa_2Cu_3O_7$, $(Pb,Bi)_2Sr_2Ca_2Cu_3O_9$ and MgB_2 multifilamentary conductors.

NiFe/$YBa_2Cu_3O_7$ Coated conductors for cables

It is well documented that ferromagnetic materials acting as flux diverters and magnetic flux screens can effectively reduce expose of the superconducting material to external magnetic field and therefore improve in-field performance of practical superconductors [1]. The external magnetic field may originate from the neighbouring elements or electromagnets such as it is in the case of current leads or neighbouring strands and phases in superconducting cables [2-4], There is also calculated strong influence of the presence of the ferromagnetic substrates, coatings and buffer layers on the magnetic flux distribution from the neighbouring filaments as it is the case of practical multifilamentary $YBa_2Cu_3O_7$, $(Pb,Bi)_2Sr_2Ca_2Cu_3O_9$ and MgB_2 conductors [5-13]. Perspective of use of low cost of the highly textured Ni-based substrates stimulates research concerning the architecture of the potential superconducting cables where ferromagnetic substrate based coated conductors can be used [2, 4], fig 1.

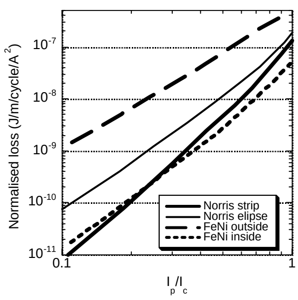

Fig.1 AC transport losses for two orientations of the ferromagnetic substrates of the coated conductor in respect to the cable surface after [2]. In the picture only segment of the cable with two parallel tapes has been schematically presented.

However these calculations are very valuable but because they are just 2D models they do not take to account the real helical configuration of the tapes in the cable [2, 4], the influence the transversal distribution of the current in the conductor is not taken to account that increases the participation of the ferromagnetic substrate material in the overall losses of the cable, fig.2.

Improvement of the transport properties of the conductors by addition of the nanoscale/sub-micron magnetic pinning centres has been recently considered more widely driven by

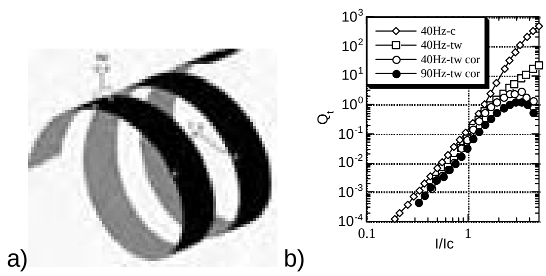

Fig.2 Transport ac losses of a helix: (a) potential taps position and potential wires arrangement on the outer surface of the central turn. White arrows - axial component of J_c flowing on outer surface, dotted white line - tangential J_c component on inner surface; (b) Measured transport ac losses. tw_{cor} represents the *tw* voltage signal corrected by the *c* voltage to provide truly transversal voltage losses [3].

the progress in understanding of the superconducting/ ferromagnetic interfaces. However, the volumetric density and chemical compatibility of magnetic nano-inclusions has to be controlled to avoid suppression of the superconducting properties over larger distance that the coherence length [3].

Superconductor/magnetic composite J_c and stability

This effect is especially beneficial for coated conductors where anisotropic properties of the superconductor are amplified by the conductor architecture, fig. 3. However, ferromagnetic coatings are often chemically incompatible with $YBa_2Cu_3O_7$ and $(Pb,Bi)_2Sr_2Ca_2Cu_3O_9$ conductors, and buffer layers have to be used. In contrast, in MgB_2 conductors an iron matrix may remain in direct contact with the superconducting core. Application of superconducting-magnetic heterostructures requires consideration of the

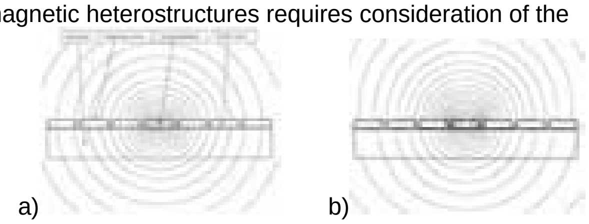

Fig. 3 Magnetic field lines (scale 6 x 10^{-10} Wb) of a model YBCO coated conductor with 7 strips embedded in a ferromagnetic cover of rectangular cross-section, when the current with current density j = 10^9 A/m^2 passes through the central filament only: (a) μ_r =1 of all the materials (substrate, buffer layer and cover); (b) ferromagnetic cover m_r =1000, substrate μ_r=1, ferromagnetic buffer layer μ_r =1000. (dimensions of the filaments: 8 μm x 2μm, thickness of the ferromagnetic layer: 0.5mm, spacing between the covered filaments = 1μm, thickness of the buffer layer= 0.5μm, thickness of the substrate equal 9.5μm).

thermal and electromagnetic stability of the superconducting materials used. On one hand, magnetic materials reduce the critical current gradient across the individual filaments, figure 4 but, on the other hand, they reduce the thermal conductivity between superconducting

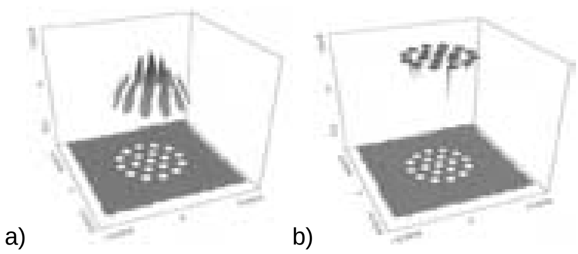

Fig. 4 Spatial distribution of the critical current density in a 19-filament MgB_2 wire cross-section in the self-field, for different values of relative magnetic permeability, μ_r, of the concentric multi-screens: (a) μ_r = 1, I_c = 442 A; (b) nonlinear Fe μ_{rmax} = 9000, I_c = 628 A [1]. The electromagnetic stability is a issues one may see that the critical current density gradient across the individual filament can be as high as 20% of its nominal value. The gradient is different for the internal filaments and also the lowest J_c values are achieved for the external filaments.

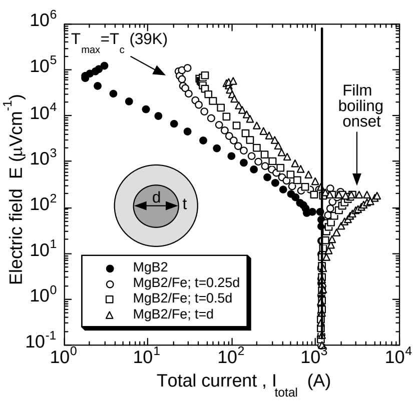

Fig. 5 Calculated voltage–current characteristics (points) of the MgB_2 superconducting composite conductors immersed in liquid He: a) Fe/MgB_2 composite wires. Bare MgB_2 wire has diameter *d* = 0.6 mm where the Fe/MgB_2 composite wires (insert) have different Fe thickness *t*. The straight vertical line is the isothermal power-law voltage–current characteristic of the bare MgB_2 wire at 4.2 K. (● - bare MgB_2, ○ - MgB_2 covered with Fe of thickness *t* = 0.25*d*, □ - MgB_2 covered with Fe of thickness *t* = 0.5*d* and △ - MgB_2 covered with Fe of thickness *t* = *d*).

core and the cryogen, which may cause destruction of the conductor in the event of thermal instability, figure 5 [1].

A possible nanoscale method of improving the critical current density of superconducting conductors is the introduction of nanoscale/sub-micron magnetic pinning centres. However, the volumetric density and chemical compatibility of magnetic inclusions has to be controlled to avoid suppression of the superconducting properties, fig.6.

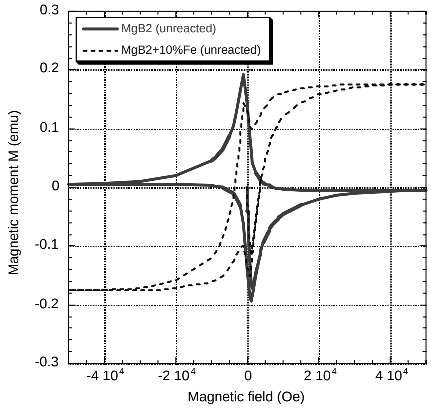

Fig. 6 Magnetic moments versus magnetic field for the ex situ MgB_2 conductor with addition of iron powder.

References

[1] B.A.Glowacki, M.Majoros, M.Vicker, M. Eisterer, S. Toenies, H.W. Weber, M. Fukutomi, K. Komori, and K.Togano, *Supercond. Sci. Technol.* 16 (2003) 297

[2] D. Miyagi, M. Umabuchi, N. Takahashi, O. Tsukamoto Physica C 463–465 (2007) 785

[3] M.Majoros, B.A.Glowacki, A.M.Campbell, Z.Han, P.Vase, Physica C 314 (1999) 1

[4] S. Sato and N Amemiya, *IEEE Trans on Appl. Supercond*.16 (2006)127

[5] B.A.Glowacki and M.Majoros, *Supercon. Sci. Technol.* 13 (2000) 971

[6] M.Majoros, B.A.Glowacki and A.M.Campbell, *Physica C* 334 (2000) 129

[7] M.Majoros, B.A.Glowacki and A.M.Campbell, *Physica C* 338 (2000) 251

[8] M.Majoros, B.A.Glowacki *AC losses and Flux Pinning and Formation of Stripe Phase*, Nova Science Publishers, Inc., Huntington, New York, 32 (2000) 1-51

[9] M.Majoros, B.A.Glowacki and A.M.Campbell *IEEE Trans. Applied Supercond*. 11 (2001) 2780

[10] B.A.Glowacki, M.Majoros, N.A.Rutter and A.M.Campbell Physica C 357-360 (2001) 1213

[11] B.A.Glowacki, M.Majoros, N.A.Rutter and A.M.Campbell *Cryogenics* 41 (2001) 103

[12] B.A.Glowacki, M.Majoros (Advances in Research and Applications) MgB_2 ed. A. Narlikar, Nova Science Publishers, Inc., Huntington, New York, 38 (2001) 361

[13] B.A.Glowacki, and M.Majoros *Physica C* 372-376 (2002) 1235

***Authors**: dr Bartłomiej Andrzej Głowacki, Department of Materials Science and Metallurgy, University of Cambridge Pembroke Street, Cambridge CB2 3QZ, England, E-mail: bag10@cam.ac.uk; dr Milan Majoros, College of Engineering, The Ohio State University, 555 MacQuigg Laboratory 105 W Woodruff AveColumbus, OH 43210, USA, E-mail majoros@ecr6.ohio-state.edu; prof. dr Archie Campbell, Department of Engineering, University of Cambridge, Trumpington Street, Cambridge CB2 1PZ, England, amc1@cam.ac.uk.*

The Correspondence address is:

dr Bartłomiej Głowacki, e-mail:, bag10@cam.ac.uk

NANOPRODUCTS BORN IN PLASMA TO OVERTAKE OIL AND ENERGY CRISIS

Zbigniew KOŁACIŃSKI

Technical University of Lodz

Abstract. *The paper is focused on applications of carbon nanotubes in energy storage sector and the main uses that were investigated such as solar cells, supercapacitors, batteries as well as thermoelectricity.*

Streszczenie. *W artykule przedstawiono możliwą ofertę zastosowania nanorurek węglowych w dziedzinie oszczędzania energii szczególnie jako bateria słoneczne, superkondensatory, akumulatory oraz termoogniwa.*

Keywords: plasma, nanomaterials, energy saving.
Słowa kluczowe: plazma, nanomateriały, oszczędność energii.

Introduction

The global demand for carbon nanostructures is growing annually by 33% [1] Early successes in years 2015-20 will be in electronics, where performance enhancing attributes offered by nanotubes will allow manufacturers of displays and other electronic components to meet increasingly demanding goals. The importance of electronics as an early application for nanotubes will drive demand in the Asia/Pacific region, which will outrank the United States as the leading market for nanotubes by 2009. Strong growth is expected in South Korea, Japan and China.

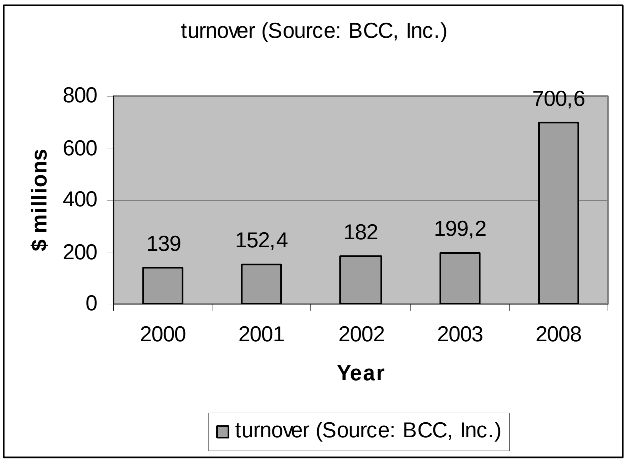

Figure 1. Total Global Sales of Nanotechnology Instruments and Tools, through 2008 [1]

This paper does not concern design in any way, the main focus of the report is to determine what can be in the near future commercially viable in terms of the use of nanoproducts in energy saving area.
The special interest is paid on applications of carbon nanotubes in energy storage and the main uses that were investigated such as solar cells, supercapacitors, batteries as well as thermoelectricity.

The focus then tuned to the application of these devices in harmony with each other and the decision was made that this would be a hybrid electric vehicle (car). The reason behind this was to determine whether it was possible to actually run a car without the use of petrol. It was therefore necessary to evaluate not only the cost of production but also whether the use of nanotubes could provide a large enough electrical capacity to actually run a car for an appropriate distance. The basis was taken that the car had a mass of one metric tonne and required a power of 20 kilo watt hours in order to possess the power equivalent to a standard petrol car of similar mass.
The plasma advanced technologies having made the input to the most of those achievements.

Plasma for nanomaterials

The carbon arc discharge method is the most common and perhaps the easiest way to produce carbon nanotubes as it is rather simple to undertake. However, it is a technique that produces a mixture of components and requires separating nanotubes from the soot and the catalytic metals present in the crude product.
The better quality products can be synthesized from gas phase in CVD technique. In latest practice the hybride methods are used with some trials of on-line process monitoring and control.

Energy storage in CNTs

Possibilities of electrochemical energy conversion using carbon nanotubes and related materials in various systems, such as lithium batteries, super capacitors, hydrogen storage, are considered. It is shown that for these applications, the electrochemical properties of multi-walled (MWNTs) and single walled (SWNTs) nanotubes are essentially dominated by their mesoporous character. The advantages of using nanotubes for energy storage are their small dimensions, smooth surface topology and perfect surface specificity. Four types of energy storage known in carbon nanotubes are: electrochemical hydrogen storage, gas phase intercalation, electrochemical lithium storage and charge storage in supercapacitors.

<u>Supercapacitors</u>

Presently supercapacitors use electrodes made of activated carbon, which is extremely porous and therefore has a very large surface area. However, the pores in the carbon are irregular in size and shape, which reduces efficiency. The nanotechnology allows to grow vertically aligned nanotubes regular in shape, and a size that is only several atomic diameters in width. The result is a significantly more effective surface area, which equates to significantly increased storage capacity. Due to its tiny size, the nanotubes supply a gigantic superficial area, in which the energy can be stored and released later. The new supercapacitors can store energy in a density of 30 kW/kg, compared with 4 kW/kg of the most advanced capacitors available commercially nowadays.

Hydrogen storage

It has been predicted that carbon nanotubes can store a liquid or a gas in the inner cores through a capillary effect. In spite of their relatively small surface area and pore volume, carbon nanotubes show very surprising high hydrogen storage capacity

Table 1 – Supercapacitors characteristics [2]

Charge/Discharge Time	Millisec to seconds
Operating Temperature	C -40 ° to +75 °
Operating Voltage Aqueous	1.1 V; Organic 2.5 V
Capitance	100 mF to > 1000 F
Life	3,000 to 50,000 hrs
Power Density	0.01 to 103 kW/kg
Energy Density	0.05 to 10 Wh/kg
Pulse Load	0.1 to 100 A

Gas phase intercalation of hydrogen in CNTs concerns the adsorption of H2, called physisorption instead of chemisorption (involving H+ and chemical bonds). This adsorption of H2 on the surface of CNTs is a consequence of the field force at the surface of the solid, that can be either physical or chemical.

Electrochemical lithium storage

SWNT bundles seem to be attractive host materials for energy storage. MWNTs could also be low-cost, high-performance anode materials for rechargeable lithium-ion batteries since they show an excellent reversible capacity and cycle ability during lithium insertion and extraction. The maximal reversible capacity found was at 650-1000mAh/g.

Solar cells

Invented by Michael Graetzel organic dye sensitised know as Graetzel cells can decrease the solar energy module price. It's a no silicon technology and it uses Titanium dioxide (TiO_2) so organic dye sensitised is no toxic for man and environmentally friendly. One Watt of power coming from organic solar cells costs approximately $2. The currently available efficiency of solar cells taking advantage of this technology is 7% and is predicted to reach 20% by 2015. Furthermore, organic solar panels are flexible, easy to install and lightweight.

Thermoelectricity

The most popular material used in thermoelectrical applications is bismuth telluride Bi_2Te_3 due to its high electrical conductivity and low thermal conductivity in room temperatures. In such a nano-superlattice the figure of merit ZT equal to 2.4 has been achieved.

Feasibility exercise

The feasibility exercise has been done for a small size personal car assuming that in this vehicle the mentioned above nanotechnologies are implemented. The frame characteristic of the car was assumed as: 1000kg of mass, 50kW of max power, 20kW of average continuous power and 15kW of boost. The car should allow to run a distance of 800km with velocity of 100km/h without charging electricity or tanking a fuel. The two supply modes were considered: BEV (Battery Electric Vehicle) and FCBEV (Fuel Cell Battery Electric Vehicle). In the first case the rechargeable batteries of the plug in charge type and with solar cells charging have been used. Also supercapacitors was helping when instant high power required. Mass of the car in which fuel tank and engine are removed and replaced by nanobatteries, electric motor and solar cells is 945 kg compared to 1795kg when convectional batteries are used. However the price of the nanotechnology implemented car is 47000€ compared to 24000€ for traditional batteries. It is expected [2] that the world demand for carbon and mineral nanoproducts will be in 2015 reaching the value 100 mld €. Taking into account the expected price decrease up to 100 times one may expect that in 10 years the nanotechnology may become competitive also in this case.

For FCBEV mode the final mass of the vehicle using hydrogen fuel cells with appropriate hydrogen tank and nanotechnological batteries is 1025kg compared to 2750 kg with hydrogen tank and conventional batteries. This will influence on the hydrogen consumption in the conventional hydrogen technology. However for the nanotechnology implemented car the dynamics is much better because of its low mass. Presently such car will be to expensive. Moreover hydrogen fuel is also expensive, difficult to handle and hardly nowadays available. The perspectives of nanotechnology commercial participation in the efficient hydrogen store are not clear yet so it is very difficult to describe the chances and time of its commercialization.

Nanotechnology can also be used to improve conventional cars energetic efficiency converting the heat waste into electric energy. The petrol combustion engine energy losses to heat varies from 65 to 85 %. About 50% of this heat is transferred from the exhaust pipe to the environment. The other half is transferred to the coolant. Let assume that nano-super-lattice of ZT=2.4 is commercially available then the wasted heat may be employed to produce electricity i.e. to charge battery and to supply air conditioning. Assuming that from 50kW car engine we have 35 kW of heat waste from which 50% from the exhaust gas gives 17.5kW and having Seebeck yield 15% we receive 2.7kW of power. From this 500W can be used to charge the battery (replacing alternator) and the rest can be transformed by the Peltier effect with the yield 60% for air conditioning. In the average car the cost of alternator and air conditioning system gives the saving of 1500€. Waste heat conversion into energy gives the petrol saving of 2.5 l/100km that multiplied by distance of 30000 km/year gives annual saving of 830€.

Conclusion

The above briefly presented examples allow to believe that expected in the next decade nanoproducts may not only change revolutionary our live in fighting with cancer or in supplying of new fastest than ever computers, implanted personal memories and microrobots but also it can be effective in saving energy the cost of which permanently grows following the oil price increase.

Acknowledgement

The paper is based on the European Semester Project worked out at International Faculty of Engineering in the Technical University of Lodz in which participated the following students: Chevalier Vincent, Henry Adrien, Szymańska Monika, Tyszkiewicz Ariel, Vieira Gisela, Marc Laing, Martin Réot, Krzysztof Padkowski, Bartek Gorzyński and Hélène Dersoir.

REFERENCES

[1] Kołaciński Z., "Plasma For Nanoproducts of the Next Decade", Introductory lecture in: *European Commission Research DG/ASEM Workshop. Conf. Materials of Europe-Asia Workshop on Clean Production and Nanotechnologies, Seoul, Korea 25-27 October, (2006), 445-457, 2006*

[2] Nano Road Map – http://www.nanoroadmap.it

Author: *prof. dr hab. inż. Zbigniew Kołaciński, Politechnika Łódzka, Katedra Aparatów Elektrycznych, ul. Stefanowskiego 18/22, 90-924 Łódź, E-mail: zbigniew@p.lodz.pl*

INFLUENCE OF MATERIAL INHOMOGENEITIES IN HTc CERAMIC SUPERCONDUCTORS ON CRITICAL CURRENT AND RELATED PHENOMENA

Jacek SOSNOWSKI

Electrotechnical Institute

***Abstract**. The influence of the materials inhomogeneities of the ceramic superconductors on the critical current and related phenomena is investigated. These inhomogeneities act as the pinning centers which interact with specific for HTc superconductors pancake shape vortices. The dependence of this interaction on the size of the inhomogeneities - pinning centers is considered and compared with experimental data. The influence of inhomogeneities connected with granular structure of oxide, ceramic superconductors on trapped flux is analyzed.*

***Streszczenie.** W pracy zbadano wpływ niejednorodności materiałowych występujących w nadprzewodnikach wysokotemperaturowych na wartość prądu krytycznego i związane zagadnienia. Zanalizowano wpływ defektów tworzących centra zakotwiczenia na wartość prądu krytycznego oraz wpływ ziarnistej struktury ceramik nadprzewodnikowych na wartość zamrożonego strumienia.*

Keywords: HTc superconductivity, critical current, trapped flux.
Słowa kluczowe: nadprzewodnictwo wysokotemperaturowe, prąd krytyczny, zamrożony strumień.

Introduction

Applications of the high temperature oxide superconductors are dependent in significant way on the critical current value achievable in these materials. Critical current influences both the transport properties of these materials, as well as the value of the trapped magnetic flux, which subject will be in the paper considered. Recent results on the trapped flux measurements performed in ISTEC, shown in the Fig. 1 indicating enormously large value of this parameter equal to 17 T at 29 K bring new point of view on these materials not only as ideal conductors but also permanent magnets. Shown in Fig. 1 data exceed much more known up to now magnetic field achievable with others permanent magnets based even on the rare earth such as Sm, Nd and others. This value of the trapped flux Ftr is strongly dependent too on the sample inhomogeneity – connected with its ceramic structure, which will be analyzed in the paper, additionally to the influence of inhomogeneities on transport critical current.

.

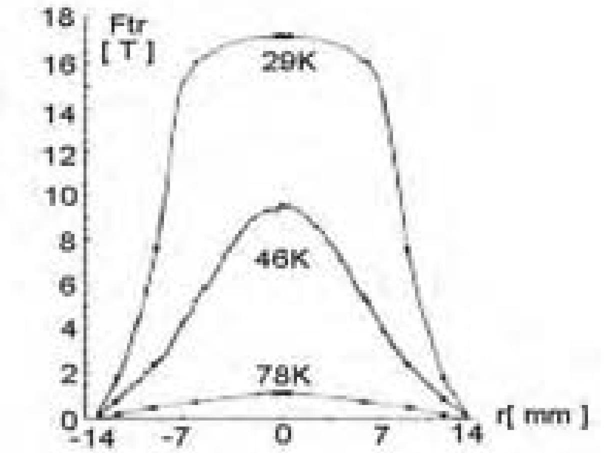

Fig.1. View of the trapped magnetic flux in cross-section of the single grain YBaCuO superconductor versus temperature (according to data ISTEC, Japan).

Influence of the pinning centers dimensions on critical current

Point inhomogeneities of the HTc superconducting tapes act as the pinning centers, which keep pancake shape vortices and then allow to flow the transport current through these materials in the form of tapes and wires.

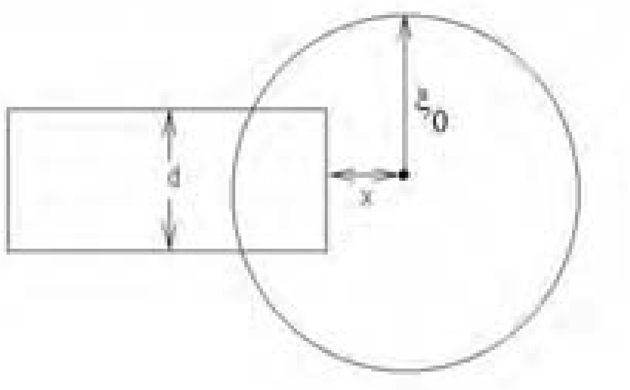

Fig. 2.. View of the pinned pancake vortex of the core radius equal to coherence length ξ_0 on the flat pinning center of the width *d*.

In Fig. 2 is shown the scheme of such interaction, for which pancake vortex is captured on the depth ξ_0 -x inside the pinning center. With the shift of the vortex core against the pinning center the potential energy of the system U increases according to the following relations:

(1) $$U_2(x)=\frac{\mu_o H_c^2 l}{2}\left[\pi\xi^2+dx-\xi^2\arcsin\frac{d}{2\xi}-\frac{d\xi}{2}\sqrt{1-\left(\frac{d}{2\xi}\right)^2}\right]$$

(2) $$U_3(x)=\frac{\mu_o H_c^2 l\xi^2}{2}\left[\frac{\pi}{2}+\arcsin\frac{x}{\xi}+\frac{x}{\xi}\sqrt{1-\left(\frac{x}{\xi}\right)^2}\right]$$

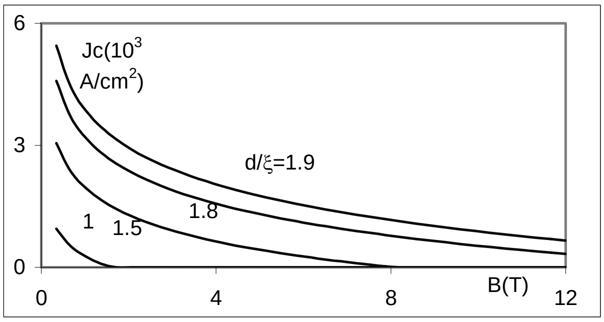

Fig. 3. Critical current density versus magnetic field in the function of the reduced size of the pinning center d/ξ.

in the respect to the initial equilibrium state for which potential energy is equal to:

$$U_1(\xi)=\frac{\mu_o H_c^2 l}{2}\left[\pi\xi^2-\xi^2\arcsin\frac{d}{2\xi}-\frac{d\xi}{2}\sqrt{1-\left(\frac{d}{2\xi}\right)^2}\right]$$

(3)

Equation 1 is valid for deflection of the vortex against its equilibrium position $x<x_C$, while Eq. 2 for $x>x_C$, where parameter x_C is described by the relation:

(4) $$x_c = \xi\sqrt{1-\left(\frac{d}{2\xi}\right)^2}$$

Difference between Equations 2-3 and 1 gives the potential barrier, which should be crossed by the vortex in the flux creep process. In this process the static potential barrier is supplemented with potential of the Lorentz force proportional to the transport current density and potential of the elasticity forces of the vortex lattice. Taking into account all mentioned effects we receive the final expression for the potential barrier height in the function of reduced transport current density.

(5) $$\Delta U(i)=\frac{\mu_0 H_c^2 l\xi^2}{2}z+\alpha\xi^2\sqrt{1-i^2}\left(\sqrt{1-i^2}-2\right)$$

where parameter ***z*** appearing in Equation 5 is given by the relation:

(6) $$z=\arcsin\frac{d}{2\xi}+\frac{d}{2\xi}\sqrt{1-\left(\frac{d}{2\xi}\right)^2}-i\sqrt{1-i^2}-\arcsin i$$

Here $i = j/j_c$ is the ratio of the real transport current density ***j*** and critical for flux creep effect current density $\boldsymbol{j_C}$, $\boldsymbol{H_c}$ critical thermodynamic magnetic field, ***l*** thickness of the pinning center. Inserting above equations into the constitutive flux creep relation describing the generated electric field in the function of potential barrier height ΔU and then according to Eq. 5 on the transport current density we obtain I-V curve:

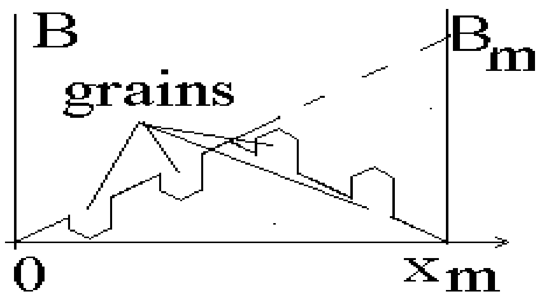

Fig. 4. Trapped magnetic induction profile in HTc superconducting slab of the thickness $2x_m$ for magnetic induction cycle $0 \rightarrow B_m \rightarrow 0$. The granular structure of ceramic superconductors is presented.

(7) $$E=-B\omega a\left[\exp\left[-\frac{\Delta U_0}{k_B T}\left(1+\frac{j}{j_C}\right)\right]-\exp\left(-\frac{\Delta U}{k_B T}\right)\right]$$

$\boldsymbol{\Delta U_0}$ is potential barrier height without current, while k_B is Boltzmann constant, ***T*** temperature, ω *flux* creep frequency on the distance ***a*** between pinning enters. Calculated influence of pinning centers size on critical current density magnetic field dependence is shown for Fig. 3. Shape of this dependence is in good accordance with experimental data, especially concerning the finite value of the magnetic induction B_{c2}, for which the critical current disappears. We notice also that in others typical models as Kim's [1] for instance critical current does not vanish up to infinity.

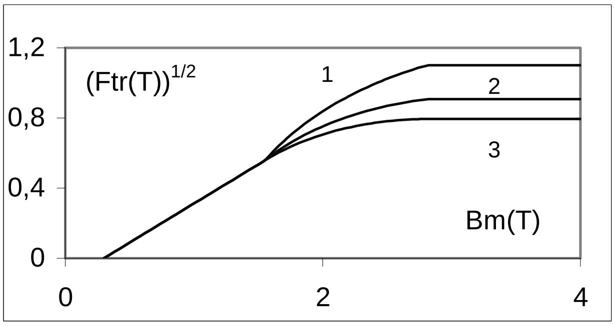

Fig. 5: *Square root of the average trapped magnetic induction in superconducting ceramic on the maximal magnetic induction B_m versus grain's concentration on cross-section unit: (1) – $3*10^5$ cm^{-2} , (2) – 10^5 cm^{-2} , (3) - 10^3 cm^{-2}.*

Flux trapping analysis

Received in previous section results concerning critical current density describe too magnetic properties of superconductors, including the trapped flux, which reaches very large values, as it was shown in Fig. 1. Inhomogeneous, granular structure of oxide ceramics leads to the anomalous shape of trapped induction profiles, shown in Fig. 4. Such anomalies are connected with intra-grain currents flowing in individual grains and weak inter-grain, josephson's currents. Fig. 5 presents the influence of grains concentration on flux trapping. This result is in qualitative agreement with previous experimental data [1].

REFERENCES

[1] Sosnowski J., Superconductivity and applications, Book Publisher of Electrotechnical Institute, Warsaw, Poland (2003) p. 1-200 – in Polish.

Author*: prof. dr hab. Jacek Sosnowski, Instytut Elektrotechniki, 04-703 Warszawa, Pożaryskiego 28, E-mail: sosnow@iel.waw.pl*

Conference **ELMECO-6**
ELECTROMAGNETIC DEVICES AND PROCESSES IN ENVIRONMENT PROTECTION
joint with
9th Seminar APPLICATIONS OF SUPERCONDUCTORS **AoS-9**
June 24 – 27, 2008 Nałęczów, Poland

AUTOMATIC CONTINUITY TEST OF SUPERCONDUCTING QUADRUPOLES

Janusz KOZAK[12]

Electrotechnical Institute in Warsaw (1), CERN (2)

Abstract. *The ACT- Automatic Continuity Test of Superconducting Quarupoles has been described in this paper. The device has been build to perform test at room temperature of all electrical circuit and connections inside quadrupole magnet before installation in the tunnel.*

Streszczenie. *W artykule opisany został automatyczny system do sprawdzania ciągłości obwodów elektromagnesu nadprzewodnikowego – quadrupola. Urządzenie zostało zbudowane w celu wykonania testu wszystkich obwodów i połączeń w elektromagnesie przed jego instalacją w tunelu.*

Keywords: superconducting magnet, electrical continuity test.
Słowa kluczowe: elektromagnes nadprzewodnikowy, elektryczny test ciągłości obwodu.

Introduction

All superconducting main magnets for LHC were tested at 1.9K in SM18 before installation in the tunnel. The power test at cold was preceded by measurements at room temperature HV-test and continuity test. The magnet V-taps are crucial for magnet protection during power test. Some of the V-taps may get loose due to thermal contraction during thermal cycles. To confirm the condition of the magnet instrumentation after power test at cold the HV and continuity test are necessary.

After the first nonconformity discovered in the tunnel, it has been decided to perform additional test just before lowering down the magnet.

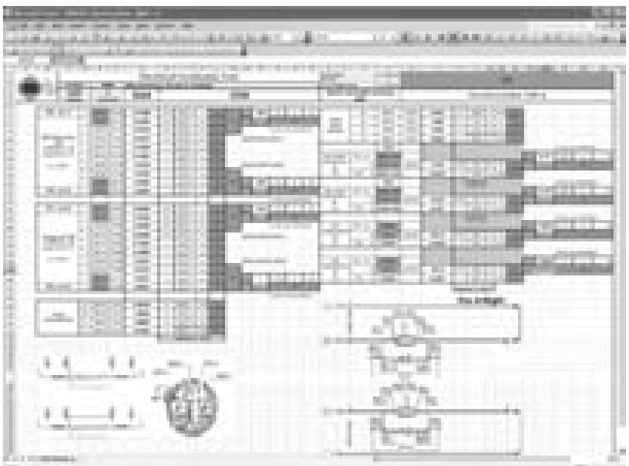

Fig.1. Excel template of final electrical continuity test of ARC SSS (Short Straight Section)

The detailed electrical test for the ARC SSS magnet has been elaborated to test all 392 ARC SSS of LHC.
The test goal was to detect:
- improper position of V taps, (full continuity test)
- absence of 20 Ohm resistors in IFS Box
- broken V taps,
- higher V taps resistance (caused by cold solder)
- swapped V taps.

For the measurement verification of all types of ARC SSS (Focusing A, Focusing B, Defocusing A and Defocusing B) the special template in Excel was prepared. The measurements of one ARC SSS magnet takes about one hour and few minutes more to enter the data to the template and upload to database.

Automatic Continuity Test

The aim was to simplify the way to perform the measurements allowing operators with minimum experience to perform electrical tests in a fast and effective way. To test full electrical instrumentation on ARC SSS magnets the automated continuity tester has been designed.

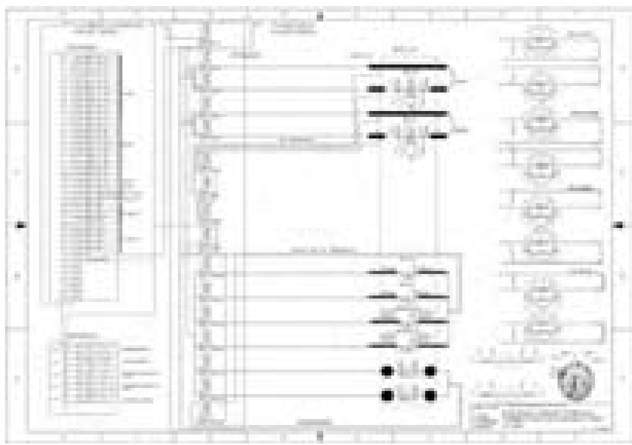

Fig.2. Electrical circuit of relays connection for continuity test of ARC SSS

Project assumed that the measurements setup will consist of computer with LabView software to control the current source, multiplexer with relays cards and voltmeter. The continuity measurements are made by injecting current and measuring the voltage drop on magnets V-taps. The resistance measurements of Quench heaters, cold temperature sensor and cryogenic heater were also necessary to confirm the condition of those elements. All measurements were compared with predefined ranges gathered in one setting table Fig.3. This table contain also relays and current source settings.

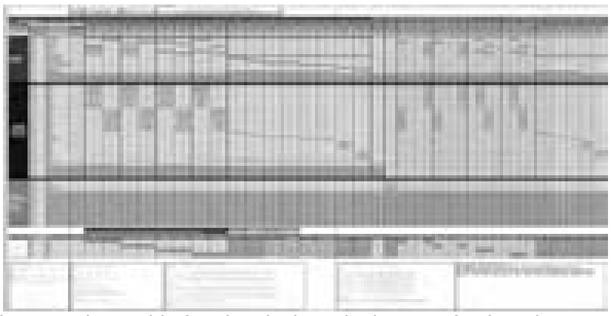

Fig.3. Settings table for electrical continuity test of stripped SSS

Hardware

The system is composed of a Agilent E3645A power supply and a Agilent 34970A DVM equipped with plug-in modules controlled by a dedicated Labview program running on a Sun workstation, via GPIB connections. This rack is mobile and equipped with a wireless network connection that allows maximum flexibility to perform test in big assembly hall.

Fig.4. ACT connected to the ARC SSS magnet

Software

This software is designed to perform continuity measurements on ARC SSS magnets which are composed of 8 independent magnets, plus additional resistance measurements on other instrumentation, such as quench heaters, cold temperature sensors and cryogenic heaters to be measured.

The ACT was checking the

- Presence and correct cabling of all voltage taps.
- Presence and correct cabling of quench heaters, temperature sensor and cryogenic sensor.
- Presence and correct cabling of 20 Ω resistors.

This test was able to detect cold soldering in IFS box also.

The software written in LabView to control all devices enables to check and visualize measurements result of all circuit of the magnet. The detailed measurements results are generated as html file after finishing measurements. The report is automatically sent to the server by wireless connection. Within few minutes the operator was able to connect all cables to the measured magnet and initiate the test.

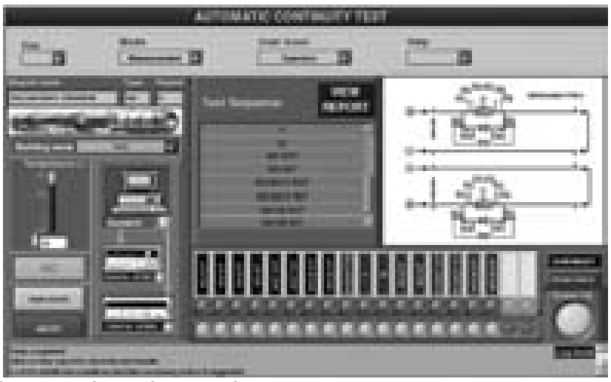

Fig.5. Interface of ACT software

Test Report

The test report is divided into two parts continuity measurements and resistance measurements. The system is doing 77 measurements and comparing measured values with the predefined ranges and also checking 18 additional conditions.

Fig.6. ACT report (first few lines of the report)

Conclusions

A first version of ACT becomes operational after 5 months for series measurements in building SMI2 to increase effectiveness of test execution and to minimise user's errors. The second ACT was build for measurement in SMA18 and the third with some modification for non stripped ARC SSS for measurements in 904 hall. The ACT fulfil requirements for the realisation of devise to perform continuity and resistance measurements on ARC SSS magnets in an automatic and reliable way in order to verify the integrity and correct cabling of the whole magnet instrumentation.

REFERENCES

[1] Kozak J. Stafiniak A. Denat M. Siemko A., Status of the present tests at SMI2, *Presentation at CERN*, 2006

[2] Mompo R. Kozak J. Stafiniak A. Siemko A., ACT Project, *EDMS 708126, CERN*, 2006

[3] Mompo R. Kozak J., Stafiniak A., ACT Project, *Presentation at CERN*, 2006

***Author**: dr inż. Janusz Kozak, Electrotechnical Institute in Warsaw Laboratory of Superconducting Technology ul. Nadbystrzycka 38A, 20-618 Lublin, E-mail: j.kozak@iel.waw.pl*

Conference **ELMECO-6**
ELECTROMAGNETIC DEVICES AND PROCESSES IN ENVIRONMENT PROTECTION
joint with
9th Seminar APPLICATIONS OF SUPERCONDUCTORS **AoS-9**
June 24 – 27, 2008 Nałęczów, Poland

WATER TREATMENT USING A PULSED DISCHARGE

Chobei YAMABE, Nakazaki SHOU and Satoshi IHARA

Saga University

***Abstract**. The treated water as an industrial waste water was the Nonylphenol ethoxylate (NPEO) diluted by pure water and the effect of treatment was estimated by the COD measurement. The active radicals such as atomic oxygen whose emission wavelength was 777 nm and OH radicals whose emission wavelength was 306.7 nm and 308.9 nm were confirmed for the different repetition rate of discharge (100 – 300 Hz). The COD removal of about 19 % was obtained and the efficiency of treatment was 0.74 mg/kWh.*

Keywords: water treatment, pulsed power, COD, OH radical, ozone

Introduction

The surfactant is a chemical compound and it has been used for washing to remove the grease in the various industrial fields such as the electronic device, mechanical parts and production processes of the fiber. In the contaminated water with the surfactant, the value of COD (Chemically Oxygen Demand) which is one of the items to be estimated for the water quality is large and its value changes to be large even though it is included with small amount of value in wasted water. In the present treatment, the adsorption with the active carbon is a general method for the low concentration but it is required the high initial cost and running cost. On the other hand, the combustion method is used for the high concentration and the large amount of fuel is consumed for the wasted water treatment with this method. Finally this process introduces the increasing carbon dioxide exhaust which influences on the global warming.

Some kinds of surfactant are difficult to be decomposed biologically, the increase of COD value of the bottom mud of lakes and marshes due to the water contamination, the soil contamination, the adsorption and accumulation at the bottom mud is worried. In the present time, the Nonylphenol ethoxylate (NPEO) is one of the surfactant used industrially and it is difficult to be decomposed biologically. Its byproduct called the Nonylphenol (NP) is suggested to have the effect as an Endocrine Disrupting Chemicals (or Endocrine Disruptor).

In this study, the treatment of wasted water exhausted from the industrial field is proposed for cleaning.[1] The purpose of this study is the estimation of the experimental results of the treatment and getting the fundamental data of the treatment effect. The sample water used here is prepared to use the NPEO actually used in the factory diluted by pure water.

Experimental setup and procedure

The experimental setup is shown in Figs.1(a) and (b). In Fig.(a), the charged capacitor C1 discharges using the thyratron switch and the pulse high voltage appears through the pulse transformer and it is applied to the needle point holder electrode. The pulse width T of the applied voltage is about 400 ns (full width at half maximum). The second electrical circuit shown in Fig.1(b) is also used. The pulse transmission line is charged using the transformer shown in Fig.1(b) and the short pulse high voltage controlled by the length of the coaxial cable and closing switch is applied to the needle point holder electrode of the discharge reactor. The pulse width of the output short pulse high voltage is changed by the length of the coaxial cable and in this study the pulse width is about T=120 ns with the length of the coaxial cable of 20 m.

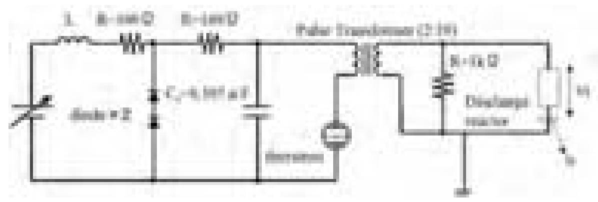

Fig.1(a) Configuration of electrical circuit with a pulse transformer

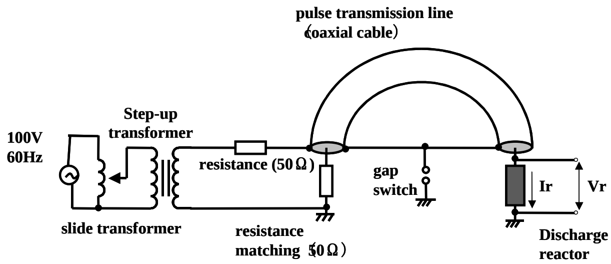

Fig.1(b) Configuration of electrical circuit with a coaxial cable

The configuration of the discharge reactor is shown in Fig.2. The reactor is made by the cylindrical Plexyglas (its inner diameter is 50 mm). This reactor installs a quartz converging lens (whose focal length is 5 cm) as a window to measure the light emission below 400 nm. The needle-point-holder electrode (its diameter is 36 mm) applied high voltage has ninety one needles whose material is stainless steel. The grounded electrode is covered with the dielectric material of enamel. The discharge occurs between the tip of needle and surface of water to be treated and the discharge distance is 2mm. The raw gas is fed into the discharge reactor at 0.5 l/min. As the raw gas, oxygen, nitrogen and argon are used independently to study about the effect on the water treatment measuring the absorbance (the removal of blue color) of the indigo-carmine solution. For this experiments the electrical circuit shown in Fig.1(a) is used and the amount of treated sample water is 50 ml and treated period by discharge is 30 minutes. Both the applied high voltage (Vr) and discharge current (Ir) are measured by the high voltage probe (P6015A, Tektronix) and current pick up coil (Pearson, Model 2877) respectively. The discharge input energy per pulse is calculated by the integration of voltage (Vr) times current (Ir) with time t and the total input power is also calculated by the product of [discharge input energy per pulse] and [number of discharge per second].

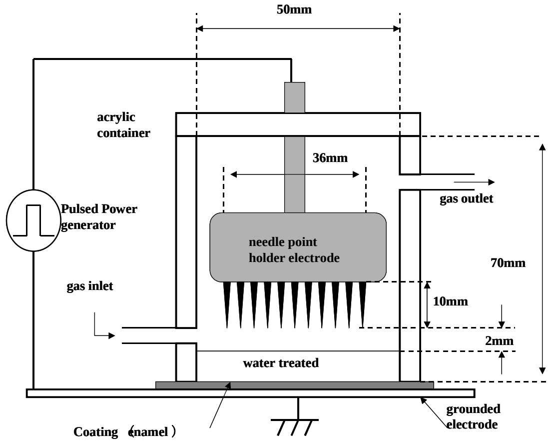

Fig.2 Configuration of the discharge reactor

The COD removal rate is defined as follows.

COD removal rate (%)

= 100 x [COD(initial)–COD(final)] / [COD(initial)]

Experimental results and discussions

Using the oxygen as a raw gas for the removal of blue color in water was best as compared with the case of argon and nitrogen. According to these results, it seemed that the active radicals which are effective for the removal of color would be generated more with oxygen.

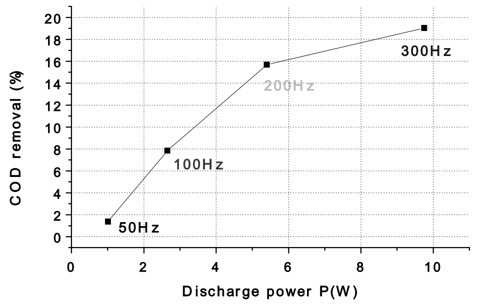

Fig.3 Removal rate of COD (%) as a function of the electrical input power

The removal rate of COD (%) as a function of the electrical input power is shown in Fig.3. In this experiments, the peak value of the applied high voltage was controlled for the different repetition rate of discharge and the removal rate increased with the electrical input power. The treatment efficiency was about 0.74 mg/kWh at the maximum removal rate of COD (i.e. about 19% with 9.8 watts) as shown in Fig.4. As shown in Figs.5(a) and (b), the generated radicals by discharge was measured by the light emission from the discharge region using the photon multi analyzer (TM-UV/VIS-CCD C10082CAH, HAMAMATSU Photonics).

The available measured region of wavelength was 200 ~ 800 nm and its resolution was 1nm. It was confirmed by photographs that the discharge occurred between the tips of the needle electrodes and water surface and the discharge appeared from almost all of tips of needles.

The light emission from OH radicals at 306.7 nm and 308.9 nm and from O radicals at 777 nm was confirmed. The OH radical has a high oxidation potential and is very effective on the decomposition of NPEO in water. The ozone was also detected by the ozone monitor at the outlet of the reactor.

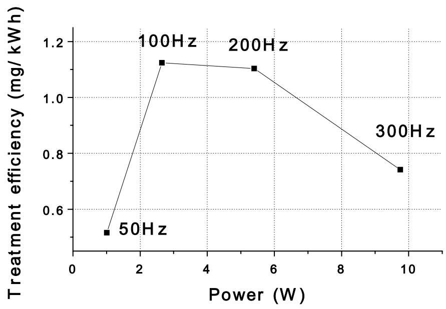

Fig.4 Treatment efficiency as a function of input power

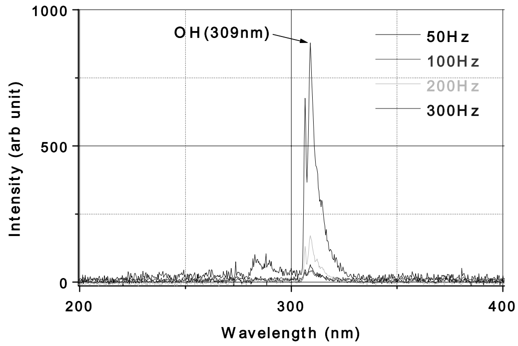

Fig.5(a) Light emission intensity spectrum measured in the region of 280~400 nm

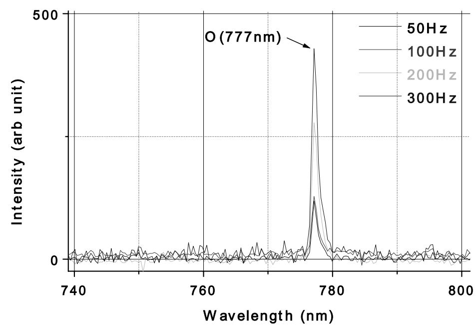

Fig.5(b) Light emission intensity spectrum measured in the region of 765~790 nm

Conclusions

The estimation of the experimental results for water treatment such as COD removal rate and its efficiency was studied to get the fundamental data of the treatment.

Acknowledgement

A part of this work was supported by the JSPS Core University Program and also a Grant-in-Aid for Scientific Research of the Ministry of Education, Science, Sports and Culture, Japan.

REFERENCES

[1] Shou Nakazaki, Satoshi Ihara and Chobei Yamabe, "A fundamental research of the water treatment using a pulsed power technology", 10th Int. Symp. on High Pressure Low Temperature Plasma Chemistry (Hakone X), Saga, Japan, 7P-12, (2006) 292-295

Authors:*Prof. Dr. of Eng. Chobei Yamabe, Saga University, Department of Electrical and Electronic Engineering, 1 Honjo-machi, Saga 840-8502, Japan, E-mail: yamabec@cc.saga-u.ac.jp*
Mr. Shou Nakazaki, has graduated from Saga University
Assoc. prof, Dr. of Eng. Satoshi Ihara, ibid. iharas@cc.saga-u.ac.jp

MEASUREMENT OF ELECTRIC DISCHARGE SOUND BY FRAUNHOFER DIFFRACTION AND ANALYSIS

Toshiyuki NAKAMIYA[1], Yoshito SONODA[1], Tomoaki IKEGAMi[2], Fumiaki MITSUGI[2], Kenji EBIHARA[3] and Ryoichi TSUDA[1]

[1]Tokai University, [2]Kumamoto University , [3]Dojindo Laboratories

Abstract*. We have previously succeeded in measuring the sound signal detected by the condenser microphone due to the electric discharge and discriminating the dominant frequency components of the sound signal. Analytical results of sound signal have showed that the appearance time of frequency components over 20kHz are comparatively well agreements with the time of discharge current and sound signal. In this paper, electric discharge sound is measured by the laser light diffraction effect of a visible laser beam.*

Keywords: electric discharge, sound signal, laser light diffraction, optical wave microphone.

1. Introduction

Creeping discharge is an electrical discharge phenomenon that is generated, and progresses along the boundary side of the dielectric substance. The research of the positive use and application about creeping discharge have been performed including the removal of the environmental pollutant such as NOx, ozonizer and etc., and the further applications are expected [1]. The phenomenon clarification of creeping discharge chiefly examines the voltage, the current, and luminescence. The example of using the electrical discharge sound is not seen as a means of the phenomenon clarification. To examine the fundamental characteristic of creeping discharge, the voltage, the current, and the electrical discharge sound are measured, and examined the fundamental relationship between the micro discharge and the acoustic properties. The electric discharge sound electric discharge sound is measured by the laser light diffraction effect and the Continuous Wavelet Transform (CWT) is applied to discriminate the acoustic sound of the micro discharge and the dominant frequency components [2],[3]. The discharge sound may be considered the utilization of the monitor for the creeping discharge.

2. Experimental procedures

2. 1 Principles

The fundamental optical setup of the Fraunhofer diffraction measurement is shown in Fg1, where the laser beam is assumed to be of Gaussian type [4]. When the incident probing laser beam crosses an sound wave as shown in Fig.1, diffracted waves are generated and propagate with the penetrating beam through the Fourier optical system and reach the observing plane, which is set at the Fraunhofer diffraction region or in the back focal plane of the first receiving lens, placed one focal length beyond the Gaussion beam waist. The diffracted optical waves are homodyne-detected there by using the penetrating optical wave as a oscillating power. The intensity of diffracted waves of higher orders is much smaller than that of the first order wave and can be neglected. The spatial intensity (I_{ac}) of the resultant optical field at the back focal plane is given by the equation (1). We are calling this setup an optical wave microphone.

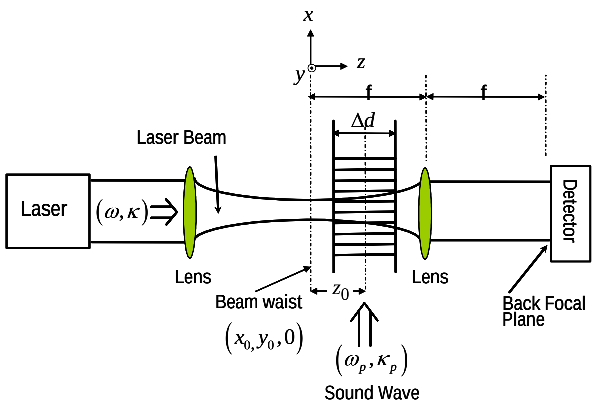

Fig.2. Schematic representation of optical wave microphone.

(1) $$I_{ac} = I_0 \Delta\phi_0 \left[\exp\left\{-\left(u^2+(u-\theta)^2\right)\right\} - \exp\left\{-\left(u^2+(u+\theta)^2\right)\right\}\right] \sin\omega_p t$$

where $I_0 = \left(2P_0 / \pi\omega_f{}^2\right)\exp\left[-2\left(y_f/\omega_f\right)^2\right]$,

$u = x_f/\omega_f$: the normalized x-coordinate in the back focal plane, $\theta = k_p\omega_0/2$: the normalized wave number, ω_f : the beam size in the focal plane, $k_p\left(=2\pi/\lambda_p\right)$: the wave number of sound wave, ω_0 : the spot size, P_0 : the total incident power, $k_i\left(=2\pi/\lambda_i\right)$: the wave number of incident beam, λ_i : the wave length of probing beam, $\phi_0 = \kappa_i\left(\mu_0-1\right)\Delta d$: the time-constant of component of phase modulation, $\Delta\phi_0 = \kappa_i\Delta\mu_0\Delta d = \kappa_i\left(\mu_0-1\right)\Delta d\Delta p/\gamma p$: the time-dependent component of phase modulation, μ_0 : the reflective index of air, γ : the specific heat ratio, Δd : the width of sound wave, p : the air pressure, Δp : the intensity of sound wave, $\rho = z_0/Z_R$: the spatial position parameter of sound wave normalized by the Rayleigh zone, z_0: the distance from the beam waist to the wave position, and $Z_R = \kappa_i \omega_0^2 / 2$: the Rayleigh zone.

2.2 Experimental apparatuses

The creeping discharge is generated in order to understand the fundamental relationship between the micro discharge and the acoustic properties. The electrode to generate the creeping discharges consists of a flat cable electrode on the dielectric material and a plane backside electrode. The high voltage (6kV: peak to peak voltage, 28.6kHz) is produced by the high frequency and high voltage power supply. The sound signal is generated by the discharge of the electrode. The discharge current is measured through the current transformer (1kHz～1MHz). The current, voltage waveforms of micro discharge and the acoustic signal detected by the optical wave microphone are stored in the digital oscilloscope (Tektronix TDS3034).

3. Results

The voltage is applied to the electrode in atmospheric pressure. The measurement result of sound and current waveforms are shown in Fig.2. When the current flows, the electrical discharge sound has been generated. The current wave form is pulse-like. The discharge currents flow during 4.3µs, 7.7µs, 19.4~21.7µs and 39.5µs. The maximum current value is 1.9mA. The sound signal is generated at 4.3µs, 7.7µs, 20.8µs and 39.5µs. These generation time of the discharge current and the sound signal are comparatively well agreements.

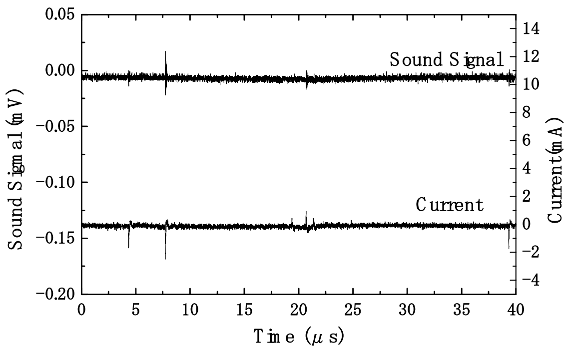

Fig.2. Sound signal and Current waveforms with applied voltage of 6kV.

Figure 3 shows the analyzing result of the acoustic signal by CNT with applied voltage of 6kV.The frequency components over 20kHz appear at 4.3µs, 7.7µs, 20.8µs and 39.5µs. These results by CWT are well agreements with the time of discharge current and acoustic signal by creeping discharge. The dominant frequency components at the time of 7.7µs have the wide frequency components from 21.9kHz to 78.1kHz. The sound signal at the time of 20.8µs contains the frequency components from 40.5kHz to 75.3kHz.

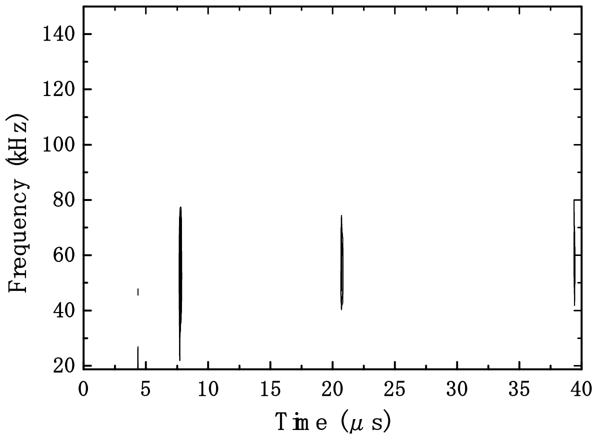

Fig.3. Time-frequency representation of sound signal using CWT with applied voltage of 6kV.

REFERENCES

[1] T. Ohkubo and Y. Nomoto, J. Inst. Electrostatic Japan, 19 (1995) 369.

[2] T. Nakamiya, K. Ebihara, T. Ikegami, Y. Sonoda and R. Tsuda, Acoustic Spectra Characteristics of Creeping Discharge, Proc. The 5th Asia-Pacific International Symposium on the Basic and Application of Plasma Technology, 5 (2007), 82-85.

[3] T. Nakamiya, K.Ebihara, T. Ikegami, Y. Sonoda and R. Tsuda, Acoustic Signal Analysis in the Creeping Discharge, Journal of Physics, vol.100, 062016 (2008).

[4] Yoshito Sonoda, Masanori, Measurement of Low-Frequency Ultrasonic Waves by Fraunhofer Diffraction, Jpn. J. Appl. Phys. 33 (1994), Part 1, No.5B, 3110-3114.

Authors: *prof. dr Toshiyuki Nakamiya, prof. dr Yoshito Sonoda, prof. dr Ryoichi Tsuda, Department of Electronics and Intelligent, Tokai University,Toroku9-1-1, Kumamoto 862-8652, Japan, E-mail: nakamiya@tokai.ac.jp; prof. dr Tomoaki Ikegami, prof. dr Fumiaki Mitsugi, Graduate School of Science and Technology, Kumamoto University, Kurokami 2-39-1, Kumamoto 860-0082, Japan; prof. dr Kenji Ebihara, Dojindo Laboratories, Tabaru 2025-5, Mashiki-machi, Kamimashiki-gun Kumamoto 861-2202, Japan.*

THE CENTENARY OF CRYOELECTROTECHNICS

Jacek SOSNOWSKI

Electrotechnical Institute

Abstract. *At 10th July 1908 year Heike Kammerlingh Onnes in his laboratory in Leiden (Netherland) has firstly in world liquefied helium. This date is treated as the border between classical low temperature sciences and new era which brought quantum phenomena as superconductivity and superfluidity, construction of new devices in the frame of new discipline cryo-electrotechnics. To description this anniversary is devoted the paper.*

Streszczenie. *10 lipca 1908 r. Heike Kammerlingh Onnes w swoim laboratorium w Ledzie (Holandia) jako pierwszy naukowiec wraz ze swoim zespołem uzyskał skroplony hel. Datę tę uważać można jako graniczną pomiędzy klasyczną nauką, głównie w zakresie niskich temperatur, a nową erą, która zaowocowała w kwantowych zjawiskach, jak nadprzewodnictwo, nadpłynność i następnie ich zastosowań głównie w krioelektrotechnice.*

Keywords: helium liquefaction, cryoelectrotechnics, superconductivity.
Słowa kluczowe: skroplenie helu, krioelektrotechnika, nadprzewodnictwo

Helium liquefication

On 10th July 1908, Professor Heike Kamerlingh Onnes and his team first liquefied helium at organized him Cryogenic Laboratory, in University of Leiden, at Netherlands. This date can be treated therefore as the border between classical sciences and new era leading to such discoveries as quantum phenomena – superconductivity and superfluidity and construction of based on them devices. This date can be therefore treated as origin of the cryoelectrotechnics, while IIR (International Institute of Refrigeration placed in Paris) announced 2008 year as Year of Cold (Anne du Froid). The liquefaction of helium by Kammerlingh Onnes was achieved as the result of the large efforts and programs directed by him, which allowed to conduct the investigations in large scale. It allowed him to achieve success and to win his rival Dewar and polish scientist Karol Olszewski [1]. They conducted their research in limited scale without significant governmental funds, in contrary to Kammerling Onnes.

Fig.1. Kammerling Onnes (left) and van der Waals (right) at the constructed first helium liquefier (1908 year). .

Fig. 2. *Liquefier compressor wheel of diameter 250 mm.*

Prof. Olszewski and Wróblewski received liquid air, argon and oxygen firstly in world in considerable amount. However lack of funding could not bring positive results in the case of liquefication of last noble gas – helium. This was realized by Kammerling Onnes, which was appointed in 1882 as Professor of Experimental Physics at Leiden, at the age of 29 years. For next 26 years he built cryogenics laboratory and conducted various low temperature programs, finally liquefied helium. After three years it is in 1911 it allowed him to discover superconductivity. On the scientific meaning of the helium liquefaction, which opened the liquid helium story, indicates the fact that after 5 years it is in 1913 year Kammerlingh Onnes was awarded with the Nobel price, just for this achievement, not for superconductivity phenomenon, which he discovered two years earlier. The key to the experimental approach of Kammerlingh Onnes was using of the preliminary cooling in liquid hydrogen temperature, which allowed him already to apply then successfully adiabatic expansion of gas in the Joule-Thomson valve and observe on the bottom of dewar condensation of helium liquid. This construction shown in Fig. 1 was improved twenty years later by Kapitza, which used instead of the hydrogen bath the piston expander.

Fig.3. General view of the complete system of the matrix magnetic separator plant for kaolin purification, working in Kaznejov (Czech Republic).

This expander during the helium gas flow moves very quickly and absorbs in this way heat from helium gas, decreasing its temperature. Presently instead of such expanders are used rotating with velocity of the range 216 000 rpm turbines, example of which is shown in Fig. 2. They allow to increase the efficiency of the liquid helium production up to industrial level, required for cooling superconducting machines. In Czech Republic liquefier of the Ferox Decin production, with two turboexpanders, provides liquid helium, to superconducting magnet system for the magnetic separation plant.

Superconducting devices

In Fig. 3 is shown matrix separator system for the kaolin purification from magnetic impurities Fe and Ti, for white paper production of improved quality, working successfully in Kaznejov in Czech. Matrix catching the ferromagnetic impurities from kaolin is composed from steel fibers, and has the form of ring of the diameter about 1,5 m. Helium liquefaction allowed to discover then Kammerling Onnes superconductivity, applied in numerous superconducting machines. Therefore this date of 1908 year can be treated as origin of cryoelectrotechnics. First steps were however not successful because initially were made attempts to construct superconducting magnets from available then superconducting materials, as Pb wires. Critical magnetic field of such magnet was of the range only 50 mT. For many years up to second world war it was believed therefore that with using superconductors cannot be generated large magnetic field, due to low critical field of type I superconductors. This point of view has been changed after discovery by Schubnikov mixed state, just before second world war and then by theoretical prediction by Abrikosov of the magnetic vortices existence. First large achievements of cryoelectrotecnics were connected with the development of technological process of the production Nb-Ti wires, in 50th years, which allowed then to built superconducting magnets creating magnetic field up to 6-8 T. Also presently Nb-Ti is further essential and cheapest material for construction superconducting wires. On the scale of this production indicates fact that in Germany largest cryogenic factory EAS Hanau makes 30 000 km of this wire in one year. This wire is used both in laboratory magnets as well as in power application of superconductors, especially in programs of the supercollider in CERN. This Nb-Ti wire is also predicted for application in near future in the project ITER (International Thermonuclear Energy Reactor) being the second after the project of construction cosmic station Alpha largest in world international program. Discovery already more than twenty years ago, of HTc superconductors created new branch of cryoelectrotechnics related to these materials, which brings just now first industrial commercial applications of them. Most promising is using HTc superconducting materials in fault current limiters, resistive or inductive type. Superconducting materials allow to built almost ideal resistive current limiter, without resistance in working state and with finite one in resistive state after fault current appearance. In Germany it is under construction now largest in Europe project of the construction resistive current limiter CULT 110 for the current 31,5 kA working in the electric network of 110 kV, using HTc BiSSCO type cut tubes as resistive elements. The programs of using inductive fault current limiters are also presently developed in world. Regarding the advantages of the application of the HTc superconducting winding in large scale machines can indicate following comparison of the mass of the 36,5 MW ship motor, constructed for US Navy by AMSC company. The weight of this motor built from conventional material would be 280 ton, while using HTc wires it reduces to 75 tons. The dimensions are also reduced then four times.

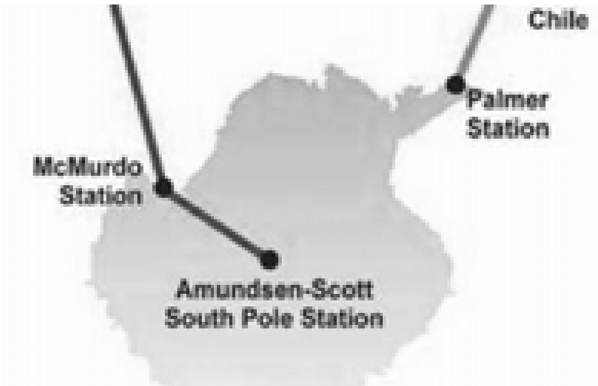

Fig.4. Map of the position scientific station at the South Pole, with indicated way of transport to this station cryogenic liquids during short Antarctic summer time.

At the end of this paper we notice that cryoelectrotechnics is used more and more widely in developed countries and there are strong expectations of solving with its help the energy crisis manifested with rapidly growing the price of oil barrels up to 120 USD presently. Both superconductivity applications as well as cryogenic liquid natural gases are promising at that aim. From other side cryogenics is developed too in such exotic regions as Antarctic, where on South Pole there are localized some scientific laboratories leading geophysical investigations. Due to clean air atmosphere precise telescope, which needs additional cooling is situated here. For supplying these laboratories with liquid helium during three monthly summer time large storages, usually of volume 13 140 liters travel by ship or be plane approximately 10,000 miles from USA and then by land to the South Pole, as shows Fig. 4. In winter it is too low temperature for airplanes for reaching this Pole.

REFERENCES

[1] Sosnowski J., Superconductivity and applications, Book Publisher of Electrotechnical Institute, Warsaw, Poland (2003) p. 1-200 – in Polish.

***Author**: prof. dr hab. Jacek Sosnowski, Instytut Elektrotechniki, 04-703 Warszawa, Pożaryskiego 28, E-mail: sosnow@iel.waw.pl*

Conference **ELMECO-6**
ELECTROMAGNETIC DEVICES AND PROCESSES IN ENVIRONMENT PROTECTION
joint with
9th Seminar APPLICATIONS OF SUPERCONDUCTORS **AoS-9**
June 24 – 27, 2008 Nałęczów, Poland

ZASTOSOWANIE MIEDZI JAKO PIERWIASTKA CHARAKTERYSTYCZNEGO PRZY POMIARACH TEMPERATURY METODĄ ORNSTEINA

Zbigniew KOŁACIŃSKI[1], Grzegorz RANISZEWSKI[1], Łukasz SZYMAŃSKI[2]

Politechnika Łódzka (1), Wyższa Szkoła Humanistyczno-Ekonomiczna (2)

Streszczenie. *. Metoda Ornsteina pomiaru temperatury opiera się na pomiarze intensywności dwóch linii spektralnych. Wybrano miedź jako pierwiastek posiadający charakterystyczne, wyraźne linie w zakresie widma światła widzialnego. Celem poniższego opracowania jest określenie przydatności zastosowania miedzi przy pomiarach temperatury plazmy metalicznej.*

Słowa kluczowe: diagnostyka plazmy, skład plazmy, metoda Ornsteina

Wstęp

Temperatura plazmy termicznej jest praktycznie nieograniczona, gdyż możliwe jest uzyskanie temperatur rzędu milionów K. W procesie utylizacji odpadów, zastosowanie znalazła plazma termiczna wytwarzana bezpośrednio w łuku elektrycznym. W praktyce niemal wszystkie związki wchodzące w skład odpadów przechodzą w stan gazowy w temperaturze rzędu tysięcy K. Temperatura taka nie jest możliwa do osiągnięcia w przypadku klasycznych spalarni odpadów.

Nierozwiązanym dotąd problemem badawczym jest określenie wpływu wsadu na trwałość wyładowania łukowego, aby w możliwie największym stopniu wykorzystać moc znamionową zasilacza. Wiąże się to z teoretyczną analizą wielu parametrów równowagowych i termodynamicznych mających wpływ na efektywny potencjał jonizacji plazmy oraz przeprowadzeniem diagnostyki spektralnej i pomiarów zmian chwilowych prądu i napięcia łuku w zależności od koncentracji substancji wsadowych w łuku. Są to zagadnienia nowe i dotąd nie rozpoznane w literaturze.

Materiał badany występuje w postaci proszku. Proszek ten w czasie kontaktu z łukiem elektrycznym początkowo topi się, a następnie paruje i wnika w kanał łuku elektrycznego zmieniając jego przewodność elektryczną, przewodność cieplną, temperaturę parametry równowagowe i termodynamiczne plazmy. Najczęściej wchodzące w skład odpadów metale to Al, Ca, Na, Si, Mg, Fe, Cr.

Temperaturę łuku określić można za pomocą analizy spektrograficznej natężenia linii widmowych miedzi (metoda Ornsteina) domieszkowanej do badanej próbki. Badanie wpływu poszczególnych pierwiastków na parametry łuku elektrycznego polega na wprowadzeniu mieszaniny danego pierwiastka wraz z pierwiastkiem pozwalającym określić temperaturę łuku – miedzią. Wprowadzenie miedzi wpływa na gęstość elektronów w łuku elektrycznym, a jednocześnie jego przewodność i temperaturę. Celem poniższego opracowania jest określenie wpływu miedzi w próbce, na skład plazmy.

Skład plazmy

Popioły lotne pochodzące z elektrowni i elektrociepłowni węglowych składają się w przeważającej części z metali. W skład tych popiołów wchodzi głównie SiO_2 (47-57%), Al_2O_3 (19-37%), Fe_2O_3 (3-16%), CaO (1-10%), MgO (do 3%) Na_2O (do 2%), K_2O (do 4,5%), SO_3 (do 1,3%). [1,2]

Łuk elektryczny zaczyna palić się w gazie roboczym, np. w argonie roztapiając te związki. Następnie następuje ich gazyfikacja i jonizacja. Wchodzą one do kanału łuku elektrycznego zmieniając szereg jego właściwości. Określenie wpływu tych związków jest związane z wyznaczeniem wielu parametrów równowagowych i termodynamicznych.

Ustalono, że w temperaturze powyżej 2000K podczas rozkładu popiołów powstają gazy zawierające następujące związki w fazie gazowej:

Al, AlO, AlO_2, Al_2O, Al_2O_2, Al_2O_3, Al_2,
Ca, CaO, Ca_2,
Cr, Cr_2O_3, Cr_2, CrO, CrO_2, CrO_3, Cr_2O, Cr_2O_2,
Fe, FeO, FeO_2,
Mg, MgO, Mg_2,
Na, Na_2, NaO, Na_2O, Na_2O_2,
O, O_2, O_3,
SiO, SiO2, Si, Si3, Si2O2.

Stabilność wyładowania łukowego zależy od dwóch czynników: od parametrów jakościowych źródła zasilania oraz od zmian rezystancji łuku skutkującej zmianą spadku napięcia na łuku. Zbadanie wpływu tlenków mineralnych pochodzących ze wsadu pieca pozwala na określenie jednego z powyższych czynników. Tlenki te zmieniając efektywny potencjał jonizacji zmieniają konduktancję łuku.

Aby określić wpływ poszczególnych związków mineralnych, które zawarte są w kanale łukowym i zachowanie się łuku elektrycznego pod wpływem zmian efektywnego potencjału jonizacji należy dokonać pomiaru temperatury łuku używając metody, która byłaby niezależna od chemii plazmy (skład plazmy nie wpływający na dokładność pomiaru temperatury).

Obliczenia

Plazma metaliczna składa się z atomów, jonów o różnym stopniu jonizacji oraz elektronów. Jako gazu roboczego użyto argonu. Dla uproszczenia założono, że tylko cząsteczki metalu pojawiają się w atmosferze argonowej. Pominięto też wpływ drugiego stopnia jonizacji ze względu na stosunkowo niską temperature obszaru badań (poniżej 10000K).

Założono, że w całej objętości łuku występuje stan lokalnej równowagi termodynamicznej.
Przeprowadzono obliczenia gęstości atomów N0, jonów N+, i elektronów Ne korzystając z układu 5 równań nieliniowych:
Równań Saha dla każdego pierwiastka wchodzącego w skład plazmy [3]:

(1) $$\frac{N_e \cdot N_{z+}}{N_z} = 2 \cdot \frac{u_{z+}(T)}{u_z(T)} \cdot \frac{(2 \cdot \pi \cdot m \cdot k \cdot T)^{3/2}}{h^3} \cdot \exp\left(-\frac{E_z - \Delta E_z}{kT}\right)$$

Prawo Daltona:

(2) $$p = \left(N_G + N_{G+} + N_{Me} + N_{Me+} + N_e\right) \cdot k \cdot T$$

Równanie ładunków dla lokalnej równowagi termodynamicznej:

(3) $$N_e = N_{G+} + N_{Me+} + N_e$$

Procentowy udział par metalu:

(4) $$x = \frac{N_{Me} + N_{Me+}}{N_{Me} + N_{Me+} + N_G + N_{G+}}$$

gdzie:
Me, G – odnoszą się do poszczególnych pierwiastków wchodzących w skład plazmy; $u_z(T)$, $u_{z+}(T)$ – suma stanów odpowiednio dla pierwiastka i jednokrotnie zjonizowanego pierwiastka; m – masa elektronu; h – stała Plancka; k – stał Boltzmanna; E – energia jonizacji; ΔE – obniżenie energii jonizacji; T – temperatura [K];
Suma stanów dla rozważanych pierwiastków została obliczona przez Drawina [4]

Wyniki obliczeń

Założono, że związki minerale będą dostarczane w sposób kontrolowany do łuku poprzez jedną elektrodę. Obliczenia przeprowadzono dla mieszaniny argonu i metalu. Rys. 1. pokazuje koncentracje plazmy argonowej z 3% zawartością miedzi w funkcji temperatury pod ciśnieniem atmosferycznym.

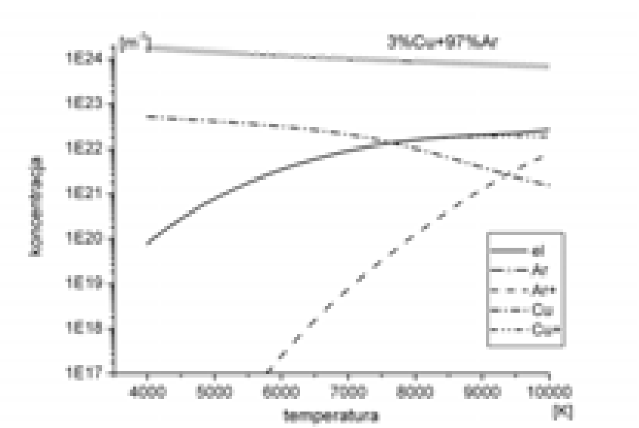

Rys.1. Skład plazmy argonowej z 3% zawartością miedzi.

Koncentracja elektronów praktycznie pokrywa się z koncentracją jednokrotnie zjonizowanych atomów miedzi do temperatury 9500K. Oznacza to dominujący wpływ domieszki miedzi.

Na Rys. 2. porównano koncentracje poszczególnych składników dla plazmy metalicznej, składającej się w 80% z glinu i w 20% z miedzi.

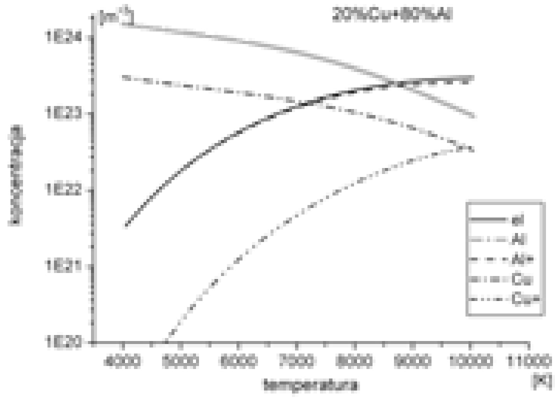

Rys.2. Skład plazmy metalicznej z 20% zawartością Cu

Obliczenia przeprowadzono dla metali wchodzących w skład odpadów. Dla każdego badanego pierwiastka uzyskano taką samą zależność – koncentracja elektronów zależy głównie od koncentracji jednokrotnie zjonizowanych atomów badanego metalu. Dlatego też w dalszych obliczeniach pominięto obecność gazu zakładając, że łuk pali się jedynie w obecności mieszaniny badanego gazu i miedzi jako pierwiastka detekcyjnego. W celu określenia składu plazmy zastosowano taki sam układ równań jak w przypadku mieszaniny argon-miedź zastępując argon badanym pierwiastkiem.

Wnioski

Wykonane obliczenia pokazują, że nawet przy zawartości kilkudziesięciu procent miedzi w plazmie metalicznej złożonej z atomów i jonów miedzi, atomów i jonów rozpatrywanego metalu oraz elektronów (ilość elektronów jest zdominowana przez ilość jonów badanego metalu dla temperatur poniżej 7000K). Oznacza to, że dodatek miedzi do próbki zawierającej Si, Al, Fe, Ca, Na, Mg lub K nie zmienia przewodności elektrycznej i może być użyty w badaniach jako pierwiastek detekcyjny dla metod spektroskopowych.

LITERATURA

[1] Ilic M., Cheesman C., Sollars C., Knight J., Mineralogy and microstructure of sintered lignite coal fly ash , *Fuel*, Vol. 82, pp. 331-336, 2003
[2] Baoguo Ma, Meng Qi, Jun Peng and Zongjin Li, The compositions, surfach texture, absorption and binding properties of fly ash In China, „*Environmental International*", Vol. 25, No. 4, pp. 423-432, 1999
[3] W.Lochte-Holtgreven, *Plasma diagnostics*, 1968
[4] Drawin H.W., *Data for plasmas in local thermodynamic equilibrium* , Gauthier-Villars, Paris 1965

***Autorzy**: prof. dr hab. inż. Zbigniew Kołaciński, Politechnika Łódzka, Katedra Aparatów Elektrycznych, ul. Stefanowskiego 18/22, 90-924 Łódź, E-mail: zbigniew@p.lodz.pl; mgr inż. Grzegorz Raniszewski, Politechnika Łódzka, Katedra Aparatów Elektrycznych, ul. Stefanowskiego 18/22, 90-924 Łódź, E-mail: larryl@o2.pl ; dr inż. Łukasz Szymański, Wyższa Szkoła Humanistyczno-Ekonomiczna, ul. Rewolucji 1905r. nr 64, 90-222 Łódź, E-mail: lusyma@p.lodz.pl*

OZONE SYNTHESIS UNDER PULSE DISCHARGE

Sławomir JODZIS, Angelika KOWALSKA

Warsaw University of Technology

Abstract. *Preliminary studies on efficiency of ozone synthesis under alternative pulse discharge conditions were carried out. Selected results concerning ozone synthesis from pure oxygen, which enabled limiting the number of process parameters, have been presented.*

Streszczenie. *Przeprowadzono wstępne badania nad efektywnością elektroplazmowej syntezy ozonu prowadzonej przy zasilaniu impulsowym o naprzemiennej polaryzacji. Przedstawiono wybrane wyniki prac prowadzonych w tlenie, co umożliwiło ograniczenie liczby parametrów wpływających na bieg procesu.*

Keywords: ozone synthesis, oxygen, alternative pulse discharge.
Słowa kluczowe: synteza ozonu, tlen, wyładowanie impulsowe o przemiennej polaryzacji.

Introduction

In every electroplasma method of ozone synthesis, atomic oxygen, which is needed for the reaction to occur, is generated by electrons with high energy, which form during discharges, according to the following reaction:

(R1) $O_2 + e \rightarrow O + O + e$

(R2) $O + O_2 \rightarrow O_3$

In commonly used barrier type discharges, ozone synthesis is performed by applying high voltage alternating current. Under such conditions the time of discharges equals approximately half of the period of the voltage change. Reaction (R1) is several orders of magnitude faster than the subsequent reactions, which occur without electron participation. However, when the discharge phase is long, ozone, which already exists in the discharge gap, may be destroyed in collision with an electron:

(R3) $O_3 + e \rightarrow O_2 + O + e$

This is an undesired effect because the main product decomposes. Moreover, there is a considerable energy loss because electrons increase the average energy of molecules. This, in turn, results in an increase in temperature in the gap.

When the average power of the discharge remains unchanged and an appropriate amount of energy is supplied in a very short time (dozens of nanoseconds), the slow reactions, which had been initiated by reactions with electrons, can occur in the intervals between the discharge cycles. In such a case the use of energy will be much more efficient. The time between the pulses enables the atomic oxygen to be used up before a new portion is produced.

Experimental

The studies were carried out in pure oxygen in an Otto-type ozonizer, with the temperature of the electrodes equal 0, 25 and 50°C. The ozonizer gap width was 0.9 mm. The scheme of the ozonizer supplying system is shown in Fig. 1. Due to the fact that rotating switches Sw1 and Sw2 were alternatively switched on, the system was operated by frequencies up to 350 Hz. The pulses, which were generated, exhibited an alternate polarization (Fig. 2) and the width approx. 180 ns (Fig. 3). Each pulse actually consists of two shorter ones (ca. 80 ns), which result from a time-shifted discharge of capacitors C2 and C3. The ozonizer was grounded by using a separating transformer, Tr2, wound around a ferrite core (3F3). The matching of the impedance of the windings was obtained experimentally, basing on the maximum ozone concentration in the outlet gas when different combinations of the number of winding turns were tested. The power of the pulse was measured with oscilloscope TDS 3032 (Tektronics) equipped with a P6015A H.V. probe and a P202 current probe. The active power of a discharge P_A was determined as follows:

$$P_A = 2\, f E_{pulse} \tag{1}$$

where: P_A – active power, f – frequency, E_{pulse} – single pulse energy.

Apart from the method presented above, the power consumed in the other areas of the electric circuit was controlled („gross” power).

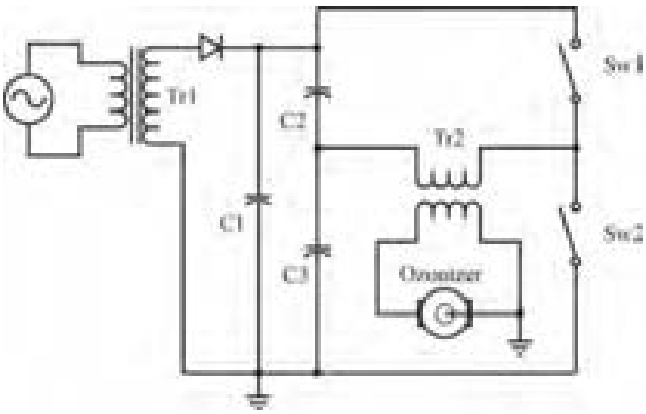

Fig.1. Scheme of the H.V. pulse supplier. C1 = 22 nF/40 kV; C2, C3 – ceramic capacitors (470 pF/30 kV)

Results and discussion

Figure 4 depict an ozone concentration vs. discharge active power (25°C; oxygen: 4, 12 and 28 Ndm^3/h) relation for a pulse supplied ozonizer, and, for comparison, one with a conventional inverter (1 kHz). It can be observed that the concentrations depend on the gas flow rate as well as on the discharge power and temperature. In a comparative range of powers the pulse discharge conditions proved to be better. For all temperatures and flow rates the ozone concentrations are higher than those obtained from barrier discharges. However, the supply system does not allow an increase in the energy.

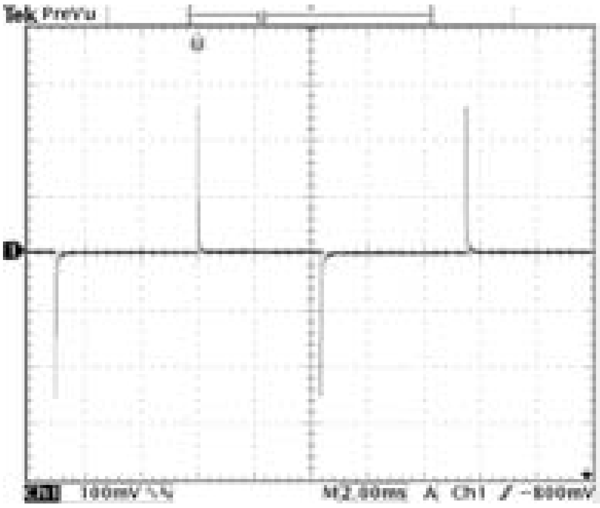

Fig.2. Voltage supplying the ozonizer. Real amplitude 13.6 kV

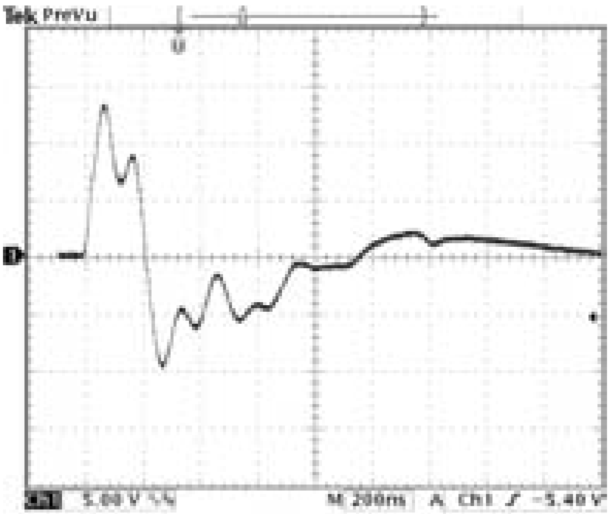

Fig.3. Positive pulse supplying the ozonizer (in real two inflicted 80 ns pulses)

In Figure 5 a comparison of the energy efficiencies of ozone obtained under alternative pulse discharge conditions and analogous results from barrier-type discharges. The studies were carried out under similar conditions, with the same discharge gap width. Since the average power pulse discharges is low, the results acquired with a constant power of 1 W were compared. It can be observed that the efficiency of the pulse discharges is about twice as higher than that of barrier discharge. It is noteworthy that the efficiencies are up to 30 % of the theoretical value (ca. 1220 g O_3/kWh). It is currently impossible to determine, if the efficiency is actually dependent on the electrode temperature. The main reason of this doubt is the low power of the discharges. In the used supply system, a significant amount of energy was lost on the switches. In barrier discharges the concentration of ozone and the energy efficiency of the process is found to depend on temperature regardless of the power and the gas flow rate [1-3].

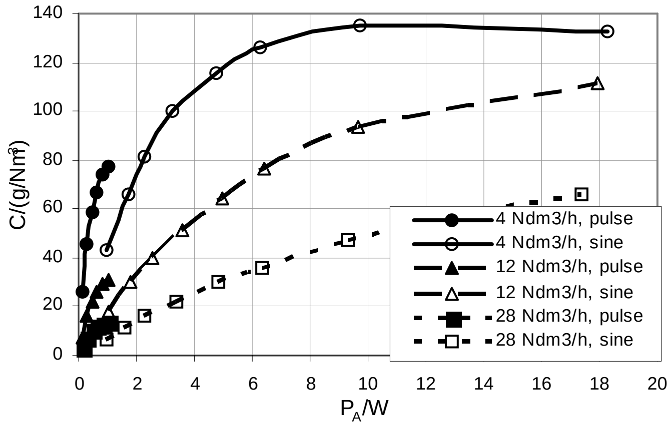

Fig.4. Ozone concentration vs. discharge active power obtained at 1kHz (sinus) and 350 Hz (alternative pulse discharge); 25°C, oxygen flow rate 4, 12 and 28 Ndm^3/h.

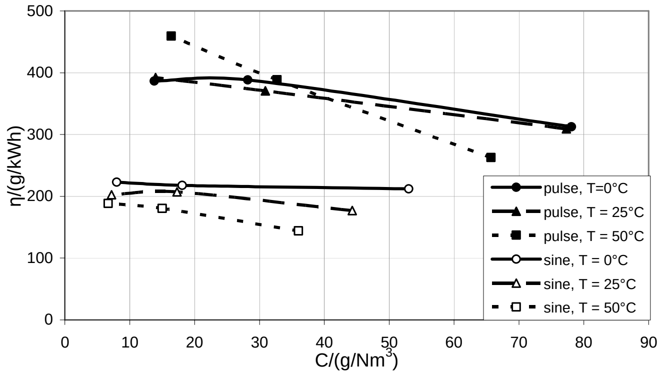

Fig.5. Energy efficiency of ozone synthesis vs. ozone concentration obtained at 1kHz (sinus) and 350 Hz (alternative pulse discharge); active power 1 W, oxygen 4 Ndm^3/h, temperature of cooling liquid 0, 25 and 50°C.

This study was financially supported by the Ministry of Science and Higher Education from Research Program (2006-2009); Nr. MNiSW N205 012 31/0628.

REFERENCES

[1] Jodzis S., Petryk J., Schmidt-Szałowski K., *J. of High Temp. Mater. Proc.*, 5 (2001), 527-534
[2] Jodzis S., *Pol. J. of Chem. Technol*., 4 (2002), No. 2, 12-16
[3] Jodzis S., *Ozone Sci. & Eng*., 25 (2003), 63-72

***Authors**: dr inż. Sławomir Jodzis, Politechnika Warszawska, Wydział Chemiczny, ul. Noakowskiego 3, 00-664 Warszawa, E-mail: jodzis@ch.pw.edu.pl.*

Conference **ELMECO-6**
ELECTROMAGNETIC DEVICES AND PROCESSES IN ENVIRONMENT PROTECTION
joint with
9th Seminar APPLICATIONS OF SUPERCONDUCTORS **AoS-9**
June 24 – 27, 2008 Nałęczów, Poland

DECOMPOSITION OF ELECTROSTATIC-PRECIPITATED PARTICULATE MATERIALS FROM DIESEL EXHAUST GAS WITH NITRIC OXIDES USING DIELECTRIC BARRIER DISCHARGE

Yukihiko YAMAGATA[1], Yosuke FUJII[1], Yozo KAWAGASHIRA[1], Katsunori MURAOKA[2]

Kyushu University (1), Chubu University (2)

***Abstract**. Diesel particulate materials (DPM) in a real diesel exhaust gas were collected in a reactor using an electrostatic precipitation (EP). Subsequently, the EP-collected DPM were treated in the same reactor by a dielectric barrier discharge in a model gas including NO molecules. It was suggested that actual DPM and NO acting as the oxidant and reductant, respectively, were decomposed simultaneously and effectively by DBD.*

Keywords: diesel particulate material, NOx, dielectric barrier discharge, electrostatic precipitation

Introduction

Exhaust gas from a diesel engine and other combustion processes contains diesel particulate materials (DPM) and nitric oxides (NO*x*). Because DPM increases the risk of lung cancer and NO*x* causes acid rain, they have been restricted in many countries. So far there have been many attempts to reduce these emissions using catalysts or alternate filter trapping-burning by auxiliary fuel injection. However, because of lack of sufficient action and/or excessive cost, promising techniques are yet to be explored.

Recently, we have developed a simultaneous decomposition method for DPM and NO*x*, which is based on the combination of dielectric barrier discharge (DBD) with condensation/localization technique [1, 2]. DPM and NO*x* are collected in a reactor using an electrostatic precipitation (EP) and a honeycomb-shaped adsorbent, respectively. After the sufficient collection, the DBD is generated in the closed space to condense the DPM and NO*x*, and decomposes these simultaneously. Another method having the same concept has been successfully demonstrated for decompositions of volatile organic compounds elsewhere [3-5]. Therefore, this method, where environmentally hazardous materials densified to a large concentration are treated in the closed space, will be one of the most promising techniques.

In this paper, we describe the experimental results of EP of DPM evacuated from a real engine and the subsequent decompositions of the collected DPM and NO by DBD.

Experimental setup and procedure

Figure 1 (a) and 1 (b) show the experimental setup and a photograph of an EP/DBD reactor. In the experiments of EP of DPM and decomposition of EP-collected DPM with NO by DBD, a specially-designed reactor was used. A raw stainless steel sheet (0.15 mm thick) as a collection electrode, and a mica electrode, in which both sides of a stainless steel sheet were fully covered by a mica sheet, were faced each other with the 2.0 mm separation. The set of these electrodes was accumulated by 10 steps to form the EP/DBD reactor. By adopting this structure, it become possible to make the electrostatic precipitation and generation of the DBD by the EP/DBD reactor.

A part of exhaust gas from a real diesel engine (AIRMAN EP3100DBL, 273 cc) was led into the EP/DBD reactor. Negative corona discharge was generated at DC 5.0 kV by multi-needle electrodes that were placed in front of the reactor. DPM in the exhaust gas flowing at 20 – 40 L/min were collected on the collection electrodes in the EP/DBD reactor heated at 100 ºC. The reduction rate of

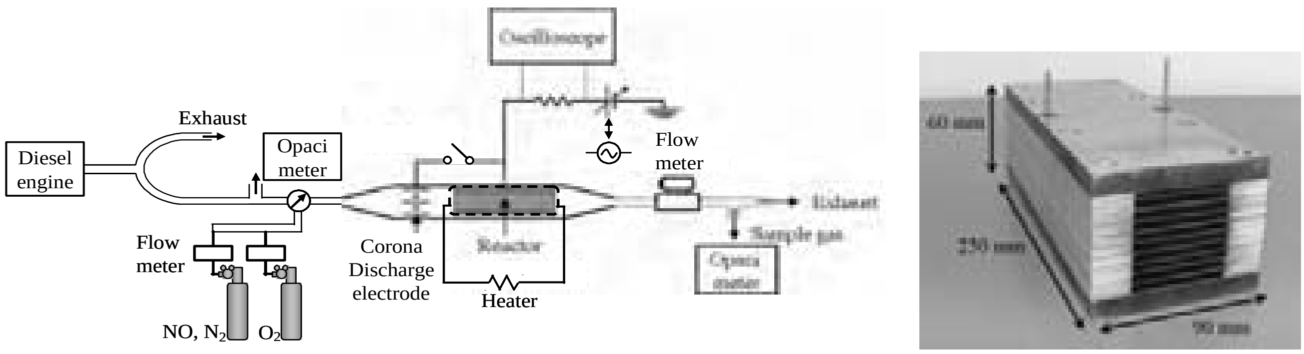

(a) experimental setup

(b) Photograph of EP/DBD reactor

Fig. 1. Schematic illustrations of (a) experimental setup for electrostatic precipitation of DPM and decompositions of DPM and NO, and (b) photograph of EP/DBD reactor.

DPM was measured by an opacimeter (HORIBA MEXA-130S) before and after the reactor. After sufficient collection of DPM, DPM decomposition was demonstrated by DBD generated in a model gas (NO: 1500 ppm in O_2/N_2:10/90 %) at 7 kV at 60 Hz. In this experiment, the model gas flow rate was kept at 2 L/min, and water vapor was added in the gas to observe the influence of water vapor on the decomposition. Concentrations of NO*x* and CO/CO_2 at the outlet of the EP/DBD reactor were monitored to measure the decomposition rate of DPM and NO.

Results and discussion

Figure 2 shows the temporal behavior of DPM reduction rates at various flow rates of 20, 30 and 40 L/min. The DPM reduction rates are seen to be kept 90 % or more even after 60 min operation at 20 and 30 L/min. At 40 L/min, DPM reduction rate decreases with the passage of time and still keeps a sufficient high value of 80 % or more after 30 min from the beginning of EP. It is thought that this decrease causes the generation instability of corona discharge by the adhesion of DPM to multi-needle electrodes. In these cases, amount of electrostatic precipitated DPM were estimated to be 0.09, 0.04, 0.15 mg at 20, 30, 40 L/min, respectively.

Subsequently, simultaneous decompositions of the EP-collected DPM and NO in a model gas were demonstrated using DBD with and without one of them. Before the experiments, DPM exhausted from the diesel engine working at 50% of load were collected for an hour or more in the EP/DBD reactor at 5 kV. The DBD was generated at 7 kV of AC 60 Hz. The gas flow rate was kept at 2 L/min for the experiments. Figure 3 shows the NO concentration measured at the outlet of the EP/DBD reactor kept at 100 ºC and the room temperature. For the case of the room temperature reactor, the decomposition of NO molecules progressed gradually with the passage of time. On the other hand, when the reactor was heated at 100 ºC, NO molecules were rapidly decomposed by the DBD. This is presumed that DBD generation is obstructed to moisture adhered to the inner wall of the reactor. However, it does not become a big problem as the installation to an actual system, because real exhaust gas has enough heat capacity to raise the reactor temperature.

Figure 4 shows the NO concentration measured at the outlet of the EP/DBD reactor with and without water vapor in the model gas. The reactor was kept 100 ºC for these decompositions by DBD. As can be seen in Fig. 4, the decomposition rate has improved greatly by adding of water vapor in the gas.

Conclusions

The characteristics of electrostatic precipitation of DPM in a real exhaust gas and simultaneous decomposition of DPM and NO*x* by DBD were demonstrated. It is suggested that water vapor in the exhaust gas improve the NO*x* decomposition rate but dose not spoil the DBD generation in the heated reactor. The usefulness of this method was proven.

This work has been partially supported by Grant-in-Aid for Scientific Research from the Ministry of Education, Science, Sports, Culture and Technology of Japan.

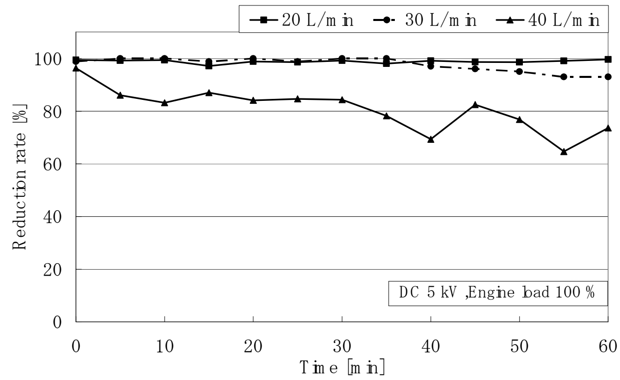

Fig. 2. Temporal behavior of DPM reduction rates at various flow rates of 20, 30 and 40 L/min.

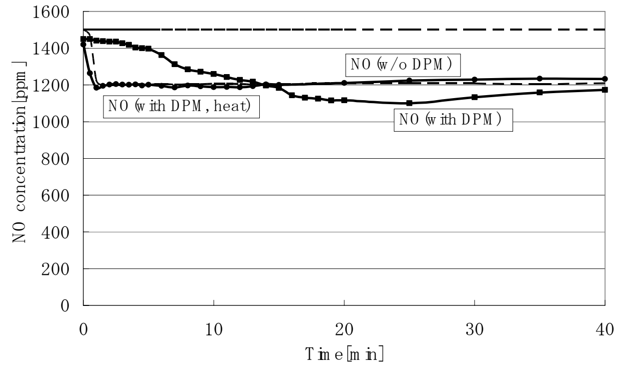

Fig. 3. NO concentration at the outlet of the EP/DBD reactor kept at 100 ºC and the room temperature.

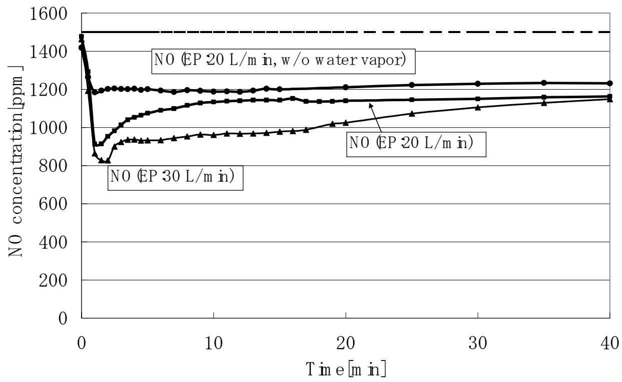

Fig. 4. NO concentration at the outlet of the EP/DBD reactor with and without water vapor.

REFERENCES

[1] T. Jyono *et. al.*, *Proc. 13th Asian Conf. Elect. Discharge (Hokkaido Univ., Japan)* **P2-15** (2006) 1.

[2] Y. Yamagata, K. Niho, T. Jono, and K. Muraoka, J. *Adv. Oxid. Technol.* **9** (2006) 134.

[3] H. Urae *et. al.*, *Trans. IEE Japan* **A-122** (2002) 965 (*in Japanese*).

[4] Y. Yamagata, K. Niho, K. Inoue, H. Okano, and K. Muraoka, *Jpn. J. Appl. Phys.* **45** (2006) 8251.

[5] H. Inoue *et. al.*, *Trans. IEE Japan* **A-127** (2007) 309 (*in Japanese*).

***Authors**: Assoc. Prof. Dr. Yukihiko YAMAGATA, Interdisciplinary Graduate School of Engineering Sciences, Kyushu University, 6-1 Kasugakouen, Kasuga, Fukuoka 816-8580, Japan, E-mail: yamagata@ence.kyushu-u.ac.jp; MC student Yosuke Fujii, Interdisciplinary Graduate School of Engineering Sciences, Kyushu University, 6-1 Kasugakouen, Kasuga, Fukuoka 816-8580, Japan; MC student Yozo Kawagashira,Interdisciplinary Graduate School of Engineering Sciences, Kyushu University, 6-1 Kasugakouen, Kasuga, Fukuoka 816-8580, Japan; Prof. Dr. Katsunori Muraoka, School of Engineering, Chubu University, 1200 Matsumoto, Kasugai, Aichi 487-8501, Japan, E-mail: muraoka@isc.chubu.ac.jp*

Conference **ELMECO-6**
ELECTROMAGNETIC DEVICES AND PROCESSES IN ENVIRONMENT PROTECTION
joint with
9th Seminar APPLICATIONS OF SUPERCONDUCTORS **AoS-9**
June 24 – 27, 2008 Nałęczów, Poland

REVIEW OF BIOMEDICAL APPLICATIONS OF SV-GMR SENSORS

Agnieszka ŁĘKAWA[1], Henryka D. STRYCZEWSKA[1], Sotoshi YAMADA, Chinthaka GOONERATNE

Lublin University of Technology(1), Kanazawa University(2)

***Abstract**. The search for new, more effective tools for biotechnology, medical diagnostics and therapy leads to application of all currently available technologies, that could prove to be useful. Spin valve giant magnetoresistance sensors were previously suggested for such bioapplications as molecular recognition and microfluidic technologies, arterial pulse diagnostic, neoplasm hyperthermia treatment and neural magnetic field detection. This paper presents a concise overview of these technologies.*

***Streszczenie.** Poszukiwanie nowych, efektywniejszych narzędzi wykorzystywanych w biotechnologii, diagnostyce medycznej i leczeniu prowadzi do badań nad wszystkimi aktualnie dostępnymi technologiami, które mogłyby okazać się pomocne. Czujniki gigantycznej magnetorezystancji z zaworem spinowym zostały do tej pory zaproponowane dla takich biozastosowań jak rozpoznawanie molekularne i technologie mikroprzepływowe, ocena tętna, terapii nowotworów metodą hipertermiczną oraz detekcji pól magnetycznych neuronów. Poniższy referat krótko je przedstawia.*

Keywords: SV-GMR, biosensors, biomedical magnetometry
Słowa kluczowe: SV-GMR, bioczujniki, magnetometria biomedyczna

Introduction

Spin valve giant magnetoresistance (SV-GMR) sensors turned out to be highly promising magnetometers for many technical applications among which the most widely utilized SV-GMR based devices are reading heads. The advantages of these sensors seem to be well suited to the requirements of biomedical applications, as well. The demands of reliability, real-time operation and small dimensions are only some of the features that should be characteristic of the biotool used in biotechnology or medical diagnostics and therapy. Spin valve structures fulfilling these requirements have been already suggested for such applications as molecular recognition, microfluidic technologies, hyperthermia treatment, spatial pulse diagnostic apparatus or neural magnetic field measurements.

Spin valve GMR sensors

The structure of exchange-biased spin valve GMR sensors comprises two ferromagnetic layers, one pinned by an antiferromagnetic layer and the second one free to change under the influence of external magnetic field, both separated by a thick nonmagnetic layer. This modified GMR structure allows one to obtain good sensitivity and a relatively high magnetoresistive ratio. Another highly desirable feature of SV-GMR as a biomedical magnetometer is the fact that it can operate at room temperature. Their micro-size dimensions render them comparable in size to the examined bioobject. These thin film structures can be deposited in complex configurations e.g. to create an array of sensors applied in biomolecular tweezers to increase the throughput of individual molecules for analysis [1] or on a needle to allow for *in-vivo* measurements inside of the body [2,3,4]. They can be easily integrated into various biochip patterns [5] or even to standard CMOS chips to facilitate detection [6].

Molecular recognition

Biomolecular recognition consists in the detection of complementary molecules. In the exemplary magnetic recognition mode particles to be detected are attached to paramagnetic particles. The immobilized on the sensors surface probe molecules combine with complementary analytes. The non-complementary molecules are washed out. Application of external magnetic field allows for the detection of bound magnetic particles (Fig.1) [7].

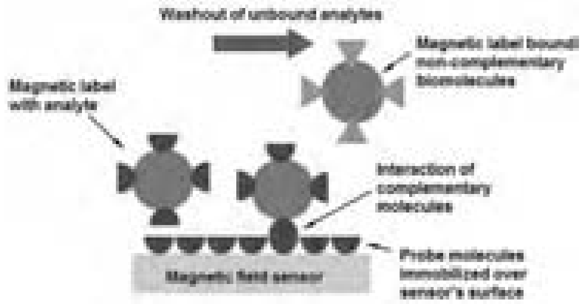

Fig. 1. Exemplary scheme of molecular recognition with the use of a magnetic sensor.

Molecular tweezers

Arrays of spin valve sensors have also been applied to build microfluidic platforms for trapping, measuring, manipulating, and sorting magnetic particles. Attaching magnetic particles to biological molecules allows for simultaneous operation on many single molecules at a time. The particles are trapped in the high magnetic field gradients present near the parallel magnetised SV-GMR structure, which is called the "ON" state. On the contrary, in the "OFF" state in the absence of external magnetic field, and for antiparallel magnetisation of layers the molecules are released. Once the molecule is trapped it can be subjected to manipulation, for instance rotation under the influence of an additional rotational magnetic field. Fig. 2 illustrates the application of torque to a DNA molecule [1].

Fig. 2. Single DNA molecule rotation, adapted from [1]

Microfluidic systems

Some studies have also been performed in the field of microfluidic systems that could be used in e. g. biochemical screening. The research encompassed the measurement of sizes and flow velocities of picodroplets of ferrofluid [8].

Spatial pulse diagnostic apparatus

The need for objectivity and standardization in the most important diagnostic method in Traditional Chinese medicine led to the idea of spin valve GMR based spatial pulse diagnostic apparatus. The suggested measurements setup is presented in Fig.3. Pad-type permanent magnets are stuck to the skin over the artery and an array of magnetoresistive sensors detects the change of signal due to vibration of the magnets resulting from spatial movement of the pulse wave in an arterial tube [9].

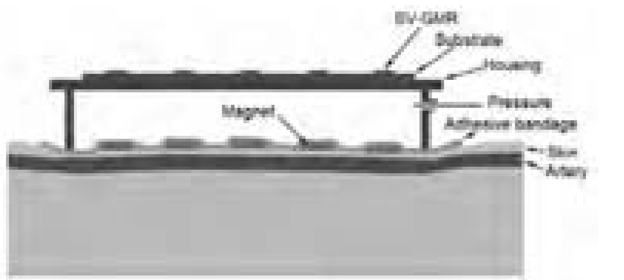

Fig. 3. The design of spatial pulse diagnostic apparatus, adapted from [8]

Hyperthermia neoplasm treatment

One of the neoplasm treatment methods - thermotherapy takes advantage of the fact that neoplasm cells are more heat-sensitive than normal, healthy cells. With increasing temperature they undergo apoptosis or at least are significantly weakened. The temperature during treatment should be precisely determined so as to be deadly for tumour and safe for healthy cells. One of the possible technical solutions to the hyperthermia treatment is injecting magnetic nanoparticles into the affected area. They can be directed to an area of interest by an external magnetic field, held there until treatment concludes and then removed. Under the influence of a time-varying external magnetic field, the particles generate heat and increase the temperature of the treated cells mainly due to hysteresis loss. After injection into the body the magnetic fluid spreads inside tissues decreasing its content density. Since the applied heat depends on magnetic flux density, exciting frequency, and amount of nanoparticles, the exact, “new” content density, should be estimated. For this purpose a needle type SV-GMR sensor can be used. Measurement of magnetic flux density by pricking a needle with SV-GMR sensor at its tip in to the treated tumour, allows one to indirectly calculate the content density and determine the temperature in question (Fig.4) [3,4].

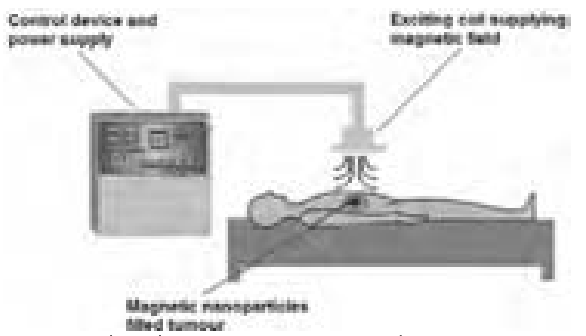

Fig. 4. Hyperthermia treatment as a cancer therapy

Neural magnetic field measurements

A Needle Type SV-GMR sensor was also employed for detection of the magnetic field distribution from a model of the neuron from peripheral nerve system. The idea of the measurement consist in touching the needle with a sensing element to the neuron lateral surface and detection of action current impulses (Fig.5). A technique for single neuronal activity detection would be very useful for example in nerve reconstruction surgery [2].

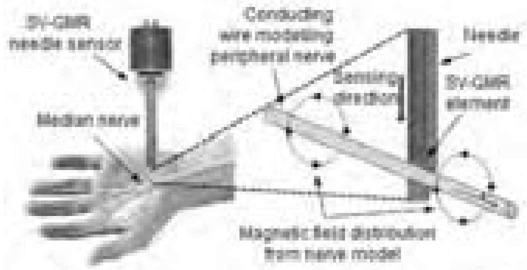

Fig. 5. Detection of magnetic field distribution from neuron model

Summary

The paper reviews several potential biomedical applications of spin valve sensors. Although still under research they seem to be promising devices to be applied in biotechnology, biochemistry or medical studies. It seems that the techniques most likely to be introduced into the widespread use are molecular recognition systems, due to highly advanced studies on this technology.

REFERENCES

[1] Mirowski E., Moreland J., Russek S., Donahue M., Hsieh K., Manipulation of magnetic particles by patterned arrays of magnetic spin-valve traps, *J. Mag. Mag. Mat.* 311 (2007) 401–404

[2] Łękawa A., Yamada S., Stryczewska H. D., Gooneratne C., Chomsuwan K., Pomiary pola magnetycznego powstającego wokół modelu neuronu przy zastosowaniu igłowego czujnika SV-GMR, *Przegląd Elektrotechniczny*, R. 84 NR 5/2008

[3] Mukhopadhyay S. C., Chomsuwan K., Gooneratne C. P., Yamada S., A Novel Needle-Type SV-GMR Sensor for Biomedical Applications, *IEEE Sens. J.,* 7 (2007) No. 3

[4] Gooneratne C., Łękawa A., Iwahara M., Kakikawa M., Yamada S., Estimation of Low Concentration Magnetic Fluid Weight Density and Detection inside an Artificial Medium Using a Novel GMR Sensor, *Sens. Trans. J., 90, Special Issue, (2008), 27-38*

[5] Li G., Sun S., Wilson R. J., White R. L., Pourmand N., Wang S. X., Spin valve sensors for ultrasensitive detection of superparamagnetic nanoparticles for biological applications, *Sens. Actuators A Phys*., 126(1) (2006) 98–106

[6] Han S.-J., Xu L., Yu H., Wilson R.J., White R.L., Pourmand N., Wang S. X., CMOS Integrated DNA Microarray Based on GMR Sensors, *Electron Devices Meeting, 2006. IEDM apos;06. International,* 11-13 Dec. 2006 pp 1 – 4

[7] Graham D. L., Ferreira H. A., Freitas P. P., Magnetoresistive-based biosensors and biochips*, Trends in Biotechnology*, 22 (2004) No.9

[8] Pekas N., Porter M. D., Tondra M., Popple A., Jander A., Giant magnetoresistance monitoring of magnetic picodroplets in an integrated microfluidic system, Appl. Phys. Let. 85 (2004) No.20, 4783-4785

[9] S.D. Choi, S.W. Kim, G.W. Kim, M.C. Ahn, M.S. Kim, D.G. Hwang, S.S. Lee, Development of spatial pulse diagnostic apparatus with magnetic sensor array, *J. Mag. Mag. Mat*. 310 (2007) e983–e985

***Authors**: Agnieszka Łękawa, student of Lublin University of Technology (LUT), E-mail: agalekawa@gmail.com; Henryka D. Stryczewska, PhD (Eng), DSc (Prof. of LUT), Institute of Electrical Engineering and Electrotechnologies, Faculty of Electrical and Computer Engineering of LUT, ul. Nadbystrzycka 38A, 20-618 Lublin, E-mail: h.stryczewska@pollub.pl.*

Conference **ELMECO-6**
ELECTROMAGNETIC DEVICES AND PROCESSES IN ENVIRONMENT PROTECTION
joint with
9th Seminar APPLICATIONS OF SUPERCONDUCTORS **AoS-9**
June 24 – 27, 2008 Nałęczów, Poland

INTRODUCTION TO QUANTUM COMPUTING

Leszek JAROSZYŃSKI

Lublin University of Technology

Abstract*. It appears that "quantum computers" has already come from science-fiction to the reality. Quantum computing shows outstanding efficiency in some numerical problems. Length of qubit registers grows noticeably last years – at least so fast as the number of interesting quantum algorithms. It's time to manufacture qubit integrated circuits. These days two promising concepts fight their way to a real usage: Josephson junction qubits and quantum dot qubits.*

Streszczenie*. Wydaje się, że tzw. komputery kwantowe przeniknęły już z kart literatury fantastyczno-naukowej do rzeczywistości. Algorytmy kwantowe wykazują znakomitą wydajność w przypadku niektórych problemów. Długość rejestrów qubitowych rośnie każdego roku – co najmniej tak szybko jak liczba interesujących algorytmów kwantowych. Nadszedł czas wytwarzania rejestrów qubitowych w postaci układów scalonych. Aktualnie ścierają się dwie obiecujące koncepcje: rejestrów qubitowych ze złączami Josephsona i kropkami kwantowymi.*

Keywords: qubit, quantum computing, Josephson junction.
Słowa kluczowe: qubit, obliczenia kwantowe, złącze Josephsona.

Introduction

A quantum (plural: quanta) in an indivisible portion of physical quantity. Energy and momentum, same scientists state that also length and time, can take only certain discrete values. The distance between two adjacent levels is a quantum. At quantum dimensions classical physics fails. A new idea – quantum physics – can explain all incredible phenomena.

The history of quantum physics is quite long. Everything started with discrepancy between the theory of a black body radiation and experimental results. After a few months of intellectual work, on 14th of December 1900 Max Planck presented explanation of his own improvement made for the black body emissivity equation. He postulated that the electromagnetic energy could be emitted only in a quantized manner - the energy could only be a multiple of an elementary quantity. That opened a new era in physics [1].

Qubit

For practical reasons we are used to do calculations using binary devices. A bit can hold binary portion of information: zero or one and nothing more. A qubit has also two basis states – let's call them ket zero |0> and ket one |1>. However, unlike a bit, qubit can hold a linear superposition of those two states (1).

$$|\psi\rangle = a|0\rangle + b|1\rangle \tag{1}$$

where: a, b – complex probability amplitudes.

The state space of a qubit is usually represented as the surface of a Bloch sphere (Fig. 1). It has two degrees of freedom so when we measure qubit we get state |0> with probability $|a|^2$ and state |1> with probability $|b|^2$. Nothing is certain, it's just probable.

Single qubit doesn't seem so interesting – only qubit register shows full potential of this idea.

Quantum entanglement

Quantum entanglement is a phenomenon where the quantum states of two or more qubits are bound together. Sometimes the state of quantum register can't be described in terms of the states of its qubits. It's called "entangled state".

Unlike bit registers, the n-qubit register has a state space of 2^n dimensions just because entanglement. Therefore, 270-bit register can hold one very big number and 270-qubit system represents in parallel more states than the number of atoms in the Universe. Unfortunately, there are some problems concerning reading of register states. Any access to a qubit – so called measurement - disturbs the quantum state. Moreover, any result is only probabilistic.

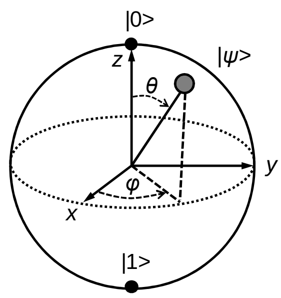

Fig. 1. A qubit representation as a Bloch sphere

Algorithms

Regardless mentioned problems, in the past few years some excellent ideas for the overcoming of the measurement problem have been found. Additionally, quantum algorithms probably outperform any known classical ones. In the Table 1, a comparison of chosen algorithms has been presented.

Table 1. Comparison of quantum and classical algorithms [2]

name	classical complexity	quantum complexity
Simon's classification	$O(2^{\frac{n}{2}})$	$O(n)$
Grover's searching	$O(n)$	$O(\sqrt{n})$
Shor's factoring	$O(e^{(\log n)^{\frac{1}{3}}(\log\log n)^{\frac{2}{3}}})$	$O(n^3)$

Implementations

Despite the catchy abstract presented above, the problem of the manufacture of usable quantum computers is still open. There are some tested concepts of building quantum computers using different approaches. They are shown at Table 2.

Table 2. Qubit implementations [2, 3]

physical object	information support	"0"	"1"
photon	photon polarization	horizontal	vertical
	number of photons	vacuum	single photon
	arrival time	early	late
coherent light	phase quadrature	amplitude squeezing	phase squeezing
electron	spin	-	+
	number of electrons	absence	single electron
nucleus	spin (NMR)	-	+
optical lattice	atomic spin	-	+
Josephson junction	charge (charge qubit)	0	2e (one pair)
	current direction (flux qubit)	clockwise current	counter clockwise current
	energy (phase qubit)	base state	excited state
quantum dot pair	charge localisation	electron on left	electron on right
quantum dot	dot spin	-	+

Solid state technologies are the most promising and can overcome scaling problem. However, nuclear magnetic resonance (NMR) is the most advanced as yet (Table 3).

Table 3. Short history of “qubit computers” [3]

1998	2 qubits (NMR), Oxford University
1998	3 qubits (NMR), Grover’s algorithm run
2000	5 qubits (NMR), Technische Universität München
2000	7 qubits (NMR), Los Alamos National Lab.
2001	Shor’s algorithm run
2005	8 qubits (qubyte), Österreichische Akademie der Wissenschaften
2007	28 qubits (???), D-Wave Systems, Inc.

Superconducting qubits

There are three main concepts of qubits utilising Josephson junctions [4]. The idea of a qubit tuned by an electric potential of the superconducting Cooper pair box is presented in Fig 2. The state of qubit may be measured as the number of Cooper pairs crossing the junction (e.g. by means of Bloch transistor).

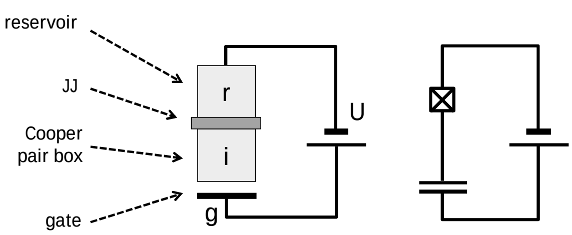

Fig. 2. Charge qubit and its symbolic diagram

Another idea is shown in Fig. 3. The qubit is tuned by microwave frequency pulses of the magnetic flux and its state is represented as the direction of the current in this RF-SQUID loop. Measurement can be achieved by means of other SQUID, coupled LC tank circuit or Andreev interferometer.

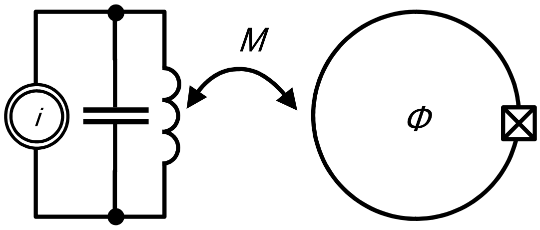

Fig. 3. Idea of a flux qubit

The third concept is depicted in Fig. 4. Qubit is tuned by current source and driven by high frequency field pulses. Its state is characterised by the energy of Cooper pairs. Phase qubit may be measured directly by a voltage sensor.

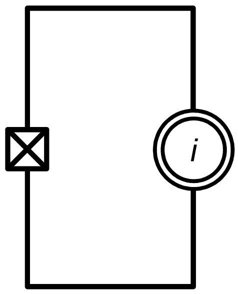

Fig. 4. Idea of a phase qubit

There is also fourth idea: charge–flux qubit. It's characterised by another ratio of the charge energy to the coupling energy of a junction and it binds some aspects of the designs mentioned before.

Conclusion

Quantum computer may exponentially speed up the solution of some problems. Superconducting qubits are very promising: they are solid-state, they can be coupled in qubit registers, they can be manufactured as integrated circuits. The biggest challenge is to minimize decoherence of quantum information and overcome scaling problems. Still, everyone must remember words of Harold Weinstock: "Never use a SQUID when a simpler, cheaper device will do."

REFERENCES

[1] Hyperphysics Portal, http://hyperphysics.phy-astr.gsu.edu/hbase/hframe.html

[2] E. Rieffel, W. Polak, An Introduction to Quantum Computing for Non-Physicists, *arXiv:quant-ph/9809016*, 19 Jan 2000

[3] L. Jacak, Komputer kwantowy: nowe wyzwanie dla nanotechnologii, *Postępy fizyki*, tom 53D, 2002

[4] M. H. Devoret, A. Wallraff, J. M. Martinis, Superconducting Qubits: A Short Review, *arXiv:cond-mat/0411174*, 7 Nov 2004

***Author**: dr inż. Leszek Jaroszyński, Politechnika Lubelska, Instytut Podstaw Elektrotechniki i Elektrotechnologii, ul. Nadbystrzycka 38a, 20-618 Lublin, E-mail: l.jaroszynski@pollub.pl.*

Conference **ELMECO-6**
ELECTROMAGNETIC DEVICES AND PROCESSES IN ENVIRONMENT PROTECTION
joint with
9th Seminar APPLICATIONS OF SUPERCONDUCTORS **AoS-9**
June 24 – 27, 2008 Nałęczów, Poland

ANALYSIS OF THE THREE-PHASE FAULT CURRENT LIMITER WITH TWO SUPERCODUCTING FUNNELS OPERATION

Michał ŁANCZONT,Tadeusz Janowski

Technical University of Lublin

***Abstract**. The wildest application of superconducting fault current limiters can be found in three phases circuits. Majority of designed solution published in scientist publications was design as a single-phase fault current limiter. We took a trial to build and to analize of operation of three phase fault current limiter with two superconducting elements in this paper.*

***Streszczenie.** Najszerszego zastosowania nadprzewodnikowych ograniczników prądu można szukać w układach trójfazowych. Większość opracowanych rozwiązań prezentowanych w publikacjach naukowych projektowana jest jako ograniczniki jednofazowy. W pracy podjęto próbę analizy pracy trójfazowego ogranicznika prądu z dwoma elementami nadprzewodzącymi.*

Keywords: Three-phase superconducting fault current limiter, high temperature superconductor, inductive fault current limiter.
Słowa kluczowe: Trójfazowy nadprzewodnikowy ogranicznik prądu, nadprzewodnik wysokotemperaturowy, indukcyjny nadprzewodnikowy ogranicznik prądu

Introduction

The regular escalation of requirement of electrical energy is caused by dynamic growth of societies, causes wide growth of existed electroenergetic network. It effectives of incrementation a frequency of apperement the short-circuits, so it results of decreasing quality of delivered electrical energy. Also it can cause damage of operating devices in the network.

The greatest threat for operating devices in the network carries first impulse of the fusion current. Applied protecting devices at present systems not always they are able to protects against this threat.

Designed constructions of the superconducting fault current limiters assure the considerable limitation of the amplitude of first impulse of the fusion current. The majority of the existing constructions of the superconducting fault current limiters was built for single-phase network. Their use in three-phase arrangements in spite the large effectiveness of the operation joins with the considerable costs of maintenance.

Several solutions provided for for three-phase arrangements were build. Paper presents construction and result of test operation of physical model of three-phase fault current limiter with two superconducting elements [1].

The principle of SFCL working

Principle of the operating of the three-phase fault current limiter, it's schema show on Fig 1, is bases on the foundation that two coupling inductive superconducting fault limiters are able to limiting short currents in three-phase arrangements.

At outside columns of superconducting fault current limiter's iron core were placed co-axially superconducting funnel, as a secondary winding, and conventional copper primary winding connected directly do protected line. At middle column of iron core were placed only conventional copper coil as a coupling winding. superconducting were placed into open cryostat and cooled by liquid nitrogen. Iron core of the limiter operate in room temperature.

Increasing temporary value of current in any one of superconducting fault current limiter phases should start the process, in the effect which one of superconducting tubes should change state of operating from superconducting to resistive. It's effects the point of the work of the foult current limiter's iron core would change, in the consequence ensue sudden incrementation if impedance in one of the limiter phases,so the temporary value of the current in protected lines will be limited to safe value.

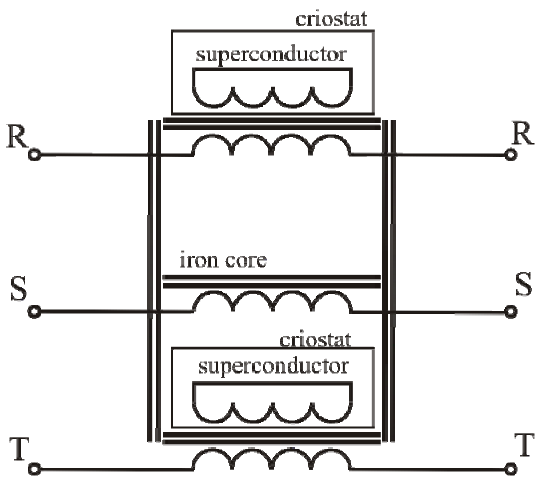

Fig 1: Three-phase fault current limiter with two supercoducting

The model of SFCL

The physical model of the three-phase fault current limiter with two superconducting elements was elaborated, as it was showed on Fig 2. The device use superconducting tubes made by Bi1.8Pb0.26Sr2Ca2Cu3O10 + x (2223 phase) produced by Can Superconductor, type CST-20 / 120.1. Critical parameters of tubes are Tc= 108 K, Ic= 900 A.

Superconducting winding d), are cooled by liquid nitrogen a), they are placed in open cryostat e) showed on Fig 2, which are use also as a carcass for primary winding f). The magnetic circuit of the limiter consists of two iron cores g) coupling by the winding placed on carcass b) join in phase S.

Carcass with the internal winding is fixed on the basis motionlessly. Two external carcasses are put in the runner and they can freely move along the runner. This solution was chose because, size of iron core could change while it's cooling, and the cryostat might submit damage.

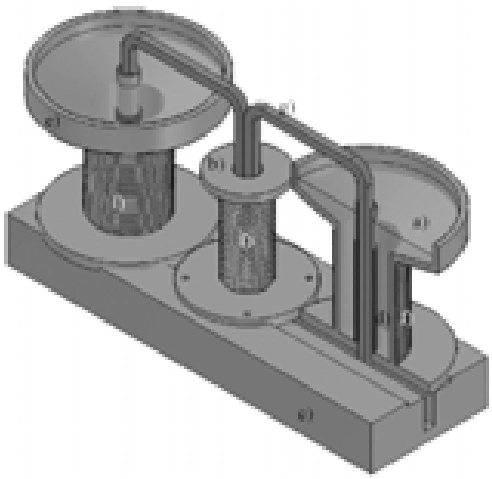

Fig 3: Construction of phisical model of three-phase fault current limiter with two superconducting tubes

At Fig 3. was shown build model of 3-f SFCL

Fig 4: Physical model of three-phase fault current limiter with two superconducting tubes

Experiment

It was build measuring arrangement to examine capability of three-phase fault current limiter with two superconducting elements to limitation of the fusion current, as shown on Fig 4.

Fig 5: Measurement system

Within experiment measurement measurements were conducted in two arrangements:

1. delimitation of the current-voltage characteristic of limiter in arrangement shown on Fig 5.
2. investigation of the effectiveness of limiting and influence among the phase of the limiter in arrangement shown on Fig 6.

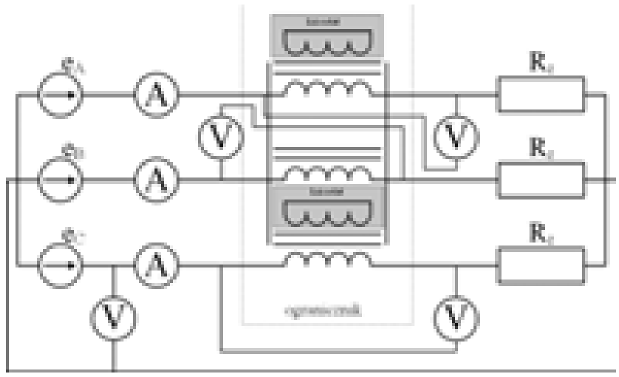

Fig 6: Measurement arrangement to delimitation of current-voltage characteristic

The measurements of the effectiveness of limiting the fusion current from technical regards were made only for single-phase short-circuits.

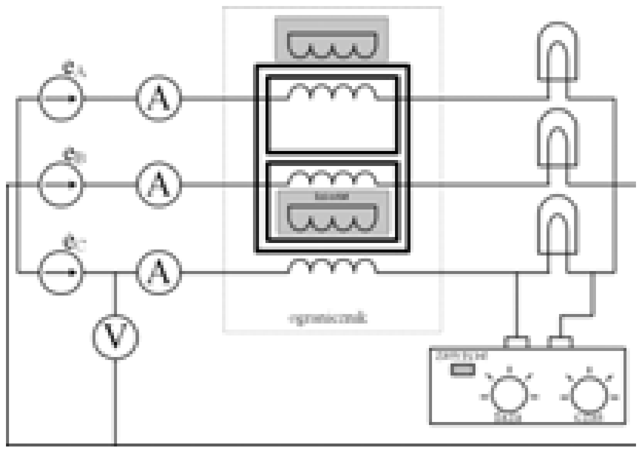

Fig 2: Measurement arrangement to test capability of SFCL to limitation of fault current

REFERENCES

[1] Seungje Lee; Eung Ro Lee; Chanjoo Lee; Suk-jin Choi; Tae Kuk Ko , The short circuit analysis of integrated three phase superconducting fault current limiter with two phase superconducting circuits, IEEE Transactions on Volume 12, Issue 1, Mar 2002 Page(s): 854 - 858

***Authors**: mgr inż. Michał Łanczont, Politechnika Lubelska, Instytut Podstaw Elektrotechniki i Elektrotechnologii, ul. Nadbystrzycka 38A, 20-618 Lublin, E-mail: m.lanczont@pollub.pl; prof. dr hab inż. Tadeusz Janowski, Instytut Podstaw Elektrotechniki i Elektrotechnologii, ul. Nadbystrzycka 38A, 20-618 Lublin, E-mail: t.janowski@pollub.pl*

EQUIVALENT ELECTROMAGNETIC AND CIRCUIT MODEL FOR HTS CURRENT LEADS

Dariusz CZERWIŃSKI, Ryszard GOLEMAN, Tomasz GIŻEWSKI

Technical University of Lublin

Abstract*. Modern current leads for superconducting devices are build of high temperature supercondutors. An equivalent electromagnetic and circuit model that describes the behaviour of a HTS superconducting lead was proposed. The model is based on the physical structure and behaviour of HTS superconductors. First purpose of this model was the numerical analysis of the superconducting current lead built of BSCCO.*

Keywords: high temperature superconductors, circuit model, FEM analysis

Introduction

High temperature superconductors operates at various conditions depending on the application solution. HTS parts are cooled with cryocooler or using cryogenic liquid. The energy losses in practical superconductor are very small under suitable working conditions. However during the quench process the amount of energy in HTS parts rapidly increases. The circuit model of HTS superconductor will improve the processes analysis during the transient states.

High temperature superconducting current leads

Current leads are used for energy transfer between superconducting devices and power supplying system. In such cryogenic application, it is necessary to pass electrical current form a power source at room temperature to a particular device at cryogenic temperatures. These current can range from a few milli-Amperes for instrumentation to 10 000 Amperes for high magnetic field superconducting magnets. The design of cryogenic power leads must attempt to minimize the refrigeration/liquefaction system capacity required for stable operation.

Most of HTS current leads are prepared as ceramic tubes made of YBCO or BSCCO superconductors (Fig. 1).

Fig.1. HTS current lead

With HTS development current leads gain new compact design and better capabilities. HTS superconducting current leads architecture usually comprises of HTS tube with silver ends (for better connection) and/or shield made of metal or plastic (Fig. 1 and Fig. 2)

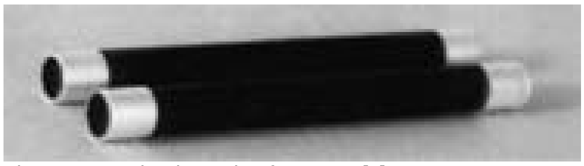

Fig.2. Current leads made of BSCCO [5]

Basing on the practical construction of the current leads produced by CAN Superconductors the equivalent model was prepared. Current lead of type CSL-12/160.2 was modelled with respect of its dimensions and physical properties. (Table 1)

Table 1. The parameters of the BSCCO leads [5]

Type	Dimensions				Critical current	
	Outer dia. mm	Length mm	Cross section mm^2	Silver contact length mm	77 K	64 K
CSL-12/160.2	12	160	34	12	250	500
CSL-12/160.3	12	160	34	12	370	740

Equivalent electromagnetic and circuit model

The model of HTS current lead was build using FE package. Geometry of the model and generated mesh is shown on Figure 3.

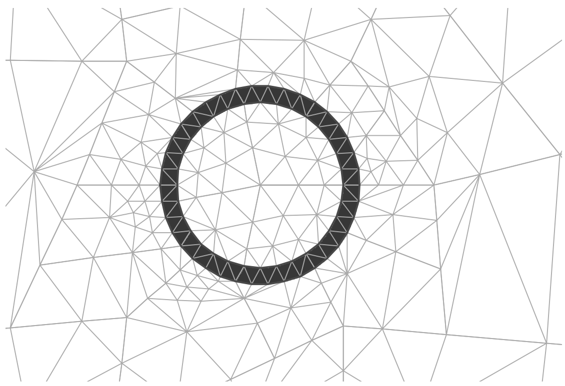

Fig.3. FEM model of the HTS lead

Electromagnetic field model was connected with sample electrical circuit. In this way the possibility of steady state and transient state was achieved. Electric circuit consists of voltage source, rezistance, HTS current lead and coil as an energy receiver (Fig. 4).

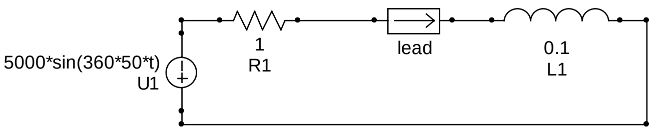

Fig.4. Electrical circuit with HTS lead

Results

The properties of modelled HTS current lead was set in this way, that the superconducting stat was achieved (lead rezistance almost 0 and relative magnetic permeability less than 1). Magnetic properties of BSCCO was modelled as and non-linear B-H curve shown on Figure 5.

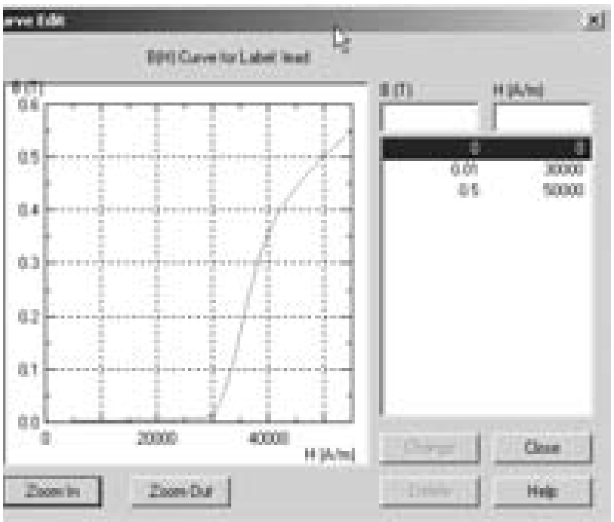

Fig.5. Sample B-H curve of BSCCO material

The sample results of numerical calculations are shown at Figure 6. The distribution of flux density in the model illustrate that the self magnetic field, derived from lead current flow, does not penetrate the inner parts of HTS current lead.

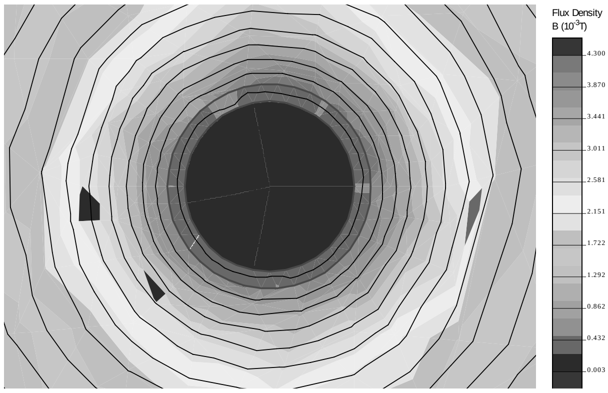

Fig.6. Distribution of the magnetic flux in the HTS lead model

Conclusions

Hysteretic losses are the main part of AC losses in high temperature superconductors.

Combining the electromagnetic model with electrical circuit gives better realizability of coupled problems.

REFERENCES

[1] Cyrot M. Pavuna D., Wstęp do nadprzewodnictwa, nadprzewodniki wysokotemperaturowe, Wydawnictwo Naukowe PWN, Warszawa 1996.
[2] Oomen, Marijn Pieter, AC loss in superconducting tapes and cables, Eerste Uitgave 2000, Universiteit Twente
[3] Applied Superconductivity Center, http://www.asc.wisc.edu/image/mo/index1.htm, 2006
[4] I. Kušević, E. BABIĆ, D. Marinaro, S. X. Dou, R. Weinstein, “Critical currents and vortex pinning in U/n treated Bi2223/Ag tapes”, Physica C 408-410 (2004) 524-525
[5] CAN SUPERCONDUCTORS – High temperature superconductors for practical applications, http://www.can-superconductors.com/, 2008

***Authors**: dr inż. Dariusz Czerwiński, dr inż. Ryszard Goleman, mgr inż. Tomasz Giżewski, Politechnika Lubelska, Instytut Podstaw Elektrotechniki i Elektrotechnologii, ul. Nadbystrzycka 38A, 20-618 Lublin, E-mail: d.czerwinski@pollub.pl*

Conference **ELMECO-6**
ELECTROMAGNETIC DEVICES AND PROCESSES IN ENVIRONMENT PROTECTION
joint with
9th Seminar APPLICATIONS OF SUPERCONDUCTORS **AoS-9**
June 24 – 27, 2008 Nałęczów, Poland

CALCULATION THE ANHYSTERETIC CURVE OF THE JILES-ATHERTON MODEL

Andrzej WAC-WŁODARCZYK, Tomasz GIŻEWSKI, Dariusz CZERWIŃSKI,

Ryszard GOLEMAN, Joanna KOZIEŁ

Lublin University of Technology

Abstract*. In this paper authors describe the way of modeling digitized form of the Jiles-Atherton lossless curve on the base of Preisach model. On the ground of weighting function properties the possibility of Langevin function parameters selection will be determined. It will be done on the base of experimental results and artificial neural networks algorithms.*

Keywords: anhysteretic curve, Preisach model, Langevin function, weighting function

Introduction

Commonly used hysteresis curve model, describing the material with energetic moves interaction and deformation of domains walls, represent the stochastic system. The fundament of this theory was presented in reference to ferromagnetic materials properties [1]

Anhysteretic curve is a fundament of the Jiles-Atherton theory of ferromagnetic material hysteresis. This curve is a set of points *(H, M)* which represent the magnetization with complex field. In the papers deal with J-A model there is no description of the magnetization general form.

In this paper the authors showed the researches of the model of lossless curve. The discussion on the specification and form of the curve with the help of statistic methods and lossless curve digitised values was lead.

Fundamentals of Jilesa-Athertona model

The theory of Weiss domains defined the influence of outer and molecular field for theoretical domain. Quantitative measure of energy *W* accumulated in magnetic field *H* in the surrounding of volume *V* was determined taking into account special cases of polycrystalline environmes. Taking into account the definition of effective magnetic field intensity (1) this energy is described with equation (2).

(1) $$h_{\mathrm{e}} = H + \alpha M$$

where: M_{e} – magnetisation, H – magnetic field, α – coefficients.

(2) $$W = -\mu \cdot \int_V v \cdot \left(H + \alpha M\right) dv$$

(3) $$M = M_s f\left(h_e\right)$$

Magnetisation, which is typical energetic state of material, was described as a function of magnetic field intensity (3). The value of magnetisation for the saturation state was designate as M_{s}.

(4) $$f\left(h_{\mathrm{e}}\right) = \frac{1 + e^{-\frac{h_{\mathrm{e}}}{\tau}}}{1 - e^{-\frac{h_{\mathrm{e}}}{\tau}}} = \mathrm{ctgh}\frac{h_{\mathrm{e}}}{\tau} - \frac{\tau}{h_{\mathrm{e}}}$$

Function $f(h_{\mathrm{e}})$ is a static specification of energy balanced state without taking consideration of metal molecular structure. In stochastic models the analysis of one dimensional spin reveal that, for the negligible power losses, dynamic transition phases and delay of working point bring us to lossless curve analogy. One of the solutions which fulfill the Curie-Weiss model criteria is a Langevin function [7].

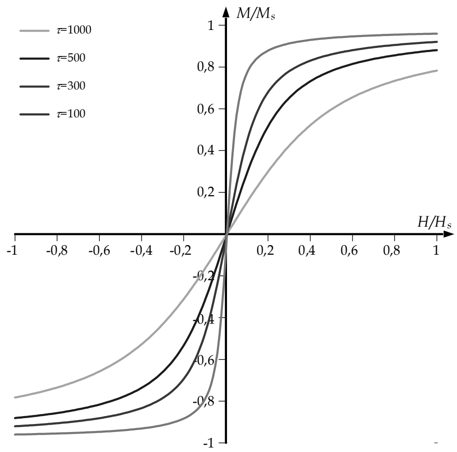

Fig. 1. Langevin function

Approximations of lossless curves were proposed for the function (5) and sigmoidal function (6)

(5) $$M = M_{\mathrm{s}} \cdot \frac{2}{\pi} \cdot \mathrm{arctg}\left(\frac{h_{\mathrm{e}}}{\tau}\right)$$

(6) $$M = -M_{\mathrm{s}} \frac{1 - \mathrm{e}^{-\frac{h_{\mathrm{e}}}{\tau}}}{1 + \mathrm{e}^{-\frac{h_{\mathrm{e}}}{\tau}}}$$

(7) $$m_0 = m - \delta \cdot k \frac{\mathrm{d}m_0}{\mathrm{d}B_\mathrm{e}}$$

Arise of power losses in single domain is connected with mechanical phenomenon occurred during remagnetisation. Magnetisation m_0 was connected with mechanical actions on the domains borders (7). In this was the energetic configuration was set. This energy is a difference between the energy essential for the change of orientation of domain magnetisation and energy which comes from hysteretic power losses [1]. Coefficient *k* was set as an constant or as an variable in the function *h*, where δ was a indicator of increment of *h*.

(8) $$\frac{\mathrm{d}m}{\mathrm{d}h} = \frac{1}{c+1} \cdot \left(\frac{m_\mathrm{a} - m_\mathrm{irr}}{\delta k - \alpha \mu_0 \left(m_\mathrm{a} - m \right)} \mu_0 + c \frac{\mathrm{d}m_a}{\mathrm{d}h} \right)$$

Mechanical properties of domains, especially the reaction during movement, borders deformations, were described as an energetic state changes. Thanks to analogy of diaphragm equations the reversible and no reversible components were set. It leads us to equation (8) wich is the final form of Jiles-Atherton theory.

Lossless curve in Preisach system

Lossless curve is an answer of the ideal ferromagnetic system. It was fount that curve represents the environment with zero value remanence in the lack of outer magnetic field.

This thesis brings authors to simulations with Preisach model. Results of simulations prove that formulation of lossless curve as a results of calculations, basing on Preisach model (9), is possible under the following conditions: domain of weighting function *μ(α, β)* must be limited to straight line *α=–β*.

(9) $$m(t) = \iint_P \mu(\alpha,\beta)\gamma_{\alpha\beta}\big(h(t)\big)\mathrm{d}\alpha\mathrm{d}\beta$$

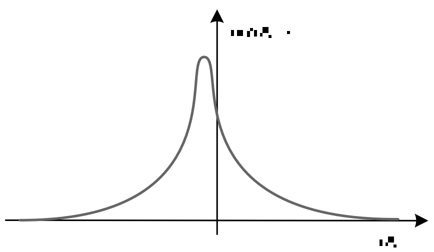

Fig.2. The values of weighting function for α=–β

In the case of weighting function which is projected on the surface (*α*, *–β*, *z*), for the values near the saturation , the function mutually and asymptotically approach at zero (figure 2).

During the modelling, the shape of lossless curve shown on (Fig. 1), require the setting of starting point for *h→∞*. Ending points of range were the values of magnetic field intensity for saturation $-h_\mathrm{sat}$ and h_sat.

Denoting *μ'*(*α*, *β*) as a function determined on the straight line *α=–β*, after the space changes the independent variables are linearly dependent on the time *τ*. Modified weighting function is given at form (10)

(10) $$\mu'(\alpha,\beta) = \begin{cases} \mu(\alpha,\beta) & \mathrm{dla}\ \alpha = -\beta \\ 0 & \mathrm{dla}\ \alpha \neq -\beta \end{cases}$$

From the equation (9) the shape of lossless curve was described as an equation (11).

(10) $$m_\mathrm{a}(t) = 2 \cdot \int_{-h_\mathrm{max}}^{h_\mathrm{max}} \mu(\xi)\mathrm{d}\tau - \int_{-h_\mathrm{max}}^{h} \mu(\xi)\mathrm{d}\tau$$

Determination of relation of the digitised values of lossless curve gives the possibilities of the experimental researches. Thanks to digitized method of weighting function *μ*(*α*, *β*) determination, the lossless curve specification require the selection of methods similar to Artificial Neural Networks algorithms

REFERENCES

[1] Jiles D. C., Atherton D. L. Theory of Ferromagnetic Hysteresis, Journal of Magnetism and Magnetic Materials 61 (1986).

[2] Baranowski J. H. Zmodyfikowane ujęcie modelu Jilesa-Athertona. Kwartalnik Elektroniki i Telekomunikacji, Wydawnictwo Naukowe PWN, Warszawa 1994.

[3] Benabou A., Clénet S., Piriou F. Comparison of Preisach and Jiles-Atherton models to take into account hysteresis phenomen for finite element analysis, Jounal of Magnetism and Magnetic Materials, Vol. 261, 2003.

[4] Chwastek K., Szczyglowski J., Najgebauer M. A direct search algorithm for estimitation of Jiles-Atherton hysteresis model parameters, Materials Science and Engineering B, Vol. 131, 2006.

[5] Jiles D. C. Introduction to magnetism and magnetic materials. Chapman & Hall 1998.

[6] Jiles D. C. Hysteresis models: non-linear magnetism on length scales from the atomistic to the macroscopic. Journal of Magnetism and Magnetic Materials 242-245 (2002).

[7] Berglung N. Adiabatic dynamical systems and hysteresis, Thesis in Institut de Physique Théorique EPFL, Lusanne Switzerland 1998.

***Authors**: dr hab. inż. Andrzej Wac-Włodarczyk prof PL, mgr inż. Tomasz Giżewski, dr inż. Dariusz Czerwiński, dr inż. Ryszard Goleman, mgr inż. Joanna Kozieł, Politechnika Lubelska, Instytut Podstaw Elektrotechniki i Elektrotechnologii, ul. Nadbystrzycka 38A, 20-618 Lublin, E-mail: t.gizewski@pollub.pl*

Conference **ELMECO-6**
ELECTROMAGNETIC DEVICES AND PROCESSES IN ENVIRONMENT PROTECTION
joint with
9th Seminar APPLICATIONS OF SUPERCONDUCTORS **AoS-9**
June 24 – 27, 2008 Nałęczów, Poland

GAS SENSOR
BASED ON MICROSTRUCTURED OPTIC FIBER

Joanna PAWŁAT[1],

Xuefeng LI[1], Tadashi SUGIYAMA[2], Takahiro MATSUO[1], Yura ZIMIN[1], Toshitsugu UEDA[1]

Graduate School of IPS, Waseda University, Japan (1)

Yokogawa Electric Corporation, Japan (2)

Abstract*. Microstructured Optical Fiber was used as a gas cell in spectroscopic measurements of a low concentration of gas.. Proposed technique allowed reducing gas sample volume to 0.01 cc. The gas flow inside core of fiber was simulated and result was confirmed experimentally. During the experimental work several types of fibers of various parameters were specially designed, produced and used. Core diameters ranged from 10.9 µm to 700 µm. Various cutting techniques for fibers such as using the fiber cleaver, Focused Ion Beam and Cross Section Polisher were investigated.*

Streszczenie*. Wykonano pomiary spektroskopowe niskich stężeń gazu przy użyciu Mikrostrukturalnych Włókien Optycznych. Proponowana technika pozwala na obniżenie objętości próbki pomiarowej do 0.01 cc. Przeprowadzono symulacje przeplywu gazu wewnatrz centralnej kapilary włókna optycznego i eksperymentalnie potwierdzono wyniki. Zaprojektowano i wyprodukowano kilka rodzajow włókien o różnych parametrach. Średnice centralnych kapilar wynosiły od 10.9 µm do 700 µm. Przetestowano różnorakie techniki cięcia włókna optycznego.*

Keywords: Gas Concentration Sensor, Microstructured Optic Fiber, Microcapillary Gas Flow
Słowa kluczowe: Czujnik Stężenia Gazu, Mikrostrukturalne Włókno Optyczne, Mikrokapilarny Przepływ Gazu.

Introduction

In dependence on the structure and wave guiding mechanism, the Microstructured Optical Fibers (MOFs) can be briefly categorized as follows [1-3]:
-Photonic Crystal Fibers (PCFs)
-Bragg Fibers (BF),
-Photonic Bandgap Fibers (PBGFs)

Developing of new technologies requires precise measurement of traces of chemical compounds. Huge possibilities of new in-situ measurement method were revealed during preliminary research using tunable laser and glass or metal tanks [4] and the PBGF [5] as the gas cells.

In this report study on the low concentration gas measurement system for the semiconductor manufacturing industry based on the MOFs and the cutting techniques of PBG fiber are presented.

Experimental Set-up

Gas was dosed into the gas cell of special design and it passed throughout the optical fiber for proper measurement of light absorption.
The gas- providing system is presented in Fig. 1. Both ends of fiber were connected to the rotary pump and slight pressure difference was kept between them to assure the gas flow.

The PBGFs had the unique structure, and light was mostly guided in a hollow, circular core surrounded by a microstructured cladding formed by a periodic arrangement of air holes in undoped silica. Up to 65 % of the fiber cross-section was composed of solid silica but less than 5 % of light propagated in glass. More than 90% of optical power was located in the hollow core or in the holes of cladding. Holes of core and cladding were filled with the tested gas. Fiber was coated with a single acrylate layer. Centre operating wavelength of fiber matched the emission wavelength of light source and the absorption band of analyzed pollutants. 1550 nm emission wavelength tunable laser was chosen for the optical measurement system. The photograph of the optical set-up is presented in Fig. 2.

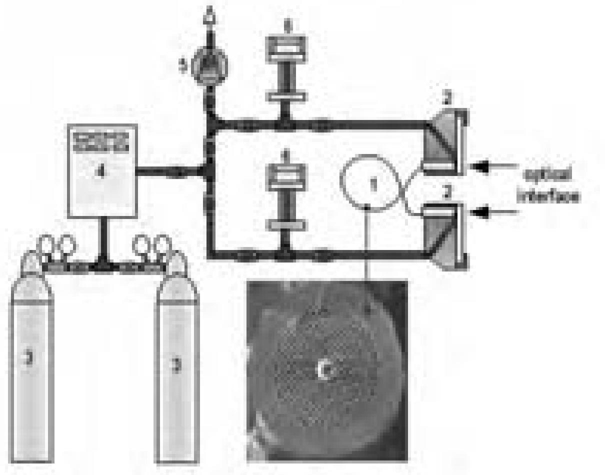

Fig. 1. Scheme of gas-providing sub-system.
(1-PBGF, 2- gas cell, 3- gas tank, 4- gas mixing device, 5- rotary pump, 6- pressure control).

The core diameters of new fibers used in the experiment were: 15.2 µm, 16.2 µm, 19.4 µm, 19.9 µm and 26.25 µm. Additionally, 10.9 µm and 20 µm core fiber, produced by Blaze Photonics and available on the market was tested.

Results and Discussion

Microcapillary nitrogen gas flow simulations were performed employing the standard mathematical software. Velocity of the gas was calculated using quasi-Panhandle equation (1) for modeling of the compressible fluid flow:

$$p_{12}\text{-}p_{22} = G^2RT/F^2\ (\lambda\ (l/d) + 2\log_e\ (v_2/v_1)) \qquad (1)$$

p_1 and p_2 are inlet and outlet pressures, G- mass flow, R- individual gas constant, T- temperature, F- core cross-section area, v_1 and v_2 - inlet and outlet velocities, λ - coefficient, which depends on Reynolds number.

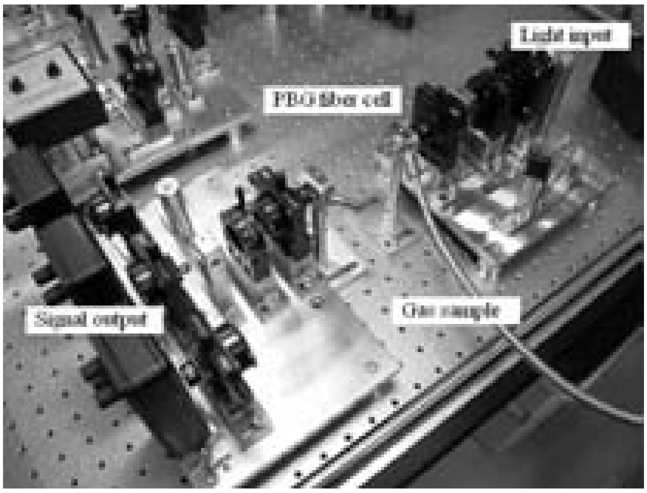

Fig.2. Photo of optical system.

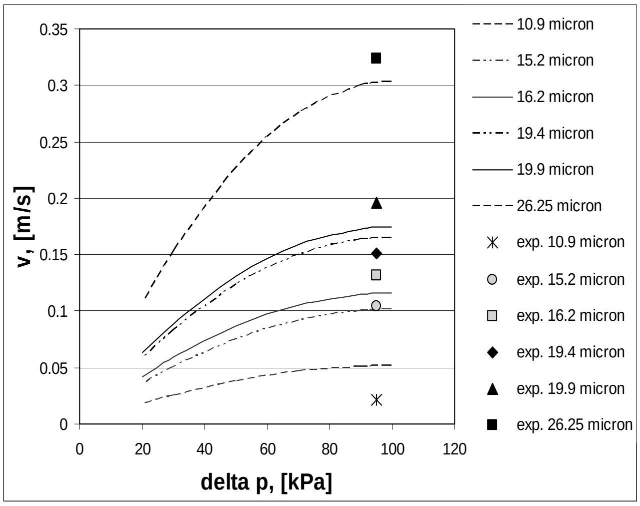

Fig.3. Simulations of gas velocity and experimental results (10.9-26.25 micron core – 0.2 m length).

It was possible to indirectly measure the flow rate of nitrogen gas inside the PBGF with various pressure differences on the opposite ends. As presented in Fig. 3 predicted gas flows were confirmed by the experimental results. In the case of 1m fiber the measurement including filling time would take about 10-15 min. In the case of ammonia concentration generation The maximum sensor's sensitivity was 0.18 ppb/m.

The length of fiber required for the experiment was adjusted using several methods as fiber cleaver, Cross Section Polisher, SM-09010 (Nihon Denshi) using argon ion beam, and the Focused Ion Beam (FIB) cutting. The microscope photograph of fiber cut using the most precise technique FIB is shown in Fig.4.

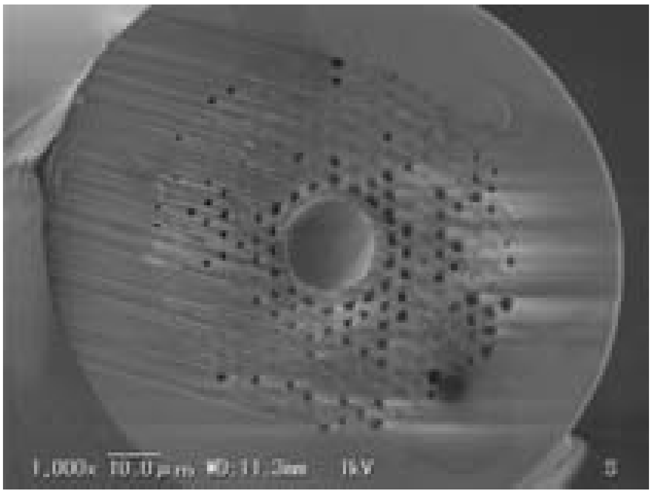

Fig. 4. PBGF cutting using FIB, SEM.

Conclusions.

The set-up for measuring of ppb concentration of ammonia was designed.

New types of PBGFs were produced. Simulations of gas velocity in dependence on applied pressure were performed.

Gas flow rate in the experimental condition was corresponding to the simulated one. It was sufficient for fast ppm-order measurement using short optic fibers as the gas cells. The measurement including filling time would take about 10-15 min for 1 m length fiber.

Maximum sensitivity for ammonia measurement expected when using this method was 0.18 ppb/m.

New methods for cutting and shaping the ends of the PBGF were tested.

Authors would like to thank to Professor Lev Zimin and Mr. Tatsuhiko Saitoh for fruitful advices and help during research work.

REFERENCES

[1] Cordeiro C., FrancoM., Chesini G., Barretto E., Lwin R., Brito-Cruz C., Large M., "Microstructured-core optical fibre for evanescent sensing applications", *Opt. Express,* 14 (2006), 13056-13066

[2] Laesgaard J. , Bjarklev, " "Microstructured optical fibers-fundamentals and applications," A., *J. Am. Ceram. Soc.,* 89 (2006), No. 1, 2-12

[3] Yeh P., Yariv A., Marom E., ""Theory of Bragg fiber", *J. Opt. Soc. Am.*,68 (1978), 1196–1201

[4] Sugiyama T., Ueda T., "In-situ Measurement for the Gas. Concentrations Using Tunable Lasers", *Proc. of Technical Meeting on Sensors and Micromachines*, CHS-03-56 (2003), 1-4

[5] Pawłat J., Matsuo T., Sugiyama T., Ueda T., "Possibility of gas concentration measurement using photonic crystal fiber", *Przeglad Elektrotechniczny*, 5 (2007), 31-35

***Authors**: dr. Joanna Pawłat, dr. Xuefeng Li, Mr. Takahiro Matsuo, Mr. Yura Zimin, Prof. Toshitsugu Ueda, Graduate School of IPS, Waseda University, 808-0135 Fukuoka ken, Kitakyushu-shi, Wakamatsu-ku, 2-7 Hibikino, Japan, Fax: +81-936925158, E-mail: askmik@hotmail.com, Mr. Tadashi Sugiyama Yokogawa Electric Corporation Tokyo, 2-9-32 Naka-cho, Musashino-shi, 180-8750, Japan*

Conference **ELMECO-6**
ELECTROMAGNETIC DEVICES AND PROCESSES IN ENVIRONMENT PROTECTION
joint with
9th Seminar APPLICATIONS OF SUPERCONDUCTORS **AoS-9**
June 24 – 27, 2008 Nałęczów, Poland

TREATMENT OF DYES FROM TEXTILE INDUSTRY IN THE FOAMING SYSTEM

Joanna PAWŁAT[1], Satoshi IHARA[2], Chobei YAMABE[2]

[1]Graduate School of IPS, Waseda University,
[2]School of Science and Engineering, Saga University

***Abstract**. Production of oxidants during the electrical discharge in the foaming environment was confirmed. The influence of electrical discharge on the removal of color caused by organic compounds used in textile industry such as methyl orange ethyl violet, and indigo in the foaming apparatus was investigated. Discoloration was observed visually and concentrations of pollutants were measured including the influence of gas kind, gas flow rate and frequency on the removal rate.*

***Streszczenie.** Potwierdzono obecność związków utleniających wytworzonych podczas wyładowania elektrycznego w systemie pianowym. Zbadano wpływ wyładowania w pianie na usuwanie barwy spowodowanej barwnikami organicznymi używanymi w przemyśle tekstylnym takimi jak oranż metylowy, fiolet etylowy oraz błękit indygo. Obserwowano odbarwianie roztworów i zmierzono zmiany stężeń związków zanieczyszczających w zależności od rodzaju i przeplywu gazu oraz częstotliwości wyładowania.*

Keywords: foaming system, colour removal, AOP, methyl orange
Słowa kluczowe: system pianowy, usuwanie barwy, zaawansowane techniki utleniające, oranż metylowy.

Introduction

Textile, toys and printing industries generate large quantities of wastewater polluted with hardly decomposable, large molecule organic dyes. It causes variety of environmental problems as conventionally used chemical treatment methods are often based on the addition of chemical compounds thus may result in the secondary pollution and dyes are usually recalcitrant to the microbiological attack. Some of directly discharged dyes have carcinogenic or teratogenic health effects [1-4]

The positive influence of Advanced Oxidation Techniques on the textile wastewaters' decomposition yield was reported by many other research groups [5-7].

Table 1. Concentrations and molecular structure of used dyes.

Concentration	*Molecular structure*
methyl orange	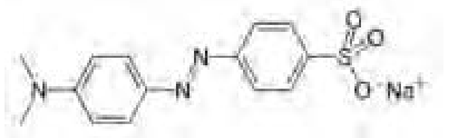
30 mg/l	
ethyl violet	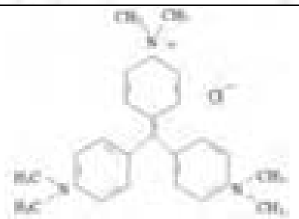
34 mg/l	
indigo blue	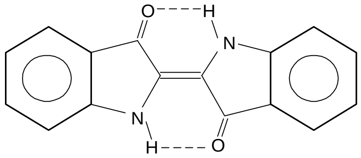
20 mg/l	

Treatment of dyes using electrical discharge in the dynamic foam was tested. Foam was formed without the addition of surface-active compounds. The simultaneous formation of hydrogen peroxide, dissolved ozone, OH radicals and of small amount of gaseous ozone in the foaming column was confirmed in the previous stages of research work [8]. Formed active species were then used for the treatment of methyl orange (MO), ethyl violet (EV), and indigo blue (IB) dissolved in water. Used concentrations and molecular structure of each compound is described in Tab.1.

Experimental set up

The main reactor of the foaming system was a cylindrical, polyacrylate column of 50 mm diameter (Fig. 1). A ceramic diffuser made of aluminum oxide was placed perpendicularly to the flow direction of media. The central high voltage (HV) electrode of 1.5 mm diameter was placed inside the cylindrical, grounded electrode (40 mm of diameter, 30 mm of height) in the homogenous foam zone, above the diffuser.

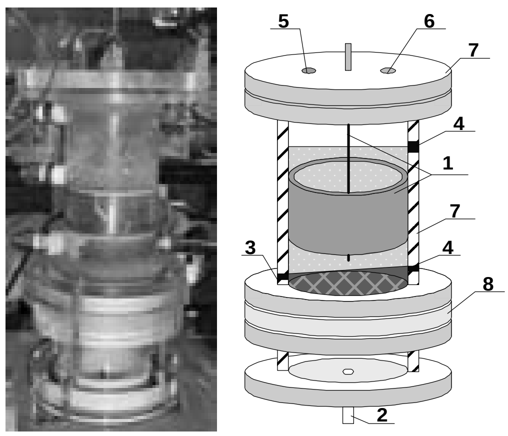

Fig. 1. Experimental apparatus (1- electrodes, 2- gas inlet, 3- water inlet, 4- overflow, 5- gas outlet, 6- sampling point, 7- polyacrylate housing, 8- ceramic diffuser).

Blumlein type pulsed power source was used in this work. The pulsed power source consisted of coaxial cables (RG-8U) for charging energy, triggered spark gap switch and switch triggering system. Discharge voltage and current were measured using the high voltage probe (P6015A, Tektronix) and the Rogowski coil (current probe model 110A, Pearson) respectively with an oscilloscope.

Results and discussion

Methyl orange (4-dimethylaminoazobenzene-4'-sulfonic acid sodium salt, $C_{14}H_{14}N_3NaO_3S$), widely used as a pH indicator in titrations, dissolves in water forming bright orange solution. 70 ml of 30 mg/l solution was dosed to the foaming reactor, gas flow, necessary to form the foaming conditions was 3 l/min. The change in absorbance at 403 nm wavelength during the application of electrical discharge is presented in Fig. 2. After 20 min. of treatment in oxygen, total discoloration was visually observed. The chemistry of azo-dyes decomposition is highly pH dependent. OH radicals and superoxide reactions are considered as the most probable decomposition pathways [9].

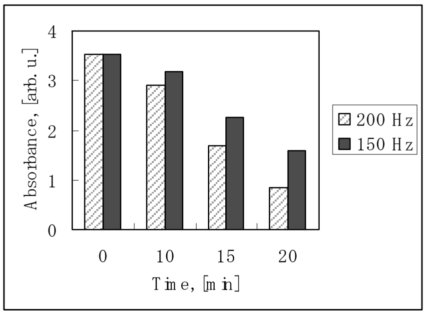

Fig. 2 Removal of color of MO in dependence on frequency.

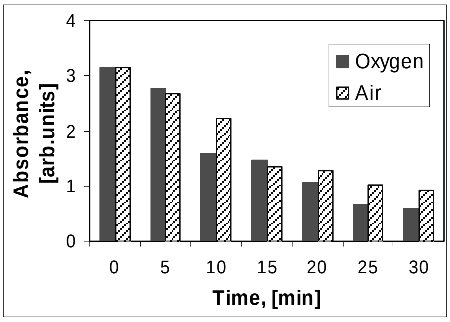

Fig. 3 Removal of color of EV in dependence on used gas.

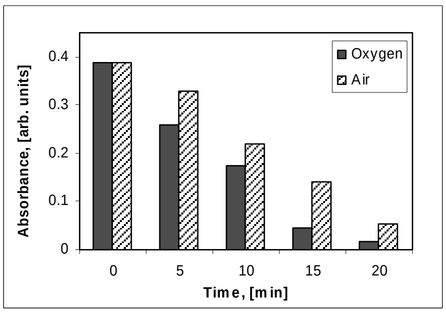

Fig. 4 Removal of color of IB in dependence on used gas.

Ethyl violet (basic violet 4, $C_{31}H_{42}N_3Cl$), which is used as an indicator in chemical and medical industry added to many carbon dioxide absorbents is a green crystalline powder, which colors water solutions in persistent, very deep purple. In the performed investigations pure water was mixed with EV to obtain 34 mg/l solution.17 ml of this highly foamable substrate liquid was dosed to the reactor. The flow rate of substrate gases: oxygen and air ranged 0.3 l/min. The measurements of the ultraviolet absorbance to confirm EV caused color removal were performed using HACH spectrometer at 596 nm (Fig. 3). For 30 minutes treatment time ethyl violet removal rate ranged 81% in oxygen. EV is also highly pH-sensitive dye [10], which reacts mostly via OH reaction route. Alkalization of solution could bring to dramatic improvement of decomposition efficiency.

The indigo blue is one of the oldest known dyes. Its intensive color disappears after the indigo molecule is decomposed onto the isatin and further onto more simple by-products. The absorption band of indigo blue at 612 nm was used for the analysis. Initial concentration was 20 mg/l. Visually, the full removal of color was achieved quickly and IB was relatively easy to decompose in the foam mainly via reaction with dissolved (but also gaseous) ozone and generated radicals.

Conclusions

The influence of the oxidants formed during electrical discharge in foaming apparatus on removal of color caused by methyl orange, ethyl violet, and indigo blue were investigated.

The most efficient generation of the oxidants, thus the highest treatment efficiency was observed for higher frequencies and the gas flow stabilized on the level, which was the most fruitful from the foam formation point of view.

REFERENCES

[1] Danish Environmental Protection Agency, „Azocolorants in Textiles and Toys” Environmental Project, no. 416, (1998), ISBN 87-7909-048-6

[2] Birhanli A, Ozmen M., „Evaluation of the toxicity and teratogenity of six commercial textile dyes using the frog embryo teratogenesis assay-Xenopus”, *Drug Chem Toxicol.* 28(1) (2005), 51-65

[3] Metcalf W., “Effect of teratogenic and related dyes on the haemoglobin nitrite sensitivity reaction “ *Br. J. Pharmacol Chemother.* 19(3), (1962), 492–497

[4] McLean P., Reid E., Gurney M., “Effect of azo-dye carcinogenesis on enzymes concerned with urea synthesis in rat liver”, *Biochem J.*, 91(3), (1964), 464–473

[5] Aleboyeh A., Aleboyeh H., Moussa Y., “Critical effect of hydrogen peroxide in photochemical oxidative decolorization of dyes: Acid Orange 8, Acid Blue 74 and methyl Orange”, *Dyes and Pigments*, 57, (2003), 67-75

[6] Choi I., Wiesmann U., “Effect of Chemical Reaction and Mass Transfer on Ozonation of the Azo Dyes Reactive Black 5 and Reactive Orange 96”, *Ozone Sci.&Eng.*, 26, (2004),539-549

[7] Chen L., “Effects of Factors and Ineracted factors on the Optimal Decolorization Process of Methyl Orange by Ozone”, *Wat. Res.*, 34(3), (2000), 974-982

[8] Pawłat J., Ihara S. “Removal of COD and color using electrical discharge in foaming column”, *Plasma Process. Polym.,* 4(7-8), (2007), 753-759

[9] Destaillats H., Turjanski A., Estron D., Hoffman M., „Molecular Structure Effects on the Kinetics of Hydroxyl Radical Addition to Azo Dyes”, J. Phys. Org. Chem, 15, (2002), 287-292

[10] Barth C., Dunning M., Bretscher L., Woehlck H., “Barium Hydroxide Lime Turns Yellow After Desiccation”, Anesth. Analg., 101, (2005), 748-752

***Authors**: dr. Joanna Pawłat, Graduate School of IPS, Waseda University, 808-0135 Fukuoka ken, Kitakyushu-shi, Wakamatsu-ku, 2-7 Hibikino, Japan, Fax: +81-936925158, E-mail: askmik@hotmail.com, dr. Satoshi Ihara, prof. Chobei Yamabe, School of Science and Engineering, Saga University, 840-8502 Saga ken, Saga-shi, 1 Honjo-machi, Japan.*

REACTOR FOR PLASMA-CATALYTIC PROCESSES IN HETEROGENEOUS SYSTEM

Michał MŁOTEK, Jan SENTEK, Krzysztof KRAWCZYK, Krzysztof SCHMIDT-SZAŁOWSKI

Faculty of Chemistry, Warsaw University of Technology,
Nowakowskiego 3, 00-664 Warszawa, Poland

Abstract. A gliding discharge three phase reactor was made for studying the effect of a spouted bed of fine catalyst's particles on methane conversion The spouted bed containing Pt or Pd change the composition of the products from acetylene to ethylene and ethane. A reduction of soot generation was also observed.

Streszczenie. Zbudowano trójfazowy reaktor do badania przemiany metanu w plazmie wyładowania ślizgowego z katalitycznym złożem fontannowym. Złoża katalityczne zawierające Pt lub Pd powodowały zmianę składu produktów reakcji z acetylenu w kierunku etylenu i etanu. Z zastosowaniem katalizatorów Pt i Pd zauważono także zmniejszenie się wydzielania sadzy

Keywords: *gliding discharges, non-thermal plasma, methane coupling*
Słowa kluczowe: *wyładowanie ślizgowe, plazma nierównowagowa, sprzęganie metanu*

Introduction

Untill now, a number of methods for low temperature methane conversion (partial oxidation, reforming, oxidative and non-oxidative coupling) has been examined, including methods which use low-temperature non-equilibrium plasmas for chemical reaction initiation[1-3]. An efficient process for methane conversion into synthesis gas in non-equilibrium plasma, has been developed using gliding discharges. It was found that unsaturated hydrocarbons (mainly acetylene) and some oxygenates, e.g. methanol, may also be obtained in these kinds of discharges [2,3-7]. In order to improve the efficiency and selectivity of these processes, some hybrid systems were investigated by combining the activation of reactants by discharges with the action of a solid catalyst, wich stimulates the generation of the desired product [8]. The efficiency of plasma-catalytic system based on gliding discharges was the object of our studies over the last years [2,3]. In order to examine the activity of selected metal catalysts for non-oxidative methane coupling under gliding discharge conditions, a new reactor, which operates with mobile catalytic beds, has been developed.

Experimental

A gliding discharge three phases reactor (Fig. 1), used for studying the effect of the spouted bed of fine catalyst particles, was made of a vertical reaction chamber lined with a ceramic material, with three main electrodes and a starting electrode. Gaseous reactants were introduced at the bottom to keep the particles moving in the inter-electrode space. The reactor was powered by a 50 Hz system. The active power which was supplied (measured by an energy meter *Pafal MOD A5*) changed in the range of 500 – 1500 W.

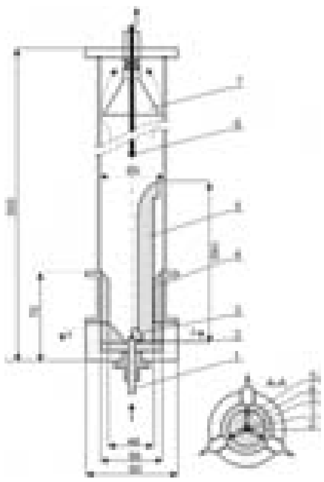

Fig1. Three phases glide arc reactor for methane conversion. 1 – nozzle, 2,4 – ceramic lining, 3 – starting electrode, 5 – high energy electrode, 6 – thermocouple, 7 - catalist capture

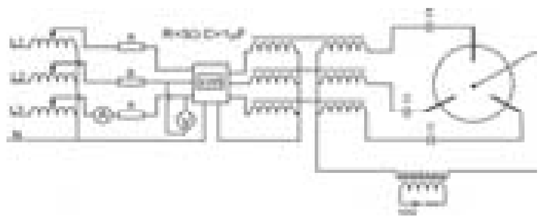

Fig 2. Energy supply scheme in the three phase glide arc reactor for methane conversion

The electrical characteristics of the discharge were recorded using oscilloscope *Tektronix TPS 2024* equipped with a *Tektronix P6015* voltage probe and *Tektronix A622* current probe (Fig. 2). The characteristics of discharges are shown in Fig. 3.

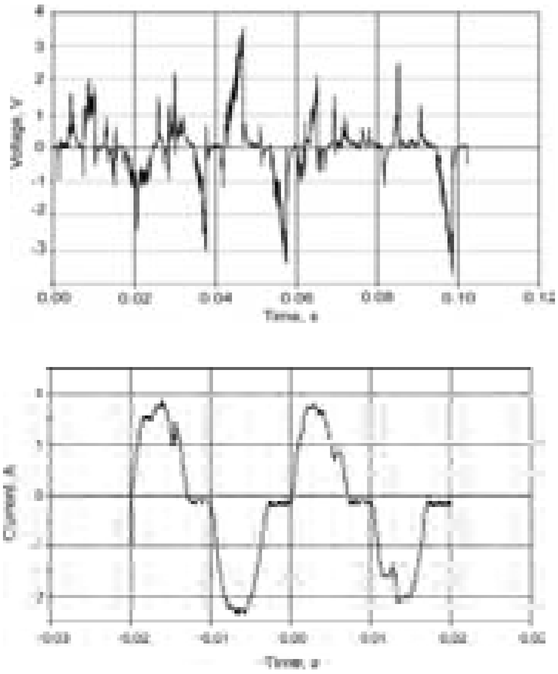

Fig. 3. Voltage and current in three phases GD. Characteristics measured on one phase with air.

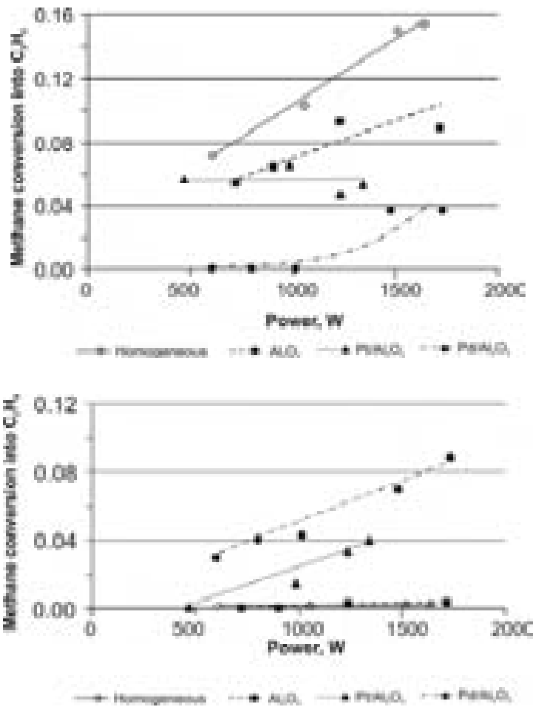

Fig. 4. Effect of catalysts on methane conversion into acetylene and ethylene.

The temperature inside the reactor volume was measured with a thermocouple over the upper end of electrodes. The gas reagent mixture $0.4CH_4$+$0.6H_2$ was passed with the flow rate of 1640 Nl/h at atmospheric pressure. The chromatographic gas analysis was used with *Chrompak CP 9002* equipped with a Carboxen 1000 column and a TCD detector or with a Porapak Q column. Effects of the selected alumina-ceramic supported catalysts, Pt/Al_2O_3 and Pd/Al_2O_3, on the methane conversion are given in Fig. 4. It was concluded that the reactor presented herein proved its usefulness in the plasma-catalytic methane conversion in gliding discharge with a mobile catalytic bed. A strong effect of the catalysts containing Pt or Pd on the methane conversion was observed, including the reduction of soot generation Fig. 5, and changes in C_2 hydrocarbons composition from acetylene to ethylene and ethane.

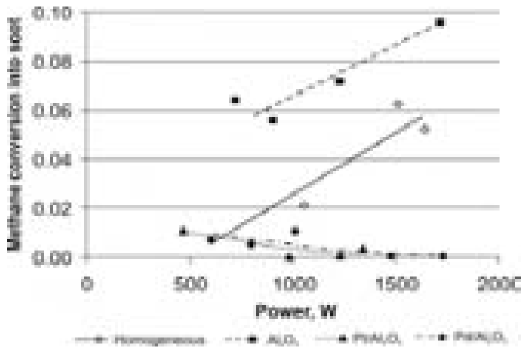

Fig. 5.Effect of catalysts on soot generation.

Acknowledgment

This work was financially supported by ERA-NET CHEMISTRY (Decision nr 139/ERA-NET/2008)

REFERENCES

[1] Petitpas G,. Rollier J.-D, Darmon A.- J., Gonzales-Aguilar, Metkemeijer R., Fulcheri L., A comparative study of non-thermal plasma assisted reforming technologies, *Int. J. Hydrogen Energy,* 32 (2007)**,** 32, 2848-2867.
[2] Schmidt-Szałowski K., Krawczyk K., Młotek M., "Catalytic effect of metals on the conversion of methane in gliding discharges", *Plasma Process. Polym.,*4 (2007)**,** 728-736.
[3] Schmidt-Szałowski K., Krawczyk K., Sentek J., Młotek M., „Plasma-catalytic system for methane conversion in gliding discharges", *Polish J. Chem.,* 81 (2007)**,** 2215-2220.
[4] Czernichowski A., Czernichowski M., Further development of plasma sources: the GlidArc-III, *ISPC 17*, Toronto 2005.
[5] Indarto A., Choi J.-W., Lee H., Song H.K., Kinetic modeling of plasma methane conversion using gliding arc, *J. Natural Gas Chemistry*, 14 (2005)**,** 13.
[6] Indarto A., Choi J.-W., Lee H., Song H.K., Effect of additive gases on methane conversion using gliding arc discharge, *Energy*, 31 (2006), 2986.
[7] Ouni F., Khacev A., Cormier J.M., Methane steam reforming with oxygen in a sliding discharge reactor*, ISPC 17*, Toronto 2005.
[8] Hammer Th., Kappes Th., Baldauf M., Plasma catalytic hybrid processes: gas discharge initiation and plasma activation of catalytic processes, *Catal. Today,* 89 (2004), 5.

Electronics address: kss@ch.pw.edu.pl

Conference **ELMECO-6**
ELECTROMAGNETIC DEVICES AND PROCESSES IN ENVIRONMENT PROTECTION
joint with
9th Seminar APPLICATIONS OF SUPERCONDUCTORS **AoS-9**
June 24 – 27, 2008 Nałęczów, Poland

MASZYNY ELEKTRYCZNE Z EKRANAMI NADPRZEWODNIKOWYMI

Ryszard PAŁKA

Politechnika Szczecińska, Katedra Elektrotechniki Teoretycznej I Informatyki

Streszczenie. *W pracy przedstawiono możliwości zastosowania monolitycznych nadprzewodników wysokotemperaturowych w maszynach elektrycznych jako ekranów magnetycznych. Dokonano klasyfikacji maszyn z ekranami nadprzewodnikowymi, omówiono ich podstawowe konfiguracje oraz dokonano porównania z rozwiązaniami konwencjonalnymi.*

Abstract. (Electrical machines with superconducting screens). *The paper shows the possibility of application of monolithic high temperature superconductors in electrical machines as magnetic screens. The classification of machines with superconducting screens has been done and their fundamental configurations compared with conventional solutions have also been discussed.*

Słowa kluczowe: monolityczne nadprzewodniki wysokotemperaturowe, nadprzewodnikowe maszyny elektryczne, ekrany magnetyczne.
Keywords: high temperature bulk superconductors, superconducting electrical machines, magnetic screens.

Wstęp

Jednym z głównych wyzwań obecnych czasów jest oszczędna i racjonalna gospodarka istniejącymi zasobami energetycznymi. Przeważająca część wytwarzanej energii elektrycznej (ok. 70%) jest przetwarzana pośrednio lub bezpośrednio na energię mechaniczną. Efektywność tego przetwarzania jest więc niezwykle ważnym czynnikiem ekonomicznym. Postęp technologiczny w inżynierii materiałowej (magnesy trwałe, materiały magnetyczne itd.) doprowadził w ostatnim czasie do stworzenia wielu nowych konstrukcji maszyn elektrycznych, a jednoczesny rozwój układów zasilania i sterowania maszyn doprowadził do znacznej poprawy efektywności przetwarzania energii elektrycznej. Kolejnym krokiem na drodze do poprawy parametrów maszyn elektrycznych może okazać się zastosowanie różnych technologii nadprzewodnikowych. Monolityczne nadprzewodniki wysokotemperaturowe (ang. *high temperature superconductors, HTSC*) mogą być w konstrukcji maszyn elektrycznych wykorzystane m.in. jako magnesy nadprzewodzące o bardzo dużych wartościach indukcji remanencji oraz jako ekrany magnetyczne. Sposób aktywacji, parametry użytkowe HTSC i specyficzne możliwości ich zastosowania doprowadziły do powstania wielu różnych konfiguracji nadprzewodnikowych maszyn synchronicznych, reluktancyjnych i histerezowych [1,2,3,4]. Wykorzystanie monolitycznych nadprzewodników wysokotemperaturowych jako silnych magnesów nadprzewodzących wiąże się z koniecznością wstępnego magnesowania nadprzewodników, co jest bardzo złożonym problemem inżynierskim, dlatego dla maszyn mniejszych (o mocy rzędu kilkuset kilowatów) celowe jest stosowanie nadprzewodników jako ekranów pola magnetycznego. W pracy tej opisano możliwości zastosowania monolitycznych nadprzewodników wysokotemperaturowych jako ekranów magnetycznych w różnych maszynach reluktancyjnych.

Ekranujące właściwości monolitycznych HTSC

Monolityczny nadprzewodnik wysokotemperaturowy ochłodzony poniżej temperatury krytycznej nie zezwala na jakiekolwiek zmiany pola magnetycznego w swoim wnętrzu. Przy aktywacji w polu magnetycznym o pomijalnie małych wartościach (ang. *zero field cooling, ZFC)* staje się on idealnym ekranem magnetycznym, zachowując swój stan również po poddaniu go działaniu zewnętrznego pola magnetycznego. Sytuację tę pokazano na rys. 1.

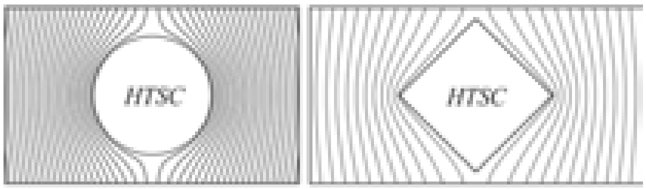

Rys. 1. Monolityczne nadprzewodniki wysokotemperaturowe zaktywizowane w trybie ZFC umieszczone w jednorodnym polu magnetycznym

Idealne wypieranie pola z nadprzewodnika przedstawione na rys. 1 (stan Meissnera) ma miejsce dla pól zewnętrznych mniejszych niż pierwsze pole krytyczne, jednak właściwości ekranujące monolitycznych nadprzewodników wysokotemperaturowych zostają w znacznym stopniu zachowane również dla pól wielokrotnie większych (mniejszych niż drugie pole krytyczne). W większości przypadków pola magnetyczne, których działaniu poddane są monolityczne nadprzewodniki wysokotemperaturowe w maszynach elektrycznych są polami rozproszenia o niewielkich wartościach, co uzasadnia przyjęcie stanu Meissnera w nadprzewodniku w stosowanych modelach obliczeniowych maszyn.

Maszyny reluktancyjne z ekranami nadprzewodnikowymi

Najbardziej obiecującą dziedziną zastosowań monolitycznych nadprzewodników wysokotemperaturowych są wszelkiego typu maszyny reluktancyjne [1,2,3,4]. Na rysunku 2 pokazano pewną reluktancyjną maszynę synchroniczną wzbudzaną przez prądy stojana. Uzwojenie w tej maszynie spełnia dwa zadania jednocześnie: jego część znajdująca się nad biegunem wirnika (fazy *1*, *5*, *6*, *7*) wytwarza klasyczne pole magnetyczne twornika, a pozostała część (fazy *2*, *3*, *4*) – pole wzbudzenia. Dobór właściwej struktury takiej maszyny polega na jednoczesnym wypełnieniu sprzecznych ze sobą wymagań związanych przede wszystkim z koniecznością zmniejszenia wielkości szczeliny powietrznej, co pociąga za sobą silną reakcję twornika.

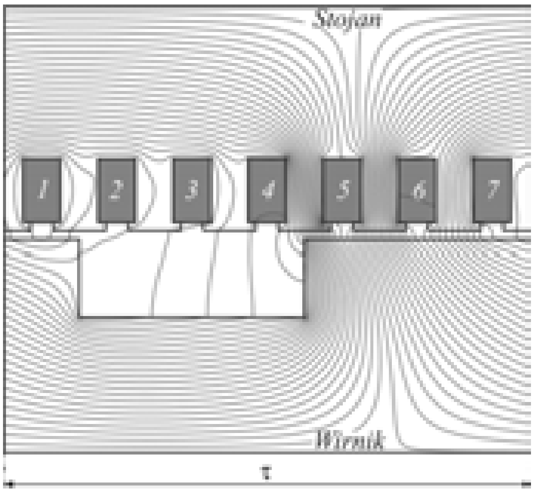

Rys. 2 Rozkład pola magnetycznego w reluktancyjnej siedmiofazowej maszynie synchronicznej ze wzbudzeniem w stojanie (model liniowy)

W przypadku tak skomplikowanego oraz drogiego zasilania wielu różnych faz stojana konieczne jest ograniczenie wszelkich niekorzystnych zjawisk w maszynie, takich jak siły hamujące i duża moc bierna zasilania. Dokonać tego można przez umieszczenie ekranów nadprzewodnikowych w strukturze wirnika (rys. 3).

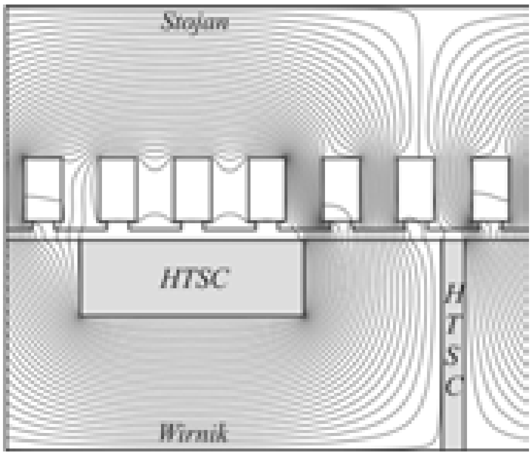

Rys. 3 Rozkład pola magnetycznego w maszynie z rys. 2 z ekranem nadprzewodnikowym pomiędzy biegunami wirnika oraz dodatkowym nadprzewodnikowym ekranem separującym

Nadprzewodnik wysokotemperaturowy zaktywizowany w trybie ZFC umieszczony pomiędzy biegunami wirnika staje się idealnym ekranem magnetycznym – pole magnetyczne zostaje całkowicie wypchnięte z obszaru międzybiegunowego w kierunku szczeliny powietrznej, powodując wzrost sił w maszynie. Dodatkowe pozytywne efekty osiągnąć można tu przez rozcięcie drogi strumienia magnetycznego za pomocą ekranu nadprzewodnikowego znajdującego się w wirniku.

Równie obiecujące jest zastosowanie ekranów nadprzewodnikowych w maszynach reluktancyjnych przełączalnych. Prostota i funkcjonalność tych maszyn jest okupiona wieloma wadami, a jedną z nich jest stosunkowo duży bezużyteczny strumień rozproszenia pomiędzy biegunami wirnika, a także między wirnikiem i stojanem. Na rysunku 4 pokazano liniowy model maszyny reluktancyjnej przełączalnej mającej trzy bieguny w stojanie i dwa bieguny w wirniku. Jest to fragment struktury okresowej – w zależności od potrzeb można ją powielić wielokrotnie i otrzymać maszynę wielobiegunową. Celem demonstracji działania ekranów nadprzewodnikowych w maszynie reluktancyjnej przełączalnej rozważa się przypadek zasilania tylko jednej fazy maszyny dla wybranego położenia wirnika i stojana.

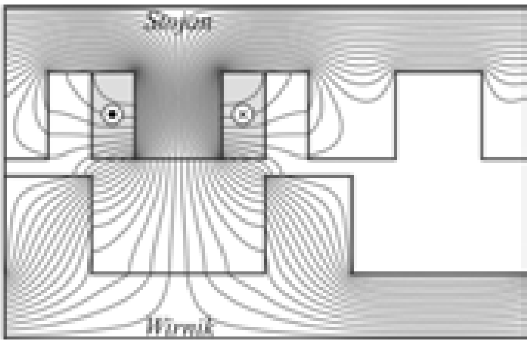

Rys. 4 Model liniowy maszyny reluktancyjnej przełączalnej

Umieszczenie nadprzewodnika wysokotemperaturowego zaktywizowanego w zerowym polu magnetycznym pomiędzy biegunami wirnika powoduje całkowite wyparcie strumienia rozproszenia z przestrzeni międzybiegunowej (rys. 5).

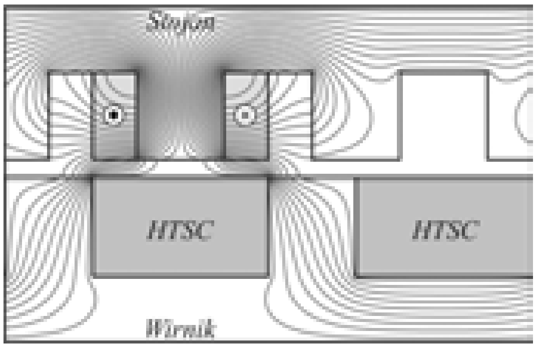

Rys. 5 Model liniowy maszyny reluktancyjnej przełączalnej z ekranami nadprzewodnikowymi

Jak wynika z rys. 5 ekrany nadprzewodnikowe chronią całkowicie wirnik przed wnikaniem niepożądanego strumienia bocznego, co prowadzi do znacznej poprawy parametrów maszyny (brak strumienia rozproszenia i sił hamujących) i wzrostu wartości otrzymywanych sił. Rozkład pola magnetycznego pokazany na rys. 5 może prowadzić do lokalnego nasycenia biegunów stojana, w związku z tym maszynę taką wykorzystuje się do pracy przy znacznie ograniczonym przepływie, uzyskując jednocześnie wzrost wypadkowych sił (momentów).

REFERENCES

[1] Canders W.-R., May H., Pałka R., Portabella E., Machines with high temperature superconducting bulk material in comparison with permanent magnet excited synchronous machines. *ICEM'2000,* Helsinki
[2] Krabbes G., Fuchs G., Canders W.-R., May H., Pałka R., *High Temperature Superconductor Bulk Materials*, Weinheim, WILEY-VCH Verlag GmbH & Co, KGaA 2006
[3] Oswald B. et al., HTS Motor Program at OSWALD, Present Status, *IEEE Trans. on Applied Superconductivity*, June 2007, Vol. 17, No. 2, 1583–1586
[4] Pałka R., *Monolityczne nadprzewodniki wysokotemperaturowe. Modele makroskopowe i zastosowania,* Wydawnictwo Uczelniane Politechniki Szczecińskiej, Szczecin 2008

Autor*: dr hab. inż. Ryszard Pałka, prof. PS, Katedra Elektrotechniki Teoretycznej i Informatyki, Politechnika Szczecińska, ul. Sikorskiego 37, 70 313 Szczecin, E-mail: rpalka@ps.pl*

FUNDAMENTAL STUDY ON BIOSENSING DEVICE FABRICATION BASED ON CARBON NANOTUBES AND DNA

Tsuyoshi Ueda[1], Fumiaki Mitsugi[1], Tomoaki Ikegami[1], Takashi Ikegami[2], and Kenji Ebihara[2]

Kumamoto University (1), Dojindo Laboratories (2)

Abstract. *In recent years, carbon nanotubes (CNTs) have been of interest for the bio-electrics application as well as the electrical or mechanical application. We consider that the carbon nanotubes have potential to apply for label-free biosensing. In this work, we introduce dispersion and stabilization technique for carbon nanotubes, DNA stabilization method and procedure for their hybrid sample. The carbon nanotubes, DNA and their CNT-DNA hybrid samples were observed by atomic force microscopy(AFM) images and the cross-sectional analysis to study the fundamentals for biosensing device fabrication.*

Keywords: Biosensing, Single-walled carbon nanotubes, DNA, AFM.

Introduction

Recently, a novel application of Carbon Nanotubes (CNTs) has attracted much interest in biosensing field. In our previous research, we have established fabrication procedures of Single-walled CNTs (SWCNTs) and Multi-walled CNTs and developed its gas sensor application [1,2]. There are large amount of studies on the development of biosensors that can detect important molecules by using chemical reaction with indicator label. However, in recent reports, several groups proposed the use of CNTs for label-free DNA (deoxyribonucleic acid) detection or immobilization. Since CNTs represent a nanomaterial group with attractive geometrical, electronic and chemical properties, it has been expected to apply CNTs for label-free detection of protein, antigen and DNA etc.

In our research, we have prepared simple samples for fundamental study, on which SWCNTs and DNA are combined. Although we have mainly concern with the electrical or the optical properties for the SWCNTs and DNA hybrid sample, we have observed the microscopic morphology to understand the structural details as the basic research. Here, we report on the fabrication procedures of SWCNTs, DNA and their CNT-DNA hybrid samples using atomic force microscopy(AFM).

Preparation of SWCNTs samples

We used commercially mass-produced SWCNTs (Nikkiso Co. LTD. Japan) grown by the direct injection pyrolytic synthesis (DIPS) method, which was developed by Advanced Industrial Science and Technology (AIST). Those DIPS-SWCNTs are used for combination with DNA because of their outstanding high purity and low defects. As grown DIPS-SWCNTs bundle and tangle each other. Dispersion process of the DIPS-SWCNTs sheet has been performed to debundle and isolate the SWCNTs in order to combine the DNA and the SWCNTs. The DIPS-SWCNTs sheets were dispersed in 1wt% SDS (sodium dodecyl sulfate) surfactant aqueous solution using an ultrasonic homogenizer (50 W, 24.5 kHz). The SWCNT aqueous solution was dropped onto the mica or silica glass substrates with the drop diameter of about 10 mm. The sample was rapidly dried in vacuum (< 0.67 Pa) and rinsed in pure water for 10 minutes to remove the residual SDS.

Hybrid of SWCNTs and DNA

We employed λ-DNA (Nippon gene, 48,502 bp, 10 mmol/L Tris-HCL(pH7.9), 1 mmol/L EDTA, A_{260}/A_{280}=1.8) which is lysogenized from bacteriophage λ (cI_{857}Sam7). This DNA solution was diluted by pure water and the concentration was adjusted to 0.03 μg/μL. For AFM measurement, the diluted DNA solution was dropped onto mica substrate, rinsed by pure water, and finally dried in vacuum.

A sample consisting of the SWCNTs and the DNA on a substrate was prepared by the following procedure. At first, the SWCNTs were stabilized by the method as mentioned above. After that, the diluted DNA was dropped on the stabilized SWCNTs, which followed by natural dry in air at room temperature.

Results and Discussions

Fig.1 show the surface morphologies of (a) DIPS-SWCNTs sheet and (b) SWCNTs dispersed and stabilized on a mica substrate observed by AFM in tapping mode (DFM: Dynamic Force Mode, Seiko Instrument SPI3800N). Fig.1 (a) shows that a large number of SWCNTs tangle each other. The microscopic structure causes the strength of the SWCNTs sheet so that we used the ultrasonic homogenizer with relatively high power for its dispersion. As can be seen in Fig.1 (b), the well-isolated SWCNTs can be observed after ultra-sonication and stabilization. The diameter of the SWCNTs is approximately 100 nm. It means that the SWCNTs still bundle each other. However, we consider that the complete separation of SWCNTs is not necessary for sensor application. The concentration of the SWCNTs could be adjusted by controlling the dilution with the solution.

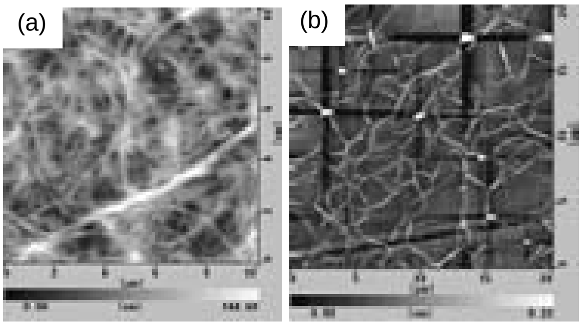

Fig.1. Surface morphologies of (a) DIPS-SWCNTs sheet and (b) SWCNTs dispersed and stabilized on a mica substrate observed by DFM.

Fig.2 (a) shows a DFM image of stabilized DNA on a mica substrate. Fig. 2 (b) is the cross-sectional profile at the position indicated in Fig.2 (a). The DNA was observed successfully but it was found from Fig.2 (b) that diameter of the DNA was very large (approximately 60 nm in full width at half maximum) in spite of the low height of about 2 nm which agrees well with actual diameter of the DNA. This result means that it is recognized like a single DNA from Fig.2 (a) but it is composed of multi DNA or surrounded by the residual substance of the solution (Tris-HCL, EDTA). It is required to improve the DNA purification and the uniform stabilization procedures.

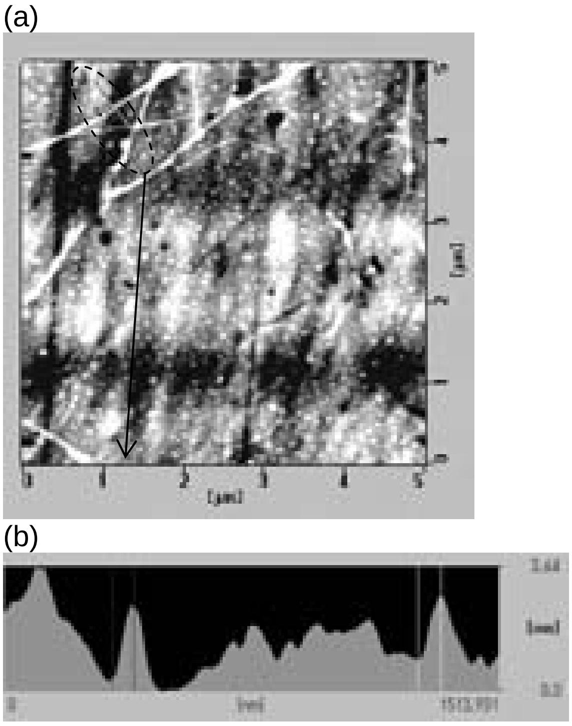

Fig.2 (a) DFM image of stabilized DNA on mica substrate and (b) the cross-sectional profile that corresponds to a line in (a).

Figure 3 shows the DFM image of the SWCNTs and DNA hybrid sample. We can see two different nanomaterials except for some impurities. These impurities may come from SDS surfactant in SWCNTs solution or the residual substance of the DNA solution. It was possible to distinguish them clearly by using cross-sectional analysis software. The DNA is placed below the SWCNTs nevertheless the DNA was dropped on the SWCNTs. Functionalization of SWCNTs may be needed for stronger contact between the SWCNTs and the DNA. Diameters of the SWCNTs and the DNA is almost same (approximately 100 nm). On the other hand, their heights are different. The electrical property of only SWCNTs stabilized sample has been already measured. It was shown that the resistance of the SWCNTs sample whose surface morphology is shown in Fig.1 (b) is 1-2 kOhm when the distance between measurement electrodes is 100 µm and the electrode length is 16 mm. However,it is difficult to estimate the accurate resistivity because evaluation of the length and cross-section area for the complex structured SWCNTs is difficult. We will investigate the electrical property of the SWCNTs and DNA hybrid sample taking into account the contact condition between the SWCNTs and the DNA.

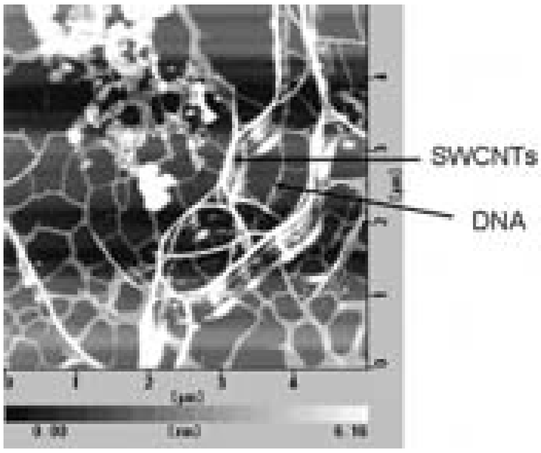

Fig. 3 DFM image of SWCNTs and DNA hybrid sample.

Summary

We studied the AFM morphology of the CNT and the DNA using the dispersion and stabilization method of the SWCNTs, the dilution and stabilization method of DNA, and the process for the SWCNTs and DNA hybrid sample. The SWCNTs and the DNA samples were stabilized relatively uniformly but improvement for their purification is needed. We could observe the SWCNTs and the DNA on a substrate simultaneously and distinguish them by using cross-sectional analysis software.

Acknowledgement

This work was supported by the Faculty of Engineering Kumamoto University, Grant-in-aid for Scientific Research.

REFERENCES

[1] T. Ueda, M.M.H. Bhuiyan, H. Norimatsu, S. Katsuki, T. Ikegami, Physica E, in press ,2008

[2] T. Ueda, S. Katsuki, K. Takahashi, H.A. Narges, T. Ikegami and F. Mitsugi, Diamond and Related Materials, in press,2008

***Authors**: Mr. Tsuyoshi Ueda, Dr. Fumiaki Mitsugi, and Prof. Tomoaki Ikegami, Graduate School of Kumamoto University, Kurokami 2-39-1, Kumamoto city, Kumamoto 860-8555, Japan, E-mail:mitsugi@cs.kumamoto-u.ac.jp.; Dr. Takashi Ikegami, Dojindo Laboratories, E-mail: takashi@dojindo.co.jp;Prof. Kenji Ebihara, Technical adviser of Dojindo Laboratories, Honourable Prof. of Kumamoto University and Lublin University of Technology, Kumamoto Techno Research Park, Tabaru 2025-5, Mashiki-machi, Kamimashiki-gun, Kumamoto 861-2202, Japan, E-mail: k-shrimp@road.ocn.ne.jp*

IMMERSED ARC-PLASMA TREATMENT OF MINERAL WASTES

Lukasz Szymanski[1]; Zbigniew Kolacinski[2]; Grzegorz Raniszewski[2]

Academy of Humanities and Economics in Lodz (1), *Technical University of Lodz, Electrical Apparatus Department* (2)

Abstract*. In the paper, a new approach to utilisation of mineral wastes using electric arc has been presented. A model of mineral arc-plasma immersed in the furnace feed charge has been elaborated for this purpose. The theory of utilisation of materials by electric arc has been verified by experimental tests in the laboratory furnace. Properties of the end-product – vitrified slag, are also presented in this paper.*

Streszczenie. *W artykule zaprezentowano podstawowe założenia dotyczące utylizacji materiałów przy pomocy łuku elektrycznego. Dla tych celów opracowano model łuku gazowo-mineralnego. Teoria utylizacji materiałów łukiem elektrycznym została zweryfikowana w laboratoryjnym stanowisku badawczym. Przedstawione zostały również właściwości produktu końcowego – witryfikatu.*

Keywords: plasma, electric arc, vitrification
Słowa kluczowe: plazma, łuk elektryczny, witryfikacja

Introduction

It has been proved that it is possible to lead a continuous process of utilization and conversion of mineral waste material using an electric arc, which is generated inside this material between an immersed electrode and a crucible.

This could be a step forward to elaborate and control an effective technological process of continuous casting with the ability of maximal absorption of arc energy by the feed charge. It should considerably increase the energetic efficiency of the waste treatment process.

The aim of this work is to present theoretical and experimental research of modelling of mineral waste pyrolytic treatment process and to demonstrate some test results of the following wastes treatment: medical ash, medical ash with different inorganic additives and medical ash with Polychlorinated Byphenyls.

Assumptions for the laboratory test stand design in the view of hitherto existing concept solutions

The main assumption for construction of a model of arc furnace arise from the thesis: „It is possible to lead a continuous process of utilisation and conversion of mineral waste material using an electric arc. The arc must be generated inside this material between an immersed electrode and the crucible." It means that the principle of this process is the arc submergence in the feed charge and also in its solution. Plasma utilisation process might be a continuous one if the feeding of charge and collection of product are continuous.

Detailed requirements concerning the design principles of the furnace are:

- the arc initiation is caused by short-circuiting of the electrode and the crucible following by the electrode enhancement,
- the continuous casting of the bath starts as soon as the feed is liquefied,
- the tap hole should be at sufficiently high temperature all the time, what makes impossible coagulation of the bath,
- the tapping should be hold without the furnace move.

Hitherto existing technical solutions in this field have been analysed on the ground patents and publications. The literature being close to the above-mentioned assumptions is very poor and it concerns mainly metallurgy of alloy steel [1, 2, 3] and production of the metallic silicon [4].

Metallurgy is the most developed branch of industry, where the electric arc is applied as a heat source. There are used mainly three-phase arc furnaces with three or six graphite electrodes, supplied with an alternating current. The hole in the electrodes allows inlet of a neutral gas like argon or nitrogen into the furnace, which also cools the electrodes. In this way, a thermal steady state of the furnace is reached. Four typical metallurgical arc furnace types are to distinguish:

- an immersed electrode – Fig. 1.a),
- an open arc – Fig. 1.b),
- a shielded arc – Fig. 1.c),
- a submerged arc – Fig. 1.d).

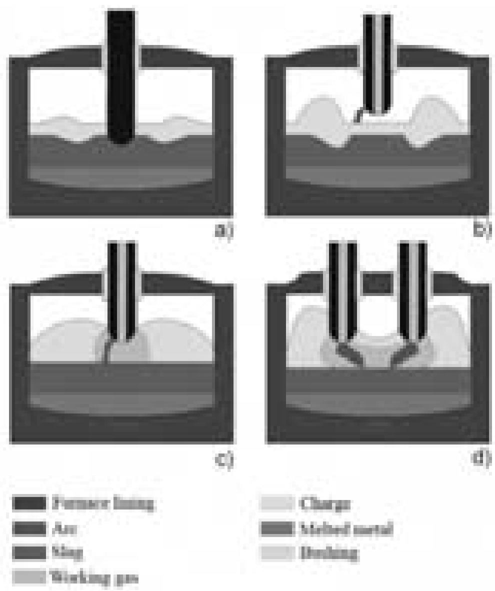

Fig.1. Examples of different configurations of metallurgical furnaces [5].

Differences between the above melting methods practically depend on position of electrodes in relation to the melted slag and to the position and depth of not melted charge-surrounding the electrodes.

In the immersed electrode system (Fig. 1.a) the electrode tip is placed inside the slag solution. Energy is generated by Joule's heat only: $P=I^2R_{slag}$. Then heated slag transfers the heat to the charge. Energy efficiency of such process is at the level of 95%. Unfortunately, it is not any of arc regime in the furnace functioning. The typical state of the arc furnace running is the state with an arc produced above the charge (Fig. 1.b). In such conditions, the large portion of energy is transferred to the external part of the furnace and then it is lost in water-cooled walls and roof.

The most similar metallurgical arc furnace to the worked out here laboratory model is this with shielded arc (Fig. 1. c). Though the arc is produced in between the electrode and the slag it burns in the atmosphere of gas flowing out from electrode, so it is not the gas-mineral arc to such extend as in this work. Moreover, it is not the initiated arc and burning in between electrode and crucible. It does not fulfil the role of the valve and regulator of the melted material flow out.

In the arrangement with submerged arc (Fig. 1.d) minimum 2 electrodes are required (if the power system is of the single-phase). Though the name of state of running "submerged arc" suggests similarity to elaborated laboratory model, the configuration of the arc is different in this case. It is the external arc initially attached to the charge, and during its fluidisation - spotted to slag. The liquid slag takes over the leadership in the current conduction with two-split arc circuit. The energy efficiency of furnace increases in this way. The arc is burning in the atmosphere of gas flowing out from electrodes here and the same it is not gas-mineral arc as in proposed laboratory model. The configuration of the arc is different in this case.

Finally, for fulfil required assumptions and their verification, it was necessary to work out the own construction of the arc furnace that will be presented in the next chapter.

The Gas - Mineral – Arc (GMA) behaviour

In axially - symmetrical configuration (Fig. 2) of an anode - the crucible (1) and a cathode – the rod electrode (3) the mineral feed charge files a space between them (2). Initially (in solid state) the feed does not lead an electric current. Anode has got in its bottom a hole enabling flowing out of excess of gas as well as tapping of the melt (bath). A DC arc, burning in the environment formed by gaseous mineral substance was named here the gas-mineral-arc (GMA). In Fig. 2 a first phase of GMA burning is presented.

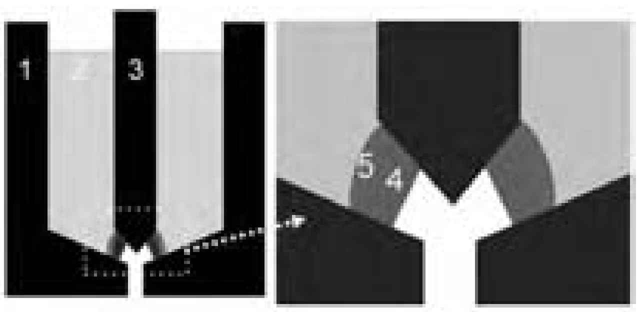

Fig.2 Draft of first phase of the GMA burning (whole object and its enlarged fragment).

The idle current starts to flow following the short-circuiting of the cathode and anode. After electrodes separation to a short gap (usually below 1 mm) a stable arc discharge named here the idle arc is initiated (4) using a gas matter (argon, nitrogen or air) from side of the hole. The increase of the feed temperature effects in the gas coming from gradually evaporating compounds according to their boiling points enters the arc atmosphere. The arc discharge produces a gas sheath (5) from the side of charge which is of mineral origin. The other wall of the gas sheath is the melted mineral material layer. It has been proved that this layer is having electrical conductivity comparable to this of some metals [6].

Melted material gravitationally driven over the crucible bottom to the hole causes an increase of the anode spot resistance. The arc anode spot will then change its position, moving to a place, where the anode voltage fall is the lowest. The electrical arc temperature will cause in this new place more intensive melting of the charge material, what in turn causes the next move of the anode spot for looking of the place with a minimum anode fall. Finally, all these makes the anode spot chaotic move around the hole. This phenomenon of effective arc drive around the crucible can be treated as "rotation" in the macroscopic scale. Such coupling makes all angular position of arc placement with the same statistical probability. The symmetry of thermal process allows to suppose that the plasmas collar occurring among cathode and crucible is separated from solid charge (as powder) by the sheath of gas and the layer of liquid (melted charge). Measurements of melted material resistivity show (Fig.4), that fluid layer connecting electrodes could shunt the arc, leading to take over the current and extinguish the arc. The resistance of fluid layer depends on its local resistivity, the cross section and the length. Is also probable, that resistivity of this layer near electrodes grows up sufficiently as a result of electrode cooling. It can prevent current shunting leading arc breaking. In every case however the arc voltage fall should be as high as possible so the arc can be elongated to the length assuring its stable regime called working arc regime. In this work experimental investigations it does not encounter any arc instability problems. However before working arc would be applied the idle arc was burning for the time up to 30 s. After such "conditioning" of the system the arc was elongated to 5 mm and it was burning always steadily, until the tapping of the full charge. The arc stable discharge with the voltage fall of 200V has been reached also in large plasma furnace (250kW power).

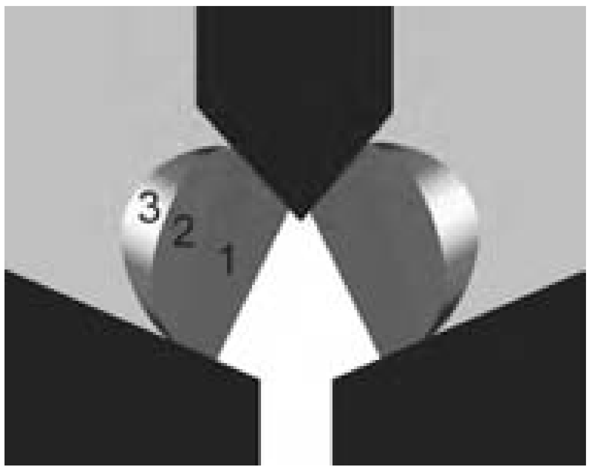

Fig. 3. Draft illustrating the phenomenon of shunting of arc current by the current conducting melt (1 - arc, 2 - gas layer, 3 - layer about consistency liquid - solid shunting arc).

It was drafted the probable schedule of resistance in the layer (3) with coloured picture, according to Fig. 4.

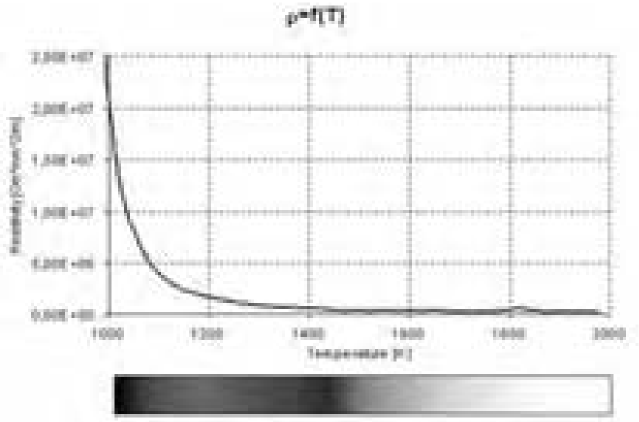

Fig. 4. Resistivity of ash coming from Heat and Power Generating Plant EC -2 (Lodz) in function of temperature [6].

Fig. 4. shows, how the high resistivity of layer near electrodes makes impossible current shunting leading to breaking of the arc.

Energy balance

The balance of energy of a plasma furnace is generally related to such conditions as parameters of heat source, flow of energy and heat losses. As areas of energy source it can be distinguished here the heat generated in the arc channel and in the electrode spots, as well as heat of electrodes by generated with Joule's heat. Despite, that the recorded arc voltage fall contains all mentioned components the precise voltage distribution is technically impossible.

The energy transfer generated in an arc furnace is on the way of the conductivity, radiation and convection. Heat losses follow in result of cooling the furnace body and the electrode.

In the arc furnace worked out here we have to deal with initiating and supporting the heat source (electric arc) inside of initially cold feed. So the configuration of heat source and charge means, that "almost whole " energy of the source is captured by the charge. Qualification "almost whole" classify as useful all the energy produced in arc channel and absorbed by charge on the way of convection and radiation. This qualification does not classify the unit of energy produced directly in electrode spots and Joule's heat produced as a result of current flow through electrode. Basing on the measured losses of energy to electrodes in metallurgical arc furnace [7] it can be correct to assume here the same value electrode losses in the range of 2%.

Then in submerged arc furnace with the arc plunged in charge it is possible to use up to 98% of delivered electrical energy.

The efficiency of thermal process depends on the value of losses to the ambient. These losses depend on temperature distribution on surface of external sheath of the furnace and the uncovered part of electrode. Simulations results show, the distribution of temperature on these surfaces mainly depend on the process duration.

The superiority of submerged arc over classic open arc will be pictured on the base of relative comparison here. The typical process of smelting in the metallurgical arc furnace runs with arc burning between external graphite electrode (cathode) and the metal charge to placed under it collecting electrode (anode) - Fig. 1. b. It is also feasible using of melted charge as auxiliary electrode in the arrangement of two external electrodes (cathode and anode) - Fig. 1. d or three graphite electrodes with three-phase supply.

The metallurgical plasma furnace works in conditions of domination of steady state. It is preceded by preheating the furnace without charge. In process of melting it can be mentioned about quasi equilibrium flows of energy among source (arc) and the ambient (the charge, electrodes, and cooling system). Large metallurgical furnaces achieve heat efficiency up to 50% [7], which means the only half of used up electrical energy is used for melting. Meanwhile in an arc furnace with the arc submerged in charge up to 98% of delivered energy may be used for melting in dependence on heat capacity of system (charge volume) and effectiveness of thermal isolation sheath furnace.

REFERENCES

[1] Barcza N.A., Curr T.R., and Jones R.T.: Metallurgy of open-bath plasma processes, Pure & Appl. Chem., Vol. 62, No.9, pp. 1761-1772, 1990.

[2] Jones R.T., Barcza N.A., Curr T.R.: Plasma Developments in Africa, Originally published as Plasma Developments in Africa, Second International Plasma Symposium: World progress in plasma applications, organized by the CMP (Centre for Materials Production) of EPRI (Electric Power Research Institute), 1993.

[3] Barcza N.A., Curr T.R., Denton G.M., Hayman D.A.: Mintek's Role in the developmentof plasma-arc technology based on a graphite cathode, Thermal Plasma Workshop on Industrial Plasma Aplications ISPC-9,1989

[4] Bakken J.A., Jensen R., Monsen B., Raaness O., Wrernes A.N.: Thermal plasma process development in Norway, Pure & Appl. Chem., Vol. 70, No. 6, pp. 1223-1228, 1998.

[5] Ma T., Bendzsak G.J., Perkins M.: Power system design for high-power electric smelting and melting furnaces, High Temp. Material Processes 5, s. 367-372, 2003.

[6] Szymański Ł.: Obliczanie rozkładu temperatur tygla nagrzewanego łukiem elektrycznym, Praca dyplomowa magisterska, 1999

[7] Pfeifer H., Kirschen M.: Thermodynamic analysis of EAF energy efficiency and comparison with a statistical model of electric energy demand, 7th European Electric Steelmaking Conference, European Coal and Steelmaking Community , pp. 1.413-1.428, 2002.

***Authors**: dr inż. Łukasz Szymański. Wyższa Szkoła Humanistyczno Ekonomiczna, ul. Rewolucji 1905r. nr 64, 90-222 Łódz, E-mail: lszymanski@wshe.lodz.pl, prof. dr hab. inż. Zbigniew Kołaciński, Politechnika Łódzka, Katedra Aparatów Elektrycznych, ul. Stefanowskiego 18/22, 90-924 Łódź, E-mail: zbigniew@p.lodz.pl;, mgr inż. Grzegorz Raniszewski, Politechnika Łódzka, Katedra Aparatów Elektrycznych, ul. Stefanowskiego 18/22, 90-924 Łódź, E-mail: larryl@o2.pl.*

Conference **ELMECO-6**
ELECTROMAGNETIC DEVICES AND PROCESSES IN ENVIRONMENT PROTECTION
joint with
9th Seminar APPLICATIONS OF SUPERCONDUCTORS **AoS-9**
June 24 – 27, 2008 Nałęczów, Poland

APPLICATION OF SUPERCONDUCTORS TO THERMONUCLEAR REACTOR MAGNETS

Paweł SURDACKI

Lublin University of Technology, Institute of Electrical Engineering and Electrotechnologies

Abstract. *In this paper, the magnetic system of the ITER reactor is depicted with some issues concerning application of the low temperature (LTS) superconducting strands. Applicability of the high temperature superconductors (HTS) desirable for use in the next generation fusion reactors is also considered.*

Streszczenie. *W pracy przedstawiono układ magnesów nadprzewodnikowych reaktora ITER ze szczególnym uwzględnieniem zastosowania przewodów z nadprzewodników niskotemperaturowych. Rozważono również możliwość zastosowania nadprzewodników wysokotemperaturowych w reaktorach następnej generacji.* ***(Zastosowanie nadprzewodników w elektromagnesach reaktora termojądrowego)****.*

Keywords: thermonuclear reactor, superconducting magnets, superconductors.
Słowa kluczowe: reaktor termojądrowy, elektromagnesy nadprzewodnikowe, nadprzewodniki.

Introduction

Thermonuclear fusion reaction, which is planned to be a future power source for the mankind, is able to deliver huge amounts of energy from deuterium, extracted from sea water, and lithium (a source of tritium) which is widely abundant in the world. The fusion of nuclei of deuterium and tritium can generate energy, which is carried by the alpha particle and the neutron generated by the reaction. The neutron will be slowed down in the blanket surrounding the plasma and it will generate the tritium, which is needed to sustain the reaction. The alpha particle will heat the plasma to maintain the very high temperature (~100 mln K) needed for the nuclear reaction to occur and continue [1].

The International Thermonuclear Experimental Reactor (ITER) project is based on the tokamak concept of magnetic plasma confinement accomplished by superconducting magnets entirely. They are required due to their ability to produce very intense magnetic fields in very extensive volumes with slight energy consumption. Project ITER should demonstrate generation of 500 MW of fusion power with a power amplification factor of 10 [2,3].

In this paper, the magnetic system of the ITER reactor is depicted with some issues concerning application of the low temperature (LTS) superconducting strands. Applicability of the high temperature superconductors (HTS) desirable for use in the next fusion reactors, is also considered.

Superconducting magnets in ITER

The superconducting magnet system confines, shapes and controls the plasma inside the toroidal vacuum vessel of the ITER reactor. It consists of three main systems (Fig.1) [2,3,4]:

1) 18 Toroidal Field (TF) magnet coils for the confinement and stabilization of plasma, generating nearly static fields, but subject to AC losses in plasma operation,
2) 6 Poloidal Field (PF) coils for the positioning and shaping of plasma, capable of very fast field changes (Fig.2),
3) A Central Solenoid (CS) coil for inducing plasma current, also capable of fast field changes (Fig.2),
4) 18 Correction Coils (CC) (Fig.2).

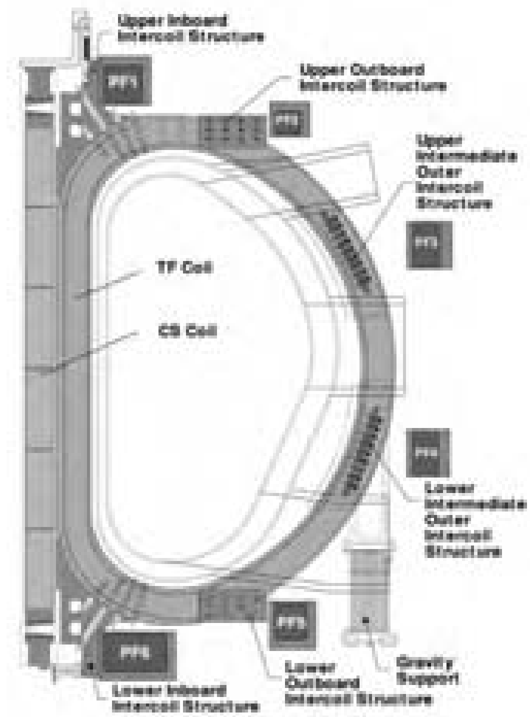

Fig.1. Schematic section in the ITER coil assembly [4,6]

The CS and TF coils will be manufactured using Nb_3Sn conductors due to the high magnetic field in the winding (13,5 T and 11,8 T, respectively) and required current (41,5 kA and 68 kA, respectively) (Table 1). The PF and CC coils will be manufactured using NbTi conductors (maximum field in the winding 6 T) (Tables 2 and 3). Total weight of magnet system is ~9 000 t.

Superconducting cables used in ITER coils carry very high current, on the order of several tens of kA. The nuclear and eddy current generated heat must be removed from the coils by appropriate cooling scheme permitting to keep their effective temperature in the 4 K range of liquid helium.

The cable-in-conduit (CICC) supercritical helium forced-flow concept is the most favourable for cooling the magnet coils of tokamak. The outer diameter is circular for the TF conductor and square for the other conductors. The cable is formed by multi-stage cabling of superconducting strands, with the final stage consisting of 6 bundles twisted around a central cooling channel (Fig.3).

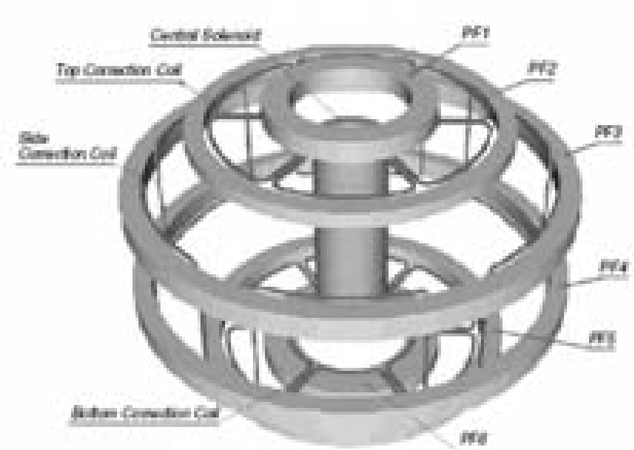

Fig.2. ITER Central Solenoid, Poloidal Field and Correction coil systems [4]

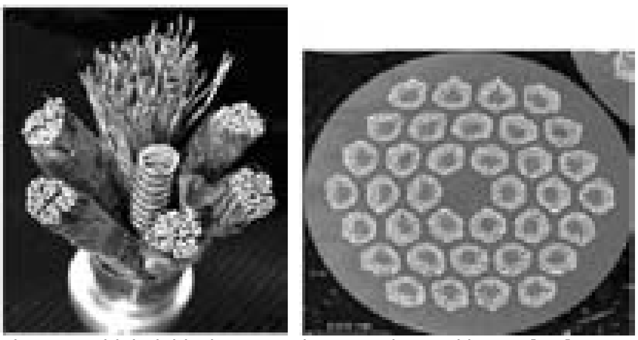

Fig.3. Toroidal Field Nb_3Sn conductor and strand layout [4,6]

Table 1. Parameters of ITER coils with Nb_3Sn/Cu conductor [2,3,5]

Coil type	**No of coils**	**Dimensions (m)**	**Weight (t)**	**B_{max} at winding (T)**	**Design approach**
TF	18	height 14 width 8	290	11,8	Each conductor in separate groove
CS	1 6 modules	height 12 diameter 4	840	13,5	Independent pancake-wound modules

Central Solenoid (CS) should produce an inductive swing of 30 Wb for plasma burn of current 15 MA, with a total inductive swing of 280 Wb. The maximum design voltage between terminals is 10 kV and the coil's design capacity is 140 MA-turns. According to the design, the Toroidal Field coil should produce magnetic flux density at the plasma axis of 5,3 T [2,7].

Table 2. Parameters of Poloidal Field coils with NbTi conductor [2]

Parameter	**PF1**	**PF2**	**PF3**	**PF4**	**PF5**	**PF6**
Winding weight (t)	145	129	385	353	255	263
Max. coil current (MA)	11,34	4,39	8,46	7,74	9,90	19,26
No of turns per coil radial vertical total	 16 16 252	 11 10 107	 12 16 118	 11 16 172	 14 16 220	 27 16 428
Conductor unit length (m) double pancake, two-in-hand	392	560	884	807	727	723
Max. turn voltage (V)	625	1750	875	1000	875	714
Ground/terminal voltage (kV)	5/10	7/14	7/14	7/14	7/14	5/10

Table 3. Parameters of Correction Coils with NbTi conductor [2,5]

Parameter	Top coil	Side coil	Bottom coil
Max. operating current (kA)	10	10	10
Max. current per coil (kA)	140	200	180
Max. total field (T)	<6	< 6	< 6

The whole magnet assembly requires 60 current leads for a total current of more than 2,5 MA. To reduce the resulting large refrigeration load at 4,5 K, HTS current leads could be used.

Prospects for HTS use in future magnet systems

The application of High Temperature Superconductors (HTS) in fusion research has, until now, been limited to the use in current leads, but it would be desirable for use in future fusion reactors, e.g. DEMO and beyond. The main driver to use HTS materials, especially YBCO coated conductors, for fusion coils is to operate the magnets either at high magnetic fields, e.g. 20 T, or at medium or high operation temperatures (50-65 K). However, AC losses, thermal stability, hot spot temperature and current distribution will play a challenging role due to the structure of the coated conductor tape. A promising new layout of a low AC loss cable for CC tapes with high aspect ratio is based on a classical ROEBEL cable concept (RACC-conductor) [8].

REFERENCES

[1] Surdacki P., Janowski T., Fusion Reactors for Future Power Generation, *International Conference ELMECO-5 Electromagnetic Devices and Processes in Enviroment Protection*, Nałęczów, 4-6 Sept.2005, Book of Abstracts, 73

[2] Komarek P., Salpietro E., Review of European Activities in Superconductivity for Thermonuclear Fusion, in the Light of ITER, *IEEE/CSC & ESAS European Superconductivity News Forum*, 4 (2008), 1-16

[3] Sborchia C., Status of ITER Magnet Design and Model Coils, *IEEE Transactions on Applied Superconductivity*, 10 (2000) 1, 554-559

[4] http:///www.iter.org/magnets.htm

[5] Bessette D., Conductors of the ITER Magnets, *IEEE Transactions on Applied Superconductivity*, 11, 1 (2001) 1550-1553

[6] Salpietro E., Status of the ITER magnets, *Superconductor Science and Technology* 19 (2006) S84-S89

[7] Libeyre P., Ciazynski D., et al., New results and remaining issues in superconducting magnets for ITER and associated R&D in Europe, *IAEA Fusion Energy Conference*, Chngdu, China, 16-21 Oct. 2006, IT/2-1Ra

[8] Janeschitz G., Heller R., et al., High Temperature Superconductors for Future Fusion Magnet Systems – Status, Prospects and Challenges, *IAEA Fusion Energy Conference*, Chngdu, China, 16-21 Oct. 2006, IT/2-2

This paper has been supported by the Ministry of Science and Higher Education (MNiSW) under the project N510 038 32/3678

***Author**: dr Paweł Surdacki, Lublin University of Technology, Insitute of Electrical Engineering and electrotechnologies, Nadbystrzycka 38a, 20-618 Lublin, E-mail: p.surdacki@pollub.pl.*

Conference **ELMECO-6**
ELECTROMAGNETIC DEVICES AND PROCESSES IN ENVIRONMENT PROTECTION
joint with
9th Seminar APPLICATIONS OF SUPERCONDUCTORS **AoS-9**
June 24 – 27, 2008 Nałęczów, Poland

THEORETICAL INVESTIGATION OF REACTIONS BETWEEN OZONE AND NITROGEN OXIDES

J. JAROSZYŃSKA-WOLIŃSKA

Department of Civil Engineering, Lublin University of Technology,

Abstract. *We have applied four different quantum chemistry methods to characterize the potential energy surface of the molecular systems involved in the reactions of the nitrogen oxides (NO or NO2) with ozone. The total molecular energy of these systems has been computed as a function of the bond distance between the N-atom of the nitrogen oxides and the O-atom of ozone. Our main goal was to find the transition states in these reactions.*

Streszczenie. *W tej pracy zastosowano cztery różne metody chemii kwantowej w celu znalezienia potencjalnej energii powierzchniowej procesu utleniania tlenków azotu (NO lub NO2) ozonem (O3) na poziomie molekularnym. Całkowitą cząsteczkową energię tego procesu obliczano jako funkcję odległości wiązania pomiędzy atomem azotu N-tlenków azotu i atomem tlenu O-ozonu. Naszym głównym celem było znalezienie stanów przejściowych w tych reakcjach.*

Keywords: ozone, nitrogen oxide, quantum chemistry methods
Słowa kluczowe: ozon, tlenki azotu, metody chemii kwantowej

Introduction

The utilization of NOx from the gas-phase based on the oxidation using ozone nowadays seems to be a very promising method for both economical and technological reasons. The determination of the main factors affecting its efficiency requires the detailed knowledge of the mechanisms of individual reactions. In principle the method can be modelled by a couple of reactions involving different nitrogen oxides and ozone (O3), which lead to the formation gas into industrially useful by–products, such as nitric acid (HNO3).

In this case, it is important to optimise the process so as to make the most efficient use of the ozone output by industrial dielectric barrier discharge ozonisers. This motivates us to investigate those factors affecting such efficiency, defined as the number of moles of NOx oxidised to a higher oxidation state per mole of ozone consumed.

Determination of the main factors affecting the efficiency of the oxidation of NOx by ozone requires detailed knowledge of the mechanisms of possible reaction paths. The overall oxidation process can be described by global reactions some or all of which reactions almost certainly incorporate intermediate stages in which intermediate species are generated:

(1) $NO + O_3 \rightarrow NO_2 + O_2$
(2) $NO_2 + O_3 \rightarrow NO_3 + O_2$
(3) $NO_2 + NO_3 \rightarrow N_2O_5$
(4) $2NO_2 + O_3 \rightarrow N_2O_5 + O_2$

One way to determine major factors which govern the process might be to perform exhaustive and expensive experimental studies but there would be no certainty that these would reveal the important processes. An attractive alternative seems to be molecular modelling based on quantum chemical methods. Quantum chemistry today delivers very powerful tools for studying varied chemical

To investigate the oxidation processes, each reaction must be characterised at the molecular level. There are two important energetic factors which need to be estimated quantum chemically, the relative energy and the activation energy. The relative energies of each reaction have been modelled and reported previously [1].

This work is aimed at the efficient removal of nitrogen oxide pollutants from gaseous waste streams through oxidation of NO_x by plasma generated ozone. The global reactions of ozone with nitrogen oxide (NO) and nitrogen dioxide (NO_2) are known to be exothermic, but $\Delta E = E_{final\ products} - E_{substrates}$ alone is not sufficient to determine the relative probability of competing reactions paths.

This work attempts to work towards estimation of activation energies of the two process initiation reactions of equations 1 and 2 ante by identifying the presence or absence of intermediate states and estimating the N-O bond distance at which such states might occur.

We have applied four different quantum chemistry models to partially characterize the potential energy surface of a system comprising nitrogen oxide reacting with ozone. The energy was computed as a function of the bond distance between the N-atom of the nitrogen oxide (NO or NO_2) and the O-atom of ozone. The models employed were: Hartree Fock (HF) method; Moller Plesset Perturbation (MP2) theory; Density Functional Theory (DFT) based Becke-3-Lee Yang Parr (B3LYP) method and Coupled Cluster with Singles Doubles (CCSD) substitutions

1. Computational details

Ab initio quantum chemical calculations have been performed to determine the reaction pathways for ozone based reactions of nitrogen oxides (nitric oxide (NO) and nitrogen dioxide (NO_2)). All calculations were carried out using a Gaussian 03 [2] suite of programs for electronic structure calculations. The potential energy curves were scanned using various levels of theory (HF, MP2, B3LYP and CCSD) to investigate the reactions under consideration. All quantum chemical calculations reported in the present work were performed using the 6-311g (d, p) 5d basis set.

In the following we present our theoretical investigations of the energetics of the molecules generated by intermediate reactions incorporated within the global reactions and the energy change of each intermediate reaction defined as $\Delta E = E_{intermediates} - E_{substrates}$.

Only by determination of the complete energy scheme of each competing reaction path, including the critical intermediate or transmission reactions, can the relative thermodynamic probability of competing reactions be found. Four different quantum chemistry methods were applied to determine the likely presence or absence of transitional or intermediate states. In three of the models transitional states in both the O_3-NO and the O_3-NO_2 reactions were indicated with varying degrees of certainty while in one model the existence of transitional states was not determined.

To compute the potential energy scans, the bond distance between the N-atom of nitrogen oxides (NO and NO_2) and the O-atom of ozone was systematically varied between 1.25Å and 2.50Å in increments of 0.05Å. At each point, the geometries were optimized using HF, MP2 and B3LYP levels of theory. For calculations using the CCSD quantum chemical method, the structures optimized at MP2 levels of theory were used and only single point calculations were carried out. The optimized geometries have been verified as global minima by carrying out the frequency calculations. The geometries with positive frequency values were considered as minima while the geometries with one negative frequency were considered as transition states. The grids were intensified between 1.40Å and 1.80Å (an increment of 0.01Å was given at each point for this range) to observe the transition state (if any) for the reactions under investigation. In certain cases, the grids were further intensified as discussed post.

2. Results and discussion

The following are the results of application of the various given levels of theory:

Hartree Fock Method – HF/6-311g (d, p) 5d

Firstly, the wavefunction based Hartree Fock method was exploited to investigate the ozone – nitric oxide and ozone – nitrogen dioxide reactions**.** The potential energy scans computed at HF/6-311G (D, P) 5D level of theory are shown in Figure 1:

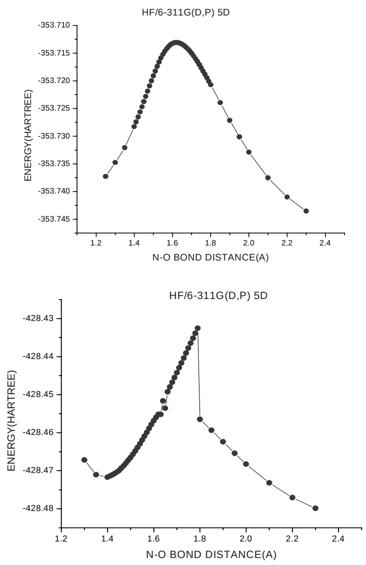

Fig 1. Potential energy vs. N-O bond distance for the reactions of O_3 with NO (left panel) and O_3 with NO_2 (right panel)

When the HF/6-311G (D, P) 5D level of theory was used to investigate these two reactions, clear formation of a transition state was seen in both cases. For the reaction of ozone with nitric oxide a transition state was observed around the N-O bond distance of 1.62Å while in the case of the reaction of ozone with nitrogen dioxide, the potential energy curve was sharper and the transition state occurred close to a longer N-O bond distance of 1.78Å. Thus, when an HF level of theory is used, modelling clearly shows that both the reactions proceed with the formation of a transition state. However, this observation cannot be considered as conclusive as to the mechanistic pathways for these two reactions because the HF method is not an optimum method for describing the ozone molecule and exchange correlation effects are neglected in this model. Hence, we need to consider other levels of theory to reach a final conclusion about the mechanistic pathways for these reactions.

Moller Plesset Perturbation Theory – MP2/6-311g (d, p) 5d

The MP2/6-311G (D, P) 5D theory was then applied to investigate the given reactions. The potential energy scans computed using MP2 theory are shown in Figure 2 for the respective reactions. In these cases we observe a small peak in the O_3-NO reaction and a pronounced peak in the O_3-NO_2 system. For the O_3-NO reaction, the peak indicating a possible transition state occurs at an N-O bond distance of around 1.6Å. In the case of the O_3-NO_2 reaction, a likely transition state is seen close to an N-O bond distance of 1.61Å. Thus, the HF and MP2 models tend to agree that a transition state exists in both reactions but there is some discrepancy in the N-O bond distance estimated by the models for the O_3-NO_2 reaction.

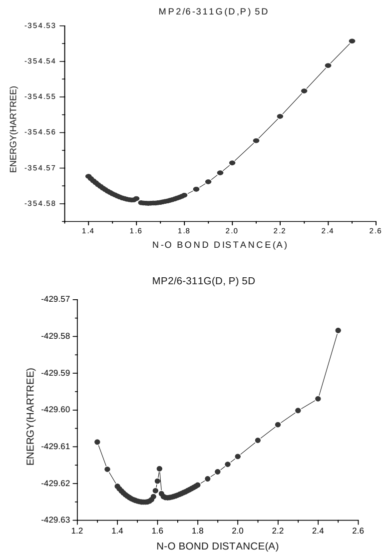

Fig 2. Potential energy vs. N-o bond distance for the reactions of o_3 with no (left panel) and o_3 with no_2 (right panel)

The presence of transition states in both reactions was indicated in the HF, MP2 and CCSD models but no clear indication could be seen in the B3LYP analysis.

REFERENCES

[1] Jaroszyńska-Wolińska, J. (2006, J. Adv. Oxid. Technol., vol. 9, 2, 1-6, (2006)
[2] Gaussian 03, Revision V.05, M. J. Frisch et al., Gaussian, Inc., Wallingford, CT, USA , (2004)
[3] PQS version 3.1, Parallel Quantum Solutions, 2013 Green Acres Road, Fayetteville, Arkansas 72703, (2003)
[4] K. Andersson, P. Borowski, P.W. Fowler, P.-Å. Malmqvist, B.O. Roos, A.J. Sadlej, Chem. Phys. Lett., 190, 367 (1992)
[5] P.C. Hariharan, J.A.Pople, Theor.Chim.Acta 28, (1973)
[6] K.Ishida, K.Morokuma, A.Komornicki, J.Chem.Phys. 66, 2153, (1977)

***Authors**: dr inż. Justyna Jaroszyńska-Wolińska, Department of Civil Engineering, Lublin University of Technology,Nadbystrzycka 40, 20-618 Lublin, Poland e-mail: jwtchem@akropolis.pol.lublin..*

Conference **ELMECO-6**
ELECTROMAGNETIC DEVICES AND PROCESSES IN ENVIRONMENT PROTECTION
joint with
9th Seminar APPLICATIONS OF SUPERCONDUCTORS **AoS-9**
June 24 – 27, 2008 Nałęczów, Poland

WYKORZYSTANIE ENERGII SŁONECZNEJ DO ZASILANIA UKŁADÓW OZONOWANIA WODY

Henryka Danuta STRYCZEWSKA, Krzysztof NALEWAJ

Politechnika Lubelska

Streszczenie. *W artykule omówiono możliwości wykorzystania energii słonecznej do zasilania układów ozonujących wodę. Zasilanie z paneli fotowoltaicznych instalacji do ozonowania wody w basenach kąpielowych na otwartym powietrzu, wydaje się najbardziej korzystne. W pracy przedstawiono wyniki badań generatora ozonu zasilanego z paneli fotowoltaicznych poprzez falownik I transformator wysokonapięciowy.*

Abstract. *Water treatment system, powered from solar energy, in domestic open air swimming pools working in summer season, seams to be very beneficial. Results of the analysis of the ozone generator powered from photovoltaic system through inverter and high-voltage transformer are presented and discussed in the paper.*

Słowa kluczowe: energia słoneczna, generator ozonu, ozonowanie wody.

Keywords: solar energy, ozone generator, water ozonization.

Wstęp

Zainteresowanie systemami fotowoltaicznymi, które przetwarzają energię słoneczną bezpośrednio w elektryczną szybko wzrasta, bowiem wytwarzają one energię bez ubocznej produkcji zanieczyszczeń, hałasu i innych czynników wywołujących niekorzystne zmiany środowiska.

W Polsce wykorzystanie energii z paneli fotowoltaicznych jest bardzo małe, choć prace badawcze prowadzone są od dawna. Warunki nasłonecznienia w Polsce nie odbiegają od tych, jakie występują w innych krajach Europy Środkowej, a są zdecydowanie lepsze niż w krajach skandynawskich, w których pracuje tysiące instalacji o mocy kilku kilowatów, szczególnie do zasilania obiektów oddalonych od sieci energetycznej.

Zasilanie z paneli fotowoltaicznych instalacji do ozonowania wody w przydomowych basenach kąpielowych na otwartym powietrzu, wykorzystywanych w sezonie letnim, wydaje się być szczególnie korzystne. Ich moce nie przekraczają zwykle kilku kilowatów, pracują sezonowo i w sposób nieciągły, a zatem nie wymagają takiej pewności zasilania jak inne odbiorniki energii elektrycznej. Ponadto, system elektroenergetyczny jest często w sezonie letnim przeciążony pracującymi urządzeniami klimatyzacyjnymi, co zdarza się coraz częściej także w naszej szerokości geograficznej, zatem, zastosowanie autonomicznych, fotowoltaicznych układów zasilania instalacji ozonowania wody w basenie może, w pewnym stopniu, odciążyć sieć zasilającą.

Badania przeprowadzone w laboratorium energii słonecznej Instytutu Podstaw Elektrotechniki i Elektrotechnologii, Politechniki Lubelskiej potwierdziły możliwości zasilania generatora ozonu z paneli fotowoltaicznych. W pracy przedstawiono wyniki analizy pracy generatora ozonu zasilanego z systemu fotowoltaicznego poprzez falownik i transformator wysokonapięciowy.

Opis laboratoryjnego systemu fotowoltaicznego

W Instytucie Podstaw Elektrotechniki i Elektrotechnologii Wydziału Elektrotechniki Politechniki Lubelskiej prowadzone są od kilkunastu lat prace z problematyki wykorzystania energii promieniowania słonecznego. Utworzono laboratorium słoneczne, które posiada w chwili obecnej system fotowoltaiczny o mocy 450Wp. Większość wyposażenia tego laboratorium zostało zakupione z projektów programu TEMPUS JEP 11030. Program był realizowany we współpracy z Uniwersytetem w Cardiff i Uniwersytetem w Londynie. System fotowoltaiczny znajduje się obecnie w budynku ASPPECT w części zajmowanej przez Instytut Podstaw Elektrotechniki i Elektrotechnologii. Schemat blokowy fotowoltaicznego systemu laboratoryjnego przedstawia rysunek 1.

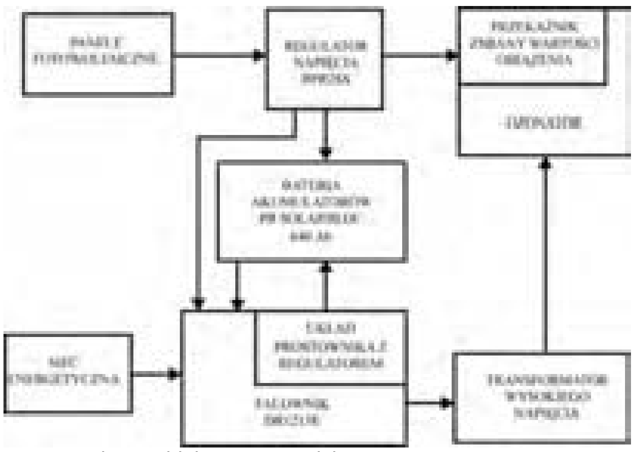

Rys. 1. Schemat blokowy stanowiska

Bateria słoneczna z której jest zasilany generator ozonu składa się z sześciu modułów typu BPS 275 firmy BP SOLAR

Parametry każdego z modułów są nastepujace:

- Moc maksymalna - 75W
- Napięcie odpowiadające mocy maksymalnej - 17,0V
- Prąd odpowiadający mocy maksymalnej - 4,45A
- Prąd zwarcia, - 4,75A
- Napięcie w stanie jałowym, - 21,4V
- Nasłonecznienie -1000W/m^2
- Temperatura ogniw -25^{0}C
- Powierzchnia baterii słonecznej ≈3,7m^2.

System ozonowania zasilany z paneli fotowoltaicznych

Generator ozonu jako odbiornik energii elektrycznej stanowi obciążenie czynno-pojemnościowe o stosunkowo niskim współczynniku mocy i o znacznie odkształconym prądzie. Uśredniony prąd wyładowania barierowego jest wypadkową statystycznie rozłożonych w przestrzeni i w czasie nano-sekundowych mikro-wyładowań, nałożonych na pojemnościowy prąd przesunięcia. Z uwagi na wysokie napięcie pracy i odkształcony prąd generatory ozonu, jeśli nie zawierają dodatkowych elementów do kompensacji i filtracji odkształceń prądu, mogą niekorzystnie wpływać na sieć zasilającą i pogarszać jakość energii elektrycznej. Zastosowanie autonomicznych źródeł fotowoltaicznych do zasilania generatorów ozonu eliminuje niekorzystny wpływ ozonatora na prace sieci energetycznej i zasilane z niej odbiorniki energii elektrycznej.

Instalacje ozonowania wody dla basenów kąpielowych, pracujące w sezonie letnim na otwartym powietrzu nie wymagają wysokiej pewności zasilania. Bateria fotowoltaiczna z akumulatorami jest wystarczającym źródłem energii dla zapewnienia , wymaganego do jej skutecznej dezynfekcji poziomu ozonu w wodzie. Przykładowy schemat systemu do ozonowania wody przedstawiono na rysunku 2. Instalacje wytwarzające ozon charakteryzują się stosunkowo małym zużyciem energii, dużą żywotnością oraz dobrymi parametrami eksploatacyjnymi i ekonomicznymi.

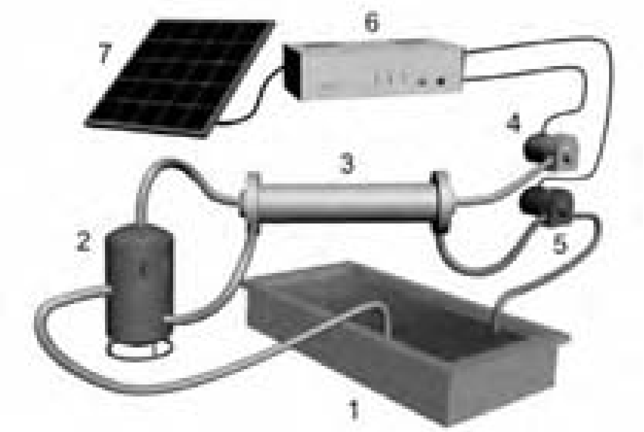

Rys. 2. Diagram systemu ozonowania wody basenowej zasilanego z fotoogniw słonecznych: 1–basen, 2–zbiornik kontaktowy, 3–ozonator, 4–pompa powietrza, 5–pompa wody, 6–przekształtnik DC/AC, 7–panel fotowoltaiczny

Główne elementy systemu to panel słoneczny (7), przetwornik napięcia stałego na napięcie przemienne bądź impulsowe (6), ozonator (3). Instalacje, o wymaganej wyższej pewności zasilania, można zaopatrzyć w akumulatory, ładowane nadwyżką energii w czasie dużego nasłonecznienia i oddające energię w nocy lub przy niedostatecznym nasłonecznieniu.

Badania laboratoryjne

Do prób laboratoryjnych został wykorzystany zbudowany w Instytucie model ozonatora o mocy 50W (rys. 3). Posiada on element wyładowczy wykonany z dielektryka w kształcie rury ze szkła borowo-krzemowego o ściankach wewnętrznych pokrytych warstwą aluminium, która stanowi elektrodę wysokonapięciową. Wysokie napięcie doprowadzane jest za pomocą elektrody w kształcie szczotki stalowej, przylegającej ściśle do napylanej warstwy aluminium i stanowiącej część czynną elementu wyładowczego. Rura dielektryczna umieszczona jest koncentrycznie wewnątrz rury ze stali kwasoodpornej, która stanowi elektrodę niskonapięciową uziemioną. Podczas pracy ozonatora między ściankami elektrody niskonapięciowej ma cyrkulować płyn chłodzący odprowadzający ciepło powstające w procesie syntezy ozonu.

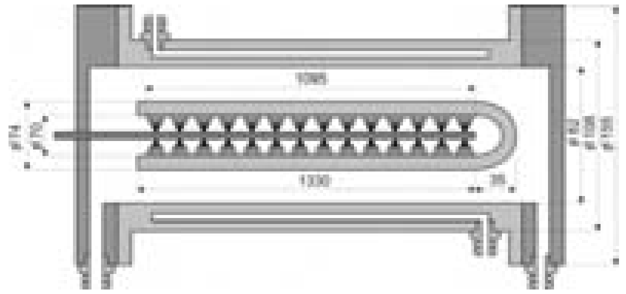

Rys. 3 Przekrój elementu wyładowczego ozonatora

Przeprowadzone badania potwierdziły możliwości zasilania ozonatora z baterii słonecznej. Na rysunku 4 przedstawiono zarejestrowane na oscyloskopie przebiegi napięcia na wybranym elemencie układu ozonowania.

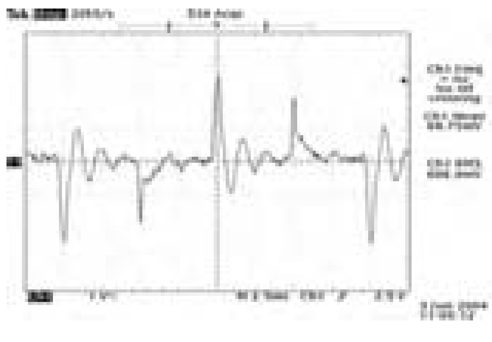

Rys. 4. Oscylogram napięcia na elemencie wyładowczym (x 1000)

Podsumowanie

Instalacje ozonowania wody, zasilane z ogniw fotowoltaicznych są przyjaznym dla środowiska i ekonomicznie uzasadnionym rozwiązaniem problemów dezynfekcji wody w przydomowych basenach kąpielowych, pracujących w sezonie letnim, na otwartym powietrzu.

Próby w laboratorium Instytutu Podstaw Elektrotechniki i Elektrotechnologii, Politechniki Lubelskiej potwierdziły możliwość zasilania generatora ozonu z ogniwa fotowoltaicznego.

Literatura

[1] Stryczewska, H. D., Nalewaj, K., Janowski, T., Stand alone PV system to supply swimming pool water treatment installation, Freiburg, Eurosun 2004, 350-356

[2] Stryczewska H. D., Nalewaj K., Ebihara K.: „Plazmowe urządzenia do obróbki wody i gleby zasilane z ogniw fotowoltaicznych" Konferencja: Zrównoważone Systemy Energetyczne – Nowe Kierunki Wytwarzania i Wykorzystania Energii, 2005, 197 – 206

[3] Kowal A. L., Świderska-Bróż M., Oczyszczanie wody, Wyd. PWN, Warszawa-Wrocław 1996

[4] Stryczewska H. D., Nalewaj K.: „Solar Energy in the Installations of Swimming Pool Water Treatment" International Conference on Electromagnetic Devices and Processes in Environment Protection ELMECO 5, Nałęczów 2005, 47 - 48

***Autorzy**: prof. dr hab. inż. Henryka, Danuta Stryczewska, Politechnika Lubelska, Instytut Podstaw Elektrotechniki i Elektrotechnologii, ul. Nadbystrzycka 38A, 20-618 Lublin, E-mail: h.stryczewska@pollub.pl, dr inż. Krzysztof Nalewaj, Politechnika Lubelska, Instytut Podstaw Elektrotechniki i Elektrotechnologii, ul. Nadbystrzycka 38A, 20-618 Lublin; E-mail: k.nalewaj@pollub.pl.*

Conference **ELMECO-6**
ELECTROMAGNETIC DEVICES AND PROCESSES IN ENVIRONMENT PROTECTION
joint with
9th Seminar APPLICATIONS OF SUPERCONDUCTORS **AoS-9**
June 24 – 27, 2008 Nałęczów, Poland

NADPRZEWODNIKOWE UZWOJENIE 2 GENERACJI DLA OGRANICZNIKA PRĄDU 6,9 kV / 1,15 kA

Grzegorz WOJTASIEWICZ, Beata KONDRATOWICZ-KUCEWICZ

Instytut Elektrotechniki w Warszawie

Streszczenie. *Aktualnie wytwarzane i dostępne na rynku cienkowarstwowe taśmy nadprzewodnikowe 2-giej generacji posiadają parametry wystarczające do budowy nadprzewodnikowych ograniczników prądu typu indukcyjnego, do ograniczania prądów zwarciowych w sieciach średniego napięcia. W pracy przedstawiono założenia do budowy uzwojenia dla nadprzewodnikowego ogranicznika prądu 6,9 kV/1,15 kA. Opisano podstawowe elementy konstrukcyjne uzwojenia, parametry, materiały i technologię wykonania.*

Abstract*. Currently produced and available 2nd generation HTS tapes have enough parameters to build inductive type fault current limiters to limit faults in medium-voltage power grid. The paper describes the assumption for superconducting winding of 6.9 kV/1.15 kA superconducting fault current limiter made of 2nd generation HTS tapes. The parameters of the winding's construction elements were described too. (****Superconducting winding for fault current limiter 6.9 kV/1.15 kA made of 2nd generation HTS tape*** *).*

Słowa kluczowe: nadprzewodnikowy ogranicznik prądu typu indukcyjnego, uzwojenie nadprzewodnikowe, taśma HTS 2-giej generacji.
Keywords: inductive type superconducting fault current limiter, superconducting winding, 2nd generation HTS tape.

Wstęp

Wśród zastosowań nadprzewodników wysokotemperaturowych w energetyce, duże szanse na zastosowanie komercyjne mają nadprzewodnikowe ograniczniki prądu. Rosnące zapotrzebowanie na energię elektryczną wymaga coraz lepszej jej jakości i niezawodności dostaw. Zastosowanie urządzeń ograniczających ewentualne prądy zwarcia umożliwia obniżenie wymaganej wytrzymałości zwarciowej elementów systemu i zapewnia redukcję jego kosztów. W nadprzewodnikowych ogranicznikach prądów zwarciowych wykorzystywane jest zjawisko niemal skokowej zmiany rezystywności elementu nadprzewodnikowego podczas przejścia ze stanu nadprzewodnikowego do stanu rezystywnego [1].

Na podstawie przeprowadzonych w latach ubiegłych, w Pracowni Technologii Nadprzewodnikowych, analiz budowy i działania nadprzewodnikowych ograniczników prądu oraz badań eksperymentalnych modeli fizycznych ograniczników, zaprojektowano nadprzewodnikowy ogranicznik prądu typu indukcyjnego 6.9 kV/1,15 kA, do ograniczania prądów zwarciowych w sieciach średniego napięcia, z uzwojeniem wtórnym wykonanym z taśmy HTS 2-giej generacji.

Budowa nadprzewodnikowego ogranicznika prądu typu indukcyjnego

Nadprzewodnikowe ograniczniki prądu typu indukcyjnego mają budowę transformatora ze zwartym nadprzewodnikowym uzwojeniem wtórnym, pełniącym rolę ekranu magnetycznego. Uzwojenie pierwotne wykonane z miedzi, włączone jest bezpośrednio do obwodu elektrycznego [1].

Projektowany ogranicznik prądu składa się z: rdzenia magnetycznego, znajdującego się w temperaturze pokojowej, miedzianego uzwojenia pierwotnego oraz nadprzewodnikowego uzwojenia wtórnego umieszczonego w kriostacie. Do chłodzenia i utrzymywania temperatury pracy uzwojenia nadprzewodnikowego, tj 77 K, wykorzystana będzie metoda chłodzenia w kąpieli z wykorzystaniem ciekłego azotu. Schemat budowy projektowanego ogranicznika prądu przedstawiono na rys. 1. W tab. 1 przedstawiono parametry techniczno - eksploatacyjne ogranicznika.

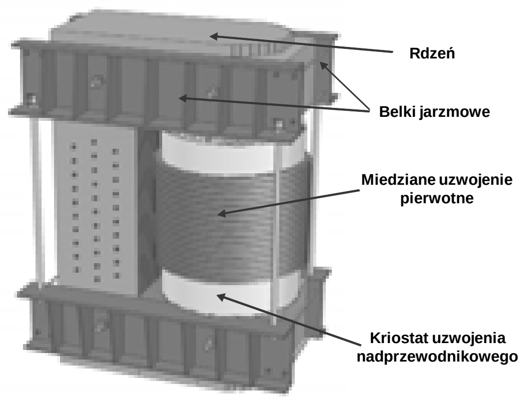

Rys. 1. Schemat budowy nadprzewodnikowego ogranicznika prądu 6.9 kV/1.15 kA

Tabela 1. Parametry techniczno eksploatacyjne nadprzewodnikowego ogranicznika prądu 6.9 kV/1.15 kA

	parametr	wartość
rdzeń	średnica	1,0 m
	wysokość kolumny	1,6 m
	szerokość okna	0,20 m
uzwojenie HTS	liczba zwojów taśmy 344/Fe	319
	średnica zewnętrzna	1,16 m
	średnica wewnętrzna	1,22 m
	wysokość	0,96 m
	długość taśmy HTS	1193 m
uzwojenie pierwotne	liczba zwojów	22
	średnica wewnętrzna	1,26 m
	średnica zewnętrzna	1,31 m
	wysokość	0,96 m

Nadprzewodnik i budowa uzwojenia wtórnego ogranicznika

Podstawowym elementem ogranicznika prądu typu indukcyjnego jest nadprzewodnikowe uzwojenie wtórne. Projektowane uzwojenie wykonane zostanie z taśmy nadprzewodnikowej 2-giej generacji YBCO 344/Fe firmy American Superconductors. Nadprzewodniki HTS 2-giej generacji to nadprzewodniki ceramiczne YBCO wykonane w technologii cienkich warstw. Taśmy YBCO składają się z szeregu warstw, z których można wyróżnić: warstwy stabilizatora, odpowiadające za parametry mechaniczne i termiczne taśmy, warstwy podłoża decydujące o jej parametrach elektrycznych, oraz warstwy nadprzewodnika.

Taśma 344/Fe jest taśmą 3 warstwowa, składająca się ze stabilizatora, podłoża oraz warstwy nadprzewodnika YBCO (rys.2) [2].

Taśma ta jest dodatkowo dwustronnie laminowana stalą co znacznie zwiększa jej rezystywności w stanie rezystywnym nadprzewodnika (tzn. w temperaturze pracy ogranicznika po wyjściu uzwojenia ze stanu nadprzewodzenia). Duża rezystywność taśmy jest warunkiem koniecznym dla odpowiedniej pracy nadprzewodnikowego ogranicznika prądu typu indukcyjnego. Dodatkowe warstewki stali wpływają także na zwiększenie wytrzymałości mechanicznej taśmy. Parametry taśmy 344/Fe zamieszczono w tab.2.

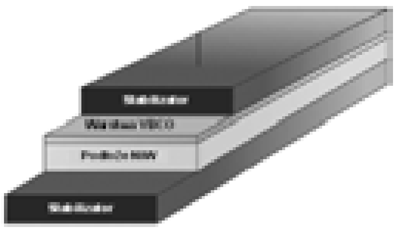

Rys. 2. Struktura taśmy HTS 344/Fe produkcji American Superconductors

Tabela 2. Parametry tasmy HTS 344/Fe produkcji American Superconductors

parametr	wartość
grubość	0,15 (± 0,02) mm
szerokość	4,33 (± 0,07) mm
max. naprężenie	250 MPa
max. odkształcenia rozciągające	0,3%
max. odkształcenia ściskające	0,3%
min. Średnica gięcia	35 mm
prąd krytyczny taśmy	60 A

Uzwojenie wtórne ogranicznika zaprojektowane jest w postaci krążkowej. Składa się z 319 zwojów nawiniętych na 20 niezależnych aluminiowych karkasach. Na każdym karkasie nawinięte będą dwa podwójne uzwojenia krążkowe, co łącznie daje 80 krążków rozmieszczonych równomiernie na całej wysokości uzwojenia. Na rys. 3 przedstawiono schemat uzwojenia wtórnego ogranicznika, a na rys. 4 schemat pojedynczego karkasu dwóch podwójnych uzwojeń krążkowych.

Rys. 3. Schemat uzwojenia wtórnego ogranicznika

Rys. 4. schemat karkasu dwóch podwójnych uzwojeń krążkowych

Konstrukcja uzwojenia nadprzewodnikowego powinna umożliwiać dobre chłodzenie uzwojenia nadprzewodnikowego oraz dobrą odporność na naprężenia mechaniczne statyczne i dynamiczne.

Do wykonanie międzyzwojowej izolacji elektrycznej uzwojenia wykorzystana zostanie folia kaptonowa HNfilm-25μm.

Kriostat uzwojenia wtórnego ogranicznika

Ze względu na konieczność chłodzenia nadprzewodnikowego uzwojenia wtórnego ogranicznika zaprojektowano kriostat zapewniający utrzymanie uzwojenia w temperaturze 77 K. Kriostat wykonany zostanie z materiału poliamidowego ERTALON 6SA. Parametry konstrukcyjne kriostatu zamieszczono w tab. 3

Tab. 5 Parametry konstrukcyjne kriostatu dla ogranicznika indukcyjnego SFCL 6,9 kV/1,15 kA

parametr	wartość
średnica wewnętrzna	1,12 m
średnica zewnętrzna	1,26 m
wysokość	1,59 m
materiał	Ertalon 6SA

Materiał ten charakteryzuje się optymalnym połączeniem wytrzymałości mechanicznej, sztywności, z korzystnymi właściwościami elektroizolacyjnymi oraz dobrą odpornością chemiczną. Elementy konstrukcyjne wykonane z ertalonu nie pękają w niskich temperaturach. Do łączenia elementów z ertalonu wykorzystuje się technologię spawania plastiku przy użyciu prętów z tego samego materiału. Podstawową izolacją cieplną elektromagnesu nadprzewodnikowego będzie stanowić będzie próżnia pomiędzy ściankami kriostatu.

Projekt finansowany ze środków projektu badawczego własnego Nr NN510 0853 33, pt: „Nadprzewodnikowy ogranicznik prądu typu indukcyjnego dla sieci średniego napięcia", realizowanego przez pracowników Pracowni Technologii Nadprzewodnikowych oraz Zakładu Wielkich Mocy, Instytutu Elektrotechniki w Warszawie. Rysunki 1, 3 i 4 - dr inż. J. Kozak i mgr inż. M. Majka

LITERATURA

[1] Janowski T., Nadprzewodnikowe ograniczniki prądu, praca zbiorowa*, Liber* 2002

[2] Wojtasiewicz G., Taśmy nadprzewodnikowe HTS pierwszej I drugiej generacji dla uzwojeń nadprzewodnikowych transformatorów,
VI Seminarium i Warsztaty Zastosowania Nadprzewodników, Kazimierz Dolny, 16-18.06.2005, 123-133

***Autorzy**: mgr inż. Grzegorz Wojtasiewicz, Instytut Elektroenergetyki w Warszawie, Pracownia Technologii Nadprzewodnikowych w Lublinie, Nadbystrzycka 36a, 20-618 Lublin, E-mail: g.wojtasiewicz@iel.waw.pl; mgr inż. Beata Kondratowicz-Kucewicz, Instytut Elektroenergetyki w Warszawie, Pracownia Technologii Nadprzewodnikowych w Lublinie, Nadbystrzycka 36a, 20-618 Lublin, E-mail: b.kondratowicz-kucewicz@iel.waw.pl.*

NADPRZEWODNIKOWE MAGNETYCZE ZASOBNIKI ENERGII Z CEWKOWO TOROIDALNYMI UZWOJENIAMI HTS

Beata KONDRATOWICZ-KUCEWICZ, Grzegorz WOJTASIEWICZ

Instytut Elektrotechniki, Pracownia Technologii Nadprzewodnikowych w Lublinie

Abstract*. Energy can be stored in the magnetic field of a coil. Superconducting Magnetic Energy Storage (SMES) is very promising as a power storage system for load levelling or power stabilizer. However, the strong electromagnetic force caused by high magnetic field and large current is a serious problem in SMES systems. A toroidal configuration would have a much less extensive external magnetic field and electromagnetic forces in winding. (****Superconducting magnetic energy storage with HTS toroidal winding)***

Streszczenie. *Energia może być magazynowana w uzwojeniu elektromagnesu. Nadprzewodnikowe Zasobniki Energii (SMES) są obiecującym rozwiązaniem systemu do gromadzenia energii dla stabilizacji jakości energii i eliminacji zakłóceń w sieci energetycznej. Jednakże silne pola magnetyczne generowane przez prąd o dużych wartościach powoduje powstawanie dużych sił elektromagnetycznych w urządzeniu. Toroidalna konfiguracja uzwojenia elektromagnesu SMES'a zapewnia o wiele mniejsze wartości pola rozproszenia i ogranicza siły elektromagnetyczne działające na uzwojenie.*

Keywords: SMES, HTS winding, toroidal magnet system.
Słowa kluczowe: Nadprzewodnikowy zasobnik energii, uzwojenie HTS, elektromagnes toroidalny.

Wprowadzenie

Głównym obszarem zastosowań SMES-ów jest zabezpieczenie przed nieplanowanymi przerwami w dostawie energii, poprawa jakości dostarczanej energii poprzez łagodzenie efektów chwilowych zaników energii i obniżeń napięcia, a także do wyrównywania obciążeń mocy odbiorników energii pracujących w sposób impulsowy lub przerywany. SMES-y mogą pracować w układach awaryjnego zasilania UPS (Uninterruptible Power Supply), kompensacji mocy, filtrów aktywnych, modulacji mocy, sterowania i stabilizacji napięcia w sieciach energetycznych. Rosnące wykorzystanie automatycznego sterowania procesami produkcyjnymi prowadzi do wzrastającej liczby odbiorców, którzy wymagają wysokiej jakości pobieranej energii. Obniżenia napięcia lub przerwy w dostawie energii trwające do 3 s stanowią 80-90% wszystkich awarii energetycznych. Mogą one być wyeliminowane poprzez użycie układów awaryjnego zasilania opartych na technologii SMES.

Podstawowym elementem układu nadprzewodnikowego zasobnika energii jest stałoprądowy elektromagnes nadprzewodnikowy utrzymywany w niskiej temperaturze zapewnianej przez układ kriogeniczny.

Działanie nadprzewodnikowego zasobnika energii polega na gromadzeniu energii elektrycznej w polu magnetycznym wywołanym przez przepływ prądu elektrycznego przez uzwojenie wykonane z nadprzewodnika. Energia gromadzona jest w urządzeniu gdy uzwojenie elektromagnesu jest w stanie nadprzewodzącym. Przejście uzwojenia do stanu rezystywnego powoduje rozładowanie energii do obwodu w którym pracuje nadprzewodnikowy zasobnik.

Energia zmagazynowana w polu magnetycznym elektromagnesu jest tym większa im większa jest objętość obszaru z silnym polem magnetycznym:

(1) $$E = \frac{1}{2} \int_V \mu H^2 \, \mathrm{d}V$$

gdzie H - oznacza natężenie pola magnetycznego (A/m),
$\tilde{\mu}$ przenikalność magnetyczną (H/m),
$\tilde{V}$ objętość, $\tilde{E}$ energię (J).

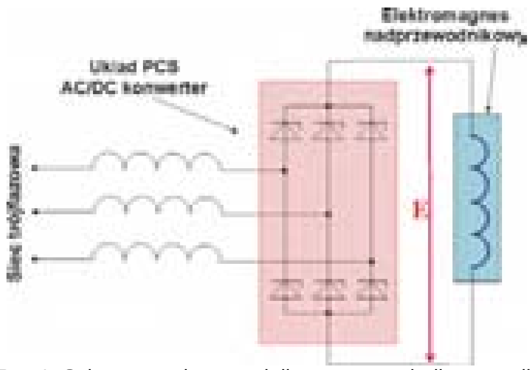

Rys.1. Schemat nadprzewodnikowego zasobnika energii.

Energię E zmagazynowaną w polu magnetycznym elektromagnesu można wyrazić równaniem:

(2) $$E = \frac{1}{2} L I^2$$

gdzie: L- oznacza indukcyjność elektromagnesu (H),
I- prąd w elektromagnesie (A),
$\tilde{E}$ energię (J).

Wartość zgromadzonej energii rośnie wraz ze wzrostem wartości prądu i indukcyjności uzwojenia nadprzewodnikowego. W analogicznym konwencjonalnym uzwojeniu miedzianym zgromadzona energia ulegałaby rozproszeniu ze względu na wystepowanie strat związanych z rezystancją uzwojenia podczas przepływu prądu. Jednakże w uzwojeniu nadprzewodnikowym w stanie nadprzewodnictwa rezystancja jest zbliżona do zera i zgromadzona energia może być przechowywana w uzwojeniu przez czas teoretycznie nieograniczony. Utrzymywanie uzwojenia w stanie nadprzewodzącym jest ograniczone działaniem i wydajnością układu chłodzenia.
Gęstość prądu w nadprzewodniku jest kilkakrotnie większa niż w uzwojeniu miedzianym, dzięki czemu energia zgromadzona w elektromagnesie nadprzewodnikowym może osiągać wartości rzędu 106 J/m^3 w zależności od rodzaju i parametrów materiału nadprzewodnikowego wykorzystanego do jego budowy.

Konfiguracje nadprzewodnikowych uzwojeń dla SMES'ów

W opracowanych na świecie rozwiązaniach konstrukcyjnych nadprzewodnikowych elektromagnesów dla zasobników energii, można wyróżnić konstrukcje oparte na wykorzystaniu pojedynczych cewek oraz układu cewek nadprzewodnikowych. Stosowane są zarówno uzwojenia solenoidalne jak i toroidalne. W rozwiązaniach z uzwojeniem solenoidalnym znaczącą zaletą jest prosta konstrukcja uzwojenia oraz większa gęstość energii na jednostkę długości przewodu nadprzewodnikowego.

Konstrukcja uzwojenia nadprzewodnikowego powinna uwzględniać siły mechaniczne oddziałujące na przewód z prądem znajdujący się w polu magnetycznym uzwojenia. W układzie solenoidalnym elektrodynamiczne siły promieniowe rozciągają uzwojenie, a osiowe ściskają je. W układach cewek lub toroidach na poszczególne cewki składowe działają znaczne siły, które muszą być zrównoważone odpowiednimi elementami konstrukcyjnymi. Rozkład tych sił zależy od geometrii i konfiguracji uzwojeń. W konfiguracji toroidalnej siła dośrodkowa ściska toroid dążąc do zmniejszenia jego średnicy.

W rozwiązaniach nadprzewodnikowych SMES'ów o dużych wartościach energii gromadzonych w uzwojeniu rzędu kilkudziesięciu MJ i GJ istnieją znaczne ograniczenia konstrukcyjne ze względu na duże wartości sił elektromagnetycznych występujących w uzwojeniu przy silnych polach magnetycznych i dużych wartościach prądu. Jednym z rozwiązań tego problemu jest zastosowanie uzwojeń toroidalnych o różnych konfiguracjach [1]. W stosowanych nadprzewodnikowych uzwojeniach toroidalnych, można wyróżnić trzy podstawowe konfiguracje, różniące się sposobem nawinięcia uzwojenia. Na rysunku 2 przedstawione są przykłady uzwojeń toroidalnych: (a) cewkowo – toroidalnego, (b) typu „forced balanced" o zrównoważonym rozkładzie sił elektrodynamicznych i (c) typu „stress-balanced" o zrównoważonym rozkładzie naprężeń.

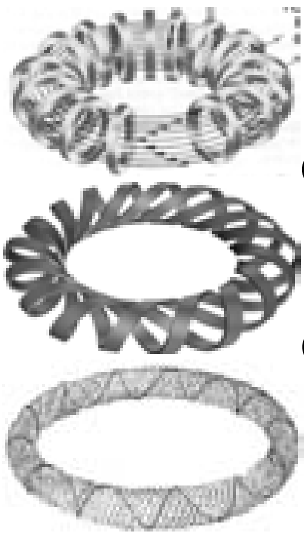

(a)

(b)

(c)

Rys.2. Konfiguracje uzwojenia toroidalnego:
(a) cewkowo-toroidalne (b) uzwojenie typu "force-balanced",
(c) uzwojenie typu „stress-balanced".

Różnice w konfiguracji uzwojeń wynikają z wartości gromadzonej energii, gabarytów urządzenia oraz zastosowanego nadprzewodnika.

Ze względu na skomplikowaną konstrukcję uzwojeń pokazanych na rysunku 2b i 2c gdzie przewód lub taśma nadprzewodnikowa są nawinięte w postaci uzwojenia helikalnego. Mniej skomplikowanym rozwiązaniem jest uzwojenie pokazane na rysunku 2a, gdzie toroid utworzony jest z cewek solenoidalnych. W wielu badaniach prowadzona jest optymalizacja takiego uzwojenia pod kątem wartości gromadzonej energii, sił działających na uzwojenie, ale także ilości nadprzewodnika i gabarytów uzwojenia, które wpływają na koszty całego urządzenia. Przykładowe konfiguracje z budowane z różnej ilości jednakowych cewek solenoidalnych pokazano na rysunku 3 [2,3].

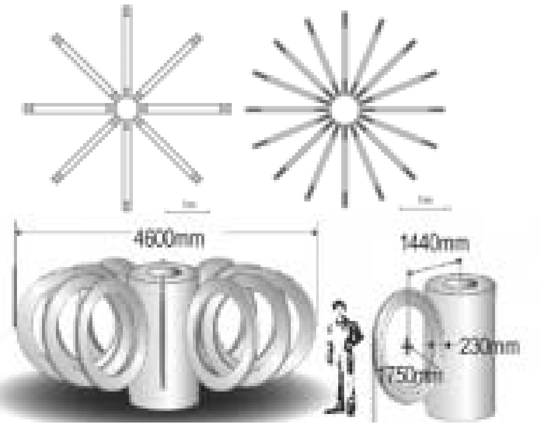

Rys.3. Konfiguracje uzwojenia cewkowo-toroidalnego[2],[3]

W Pracowni Technologii Nadprzewodnikowych w Lublinie zbudowano 14 cewek z nadprzewodnika Bi-2223/Ag dla SMES'a o konstrukcji solenoidalnej (rys.4.) i energii 10 kJ / 50 K. Zostaną one wykorzystane do budowy modelu uzwojenia cewkowo-toroidalnego.

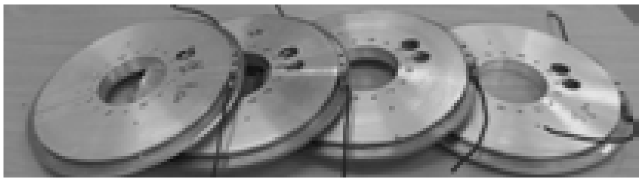

Rys.4. Cewki z nadprzewodnika B-2223 dla modelu SMES'a
o konstrukcji cewkowo-toroidalnej.

Podsumowanie

W nadprzewodnikowych SMES'ach o dużych wartościach energii gromadzonej w uzwojeniu rzędu kilkudziesięciu MJ i GJ istnieją znaczne ograniczenia konstrukcyjne ze względu na duże wartości sił elektromagnetycznych występujących w uzwojeniu przy silnych polach magnetycznych i dużych wartościach prądu. Jednym z rozwiązań tego problemu jest zastosowanie uzwojeń toroidalnych.

LITERATURA

[1] Nomura S., Watanabe N., Suzuki C. i inni, Advanced configuration of superconducting magnetic energy storage, *Energy* 30 (2005) 2115–2127
[2] Noguchi S., Ishiyama A., Akita S., Kasahara H., i inni,: An Optimal Configuration Design Method for HTS-SMES Coils, IEEE Trans.on App. Sup., vol. 15, No. 2, (June 2005), 1927-1930
[3] Ichinose A., Kasahara H., Sakaki H., Akita S., i inni,: Research and Development of High-Tc SMES, IEEE Trans.on App. Sup., vol. 15, No. 2, (June 2005), 1947-1950

***Authors**: mgr inż. Beata Kondratowicz-Kucewicz, mgr.inż.Grzegorz Wojtasiewicz, Instytut Elektrotechniki, Pracownia Technologii Nadprzewodnikowych w Lublinie, ul.Nadbystrzycka 38a, 20-618 Lublin, E-mail: b.kondratowicz-kucewicz@iel.waw.pl*

Conference **ELMECO-6**
ELECTROMAGNETIC DEVICES AND PROCESSES IN ENVIRONMENT PROTECTION
joint with
9th Seminar APPLICATIONS OF SUPERCONDUCTORS **AoS-9**
June 24 – 27, 2008 Nałęczów, Poland

WYKORZYSTANIE TAŚM HTS I i II GENERACJI DO BUDOWY NADPRZEWODNIKOWYCH OGRANICZNIKÓW PRĄDU

Michał MAJKA, Sławomir KOZAK

Instytut Elektrotechniki

Streszczenie. *Obecnie na rynku dostępne są dwa typy nadprzewodnikowych przewodów wysokotemperaturowych, które mogą zostać użyte do budowy nadprzewodnikowych ograniczników prądu. Są to przewody pierwszej generacji 1G HTS (zwykle wykonane w procesie rurowo-proszkowym z nadprzewodnika Bi-2223) oraz przewody drugiej generacji 2G HTS (przewody powlekane, zwykle wykonane na bazie nadprzewodnika wysokotemperaturowego YBCO). W artykule przedstawiono komercyjnie dostępne taśmy 2G HTS które mogą być użyte w budowie SFCL.*

Abstract. *Two types of HTS conductors are currently available for use to make different HTS devices. They are know as first generation 1G HTS (usually Bi-2223 systems made with "powder-in-tube" methods) and second generation 2G HTS (coated conductors, usually made on the base of YBCO superconductor). This paper presents commercially available 2G HTS can be used in superconducting fault current limiters.*

Słowa kluczowe:, nadprzewodnikowy ogranicznik prądu, przewód powlekany, taśma nadprzewodnikowa.
Keywords: superconducting fault current limiter, coated conductor, superconducting tape.

Wstęp

Komercyjnie dostępne taśmy drugiej generacji (2G) bazujące na nadprzewodniku wysokotemperaturowym YBCO stopniowo zastępują taśmy pierwszej generacji (1G) wykonane z użyciem nadprzewodnika Bi-2223. W stanie nadprzewodzącym taśmy 2G mające warstwę podłoża o dużej rezystywności przewodzą setki amperów z bardzo małymi stratami, podczas gdy w stanie rezystywnym wykazują dużą wartość rezystancji. W związku z wykazywanymi właściwościami przewody 2G są odpowiednie do zastosowania w nadprzewodnikowych ogranicznikach prądu (SFCL) zarówno typu rezystancyjnego jak i indukcyjnego. Taśmy 1G w porównaniu z przewodami 2G posiadają mniejszą wartość rezystywności w stanie rezystywnym i niewielkie wartości prądu krytycznego, z tego względu wykorzystanie ich do budowy nadprzewodnikowych ograniczników prądu jest mniej korzystne.

Taśmy HTS I i II generacji dla SFCL

Taśmy pierwszej generacji mają kompozytową budowę składającą się z kilkudziesięciu włókien nadprzewodnika Bi-2223 umieszczonych wewnątrz srebrnej matrycy. Dostępne są również taśmy o podwyższonej wytrzymałość mechanicznej pokryte dwustronnie laminatem ze stali. Taśmy 1G wykonywane są w procesie rurowo-proszkowym. AMSC produkuje taśmy 1G o maksymalnej długość do 800 m przy prądzie krytycznym do 155 A dla taśm o szerokości 4,3 mm i grubości 0,23 mm [4].

Taśmy drugiej generacji (2G) bazują na nadprzewodniku wysokotemperaturowym YBCO naniesionym na warstwę podłoża. Taśmy nadprzewodnikowe 2G składają się z szeregu warstw, wśród których można wyróżnić: warstwę podłoża decydujące o jej parametrach elektrycznych, warstwę stabilizatora, odpowiadającą za parametry mechaniczne i termiczne taśmy oraz warstwę nadprzewodnika. W produkcji taśm II generacji na podłoże metalowe posiadające odpowiednie właściwości mechaniczne, cieplne i elektryczne nanoszona jest warstwa odpowiedniego prekursora nadprzewodnika, z którego po obróbce cieplnej w atmosferze tlenowej tworzy się nadprzewodnik. Materiały nanoszone są na podłoże w procesie fizycznego (PVD) lub chemicznego (CVD) osadzania próżniowego lub w procesie osadzania metalo-organicznego (MOD). Parametry komercyjnie dostępnych taśm 2G zostały przedstawione w tabeli 1.

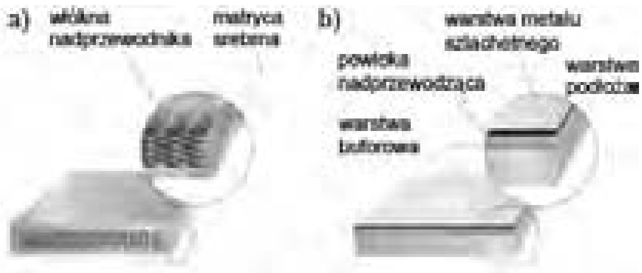

Rys. 1. Architektura przewodów wysokotemperaturowych: a) pierwszej generacji (1G), b) drugiej generacji (2G) [4]

Tab. 1. Parametry komercyjnie dostępnych taśm drugiej generacji (2G) wykorzystywanych do budowy SFCL [4,5]

Producent	**AMSC**	**AMSC**	**Super Power**	**Super Power**
Typ taśmy	344	344S	SF 12050	SF 12100
Grubość, mm	0,15	0,20	0,055	0,105
Szerokość, mm	4,33	4,33	12	12
Min. średnica gięcia, mm	25	25	25	25
Prąd krytyczny (77 K)	60-90 A	70-90 A	200- 300 A	200-250 A
Laminat	Miedź Cu155 50 µm	Stal 316L 25 µm	brak	brak
Maks. długość taśmy, m	< 100		> 600	
Warstwa Ag	1 µm		2 µm	
Warstwa YBCO	1 µm		1 µm	
Warstwa podłoża	Ni-5%W 75µm		Hastelloy C276	
			55 µm	105 µm
Rezystywność podłoża	b/d		$125 \cdot 10^{-6}$ Ωcm	

Z punktu widzenia pracy nadprzewodnikowych ograniczników prądu najważniejszym parametrem taśm HTS jest duża wartość rezystancji w stanie rezystywnym oraz duża gęstość prądu krytycznego [2]. Warunki te spełniają taśmy drugiej generacji. Produkowane przewody powlekane 2G z przeznaczeniem do pracy w ogranicznikach mają warstwę podłoża wykonaną z niemagnetycznego materiału o dużej rezystywności. W przypadku przewodów z serii 344 produkowanych przez AMSC warstwę podłoża stanowi stop Ni-5%W (słaby ferromagnetyk), natomiast firma SuperPower stosuje do swoich przewodów niemagnetyczny stop Hastelloy C276 (Ni-57%, Mo-16%, Cr-15.50%, Fe-5.50%, W-4.00%, Co-2.50%). Materiał ten wykazuje rezystywność 130 $\mu\Omega\cdot$cm w temperaturze pokojowej. Zastosowana w obu taśmach warstwa srebra służy poprawie kontaktu elektrycznego. Taśmy z serii 344 produkowane przez AMSC są dwustronnie laminowane miedzią (344) lub stalą nierdzewną (344S). Taśmy 2G produkcji SuperPower dostępne są ze stabilizatorem miedzianym (seria SC) oraz bez takiego stabilizatora (seria SF). Laminacja taśmy poprawia wytrzymałość mechaniczną, elektryczną i termiczną stabilność, oraz ułatwia proces nawijania. Laminacja stalą nierdzewną znacznie zwiększa rezystywność taśmy w stanie rezystywnym.

Wykorzystanie taśm I i II generacji do budowy nadprzewodnikowych ograniczników prądu

W celu przeciwdziałania dynamicznym skutkom prądów zwarciowych i towarzyszącym im siłom mechanicznym w sieci elektroenergetycznej idealnym rozwiązaniem jest zastosowanie nadprzewodnikowego ogranicznika prądu. Ogranicznik tego typu ma impedancją bliską zeru w normalnych warunkach pracy, w chwili wystąpienia zwarcia w chronionym obwodzie samoistnie w pierwszych milisekundach przechodzi do stanu wysokiej impedancji, jednocześnie po ograniczeniu prądu zwarciowego bez wykonywania żadnych czynności wraca do stanu o niskiej impedancji. Użycie nadprzewodników wysoko-temperaturowych różnej postaci: taśm I lub II generacji, nadprzewodników masywnych czy też cienkowarstwowych, pozwala budować nadprzewodnikowe ograniczniki prądu o różnych konfiguracjach. Prace badawcze nad różnego typu nadprzewodnikowymi ogranicznikami prądu doprowadziły do opracowania wielu projektów i prototypów, których wybrane parametry elektryczne zostały przedstawione w tabeli 2.

Tab. 2. Wybrane projekty SFCL wykonane i realizowane na świecie (TF – nadprzewodniki cienkowarstwowe, CC – przewody powlekane) [1]

Wykonawca	Typ	Materiał HTS	Parametry elektryczne
ABB	1f. rez.	Bi-2212	8 kV | 800 A
ABB	1f. ind.	Bi-2212	10,5 kV | 70 A
ACCEL/Nexans	3f. rez.	Bi-2212	6,9 kV | 600A
Nexans	1f.rez.ind.	Bi-2212	63,5 kV |1,8 kA
KEPRI, Korea	3f. rez.	Bi-2212	13,2 kV | 63 A
CAS, Chiny	3f. most.	Bi-2223	6 kV | 1,5 kA
KEPRI, Korea	3f. rez.	Y123 TF	3,8 kV | 200 A
Siemens	3f. rez.	Y123 TF	4,2 kV | 100 A
Siemens/AMSC	1f. rez.	Y123 CC	7,5 kV | 300 A
Alcatel	1f. rez.	Y123 CC	100 V | 1,4kA
IGC Superpower	3f. rez.	Y123 CC	80 kV | -- kA
Rolls Royce	Rez.	MgB2	6,6 kV | 400 A

W ostatnich latach największym zainteresowaniem badawczym cieszą się nadprzewodnikowe ograniczniki prądu typu rezystancyjnego (budowane w oparciu o taśmę II generacji) ze względu na prostszą konstrukcję, mniejsze wymiary i mniejszy koszt wykonania w porównaniu z ogranicznikiem typu indukcyjnego. Na rys. 2 przedstawiono jeden z modułów ogranicznika rezystancyjnego wykonanego przez firmę Siemens. Moduł jest przeznaczony do pracy w jednej z faz 3-fazowego ogranicznika rezystancyjnego pracującego w sieci 13 kV.

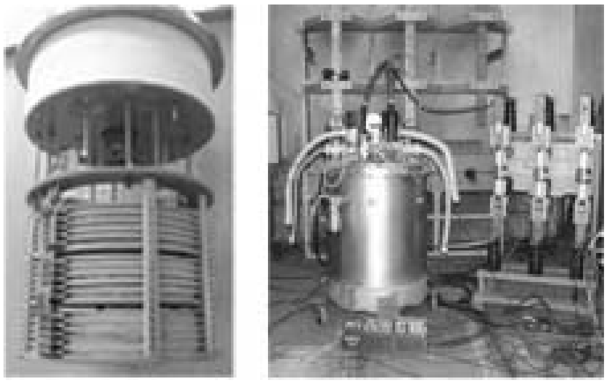

a) b)

Rys. 2. Jednofazowy moduł ogranicznika prądu typu rezystancyjnego Siemens: a) uzwojenie nadprzewodnikowe ogranicznika wykonane z taśmy 344S firmy AMSC, b) moduł ogranicznika na stanowisku pomiarowym [2]

Ogranicznik składa się z 15 bifilarnych cewek nawiniętych z 50 metrowych odcinków taśmy 344S AMSC. Moduł ma prąd znamionowy 300 A, oraz napięcie znamionowe 7,5 kV, Uzwojenia chłodzone są w kąpieli ciekłego azotu przy ciśnieniu atmosferycznym. Ogranicznik składa się z trzech stosów połączonych szeregowo, każdy ze stosów zawiera 5 cewek połączonych równolegle. Kompletny moduł ma rezystancję 10,4 Ω (295 K) i prąd krytyczny 440A (77 K). W najbliższych latach AMSC wraz z firmą Siemens planują realizację projektu DOE USA na wykonanie trójfazowego ogranicznika dla sieci 115 kV z wykorzystaniem taśmy 344S AMSC.

Praca naukowa finansowana ze środków na naukę w latach 2007-2009 jako projekt badawczy (N N510 0853 33).

LITERATURA

[1] Noe M., Steurer M., High-temperature Superconductor fault current limiters: concepts, applications, and development status, *Supercond. Sci. Technol.* 20 (2007), R15-R29

[2] Kozak S., Janowski T., Materiały nadprzewodnikowe dla nadprzewodnikowych ograniczników prądu, *Prace Naukowe Instytutu Podstaw Elektrotechniki i Elektrotechnologii Politechniki Wrocławskiej nr 44, (2006)*

[3] Kraemer H.P., Schmidt W., Wohlfart M., Neumueller H.W., Otto A., Verebelyi D., Schoop U., Malozemoff A.P., Test of a 2 MVA medium voltage HTS fault current limiter module made of YBCO coated conductors, *Journal of Physics: Conference Series,* 97 (2008), 012091

[4] Strona internetowa producenta: www.amsuper.com - American Superconductors

[5] Strona internetowa producenta: www.superpower-inc.com – SuperPower Inc.

***Authors**: mgr inż. Michał Majka, Instytut Elektrotechniki, Pracownia Technologii Nadprzewodnikowych, ul. Nadbystrzycka 36a, 20-618 Lublin, E-mail: m.majka@iel.waw.pl, dr hab. inż. Sławomir Kozak, Instytut Elektrotechniki, Pracownia Technologii Nadprzewodnikowych, ul. Nadbystrzycka 36a, 20-618 Lublin, E-mail: s.kozak@iel.waw.pl.*

Conference **ELMECO-6**
ELECTROMAGNETIC DEVICES AND PROCESSES IN ENVIRONMENT PROTECTION
joint with
9th Seminar APPLICATIONS OF SUPERCONDUCTORS **AoS-9**
June 24 – 27, 2008 Nałęczów, Poland

THE INFLUENCE OF MAGNETIC COUPLING FACTOR k ON VALUE IMPEDANCE LIMITING FAULT CURRENT

Joanna KOZIEŁ, Tadeusz JANOWSKI

Lublin University of Technology, Institute of Electrical Engineering and Electrotechnologies

Abstract*. The society require infallible power network, that provides electric energy. In this article the rule of operation and construction of the superconducting fault current limiter type transformer, which can be used in the future to increase security power network was described. The influence of magnetic coupling factor on value impedance limiting fault current was theoretically analysed.*

Streszczenie. *Społeczeństwo wymaga niezawodnej sieci energetycznej dostarczającej energię. W tym artykule opisano zasadę działania i budowę nadprzewodnikowych ograniczników prądu typu transformatorowego, które mogą być w przyszłości stosowane dla zwiększenia bezpieczeństwa sieci energetycznej. Przeanalizowano teoretycznie wpływ współczynnika sprzężenia magnetycznego na wartość impedancji ograniczającej prąd zwarcia.*

Keywords: fault current, superconducting fault current limiter (SFCL), magnetic coupling factor, transformer .
Słowa kluczowe: prąd zakłóceniowy, nadprzewodnikowy ogranicznik prądu, współczynnik sprzężenia magnetycznego, transformator.

Introduction

The short – circuits in power network are very important risks for transformers, generators, busbars and transmission lines as well as they decrease the energy supplies realibility to consumers of electric energy. The limitation of fault current with the use of impedance coil and adequately big reactance of transformer has have an significant effect on the increase of the costs of building and operation electric power system, as well as the price of electric power. The biggest actual value of fault current (dynamic current) causes that the dynamic effects forces arised in electromagnetic devices flow through them during the short - circuits. The maximum value of the mechanic forces of fault current usually appears, when the current reaches the first maximum after the short- circuit, it is 0.005 second and the frequency 50Hz. If we break off the short circuit or we increase its impedance rapidly in much shorter time, than 0.005 second, then dynamic force do not reach first maximum and do not make excissive stretchs as well as electromagnetic devices defects in short circuit.

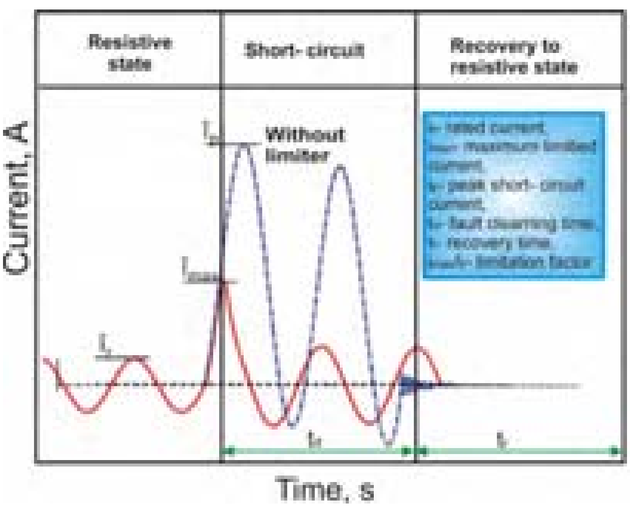

Fig.1. Idea the operation of superconducting fault current limiter.

Quick and infallible operation of electric power network may be assured by superconducting fault current limiters, because the time when superconductor transforms from superconductor to resistance state lasts tens microsecond, but their return to usual operation is almost immediate and do not require any human interference.
Superconductors reveals entire disappearance of resistivity only in conditions, when parameters like: temperature, current density, magnetic flux density do not exceed certain values, called critical values. Properties of the rapid resistance value increase in the superconducting limiting element enables to build superconducting fault current limiter in power network, only when superconducting limiting element exceed current critical value.

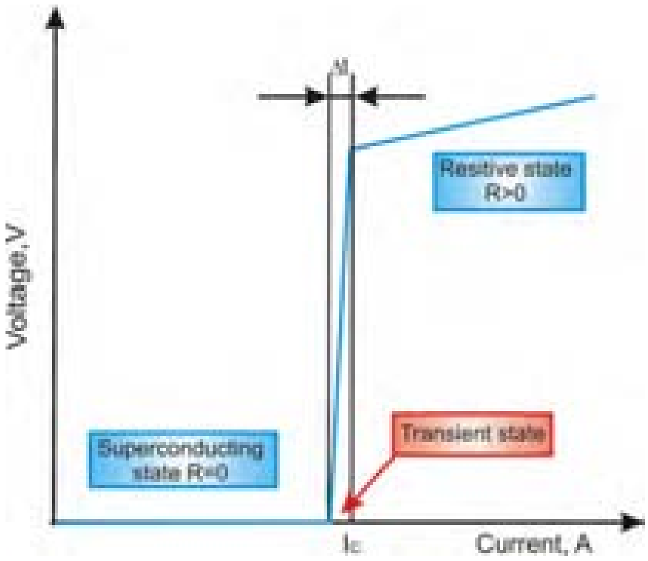

Fig.2 Real value I-U of superconducting fault current limiting

Superconducting Fault Current Limiting Transformer Type

There exist two types of superconducting fault current limiters: resistance and inductance one. Resistance limiters are very simple in its structure, but they require working current being conduced to the superconducting limiting

element by using current leads. Inductive fault current limiter are very similar in structure to current transformers, in which secondary winding is shorted by a superconducting wire, the most widely is used ring made of superconducting ceramics.
Superconducting fault current limiting transformer type is a kind of inductive limiter, in which secondary winding is classically designed, but is shorted for a superconducting limiting element.

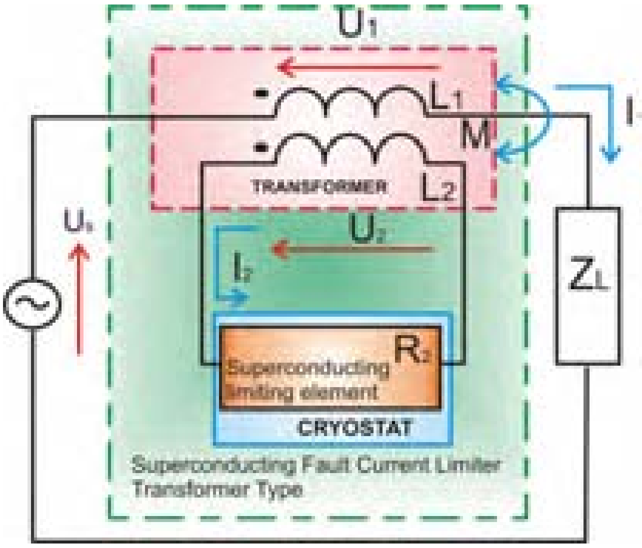

Fig. 3. Circuit configuration of transformer type superconducting fault current limiter

The one of advantages of superconducting fault current limiter transformer type is the possibility of using superconducting element of any shape in simple cryostat, without current transformers.
The main defect of superconducting fault current limiter transformer type is the require of bigger resistance in non-superconducting state, in order to fill up desired level limited current.

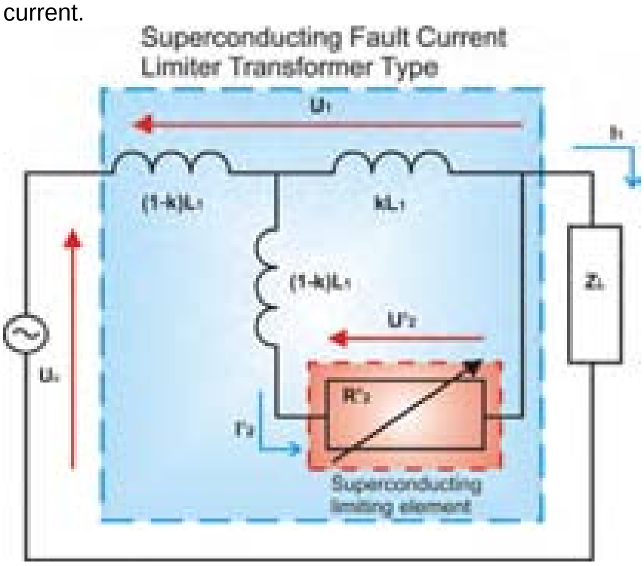

Fig.4 The equivalent circuit of transformer type superconducting fault current limiter.

Theoretical characteristics

From Fig. 4 the voltage and current equations of the fault current limiter can be derived as follows:

(1) $$\begin{bmatrix} U_1 \\ 0 \\ U'_2 \end{bmatrix} = \begin{bmatrix} jX & jkX \\ jkX & jX + R'_2 \\ 0 & -R'_2 \end{bmatrix} \cdot \begin{bmatrix} I_1 \\ -I'_2 \end{bmatrix}$$

(2) $$U_S = U_1 + Z_L \cdot I_1,$$ where:

(3) $$X = \omega \cdot L_1 = \omega \cdot a^2 L_2$$

The influence of magnetic coupling factor k and current limiting device resistance R_{2n} on current limiting impedance Z_{1n} is obtained on fig. 5.

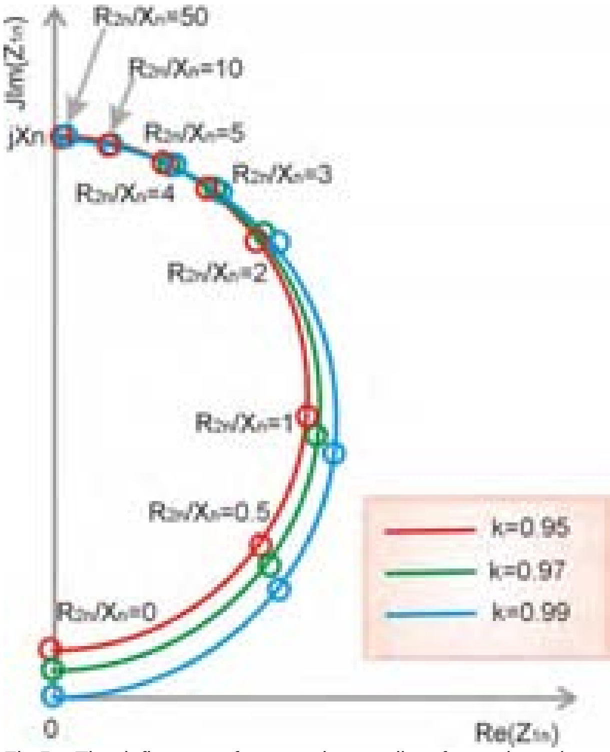

Fig.5 The influence of magnetic coupling factor k and current limiting device resistance R_{2n} on current limiting impedance Z_{1n} [3]

REFERENCES

[1] Kozak S., Janowski T., *Materiały nadprzewodnikowe dla nadprzewodnikowych ograniczników prądu,* Prace Naukowe IPEE Politechniki Wrocławskiej,nr 44, s. Konferencje nr 18 (Postepy w Elektrotechnologii), Wrocław – Jamrozowa Polana, 20-22 września 2006, str. 277-284
[2] Yamaguchi H., Kataoka T.: *Current Limiting Characteristics of Transformer Type Superconducting Fault Current Limiter With Shunt Impedance,* IEEE Transactions on Applied Superconductivity, VOL. 17, NO.2, JUNE 2007 p.1919-1922
[3] Yamaguchi H. and Kataoka T.: *Effect of magnetic saturation on the current limiting characteristics of transformer type superconducting fault current limiter*, IEEE Transactions on Applied Superconductivity, vol.16, pp.691-694, June 2006.
[4] Janowski T. i inni, *Nadprzewodnikowe ograniczniki prądu*, Wydawnictwo LIBER, 2002.

Authors: ***Prof. dr hab. inż. Tadeusz Janowski****, Politechnika Lubelska, Wydział Elektrotechniki i Informatyki, Instytut Podstaw Elektrotechniki i Elektrotechnologii, ul. Nadbystrzycka 38A, 20-618 Lublin, E-mail:t.janowski@pollub.pl;* ***mgr inż. Joanna Kozieł*** *Politechnika Lubelska, Wydział Elektrotechniki i Informatyki, Instytut Podstaw Elektrotechniki i Elektrotechnologii, ul. Nadbystrzycka 38A, 20-618 Lublin, E-mail: j.koziel@pollub.pl.*

Conference **ELMECO-6**
ELECTROMAGNETIC DEVICES AND PROCESSES IN ENVIRONMENT PROTECTION
joint with
9th Seminar APPLICATIONS OF SUPERCONDUCTORS **AoS-9**
June 24 – 27, 2008 Nałęczów, Poland

BADANIA EKSPERYMENTALNE ZASILACZA REAKTORA PLAZMOWEGO Z RDZENIEM PIĘCIOKOLUMNOWYM

Grzegorz KOMARZYNIEC, Jarosław DIATCZYK, Henryka Danuta STRYCZEWSKA

Politechnika Lubelska, Wydział Elektrotechniki I Informatyki
Instytut Podstaw Elektrotechniki I Elektrotechnologii

***Abstract**. Repeatability of the plasma-chemical process depends on stability of plasma parameters, which influence the proper chemical reaction path. The great role in the process of plasma generation plays appropriately selected power supply system. For industrial applications the non-thermal plasma reactor together with its supply system should present: high efficiency of energy transfer to the plasma; the possibility to control plasma parameters according to the plasma-chemical process requirements, proper cooperation with the supply net while having low power consumption, simple, reliable and save operation and servicing.*

***Streszczenie.** Powtarzalność procesów plazmo-chemicznych w istotny sposób zależy od stabilnych parametrów plazmy. Duży wpływ na generowaną plazmę ma odpowiednio dobrany układ zasilania. Przeznaczony do zastosowań przemysłowych reaktor plazmowy i jego układ zasilania powinny charakteryzować się: dużą sprawnością, możliwością wpływania na parametry plazmy, właściwą współpracą z siecią zasilającą, łatwą obsługą i niskim kosztem eksploatacji.*

Keywords: plasma reactor, power supply, five limb transformer.
Słowa kluczowe: reaktor plazmowy, transformator pięciokolumnowy.

Wprowadzenie

Prowadzenie dowolnego procesu technologicznego z wykorzystaniem plazmy, musi opierać się na znajomości jej właściwości oraz opanowaniu metod jej otrzymywania.

Duże wpływ na uzyskiwanie plazmy nietermicznej i nierównowagowej ma układ zasilania. Od jego parametrów zależy moc wyładowania, temperatura generowanej plazmy i stopień jej jonizacji. Reaktory plazmowe są odbiornikami energii elektrycznej o nieliniowych charakterystykach prądowo-napięciowych i szybkich zmianach wartości chwilowych prądów, napięć i konduktancji przestrzeni wyładowczej [2]. Układ zasilania, aby sprostać wymaganiom takich nietypowych odbiorników energii elektrycznej, powinien zapewniać zapłon wyładowań, ich podtrzymanie po zapłonie przy znacznie niższej wartości napięcia niż niezbędna do zapłonu, ograniczając jednocześnie prąd elektrod roboczych, tak aby zapewnić nierównowagowe warunki generowanej plazmy. Do zasilania łukowych reaktorów plazmowych, zwłaszcza w instalacjach przemysłowych stosuje się transformatory specjalne.

Jednym z takich rozwiązań może być transformator trójfazowy na rdzeniach zwijanych, w którym uzwojono kolumny zewnętrzne (rys. 1), aby wykorzystać indukowane w nich napięcie do zasilania elektrod zapłonowych reaktorów plazmowych.

Rys. 1. Transformator trójfazowy o rdzeniach zwijanych: 1/2 – współśrodkowo nawinięte fazowe uzwojenia pierwotne i wtórne, 3 – uzwojenia wtórne kolumn zewnętrznych.

Układ pomiarowy

Układ pomiarowy do badań zasilacza z transformatorem pięciokolumnowym obciążonym trójelektrodowym reaktorem plazmowym z elektrodą zapłonową przedstawiono na rysunku 2. Parametry transformatora zestawiono w tabeli 1.

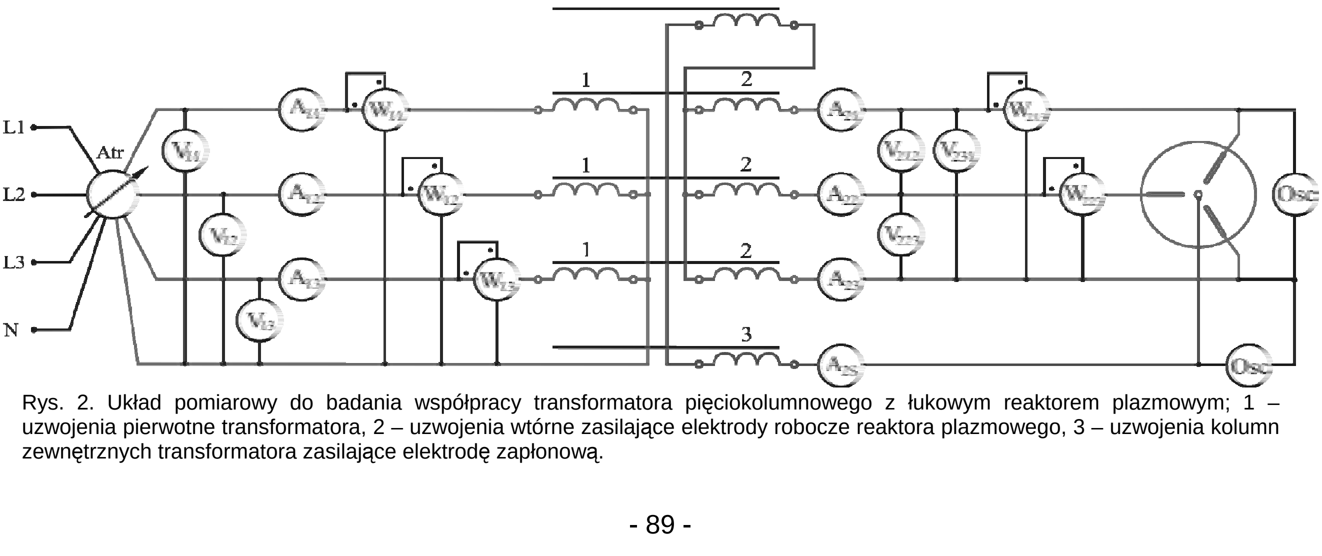

Rys. 2. Układ pomiarowy do badania współpracy transformatora pięciokolumnowego z łukowym reaktorem plazmowym; 1 – uzwojenia pierwotne transformatora, 2 – uzwojenia wtórne zasilające elektrody robocze reaktora plazmowego, 3 – uzwojenia kolumn zewnętrznych transformatora zasilające elektrodę zapłonową.

Tabela 1. Dane znamionowe zasilacza.

Napięcie pierwotne fazowe	230 V
Napięcie wtórne fazowe	1,5 kV
Napięcie wtórne uzwojeń kolumn zewnętrznych	3,8 kV
Prąd pierwotny	16 A
Prąd wtórny	2,4 A
Prąd wtórny uzwojenia kolumny zewnętrznej	350 mA
Moc transformatora	11 kVA

Wyniki badań

Mimo silnego odkształcenia od sinusoidy napięć fazowych strony wtórnej zasilacza, pracującego przy obciążeniu reaktorem plazmowym (rys. 3), prąd strony wtórnej wszystkich faz zachowuje przebieg sinusoidalny (rys. 3). W oscylogramach prądu nie obserwuje się również, charakterystycznych dla łuków intensywnie chłodzonych, przerw bezprądowych przy przejściu prądu przez zero.

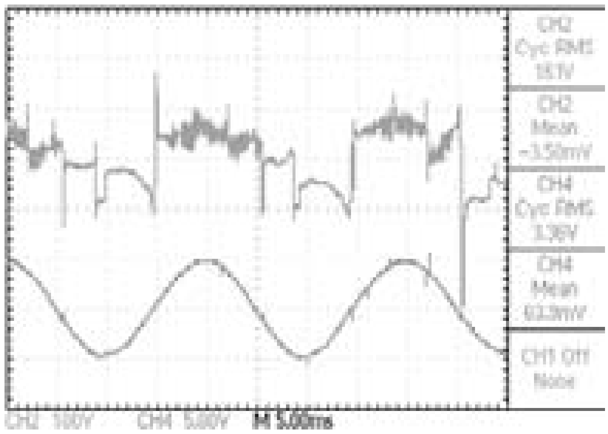

Rys. 3. Przebieg napięcia (CH2) i prądu (CH4) strony wtórnej jednej fazy zasilacza przy obciążeniu reaktorem plazmowym.

Dla prawidłowej pracy reaktora plazmowego istotnym problemem jest uzyskanie pewnego zapłonu wyładowania na elektrodzie zapłonowej. Na rysunku 4 przedstawiono przebieg napięcia zapłonowego, między elektrodą zapłonową a jedną z elektrod roboczych, pracującego reaktora plazmowego. Szumy w napięciu świadczą, że wyładowanie na elektrodzie zapłonowej pali się nieprzerwanie w trakcie cyklu pracy reaktora i ma charakter iskry elektrycznej występującej wielokrotnie w jednym okresie zmian napięcia.

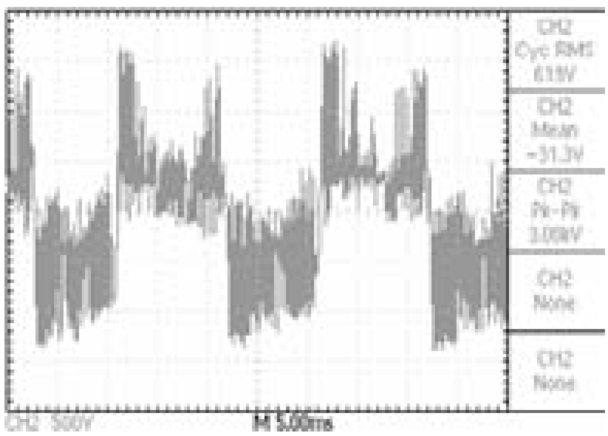

Rys. 4. Przebieg napięcia w obwodzie zapłonowym zasilacza.

Podatna (miękka) charakterystyka zewnętrzna obwodu zapłonowego zasilacza (rys. 5) zapewnia pewny zapłon wyładowania przy równoczesny zabezpieczeniu przed przeciążeniem prądowym oraz termicznym systemu zapłonowego reaktora. Natomiast poprzez kształtowanie uzwojeń fazowych transformatora, tym samym wartości jego reaktancji rozproszenia, można wpływać na wartość prądu pobieranego przez wyładowanie. Wartość tego prądu decyduje o mocy, z jaką pracuje reaktor plazmowy oraz wpływa na parametry generowanej plazmy.

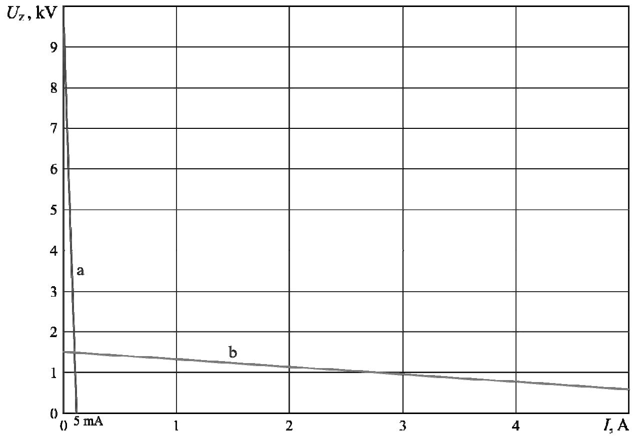

Rys. 5. Charakterystyki zewnętrzne: a – charakterystyka obwodu zasilania elektrody zapłonowej, b – charakterystyka obwodu zasilania elektrod roboczych.

Podsumowanie

Przeprowadzona badania eksperymentalne pozwoliły potwierdzić, wysoką sprawność transformatorów pięcio-kolumnowych z uzwojonymi kolumnami zewnętrznymi jako układów zasilania łukowych reaktorów plazmowych.

Zasilacze te nie wymagają specjalnej obsługi, są niewrażliwe na zakłócenia generowane przez łuk elektryczny [3] oraz wykazują możliwość pracy z różnymi gazami roboczymi, co w szczególności predestynuje je do zastosowań przemysłowych.

Literatura

[1] A. Czernichowski, Gliding arc. Application to engineering and environmental control. Pure Appl. Chem. 1994, 66, 1301-1310.

[2] Stryczewska H. D., Komarzyniec G., Diatczyk J., Janowski T.: Multi-electrode Gliding Arc Plasma Reactors Powered from Special Transformers, The 17th International Symposium on Plasma Chemistry, Toronto – Kanada, August 7th - 12th, 2005, str. CD

[3] Ph. G. Rutberg, A. A. Safronov, S. D. Popov, A. V. Surov, Gh. V. Nakonechny, Investigation of voltage and current variations in a multiphase AC electric arc system, 12th International Congress on Plasma Physics, 25-29 October, Nice (France) 2004

[4] Sikorski A. Ruszczyk A: Control of DC/AC inverter current to minimize the current error vector, 9th International Conference and Exhibition on Power Electronics and Motion Control, EPE-PEMC 2000, Kosice, Słowacja, 2000, s. 7.174-7.179

***Autorzy**: dr hab. inż. Henryka Danuta Stryczewska, h.stryczewska@pollub.pl,*

mgr inż. Grzegorz Komarzyniec, g.komarzyniec@pollub.pl,

mgr inż. Jarosław Diatczyk, j.diatczyk@pollub.pl,

Politechnika Lubelska, Instytut Podstaw Elektrotechniki i Elektrotechnologii, ul. Nadbystrzycka 38a, 20-618 Lublin

MEASURING POSITION TO ANALYSE THE ESD IMMUNITY OF ELECTRIC DEVICES

Paweł A. MAZUREK

Lublin University of Technology, Institute of Electrical Engineering and Electrotechnologies

***Abstract**. Measuring position to analyse the electrostatic discharge immunity of electric devices was created in IPEE Institute's labaratory. The electrostatic discharge phenomenon is becoming an increasingly important concern with today's integrated circuit technology. Basic information about the phenomenon of ESD and typical ESD tests are described in this article.*

***Streszczenie.** Artykuł prezentuje zagadnienia dotyczące badań odporności elektromagnetycznej realizowanych w ramach określania kompatybilności elektromagnetycznej urządzeń. W modernizowanym laboratorium kompatybilności elektromagnetycznej Instytutu IPEE utworzono stanowisko do testów na zaburzenia elektrostatyczne. System pomiarowy realizowany jest pod normę EN61000-4-2. (**Stanowisko do badania odporności elektromagnetycznej urządzeń elektrycznych**)*

Keywords: EMC, ESD, electromagnetic immunity. EMC test system.
Słowa kluczowe: kompatybilność elektromagnetyczna, wyładowania elektrostatyczne, odporność elektromagnetyczna, laboratorium EMC.

Introduction

The age of electronics brought with it new problems associated with static electricity and electrostatic discharge. And, as electronic devices became faster and smaller, their sensitivity to ESD increased. Today, ESD impacts productivity and product reliability in virtually every aspect of today's electronics environment [4].

Electrostatic discharge can change the electrical characteristics of a semiconductor device, degrading or destroying it. Electrostatic discharge also may upset the normal operation of an electronic system, causing equipment malfunction or failure. Controlling electrostatic discharge begins with understanding how electrostatic charge occurs in the first place. Electrostatic charge is most commonly created by the contact and separation of two materials [1,2,3,4,5].

International Standards and European Union's EMC Directive relates to the immunity requirements and test methods for electrical and electronic equipment subjected to static electricity discharges, from operators directly, and to adjacent objects.

Electromagnetic immunity is the ability of a device, equipment or system to perform without degradation in the presence of electromagnetic disturbances. Electromagnetic susceptibility is the inability to perform without degradation, i.e. susceptibility is the lack of immunity. The aim of basic immunity standards is to provide test procedures and test levels to verify electromagnetic immunity.

The IPEE Institute received the grant on the modernization of the existing laboratory of electromagnetic compatibility. The modern laboratory test-system was created to the analysis of the electromagnetic immunity, in this to tests ESD.

ESD

Electrostatic Discharge (ESD) is a common phenomenon in the nature: its name comes from the fact that different materials can carry static positive or negative charges resulting into a built-in static voltage. The amount of this static charge depends on the triboelectric characteristics of the material and from external parameters like the relative humidity. But once the statically charged material is put in contact with a grounded object, charge balance will be restored through a discharge of the charged material towards the ground. In spite of the phenomenon's name the discharge is extremely fast, in the order of some tens of nanoseconds. A human body has a typical capacitance of about 100pF and a contact resistance of about 1.5K: with these characteristics, an electrostatic potential of several KV's (depending on the environmental conditions) may mean current up to several amperes [1,2].

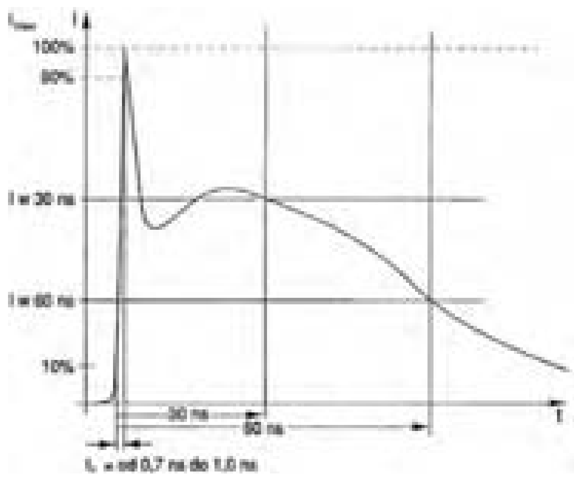

Fig. 1. Typical waveforms of the discharge current in an ESD event

Typical risetimes are of order 200 ps–70 ns, with a total duration of around 100 ns– 2 ms [ ]. The peak current levels may approach tens of amperes for a voltage difference of 10 kV. This indicates that the spectral content of the arc may have large amplitudes, and can extend well into the GHz frequency range.

Measuring position

The test set-ups for these tests are not difficult to achieve in a typical manufacturing company, as they don't need special test chambers or open area sites, at the most just an area of ground plane and a wooden table.

The basic setup is shown in Figure 2. On the laboratory floor is a metallic Ground Plane (GP) that is electrically tied to the building ground of the laboratory. A wood table is placed on the Ground Plane. On top of the table is a metallic Horizontal Coupling Plane (HCP) covered by a 0.5mm thick insulator. The HCP is connected to the GP through a pair of 470kΩ resistors in series, one close to the GP and one close to the HCP. To prevent interference from the surrounding environment, the test setup must be kept away from other equipment and objects such as metal walls.

Fig. 2: Measurement position for ESD testing (specified by IEC 61000-4-2)

The Human Body Model is the oldest and most commonly used model for classifying device sensitivity to ESD. The HBM testing model represents the discharge from the fingertip of a standing individual delivered to the device [1].

The ESD simulator used for testing to EN 61000-4-2 is based upon the 150pF/330 Ohms human body model, and generates a waveform with a risetime of between 700ps and 1ns to reach a peak of several kV, which then decays to about 50% in 50ns. At a voltage of 8kV the peak current into a 50 Ohms calibration load is close to 20A. The frequency content of such an ESD waveform is flat to around 300MHz before it begins to roll off, so contains significant energy at 1GHz and above [2,3].

Fig. 3: The ESD generator – NSG435 (TESEQ)

Testing to EN61000-4-2 (personnel discharge) involves the following [5]:

- Air discharges of up to ±8kV (using an 8mm round tip to simulate a human finger) are applied to everything non-metallic which is normally accessible to the operator.
- Contact discharges of up to ±4kV (using a sharp tip which is touched against the product before the discharge) are applied to operator-accessible metal parts - and also to nearby vertical and horizontal metal planes. Test voltages are increased gradually from low values, often using the settings 25%, 50%, 75%, and then 100% of the test voltage. The highest test level on an ESD test is not necessarily the one most likely to cause a failure (this is also true for other types of transients).

Test verification

The ESD test aims to simulate the effects of discharges from the fingers of personnel, either directly or via keys or other metal objects held in the hand, the personnel having been charged to a high voltage by tribo-electric charging, usually due to rubbing contacts between their shoes or clothing and dissimilar materials used for flooring, storage.

The Equipment Under Test (EUT) is placed on the insulator away from the edges of the insulator and HCP. If the unit is mains powered, it is plugged into the building power in a situation close to use condition. If it is battery–powered, there is no explicit ground connection.

When the environment for the EUT has been established, the actual stress to the system must be defined. There are two types of stress, air discharge and contact discharge (each with two subsets). Contact discharge is the preferred test method. Air discharges shall be used where contact discharge cannot be applied. The voltages are different for each method due to the differing methods of test.

The IEC standard calls for 10 discharges at each test point for both positive and negative stresses [5]. The preferential range of test levels for the ESD test is given in polish and international standards (in full article will presented). The results of tests are classified in terms of the loss of function or degradation of performance of the equipment under test.

Summary

ESD is a very pervasive problem today. In the laboratory of Institute of Electrical Engineering and Electrotechnologies the electromagnetic immunity system test was created. Laboratory can test in accordance with virtually all applicable international EMC standards.

ESD tests are intended to simulate real world events, with different test standards intended to cover different situations. There is modern generator ESD in the EMC laboratory. Generator is intended to simulate a person becoming charged and discharging from a bare finger to ground through the circuit under test.

The full article will introduce the current waveforms for system level ESD testing, the test setup, the types of stresses and how to interpret measurements values.

REFERENCES

[1] Montrose M., Nakauchi E, Testing for EMC compilance, *IEEE PRESS*, 2004

[2] Williams T, Armstrong K., EMC for Systems and Installations, Newnews, 2000

[3] Kodali P., Engineering Electromagnetic Compatibility, *IEEE PRESS,* 2001

[4] Mazurek P. A., *Wpływ właściwości materiałów magnetycznych rdzeni dławików przeciwzakłóceniowych na skuteczność filtrowania zakłóceń przewodzonych*, PHD thesis, Lublin University of Technology, 2007

[5] International standards IEC 61000-4-2.

Author*: dr inż. Paweł A. Mazurek, Politechnika Lubelska, Instytut Podstaw Elektrotechniki i Elektrotechnologii, ul. Nadbystrzycka 38a, 20-618 Lublin, E-mail:* p.mazurek@pollub.pl.

ELECTROMAGNETIC IMMUNITY TEST SYSTEM

Paweł A. MAZUREK

Lublin University of Technology, Institute of Electrical Engineering and Electrotechnologies

***Abstract**. The electromagnetic immunity test system are designed to perform radiated and conducted immunity tests according to the IEC 1000-4-xx standards. The author presents informations about immunity tests. This tests are performed to determine a product's susceptibility when exposed to a high RF field or conducted disturbances.*

***Streszczenie.** Artykuł prezentuje zagadnienia dotyczące badań odporności elektromagnetycznej urządzeń w laboratorium Instytutu IPEE. W utworzonym zintegrowanym stanowisku możliwa jest realizacja badań w zakresie oddziaływań ESD, Burst, Surge, PQT i pól magnetycznych.*

Keywords: immunity test, EMC, Burst, Surge, magnetic field.
Słowa kluczowe: badania odporności elektromagnetycznej, kompatybilność elektromagnetyczna, zaburzenia elektromagnetyczne.

Introduction

All electrical and electronic equipment should be assessed against the essential requirements of the European EMC (Electromagnetic Compatibility) Directive as part of the process necessary to affix the CE marking. Most manufacturers will carry out a practical EMC assessment on their equipment either by using their own test facilities or using a third party accredited laboratory.

Electromagnetic immunity is the ability of a device, equipment or system to perform without degradation in the presence of electromagnetic disturbances. Electromagnetic susceptibility is the inability to perform without degradation, i.e. susceptibility is the lack of immunity. The aim of basic immunity standards is to provide test procedures and test levels to verify electromagnetic immunity.

Both conducted and radiated phenomena are considered. The results of tests are classified in terms of the loss of function or degradation of performance of the equipment under test.

The Institute IEEE modernizes the EMC laboratory since several years. The government grant was received the last year. The modern apparatus was bought and the measuring position to immunity tests was created. In this article author presents basic information about immunity test and about first tests on measuring position.

Test system

The immunity tests are performed to determine a product's susceptibility when exposed to a high RF field or conducted disturbances. Immunity/Susceptibility tests are performed in accordance with countries and government agencies requirements to determine if the product continues to perform properly when subjected to various electromagnetic compatibility (EMC) upsets and fields.

The immunity system in IEEE's laboratory uses:

- Modula (Schaffner) - multifunction generator for immunity testing in accordance with the IEC/EN 61000-4-x series. With burst generator EFT 6501, surge generator SRG 6501, power quality tester PQT 6501
- VAR 6501 - manual/automatic variable transformer
- INA 6501 - manual/automatic step transformer
- MFO 6501 - manual/automatic power line frequency magnetic field generator
- INA 701 - magnetic field antenna
- CDN 8014 - capacitive coupling clamp for data line testing with burst generators.
- CDN 117 - data line coupling network for surge pulses.

Modula represents the latest technology for pulse generators and systems intended for investigating the immunity of products to electromagnetic interference. Modula is the most convenient multifunction generator to simulate electromagnetic interference effects for immunity testing in conformity with international, national and in-house standards including the new IEC/EN standard. Generator Modula generation the classic interference pulses such as Burst and Surge as well as Power Quality simulations.

WIN Modula is a comprehensive test software package that features a library of pre-programmed test routines to meet relevant standards and allows the creation of custom test suites. WIN Modula prepares test reports automatically, including EUT reactions, if the electrical monitoring facility is used.

That immunity test system is able to ensure compliance for electric and electronic equipment by measuring across a wide range of tests, including: radiated immunity, EFT/Burst immunity, surge immunity, conducted immunity, magnetic field immunity and voltage dips/interruptions

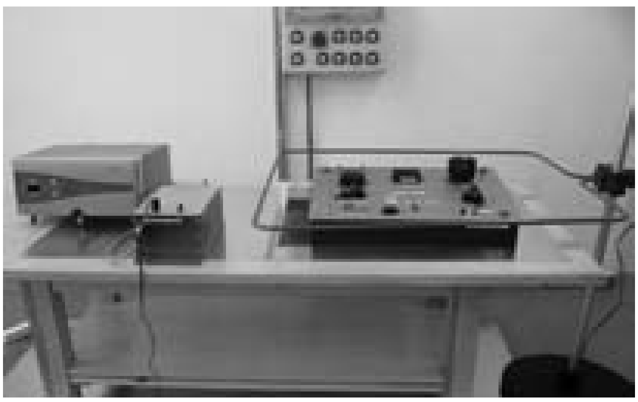

Fig.1. Immunity test system in IPEE labaratory
(Modula generator in left side)

Fig.2. Measuring position with capacitive coupling clamp

Radiated Immunity
The radiated immunity test is applicable to all products, where radio frequency fields are present. The test is performed by applying an electromagnetic far field of defined strength while varying the frequency in the range 80...1000 MHz. The EMC standard (EN61000-4-3) gives the field strength of the unmodulated signal. For testing, this signal is 80% amplitude modulated with a 1 kHz sinewave.

EFT/Burst Immunity
The fast transients test is applicable to products which are connected to AC or DC power systems or have cables in close proximity to such sources. It is intended to demonstrate immunity to transient disturbances such as those originating from switching transients. The waveform of a single transient is characterized by a rise time of 5 ns, a time to half-value of 50 ns and a maximum energy of 4 mJ at 2 kV into a 50 W load. The impedance of the transient source is 50 W. The repetition frequency of the transients is a function of the test level. Burst duration is 15 ms and burst period 300 ms. Coupling is performed via a coupling/decoupling network with coupling capacitors for power supply ports and via a capacitive coupling clamp with a capacitance of 50...200 pF for signal, data and control ports.

Surge Immunity
Surges are mainly generated by switching transients or by lightning strokes injecting high currents producing voltages or inducing high voltages/currents via electromagnetic fields. Switching transients can be generated by power system switching, load changes, short circuits or arcing faults to the earthing system of the installation. The surge immunity test is applicable to products, which are connected to mains supplies or other networks leaving the building. It is intended to demonstrate immunity to surge voltages caused by switching and lightning effects. The standard EN61000-4-5 specifies two different open-circuit surge waveforms.

Conducted Immunity
The source of conducted disturbances is basically an electromagnetic field, emamating from RF transmitters, that may act on the whole length of cables connected to installed equipment. The in-going and out-going leads behave as passive antenna networks if they are several wavelengths long. The conducted immunity test is applicable to products operating in environments where radio frequency fields are present and which are connected to mains supplies or other networks (signal or control lines). This test is a supplement to IEC/EN 61000-4-3 which defines test methods for immunity to radiated electromagnetic energy. The test is performed by applying a voltage of a defined value to the port to be tested while varying the frequency in the range 150 kHz...80 MHz. The signal is 80% amplitude modulated with a 1 kHz sinewave. The waveform is coupled to each of the n lines of the port to be tested (common mode).

Magnetic Field Immunity
The power frequency magnetic field is mainly generated by power frequency currents in conductors. In general this test is limited to products which are susceptible to magnetic fields (e.g. hall effect devices, CRTs and special products to be installed in high magnetic field environments). It has no relevance to power supplies. The test is performed by applying a 50 or 60 Hz magnetic field of a defined strength to the equipment to be tested (EN61000-4-8).
Pulse magnetic fields are generated by lightning strokes on buildings and metal structures including aerial masts, earth conductors and earth networks and by initial fault transients in low voltage, medium voltage and high voltage systems. This test is mainly applicable to products to be installed in electrical power plants (e.g. telecontrol centres in close proximity to switchgear). It is not relevant for distribution network equipment. The test is performed by applying 6.4/16 ms magnetic field pulses of defined strength to the equipment to be tested.

Voltage Dips/Interruptions
Voltage dips and short interruptions are caused by faults in the network or in installations or by a sudden large change of load. Voltage variations are caused by the continuously varying loads connected to the network. These tests are applicable to equipment connected to AC mains with rated input currents not exceeding 16 A per phase. The test for immunity to voltage dips and short interruptions is performed by an abrupt change of the supply voltage of the equipment under test at any phase angle on the mains voltage at the lower and at the upper voltage of the nominal voltage range. For power supplies, immunity to these phenomenon can normally be derived from the specifications of input voltage range and hold-up time.

REFERENCES

[1] Montrose M., Nakauchi E, Testing for EMC compilance, *IEEE PRESS*, 2004
[2] Williams T, Armstrong K., EMC for Systems and Installations, Newnews, 2000
[3] Kodali P., Engineering Electromagnetic Compatibility, *IEEE PRESS,* 2001
[4] Mazurek P. A., Wpływ właściwości materiałów magnetycznych rdzeni dławików przeciwzakłóceniowych na skuteczność filtrowania zakłóceń przewodzonych, PHD thesis, Lublin University of Technology, 2007
[5] International standards IEC 61000-4-1 to 61000-4-12.
[6] Armstrong K., Clough C., Williams T., EMC Testing Part 1-6, www.compliance-club.com
[7] *Directives & Standards Technical Information EMC* Edition 3/5.98/CD 1.98 - © Melcher AG

***Author**: dr inż. Paweł Mazurek, Politechnika Lubelska, Instytut Podsatw Elektrotechniki i Elektrotechnologii, ul. Nadbystrzycka 38a, 20-618 Lublin, E-mail:* p.mazurek@pollub.pl;

Conference **ELMECO-6**
ELECTROMAGNETIC DEVICES AND PROCESSES IN ENVIRONMENT PROTECTION
joint with
9th Seminar APPLICATIONS OF SUPERCONDUCTORS **AoS-9**
June 24 – 27, 2008 Nałęczów, Poland

INFLUENCE OF NONWOVEN STRUCTURES ON SURFACE RESISTIVITY OF PLASMA TITANIUM FILMS

Jan ZIAJA[1], Joanna KOPROWSKA[2], Paweł ŻYŁKA[1]

Wroclaw University of Technology (1), Textile Research Institute, Łódź (2)

Abstract. *Titanium thin films were obtained by standard magnetron sputtering process. Films have been deposited on nonwoven fabric substrates made of PEC, VIS+PEC and PP and characterized by different basis weight. It was found out that the type and basis weight of the nonwoven fabrics has a considerable influence of on the surface resistivity ρ_s of titanium films. The observed values of ρ_s varied from 130 Ω to 150 MΩ.*

Streszczenie. *Cienkie warstwy tytanu otrzymane zostały w standardowym procesie rozpylania magnetronowego. Warstwy nanoszono na podłoża z włókniny PEC, VIS+PEC oraz PP o różnej gramaturze. Stwierdzono, iż rodzaj materiału włókniny oraz jej gramatura mają znaczny wpływ na rezystywność powierzchniową ρ_s tak otrzymywanych cienkich warstw tytanu. Uzyskano zakres zmienności wartości ρ_s od 130 Ω do 150MΩ.*

Keywords: magnetron sputtering, electromagnetic field, surface resistivity.
Słowa kluczowe: rozpylania magnetronowe, PEM, rezystywność powierzchniowa.

1. Introduction

A considerable increase in number of electromagnetic field (EMF) sources (including radio broadcasting, television, radio-communication and cellular telephony) has been observed during last decade. Not only the frequency range has broadened but also the power emitted by EFM sources has increased. Therefore, protection of various compartments (e.g. in banks, hospitals or database server rooms) against external EFM-induced perturbations or unauthorized remote data access ("data leakage") becomes necessary. Lightweight and low-cost textile products may become one of means for a human being or sensitive equipment protection against adverse effects of EMF radiation. EMF shielding effectiveness of the order of 70 dB was demonstrated in earlier works [1] related to deposition of Zn, Zn-Bi and indium thin films on polypropylene (PP) nonwoven fabrics. Therefore, development of novel metallization methods for nonwoven fabrics is well-founded.

Metallization of some textile products manufactured of polymeric materials like PP or polytetrafluoroethylene (PTFE), due to its surface properties, is tremendously difficult. Classical thin metallic film deposition methods (vacuum physical vapor deposition PVD, electron beam physical vapor deposition EBPVD or metalorganic chemical vapor deposition MOCVD) do not prove true in case of those specific polymers. Deposited films have very poor adhesion and are easily worn off. The only way to metalize those polymeric materials is to combine surface plasma activation and a subsequent metallization by PVD, EBPVD or MOCVD. Yet it is a two-step process.

Pulsed magnetron plasma sputtering (PMS) method comprises both steps itself. It is a rapid and environmentally friendly process. It makes possible deposition of metallic, semiconducting or dielectric thin films. The deposition rate is much higher than obtained in case of cathode sputtering; for metals it is of the order of µm/min and for oxide layers it is in the range from 40 to 600 nm/min [2, 3 and 4]. Very good adhesion of deposited films is an additional advantage of PMS method.

EMF shielding effectiveness of metalized nonwoven fabrics depends on the resistivity of deposited metallic layers, the latter being strongly related to magnetron sputtering process parameters and the substrate properties. The work presents influence of nonwoven fabric substrate morphology and magnetron-supply group frequency f_g on the surface resistivity of Ti thin films deposited by PMS method.

2. Experiment

Titanium thin films have been deposited on selected nonwoven fabrics by PMS sputtering of metallic Ti target (of 99.999 purity) in argon atmosphere at Ar pressure of $p_{Ar} = 2*10^{-2}$ Tr. Magnetron sputterer was supplied from an impulse current source of maximal power P = 16 kW and maximal voltage U = 1.2 kV. The current source have capacity for supplying plasma sputterer with either modulated bipolar (AC-M) current at frequency f = 80 kHz or biased unipolar (DC-M) current at f = 160 kHz (Fig. 1). In both cases the current train may be group-modulated by rectangular signals of frequency fg ranging from 100 Hz to 5 kHz. Sputtered material is accumulated in plasma region during t_1 time period and is then deposited on a substrate during t_2-t_1 time period. Value of t_1/t_2 ratio influences structural and electrical properties of deposited films and is characteristic for a given material. The impact is strongly evident in case of reactive processes.

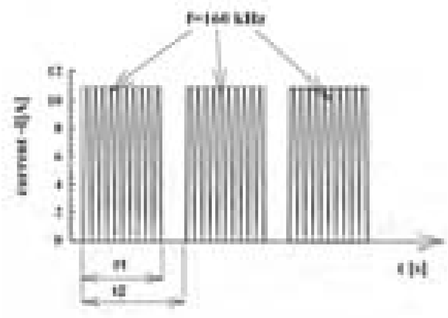

Fig 1. Rectangular modulated discharge current pulse in DC bias mode DC-M (t_1 is the sputtering time)

3. Result

Titanium thin films were deposited on nonwoven PP fabrics of 60 g/m2 and 150 g/m^2 basis weight as well as on VISC30+PES70 nonwoven fabric composed of 30% of viscose (VISC) and 70% of polyester (PES) having basis weight 70 g/m^2. Cross-section of the samples was visually examined at 300x optical magnification in order to determine structure of the fabricated films.

Fig. 2 presents photographs of nonwoven fabric surface before plasma processing and after Ti sputtering metallization. VIS30+PES70 nonwoven fabric is characterized by a non-uniform, broadly developed surface with distinct fibers. Influence of the basis weight on nonwoven fabric morphology is also evident in case of PP nonwoven fabric. PP samples of 60 g/m^2 have still visible single fibers and the most homogenous surface is found in case of 150 g/m^2 PP samples.

Microscopic investigations revealed that the deposited Ti layers are not uniform. It is likely to be related to penetration of deposited metal into free spaces between fibers. Metallic layers have not much cracks and delaminations and their adhesion to the polymeric substrate is very good. In case of PP nonwoven fabric substrates Ti film is also formed in regions between splices. Increase in basis weight results in formation of more monolithic and homogenous metallic layers. For VISC+PES substrates titanium thin film is not continuous and has a grayish tint.

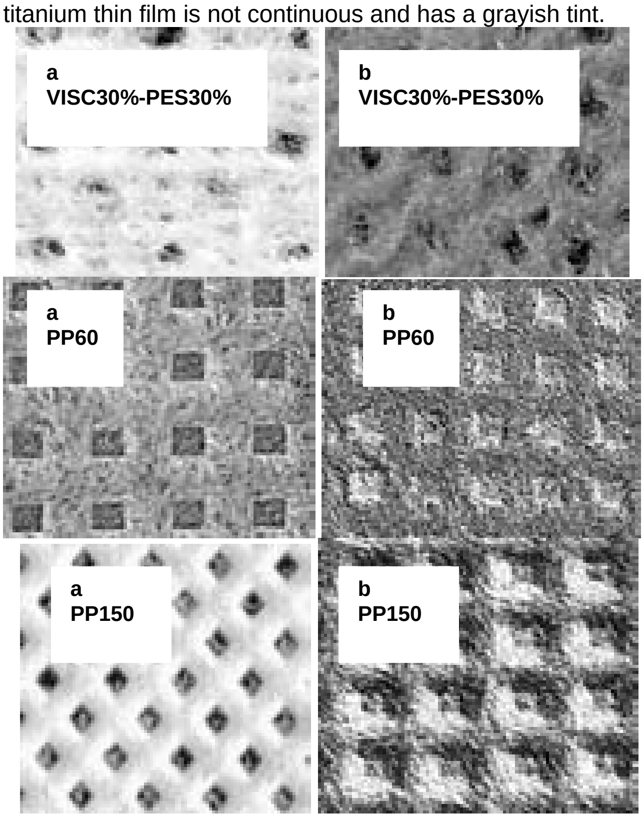

Fig. 2. Nonwoven fabrics surface: a – before processing, b – after Ti sputtering metallization

Surface resistivity ρ_s measurements were performed according to PN- 91/P-04871 test standard at relative humidity RH = 50 ± 5 % and temperature T = 23 ± 2 °C. It was determined that the surface resistivity value depends on basis weight of the substrate fabric. 150 g/m^2 PP nonwoven fabrics are characterized by the lowest ρ_s values in the range of 10^3 Ω (Fig. 3). This value is relatively high and results from expanded surface morphology of the fabric and presence of numerous resistive bridges although a magnified image of the cross-section suggests uniform continuity of the metallic covering. In case of 60 g/m^2 PP nonwovens an order of magnitude higher ρ_s is observed. The highest resistivity values were recorded for VISC30+PES70 fabric substrates, in which ρ_s exceeds 10^7 Ω. Such elevated values of ρ_s result from the lack of continuity of the metallic layer.

It was also observed that ρ_s values undergo a slight increase together with the raise in the magnetron power supply group frequency (Table 1). It is a consequence of a prolonged sputtering time t_1 and thus extended period of time spent by the substrate in active plasma region. It may possibly lead to a chemical decomposition of the polymeric substrate at elevated temperature. By-products given off in this process may then react with titanium layer and alter its electrical properties.

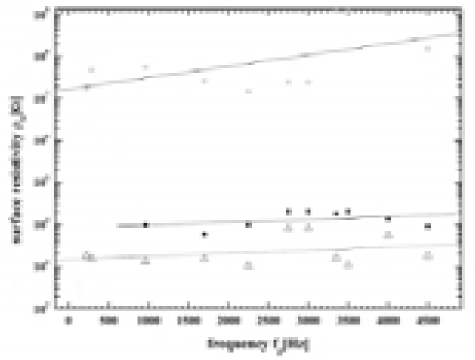

Table 1. Influence of group frequency f_g on surface resistivity ρ_s of Ti thin films: I – plasma current, t_1 – pulse packet duration time, argon pressure p_{Ar} =2*10^{-2} Tr, power released on the target P=1 kW, sputtering time t=10 min.

4. Conclusion

Metallization of PP nonwoven fabrics by PMS method guarantees that the titanium thin film coverings are characterized by excellent adhesion, impossible to achieve in other metallization techniques. EMF shielding effectiveness factor determined for double-sided metalized 150 g/m^2 PP nonwoven fabrics exceeds 60 dB which gives ground for application of this composite textile material in shielding of hospital rooms.

Acknowledgments

This research work was carried out in the framework of the statutory research grant no. 341701.

References

[1] Ziaja J., Koprowska J. Janukiewicz J., The use of plasma metallization in the manufacture of textile screens for protection against electromagnetic fields, paper accepted for publication in *FIBRES & TEXTILES in Eastern Europe.*
[2] Ziaja J., ZnO Thin Film Deposition With Pulsed Magnetron Sputtering, *Przegląd Elektrotechniczny.*
[3] Ziaja Jan, Mielcarek W,: Mikrostruktura i skład fazowy plazmowych warstw ZnO. W: Postępy w elektrotechnologii. VI Konferencja naukowa. Jamrozowa Polana, 20-22 września 2006. Prace Naukowe Instytutu Podstaw Elektrotechniki i Elektrotechnologii Politechniki Wrocławskiej; nr 44, Konferencje, nr 18, s. 186-188.
[4] Mista W., Ziaja J., Gubański A., Varistors perfomance of nanocrystaline Zn-Bi-O thin films prepared by RF magnetron sputtering, *Vaccum,* vol. 74, 2004, pp. 293-296

***Authors**: dr inż. Jan Ziaja, Politechnika Wrocławska, Instytut Podstaw Elektrotechniki i Elektrotechnologii, ul. Wybrzeże Wyspiańskiego 27, 50-370 Wrocław E-mail: jan.ziaja@pwr.wroc.pl.; mgr Joanna Koprowska, Instytut Włókiennictwa, ul. Brzezińska 5/15 , 92-103 Łódź, E-mail joanna.koprowska@mail.iw.lodz.pl.; dr inż. Paweł Żyłka, Politechnika Wrocławska, Instytut Podstaw Elektrotechniki i Elektrotechnologii, ul. Wybrzeże Wyspiańskiego 27, 50-370 Wrocław E-mail: pawel.zylka@pwr.wroc.pl.;*

The Corresponding Author address:
jan.ziaja@pwr.wroc.pl

Conference **ELMECO-6**
ELECTROMAGNETIC DEVICES AND PROCESSES IN ENVIRONMENT PROTECTION
joint with
9th Seminar APPLICATIONS OF SUPERCONDUCTORS **AoS-9**
June 24 – 27, 2008 Nałęczów, Poland

PRODUCTION OF HYDROGEN VIA METHANE CONVERSION USING MICROWAVE PLASMA SOURCE WITH CO_2 SWIRL

Mariusz JASIŃSKI[1], Mirosław DORS[1], Jerzy MIZERACZYK[1,2]

The Szewalski Institute of Fluid Flow Machinery (1), Gdynia Maritime University (2)

***Abstract**. In this paper, results of hydrogen production via methane conversion in the atmospheric pressure microwave plasma with CO_2 swirl are presented. A waveguide-based nozzleless cylinder-type microwave plasma source (MPS) with CO_2 swirl was used to convert methane into hydrogen. The plasma generation was stabilized by an additional CO_2 swirl having a flow rate of 50 l/min. The methane flow rate was 175 l/min. The absorbed microwave power was 3000 W. The hydrogen mass yield rate and the corresponding energetic hydrogen mass yield were 952 g[H_2]/h and 317 g [H_2] per kWh of microwave energy absorbed by the plasma, respectively. These parameters are better than our previous results when nitrogen was used as a swirl gas and much better than those typical for other plasma methods of hydrogen production (electron beam, gliding arc, plasmatron).*

***Streszczenie.** W artykule przedstawiono wyniki produkcji wodoru w procesie konwersji metanu pod wpływem plazmy mikrofalowej pod ciśnieniem atmosferycznym w atmosferze CO_2. Do badań wykorzystano generator o konstrukcji współosiowej z dodatkiem CO_2 w formie przepływu wirowego (50 l/min), który stabilizował plazmę. Natężenie przepływu metanu wynosiło 174 l/min. Absorbowana moc mikrofal wynosiła 3000 W. Uzyskana wydajność masowa i wydajność energetyczna produkcji wodoru wynosiły odpowiednio 952 g[H_2]/h i 317 g[H_2]/kWh. Wyniki te są lepsze od uzyskanych z zastosowaniem azotu w przepływie wirowym oraz innymi metodami plazmowymi (plazmotron, ślizgające się wyładowanie łukowe, strumień elektronów).*

Keywords: hydrogen production, methane reforming, microwave plasma.
Słowa kluczowe: produkcja wodoru, reforming metanu, plazma mikrofalowa.

Introduction

Recently developed microwave plasma sources (MPSs) operated at atmospheric pressure [1-6] seem to have a high potential for hydrogen production via hydrocarbon reforming. The microwave plasma at atmospheric pressure is one of the plasma techniques providing the electron temperature of 4000-10000 K, and the heavy particle temperature of 2000-6000 K [5, 6].

Our previous investigations in methane reforming to hydrogen [2] were carried out using methane (17.5-175 l min^{-1}) and nitrogen swirl (50-100 l min^{-1}) at relatively high absorbed microwave powers (3000-5000 W). The best conditions corresponded to the absorbed microwave power of 3000 W and methane flow rate of 175 l min^{-1}. Since the hydrogen production presented in [2] was carried out in the presence of nitrogen without any oxygen carriers, the main chemical reaction producing hydrogen was methane pyrolysis ($CH_4 \leftrightarrow C + 2\,H_2$).

Unfortunately, methane conversion rate was only 20%, which suggests that a lot of energy delivered to the plasma was lost. In order to use more of the energy delivered to the MPS for methane conversion we propose to replace nitrogen with CO_2. Since thermal conductivity of CO_2 is 1.6 times lower than nitrogen we expected lower heat loses and consequently higher methane conversion rate.

Experimental set-up

The main parts of the experimental setup used in this investigation were: a microwave generator (magnetron), microwave plasma source (MPS), microwave supplying and measuring system, and gas supplying system (Fig. 1). The microwave power (2.45 GHz, 6 kW) was supplied from the magnetron to the MPS via a rectangular waveguide (WR-430) having a reduced-height section.

The absorbed microwave power P_A (3 kW), i.e. microwave power delivered to the discharge was calculated as P_I - P_R, where P_I and P_R are the incident and reflected microwave powers, respectively. The incident and reflected microwave powers P_I and P_R were directly measured using directional coupler equipped with bolometric heads and HP power meters (Fig. 1).

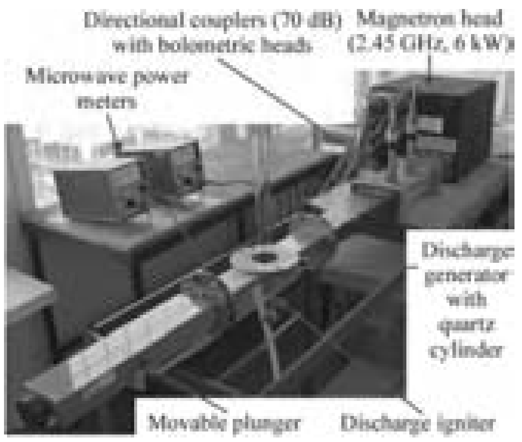

Fig.1. Photo of the experimental setup with the waveguide-based nozzleless cylinder-type MPS.

For hydrogen production via methane reforming we used the same waveguide-based nozzleless cylinder-type MPS as in our previous work [2]. The processed methane (175 l/min) was introduced to the plasma by the central duct of MPS. The plasma generation was stabilized by an additional flow of CO_2 (50 l/min) in the form of a swirl that concentrated near the quartz cylinder wall. The CO_2 swirl held the discharge in the centre of the cylinder and thus protected the cylinder wall from overheating. The inner diameter of the used quartz discharge tube was 26 mm**.**

Diagnostics of the working gas composition before and after the microwave plasma processing of methane was carried out using gas chromatograph (SRI 8610C) and Fourier Transform Infrared spectrophotometer (Perkin

Elmer 16 PC). Production of hydrogen was calculated from methane and its conversion products mass balance.

Results

Diagnostics of working gas mixture composition after the microwave plasma processing showed that unprocessed methane CH_4, CO_2, CO and acetylene C_2H_2 were found as by-products. The methane decomposed to hydrogen H_2, acetylene C_2H_2 and carbon (soot). The soot deposit could be easily noticed on the reactor walls. The soot deposition started just after plasma ignition, however not all soot deposited on the reactor walls. Major part of the soot was blown off the reactor by the high gas flow. As a result, the thickness of the soot layer deposited on the reactor walls has not exceeded 2 mm and did not influence the reactor lifetime.

Concentration of H_2, C_2H_2 and CO in the exit gas were 59.8%, 0.8% and 0.9%, respectively. The total methane decomposition degree $[(CH_4)_{conv} / (CH_4)_{tot} \times 100\ \%]$ was 58.5%, where $(CH_4)_{tot}$ is the total (initial) mass of CH_4, and $(CH_4)_{conv}$ is the converted mass of CH_4. The hydrogen conversion selectivity $[H_2 / (2CH_4)_{conv} \times 100\ \%]$ was 93.7%.

The energetic parameters of the hydrogen production via the methane reforming, i.e. the hydrogen mass yield rate and energetic hydrogen mass yield were 952 g$[H_2]$ h^{-1} and 317 g$[H_2]$ per kWh of microwave energy absorbed by the plasma, respectively. In our experiment, the plug efficiency of the microwave magnetron generator was higher than 66 %, so taking into account this efficiency, the energetic hydrogen mass yield is 210 g$[H_2]$ per kWh of electrical energy used.

Comparison of the energetic hydrogen mass yields for different methods in which electric energy is directly used for methane conversion into hydrogen, is given in Table 1.

Table 1. Comparison of the energetic hydrogen mass yields for different methods in which electric energy is directly used for methane conversion into hydrogen.

Hydrogen production method	Initial composition	Energetic mass yield [g $[H_2]$ kWh^{-1}]
CONVENTIONAL METHODS		
Water electrolysis [7]	H_2O	21
PLASMA METHODS		
Waveguide-based cylinder-type MPS (our result)	$CH_4 + CO_2$	210*
Electron beam [8]	$CH_4 + H_2O$	3.6
Dielectric barrier discharge [9]	CH_4 + air	6.7
Gliding arc [10]	$CH_4 + H_2O$ + air	40
Plasmatron with catalyst [11]	$CH_4 + H_2O$ + air	225

* total electric energy used

It must be pointed out that the energetic hydrogen mass yields shown in Table 1 take into account only the electrical energy used in the reforming (in some cases it is not clear either the total electric energy used or absorbed by the plasma is considered). In the plasma methods presented in Table 1, the energy equivalent of methane used in the reforming was not considered.

It is seen from Table 1 that the plasma methods (except the electron beam [9] and dielectric barrier discharge [13]) exhibit higher energetic hydrogen mass yield than the conventional water electrolysis [29]. However, when the energy equivalent of methane used in the conversion is taken into account, the energetic hydrogen mass yields for the plasmatron with catalyst [2] and our method, which exhibit the highest yields, are comparable with that of the conventional water electrolysis.

Considering both the cost of methane and the total energy consumption (including losses in power supplies), nowadays, among the hydrogen production methods, it seems that the conventional steam reforming of methane [28] ensures the lowest cost of hydrogen production. However, the conventional steam reforming of methane is a large volume hydrogen production method. When the distributed hydrogen production method are considered, the microwave plasma method presented in this paper seems to be attractive.

Conclusions

The results of this investigations show that the energetic parameters of the hydrogen production, i.e. the hydrogen mass yield rate (952 g$[H_2]$ h^{-1}) and the energetic hydrogen mass yield (317 g$[H_2]$ kWh^{-1}), via methane reforming in the atmospheric pressure microwave plasma are attractive.

Taking into account the energy losses in the microwave power supply (~33 %), the energetic hydrogen mass yield reaches about 210 g$[H_2]$ per kWh of the total electric energy used.

The proposed atmospheric pressure microwave plasma system for hydrogen production via methane reforming is expected to be of low cost and effective, and thus promising for applications in the distributed hydrogen production.

This research was supported by the Ministry of Science and Higher Education (MNiSW) under the programme 3020/T02/2006/31.

REFERENCES

[1] Deminsky M., Jivotov V., Potapkin B., Rusanov V., *Pure and Applied Chemistry*, 74 (2002) 413-418

[2] Jasiński M., Dors M., Mizeraczyk J., *Journal of Power Sources*, 181 (2008), 41-45

[3] Moisan M., Sauve G., Zakrzewski Z., Hubert J., *Plasma Sources Sci. Technol.*, 3 (1994) 584

[4] Moisan M., Zakrzewski Z., Rostaining J.C.. *Plasma Sources Sci. Technol.*, 10 (2001) 387

[5] Green K.M., Borras M.C., Woskow P.P., Flores G.J., Hadidi K., Thomas P., *IEEE Trans. Plasma Sci.*, 29 (2001) 399

[6] Uhm H.S., Hong Y.C., Shin D.H., *Plasma Sources Sci. Technol.*, 15 (2006) S26

[7]http://www.loim.vrn.ru/index.php?m=63&page=58&nm=74&p=.2. 3.56.64.70. 71.72.73. 74

[8] Kappes T., Schiene W., Hammer T., *Proc. 8th Int. Symp. on High Pressure Low Temperature Plasma Chemistry*, Puhajarve, Estonia (2002) 196-200

[9] Heintze M., Pietruszka B., *Catal. Today*, 89 (2004) 21-25

[10] Cormie J.M., Rusu I., *J. Phys. D: Appl. Phys.*, 34 (2001) 2798–2803

[11] Bromberg L., Cohn D.R., Rabinovich A., Alexeev N., Samokhin A., Ramprasad R., Tamhankar S., *Int. J. Hydrogen Energy*, 25 (2000) 1157-1161

Conference **ELMECO-6**
ELECTROMAGNETIC DEVICES AND PROCESSES IN ENVIRONMENT PROTECTION
joint with
9th Seminar APPLICATIONS OF SUPERCONDUCTORS **AoS-9**
June 24 – 27, 2008 Nałęczów, Poland

THE COMPARISON OF CRITICAL CURRENT DENSITY OF NbTi/Cu WIRES WITH MgB_2/Fe WIRES

Daniel GAJDA[1], Andrzej MORAWSKI[2], Andrzej ZALESKI[3]

[1]International Laboratory of High Magnetic Fields and Low Temperature
[2]Institute of High Pressure Physics, Polish Academy of Sciences
[3]Institute of Low Temperature and Structure Research Polish Academy of Sciences,

Abstract: In this paper we compare critical current density J_c wires NbTi/ Cu and MgB_2/ Fe. We show measurements of critical current I_c wires NbTi/Cu and MgB_2/Fe at a temperature of 4.2K. We describe advantages and disadvantages of the examined superconducting wires

***Streszczenie.**.W artykule zostaną porównane krytyczne gęstości prądów drutów wykonanych z NbTi/Cu z drutami wykonanymi z MgB2/Fe.*

Keywords: NbTi, MgB_2, critical current.
Słowa kluczowe: NbTi, MgB_2, prąd krytyczny.

Introduction

NbTi and MgB_2 belong to the group of superconductors of the second kind. The superconducting material NbTi was discovered in 1960s. It was constantly improved and researched by means of various methods. The main objective of the research was to obtain the high Jc. The wire NbTi is the most often used superconducting material in the world. Its main advantages are as follows: high critical current in a low magnetic field, resistance to mechanical stresses, large plasticity, and an easy method of preparation. However, this material also has some defects: it can work only in the liquid helium, a small critical temperature T_c, a high cost of wire components and a large resistance in a normal state 60μΩcm. As far as MgB_2 is concerned, it was discovered in 2001 by the group of prof. Akimitsu with Aoyoma Gakuino University in Tokyo. At present, this material is being intensly investigated and enhanced by many research groups in the world. The main objective of the research is to obtain the greatest J_c in the highest magnetic field. The superconducting material MgB_2 possesses various advantages such as: a high critical temperature, a high critical field B_{c2}, a low cost of material components, a low resistance in the normal state 0.4μΩcm, small anisotropy and relatively high critical current at a temperature of liquid hydrogen. Yet, MgB_2 also possesses some disadvantages: brittleness and large hardness. Another problem concerning this material is its components which react with the oxygen and lower the critical parameters of MgB_2.

The methods of MgB_2/Fe wires and NbTi wires preparation

Wires NbTi are received by means of annealing Nb and Ti at the temperature of about 750C. The height of temperature of annealing directly influences the αTi precipitations and this influences Jc. Then wire NbTi goes through: HE, drawing, rolling, pressure, ECAP and ECMAP. The superconducting material NbTi is placed on copper or iron shields. MgB_2 wires can be received by means of several methods: diffusive method, the layer technique, the PIT method, ex situ and in situ. In the next step the wire goes through drawing, rolling and cold rolling. Currently, the majority of MgB_2 wires have the iron shield. Nowadays, a lot of research is done in order to develop a technology that would allow to receive MgB_2 wire in a copper shield.

Factors influent on J_c wires MgB_2 and NbTi

The J_c in superconductive wires depends on several major factors such as: grains size, the boundary of grains, admixture, defects and the heat treatment method. As far as NbTi is concerned, the size of precipitations of phase α Ti and the proportional selection of Nb to Ti heavily influences J_c. The material MgB2 of the J_c mostly depends on the size of grains and the admixtures. J_c in wires NbTi and MgB_2 wires can be raised by means of radiation, pressure, and drawing.

The Measurements

The measurement I_c was made via four - probe resistive method in constant magnetic field. The research was done for several wires made of MgB_2 in an iron shield and for some wires made NbTi in a copper shield. All the measurements were made in the liquid helium temperature. The examined samples had a length of approximately 25 mm. I_c was determined according to the 1μV/cm criterion.

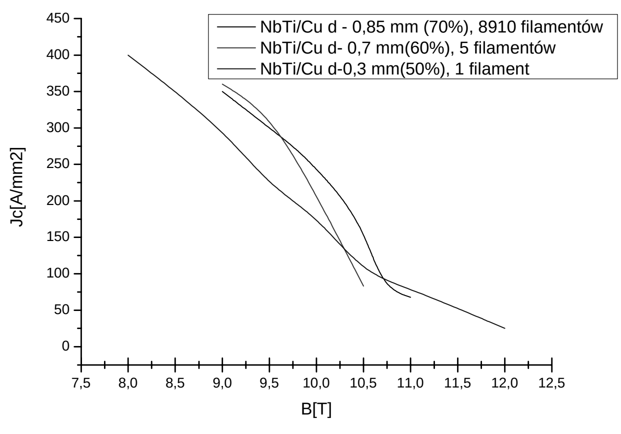

Fig.1. Jc vs magnetic field measured at 4.2K for NbTi wires

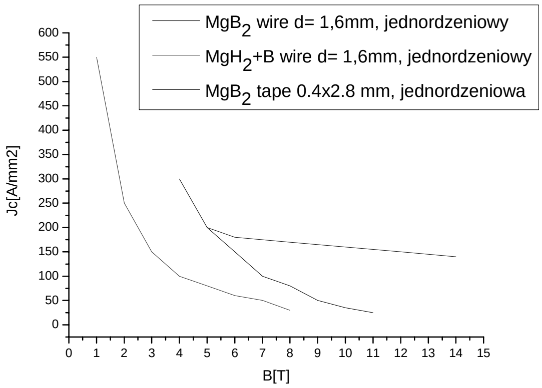

Fig.2. Jc vs magnetic field measured at 4.2K for MgB_2 wires and MgB_2 tape

Conclusions

The main advantage of wires performed with MgB_2 is the fact that they work at the liquid hydrogen temperature, in which J_c is about 10^3A/mm^2 when the magnetic field equals zero. The measurement performed for MgB_2 showed that I_c decreases very quickly with the increase of the magnetic field. This process can be diminished by doping the material MgB_2 with silicon and carbon. The small critical temperature of NbTi considerably lowers its usability and enlarges the operating costs in devices.

REFERENCES

[1] Flukiger R, Senatore C , Cesaretti M , Buta F, Uglietti D and Seeber B, *Optimization of Nb3Sn and MgB2 wires*, Supercond. Sci. Technol. 21 (2008) 054015 (8pp)

[2] Fujii H, Togano K and Ozawa K, *Effects of both addition and chemical treatment of SiC nanoparticles on the grain coupling and critical current density in ex situ processed MgB2 tapes*, Supercond. Sci. Technol. 21 (2008) 015002 (7pp)

[3] Matsushita T, Kiuchi M, Yamamoto A, Shimoyama J and Kishio K, *Essential factors for the critical current density in superconducting MgB2:connectivity and flux pinning by grain boundaries*, Supercond. Sci. Technol. 21 (2008) 015008, (7pp)

[4] Putti M, Vaglio R and Rowell J M., *Radiation effects on MgB2: a review and a Comparison with A15 superconductors*, Supercond. Sci. Technol. 21 (2008) 043001 (25pp)

[5] Stenvall A, Hiltunen I, Jarvel¨a J, Korpela A, Lehtonen J and Mikkonen R., *The effect of sample holder and current ramp rate on a conduction-cooled V –I measurement of MgB2*, , Supercond. Sci. Technol. 21 (2008) 065012 (6pp)

***Authors**:*

mgr inż.Daniel Gajda, International Laboratory of High Magnetic Fields and Low Temperature ,Gajowicka 95, 53-421 Wrocław, Poland,e-mail: dangajda@op.pl

dr Andrzej Morawski, Institute of High Pressure Physics, Polish Academy of Sciences,Sokołowska 29/37, 01-142 Warszawa. Poland , e-mail: amor@unipress.waw.pl

prof. Andrzej Zaleski· Institute of Low Temperature and Structure Research Polish Academy of Sciences, Okólna 2, 50-422 Wrocław, Poland

Conference **ELMECO-6**
ELECTROMAGNETIC DEVICES AND PROCESSES IN ENVIRONMENT PROTECTION
joint with
9th Seminar APPLICATIONS OF SUPERCONDUCTORS **AoS-9**
June 24 – 27, 2008 Nałęczów, Poland

THE INFLUENCE OF COLD-DRAWING NbTi WIRE ON CRITICAL CURRENT DENSITY

Daniel GAJDA[1], Andrzej MORAWSKI[2], Andrzej ZALESKI[3]

[1]International Laboratory of High Magnetic Fields and Low Temperature
[2]Institute of High Pressure Physics, Polish Academy of Sciences
[3]Institute of Low Temperature and Structure Research Polish Academy of Sciences,

***Abstract**.: In the article we show the results of measurement of the critical current for NbTi multifilament wire. The main objective of the research was to determine the influence of cold – drawing of NbTi wire on J_c or the definition of the change of J_c. The NbTi wire had diameters 0.85mm, next step was drawing the wire of the diameter 0.7mm, 0.6mm and 0.5mm.*
.
***Streszczenie.** W artykule przedstawimy wyniki pomiarów prądu krytycznego dla drutu NbTi o średnicy 0,85mm, który był następnie przeciągany do średnicy 0.7 mm, 0.6mm i 0.5mm.*

Keywords: critical current, cold – drawing, NbTi wire .
Słowa kluczowe: prąd krytyczny, ciągnięcie na zimno, NbTi drut .

Introduction

The superconducting material NbTi was discovered in 1960. It possesses the crystalline structure of the cubic - centre type (BBC) A2. NbTi belongs to the groups of superconductors of the second kind. In superconductors of this kind the critical current I_c depends on the state of material. NbTi can be in two states: mixed state and the state of superconductors of the first kind. When the superconductor is in the state of superconductor of the first kind, the total current flows on the external surface of the wire. In the mixed state the flow of current takes place not only on the external surface, but also within the whole volume of superconducting material. As far as the magnitude of critical current is concerned, normal cores have great influence on it. Namely, they block material defects. If the Lorentz force is not too large, the cores remain at rest [2]. When the value of the flow of critical current increases together with the increase of external magnetic field, the Lorentz force also rises. When the value of the Lorentz force exceeds the critical size of a particular superconducting material, the centre anchors separate and the system of network of normal cores is destroyed. The materials that possess very many imperfections, deformations and defects, have large critical current. It is caused due to the fact that a great many anchored normal cores need the use of considerably bigger Lorentz force, in other words bigger current value. The composition of the superconducting material was determined as a result of long research works. Wires having from 50% to 60% Ti possess the highest critical current. The magnitude of J_c in superconducting wires depends on several major factors such as: grains size, the boundary of grains, admixture defects, the heat treatment method, pressure, wire drawing, HE and the size of precipitations of α Ti. In the case of NbTi the most effective pinning centres are created by precipitations of α Ti. The highest quantity of α Ti precipitations could be obtained when the wire was annealed at 700C. The body structure of NbTi allows for the elongation of the size of grains towards the axis of the wire [1]. The elongation of the length of grains causes the increase of J_c in higher external magnetic fields. The elongation effect can be obtained by means of mechanical methods such as: cold –drawing. Currently, the best NbTi wires possess B_c=14 [T], T_c=10[K], $J_c(0)=10^4$A/mm^2 at T=4,2 [K].

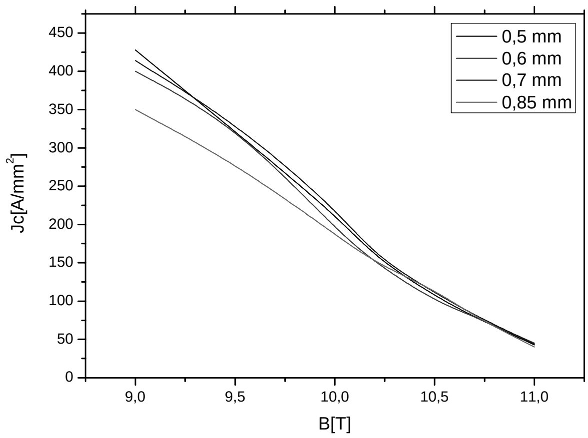

Fig.1. Jc=f(B) for NbTi/Cu multifilament wires – SKNE type

The experiment

The measurement of I_c was made via four-probe resistive method in a constant perpendicular magnetic field. All the research was done for wires made of NbTi in a copper shield of the diameter of about 0,85mm (8190 fibres – SKNE type) which was later drawn to the diameter of 0.7mm, 0.6mm and 0.5mm. The NbTi multifilament wire has about 70% the superconductor material. All the measurements were made in the liquid helium temperature. The examined samples had the length of approximately 25 mm. I_c was determined according to 1 μV/cm criterion.

Conclusions

The drawing of the NbTi multifilament wire caused the breaking of several superconducting fibres. The decrease of the diameter of the wire 41% did not cause the decrease of J_c. However, the obtained results suggest that J_c has not worsened dramatically. The critical current density for NbTi wires of the diameter of about 0.5 mm, 0.6mm and 0.7mm was increased for about 28% in comparison with the wire of the diameter 0.85mm within the range of magnetic fields from 9 T to 10 T. Low decrease of J_c can be caused by two factors. First is connected with the quantity of superconducting fibres, as only few of them broke. Second factor which is responsible for such a small worsening of J_c is probably the elongation of the length of grains which appeared as the result of drawing the wire.

REFERENCES

[1] Głowacki B., Pinning mechanism of Nb-based A15 conductors for high magnetic field and high magnetic current application, *V Seminar Applications of Superconductors, Lublin 2005, 11-23*

[2] Janiczek S., *Podstawy Krioelektrotechniki*, Częstochowa 1993

[3] Shevtsova O. N., *Giant vortex structures in nanometer-scale spherical type-II superconducting samples*, Supercond. Sci. Technol. 21 (2008) 065010 (5pp)

[4] Wilson M.N., *Superconducting Magnets,* Oxford 1983

Authors:

mgr inż.Daniel Gajda, International Laboratory of High Magnetic Fields and Low Temperature ,Gajowicka 95, 53-421 Wrocław, Poland,e-mail: dangajda@op.pl

dr Andrzej Morawski, Institute of High Pressure Physics, Polish Academy of Sciences,Sokołowska 29/37, 01-142 Warszawa. Poland , e-mail: amor@unipress.waw.pl

prof. Andrzej Zaleski: Institute of Low Temperature and Structure Research Polish Academy of Sciences, Okólna 2, 50-422 Wrocław, Poland

COMPARISON OF DC AND PULSED CRITICAL CURRENT CHARACTERISATION OF NBTi SUPERCONDUCTING WIRES

Mariusz WOZNIAK[1], Simon C. HOPKINS[2], Bartek A. GLOWACKI[2], Tadeusz JANOWSKI[1]

Lublin University of Technology (1), University of Cambridge (2)

***Abstract**. The use of pulsed magnetic fields and currents for transport critical current characterisation has many potential benefits, but introduces challenges in obtaining measurements consistent with conventional DC characterisation for some types of sample. This will be illustrated by comparative DC and pulsed critical current testing of two dissimilar NbTi conductors. The factors influencing pulsed measurements will be identified, the prospects for pulsed critical current testing assessed, and recommendations made for obtaining good agreement with DC characterisation.*

***Streszczenie.** Użycie impulsowego prądu i pola magnetycznego do wyznaczania krytycznego natężenia prądu przewodów nadprzewodnikowych oferuje wiele korzyści, jednocześnie powodując trudności w interpretacji i porównaniu wyników z tradycyjnymi pomiarami prądem stałym. Na podstawie porównania wyników pomiarów prądem stałym z pomiarami impulsowymi, dla dwóch różnych przewodów NbTi, zostaną określone główne czynniki powodujące rozbieżności, a także zostaną określone zalecenia mogące poprawić zgodność pomiarów.*

Keywords: pulse, critical current, transport measurements, niobium-titanium
Słowa kluczowe: pomiar impulsowy, prąd krytyczny, Nb-Ti

Introduction

The use of pulsed magnetic fields and transport currents for the critical current characterisation of superconducting wires has several potential benefits: in particular, large magnetic flux densities exceeding 30 T can be brought within the cost and infrastructure capabilities of typical research laboratories, and the heating associated with high current testing can be greatly reduced. However, this approach brings its own challenges in ensuring that the results are compatible with conventional direct current (DC) characterisation: the small bore diameter of a typical pulse magnet requires short samples to be used and, in combination with the need for rapid measurement, this usually results in a less sensitive electric field criterion [1,2]. Operating away from steady state conditions also introduces the possibility of time- and frequency-dependent effects, which are inconvenient for routine critical current characterisation but may be of relevance for assessing transient losses and for applications including SMES.

Experimental Methods

Two contrasting multifilamentary NbTi samples were selected for investigation. To identify the discrepancies between DC and pulsed testing, their critical current behaviour was investigated using the Cryo-BI-Pulse system developed with Metis Instruments and Equipment NV (Leuven, Belgium) [3], and a comparison made to DC measurements. The first wire, from IMI, had a diameter of 0.25 mm and contained 60 NbTi filaments in a copper matrix, fig. 1(a); the second, from Luvata (OK3900), contained 3900 filaments embedded in a more resistive Cu-Mn matrix to reduce AC losses [4], with internal and external copper stabilisation, and was 0.575 mm in diameter, fig. 1(b).

To better understand the effects of sample size and configuration, both short straight samples and longer U-shaped samples were tested in the Cryo-BI-Pulse system, with the voltage measured across a length of approximately 5 mm perpendicular to the applied magnetic field in each case. The magnetic field pulse was 16.4 ms in duration, and shaped to give a broad plateau at near the maximum field. The current pulse was more sinusoidal in shape and timed to coincide with the maximum field; measurements were performed for two current pulse durations, 2.0 ms and 3.8 ms, as shown in Fig. 2. Critical currents were determined from a series of pulses in the Cryo-BI-Pulse system as described previously [1-3].

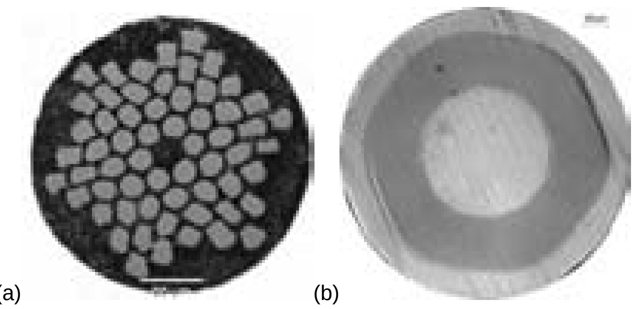

(a) (b)

Fig.1. Cross-sections of NbTi superconducting wires: (a) IMI wire (backscattered electron micrograph) and (b) Luvata OK3900 (optical micrograph)

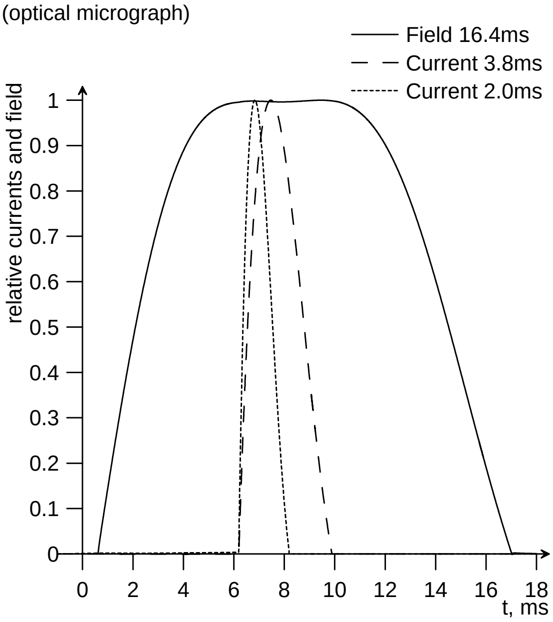

Fig.2. Shape and timing of the magnetic field and current pulses used in the Cryo-BI-Pulse system for critical current testing.

Results and Discussion

Very good agreement has been obtained between DC and pulse measurements of the copper-matrix IMI NbTi wire (Fig. 3) [3].

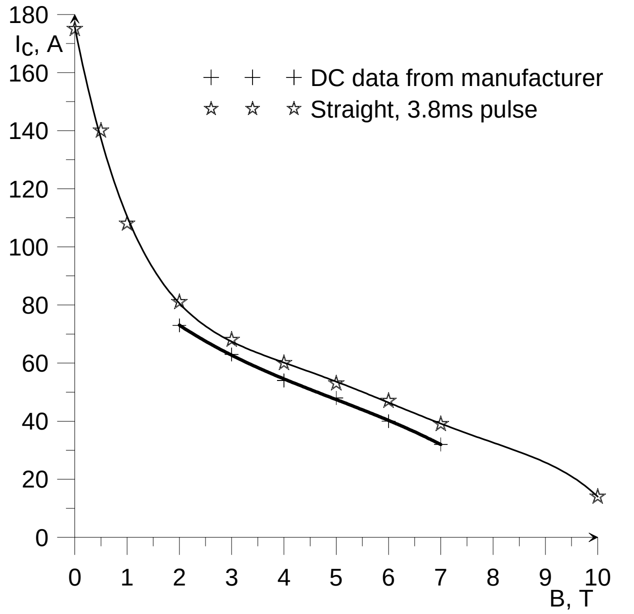

Fig.3. Transport critical current measurements for the IMI Titanium NbTi wire, by DC and pulse techniques.

In contrast, the critical current of OK3900 samples measured by pulsed techniques was very much lower than the DC value: at 1 T, the apparent critical current measured on a short straight sample perpendicular to the magnetic field was more than 400 A lower than the DC critical current, only 40% of the expected value. Longer, U-shaped samples came closer to the DC value, but the measured critical current was still 300 A lower than for DC testing. Further measurements on samples after selective chemical etching of the copper stabilisation and Cu-Mn matrix were then performed, and the complete set of critical current values are presented in Fig. 4.

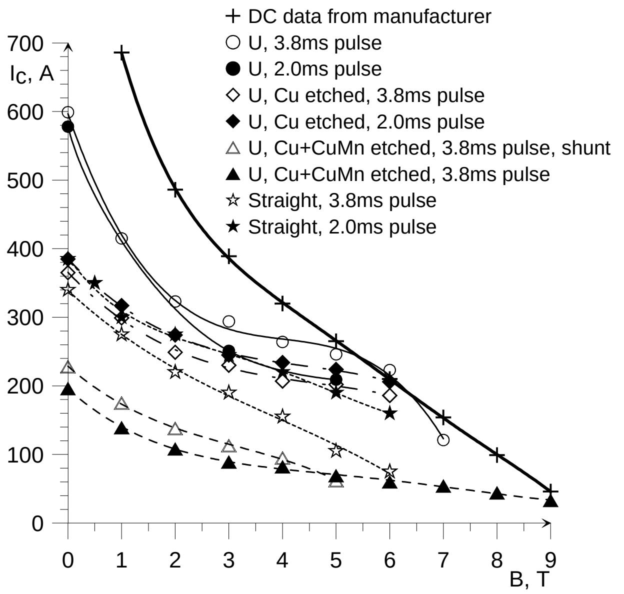

Fig.4. Critical current data for OK3900 samples, tested as short straight pieces ('straight') and U-shaped samples ('U') by DC and pulse techniques.

The transition criteria applied to DC and Cryo-BI-Pulse measurements are certainly different, and might explain the small discrepancy for the IMI NbTi wire [1-2]; but this cannot explain the much larger discrepancy for OK3900, as the *n* values and sample configurations are similar for both wires.

The observation of a higher critical current for U-shaped samples than for short straight pieces suggests a contribution from ohmic heating from the current leads and contacts: the longer U-shaped samples have a greater separation between current and voltage contacts, reducing the influence of this contribution and of current transfer effects [5]. This may also explain the better agreement at higher magnetic fields, for which the critical current is lower. Heating and current transfer effects would both be expected to be more significant for the OK3900 wire than the IMI wire because of its higher critical current and lower interfilamentary electrical conductivity.

The small filament diameters in OK3900 might be expected to confer improved flux-jump and cryo-stability, but the higher thermal and electrical resistivity of the interfilamentary matrix has the opposite effect [6]. Chemical etching to remove the external copper stabilisation reduced the measured critical current, and further etching to remove the resistive Cu-Mn matrix further reduced the critical current. This was probably due to the progressively poorer stability, and confirms that differences in stabilisation can contribute to the discrepancies between DC and pulsed critical current measurements.

The effect of current pulse duration is less consistent: shorter pulses result in less heating, but also a larger rate of change of current, which may introduce transient effects. There is some evidence in fig. 4 of reduced pulse lengths resulting in both increased and decreased critical currents, depending on the sample length and stability. Time-dependent effects and the contribution of magnetic field will be the focus of future work.

References

[1] Rogacki, A. Gilewski, M. Newson, H. Jones, B.A. Glowacki and J. Klamut, *Supercond. Sci. Technol.*, **15** (7) 1151 (2002)

[2] B.A. Glowacki, A. Gilewski, K. Rogacki, A. Kursumovich, J.E. Evetts, H. Jones, R. Henson and O. Tsukamoto, *Physica C*, **384** 205 (2003)

[3] V. Stehr, K.S. Tan, S.C. Hopkins, B.A. Glowacki, A. De Keyser, L. Van Bockstal and J. Deschagt, *J. Phys.: Conf. Ser.*, **43** 682 (2006)

[4] R.B. Goldfarb, D.L. Ried, T.S. Kreilick and E. Gregory, *IEEE Trans. Magn.*, **25** (2) 1953 (1989)

[5] J.W. Ekin, *J. Appl. Phys.*, **49** (6) 3406 (1978)

[6] M.N. Wilson, C.R. Walters, J.D. Lewin, P.F. Smith and A.H. Spurway, *J. Phys. D: Appl. Phys.*, **3** (11) 1517-1585 (1970)

***Authors**: Mariusz Woźniak and prof. dr hab. inż. Tadeusz Janowski, Institute of Electrical Engineering and Electrotechnologies, Lublin University of Technology, 20-618 Lublin, ul. Nadbystrzycka 38 D, Poland, E-mail: co.nic@wp.pl and t.janowski@pollub.pl; Drs Simon Hopkins and Bartek Glowacki, Department of Materials Science and Metallurgy, University of Cambridge, Pembroke Street, Cambridge, CB2 3QZ, UK, E-mail: sch29@cam.ac.uk and bag10@cam.ac.uk.*

Conference **ELMECO-6**
ELECTROMAGNETIC DEVICES AND PROCESSES IN ENVIRONMENT PROTECTION
joint with
9th Seminar APPLICATIONS OF SUPERCONDUCTORS **AoS-9**
June 24 – 27, 2008 Nałęczów, Poland

MAGNETIC MEASUREMENTS OF PERCOLATION IN COATED CONDUCTORS AS AN ANALOGUE OF DETERIORATING LIVING NEURAL NETWORKS

Agnieszka ŁĘKAWA[1], Bartek A. GŁOWACKI[2], Mariusz WOŹNIAK[1], Simon HOPKINS[2], Grzegorz KOZŁOWSKI[3], Henryka D. STRYCZEWSKA[1], Tadeusz JANOWSKI[1]

Lublin University of Technology(1), University of Cambridge (2), Wright State University (3)

Abstract. *The possible analogy between the concept of the giant component, that occurs in 2D living neural networks and induced superconducting currents in granular coated conductors was investigated. Studies of YBCO coated conductors were conducted using transport and Hall probe magnetometry. Encouraging results suggest that the design of superconducting polycrystalline coatings can benefit from knowledge of degrading neural networks.*

Streszczenie. *Badano możliwość istnienia analogii pomiędzy pojęciem wielkiego komponentu pojawiającego się w dwuwymiarowych żywych sieciach neuronowych oraz indukowanych prądach nadprzewodnikowych w ziarnistych cienkowarstwowych taśmowych przewodach nadprzewodzących. Badania przewodów YBCO były prowadzone przy pomocy czujników Halla. Wyniki przeprowadzonych eksperymentów dowodzą, że wiedza na temat rozpadających się sieci neuronowych może być korzystna dla projektowania polikrystalicznych powłok.*

Keywords: percolation, coated conductors, living neural networks
Słowa kluczowe: perkolacja, cienkowarstwowe taśmowe przewody nadprzewodzące, żywe sieci neuronowe

Introduction

Percolation of the current in superconducting coated conductors is a significant issue for optimization and design of multifilamentary structures for ac applications. The main challenge is to define the minimum width of the filaments and possible interfilamentary connections to preserve the required longitudinal current of the ac conductor. We have investigated the possible analogy between the concept of the giant component, g, that occurs for complex networks in nature e.g. in 2D living neural networks and induced superconducting currents in granular coated conductors. Systematic studies of YBCO coated conductors were conducted using Hall probe magnetometry. Superconducting measurements were conducted at 77K in Zero Field Cooling conditions. Encouraging results suggest that design of superconducting polycrystalline coatings can benefit from the knowledge on degraded neural networks.

Percolation in coated conductors

The intrinsic uniformity of granular coated conductors is to a considerable extent determined by the misorientation of the grains. The presence of higher angle grain boundaries degrades the transport critical current density as the misorientation poses an obstacle for current transport, forcing it to percolate. Figure 1 illustrates the dependence of transport critical current density on magnetic field parallel to the c axis of $YBa_2Cu_3O_7$ grown epitaxially with different in- plane misorientation [001] tilt. As may be observed from Figure 1 even a slight misalignment of the grain results in a decrease in the critical current density [1, 2].

The undesirable large ac losses of mono-layer coated conductors can be substantially lowered by introducing a multifilamentary structure. However, due to the small width of individual filaments they can easily be destroyed, bringing about disturbance of the conduction. Therefore, the bridging of striated samples is studied. Bridges allow for transfer of the current to another filament in case of damage to any conducting path.

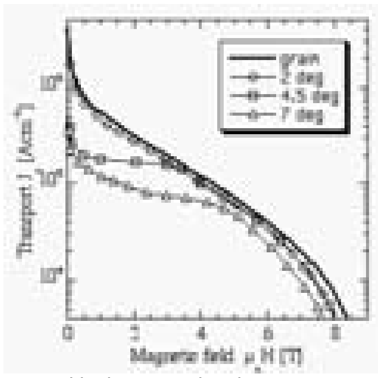

Fig. 1. Transport critical current density versus magnetic field for $YBa_2Cu_3O_7$, reproduced from [2]

Figure 2 shows the map of trapped magnetic field in the striated tape with interlocking cuts. It can be easily noted that there are regions with lower trapped flux in some of the filaments, which is due to intrinsic imperfections of the superconducting material. Figure 3 presents the comparison of ac losses in mono-layer, striated and bridged multifilamentary coated conductors [3].

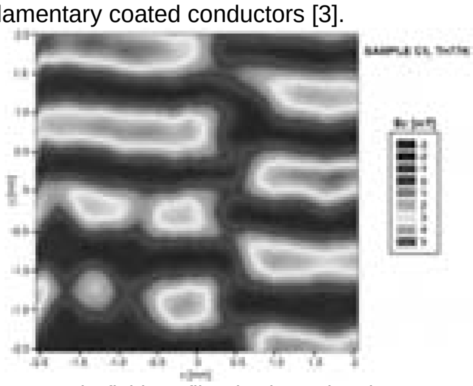

Fig. 2. Magnetic field profiles in the striated YBCO tape with interlocking cuts, (J. Kvitkovic and B. A. Glowacki, private communication)

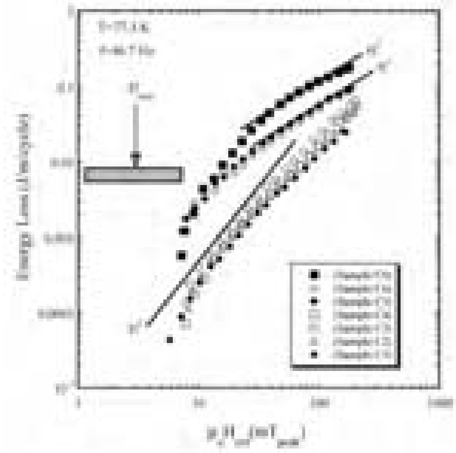

Fig. 3. Comparison of AC energy losses in seven structures of YBCO tape, C0 - mono-layer, striated samples: C1- no filament bridging, C2 - one central bridge, C3 - alternating bridges, C4 - one interlocking cut, C5 - interlocking cuts, C6 - alternating bridges [3]

Living neural networks

The latest research on living neural networks conducted on an artificially cultured 2D network has shown that it undergoes a percolation transition in response to a reduction in connectivity by chemical blocking of neurotransmitter receptors. The phenomenon was described by a model based on bond-percolation using a graph theory approach. Fluorescence image of a living neural culture is presented in Figure 4 (a). Figure 4 (b) illustrates the disintegration of the giant component, the largest cluster of neurons that emerges while the connectivity, *c*, of the network is gradually weakened.

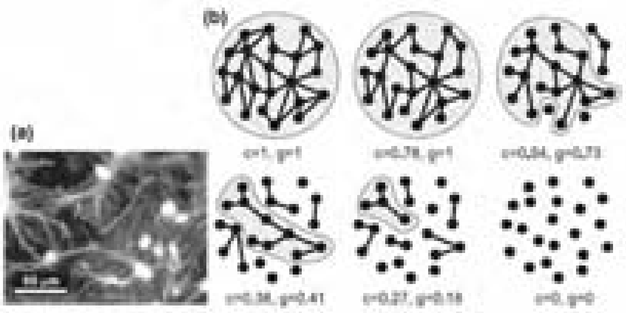

Fig. 4. (a) Fluorescence image of living neural network culture [1], (b) The illustration of the idea of giant component decomposition [2]

Connectivity refers here to a measure of synaptic strength, and is defined as:

(1) $$c=1/(1+P)$$

where, *P* is a parameter dependent on the amount of a chemical substance that blocks the neurotransmitter receptors. As can be seen from Figure 4 (b) the fraction of neurons belonging to the giant component is reduced with the decrease of parameter *c* [4,5].

Analogy between percolation phenomena in superconductors and living neural networks

The in-depth analysis of percolation in both coated conductors and living neural networks allows one to put forward the hypothesis that the behaviour of these structures is analogous. To investigate the problem, the decomposition of the neural network was modelled by damaging the integrity of the coated conductor by scratching its surface. Scanning the trapped magnetic field in an undamaged and progressively more damaged conductor can illustrate the defragmentation of superconducting screening paths. A low temperature Hall probe sensor integrated with an XYZ positioning system was used for magnetic flux measurements. Figure 5 (a), (b) and (c) depicts the trapped magnetic field profiles for a uniform fragment of coated conductor YBCO tape, the same sample with three 2 mm long scratches, and 7 scratches respectively. As depicted in Figure 5 strong scratching of the tape surface results in division of the high flux area into smaller ones. What is more, the signal becomes weaker until it disappears almost completely.

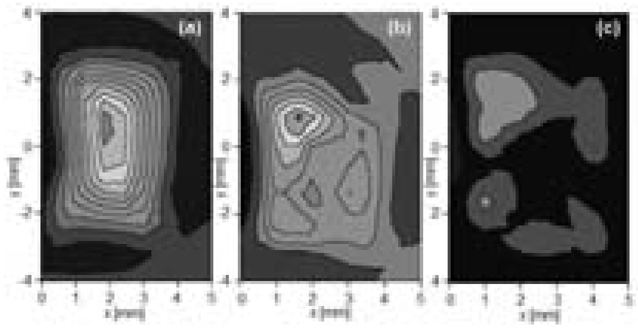

Fig. 5. Maps of magnetic field trapped in: (a) one of the pieces of YBCO coated conductor – unscratched sample, (b) sample with 3 about 2mm long scratches and (b) the same sample with 7 scratches

Summary

The striking similarity between images in Figure 4 and 5 (b) leads to the conclusion that the parameters describing living neural networks can be somehow translated into superconductor properties. Assuming that the areas of trapped flux are analogous to the giant component grey area, one may infer that Figure 5 (b) can be translated into the picture with g ≈ 0.18, since the main path for current flow would be destroyed. Considering the Equation 1 that defines connectivity *c* and substituting parameter *P* with a quantitative expression for an increasing amount of scratching, the parallel parameter of connectivity strength may be obtained. These first deductions indicate that probably further analogies may be found between percolation phenomena in deteriorating living neural networks and coated conductors.

REFERENCES

[1] Glowacki B., A., (RE)$Ba_2Cu_3O_7$ coated Conductors for AC And DC Applications, in: Studies of HTS Superconductor Applications (Advances in Research and Applications): *Springer Verlag*,Vol.1 Materials, (2003), 239-279D.

[2] T. Verebelyi, D. K. Christen, R. Feenstra, C. Cantoni, A. Goyal, D. F. Lee, M. Paranthaman, P. N. Arendt, R. F. DePaula, J. R. Groves, and C. Prouteau, Appl. Phys. Lett. 76 (2000) 1755

[3] Majoros M., Glowacki B. A., Campbell A. M., Levin G. A., Barnes P. N., Polak M., AC Losses in Striated YBCO Coated Conductors, *IEEE Trans. Appl. Sup*., 15, (2005), No. 2, 2819-2822

[4] Breskin I., Soriano J., Moses E., Tlusty T., Percolation in Living Neural Networks, *Phys. Rev. Let.*, 97 (2006), 188102

[5] Eckmann J.-P., Feinerman O., Gruendlinger L., Moses E., Soriano J., Tlusty T., The physics of living neural networks, *Phys. Rep.*, 449 (2007), 54-76

***Authors**: Agnieszka Łękawa, student of Lublin University of Technology (LUT), E-mail: agalekawa@gmail.com; Dr Bartek A. Glowacki, University of Cambridge, Department of Materials Science and Metallurgy, Applied Superconductivity and Cryoscience Group, Pembroke Street, Cambridge CB23QZ, UK, E-mail: bag10@cam.ac.uk; Mariusz Woźniak, student of LUT, E-mail: co.nic@wp.pl; Dr Simon Hopkins, E-mail: sch29@cam.ac.uk; Grzegorz Kozłowski, Ph.D., D.Sc., E-mail: gregory.kozlowski@wright.edu; Henryka Danuta Stryczewska, Ph.D. (Eng), D.Sc. (Prof. of LUT), E-mail: h.stryczewska@pollub.pl; Tadeusz Janowski, Ph.D. (Eng), D.Sc., E-mail: t.janowski@pollub.pl.*

TECHNOLOGIA WYTWARZANIA MgB_2 I ZAGROŻENIA DLA ZDROWIA

Jacek RYMASZEWSKI, Marcin LEBIODA, Ewa KORZENIEWSKA[1], Krzysztof POLITOWSKI[2]

Politechnika Łódzka (1), Pharm-Hand s.j (2)

***Abstract**. The toxic boron features in connection to the technology of fabricating of MgB_2 samples are presented in the article.* TECHNOLOGY OF PREPARING OF MGB2 AND THE DANGER OF BORON USING FOR HEALTH

***Streszczenie.** W pracy zaprezentowano toksyczne własności boru w powiązaniu z technologią wytwarzania masywnych próbek MgB_2..*

Keywords: superconductivity, magnesium diboride, boron. toxicity
Słowa kluczowe: nadprzewodnictwo, dwuborek magnezu, bor, toksyczność.

Wstęp

Poszukiwanie nowych materiałów nadprzewodzących o jak najwyższej temperaturze krytycznej we wszystkich dostępnych związkach chemicznych dało rezultat w odkryciu nadprzewodnictwa w – znanym od lat 50-tych XX wieku prostym związku międzymetalicznym MgB2 [1]. Jest to prosty związek dwóch pierwiastków: bezpiecznego magnezu i toksycznego boru. Bor, pierwiastek występujący w niewielkiej ilości w przyrodzie głównie w postaci oksoboranów (sassolind, kernit, boraks, kolemanit) znalazł zastosowanie w przemyśle chemicznym, spożywczym, metalurgii, jako dodatek do paliw rakietowych, w medycynie jako środek łagodnie odkażający przyczynił się do ukazania nowych perspektyw nadprzewodnictwa. W stanie czystym bor tworzy strukturę krystaliczną o dużej twardości lub występuje jako bezpostaciowy proszek.

Badania nad właściwościami boru wskazują, że jest on pierwiastkiem korzystnie wpływającym na rozwój organizmów tak roślinnych jak i zwierzęcych, ale z drugiej strony wykazują jego wysoką toksyczność. Należy nadmienić iż dzienna dawka przyjmowana z pożywieniem waha się od 0,3-20 mg [2]. Podawana wartość nie powinna być przekraczana.

Technologia wytwarzania a toksyczność boru

Jedną z metod otrzymywania dwuborku magnezu (MgB2) jest podgrzewanie w wysokich temperaturach magnezu i boru w postaci sproszkowanej. W wyniku prostej reakcji chemicznej powstaje interesujący nas związek:

$$Mg + 2B \rightarrow MgB_2 \qquad (1)$$

Pociąga to za sobą niebezpieczeństwo zatrucia borem, gdyż z płynami ustrojowymi organizmów żywych bor tworzy kwas borny i borany.

Związki boru (kwas borny, borany) łatwo wchłaniają się z błon śluzowych, drogą oddechową oraz przez uszkodzoną skórę. W organizmie dobrze kumuluje się głównie w mózgu, tkance tłuszczowej, wątrobie, nerkach oraz w tkance kostnej [3]. Jest dosyć szybko eliminowany z ustroju, w większości przez nerki, ale przy codziennym narażeniu na ekspozycję niewielkimi dawkami może dojść do skumulowania dawek i zatrucia. Wyjątkiem jest kwas borny, który wydalany jest bardzo powoli.

Dawka śmiertelna dla osoby dorosłej wynosi ok 15-20 g. Przyjmuje się, że dawka dzienna, która może spowodować kumulację i objawy zatrucia to 100 mg. Dokładniejszym wyznacznikiem dawki toksycznej jest stężenie kwasu borowego w surowicy gdzie dawkę 25-100mg% uważa się za śmiertelną [4].

Mechanizm działania toksycznego nie został w pełni wyjaśniony, niemniej biorąc pod uwagę skutki (odwodnienie protoplazmy komórkowej) należy zaliczyć bor do trucizn komórkowych.

Zatrucia ostre zdarzają się rzadko i charakteryzują się 50% śmiertelnością [5]. Zazwyczaj dochodzi do nich w wyniku omyłki (wypicie roztworu kwasu bornego) bądź poprzez wdychanie pyłów boru i jego związków, co przy wytwarzaniu nadprzewodzących próbek MgB2 podnosi ryzyko zatrucia. Objawami zatrucia ostrego są: gorączka, bezmocz (uszkodzenie nerek), złuszczenie skóry. W zatruciach drogą pokarmową obserwuje się śluzowe bądź krwawe wymioty, biegunki, zaczerwienienie skóry wraz ze złuszczaniem i tworzeniem pęcherzy, senność, skurcze mięśni twarzy i kończyn przechodzące w drgawki, wysoką gorączkę, żółtaczkę, skąpomocz lub bezmocz, sinicę, spadek ciśnienia krwi, śpiączkę i zgon.

Nie ma swoistej odtrutki w zatruciach borem. Postępowanie w przypadku zatruć doustnych: stosuje się płukanie żołądka wraz z węglem aktywnym oraz środki przeczyszczające. Ponieważ bor uszkadza nerki, a to jest jak wspomniano wcześniej główna droga eliminacji tego pierwiastka z ustroju, najlepsze efekty w leczeniu zatruć przynosi dializa otrzewnowa [6].

Podsumowanie

Przy wytwarzaniu próbek dwuborku magnezu należy zwrócić szczególną uwagę na toksyczne właściwości boru. Należy zachować wszelkie środki ostrożności, aby w trakcie przygotowywania próbek nie doszło do zatrucia organizmu.

REFERENCES

[1] Nagamatsu J., Nakagawa N., Muranaka T., Zenitani Y., Akimitsu J., Superconductivity at 39 K in magnesium diboride, *Nature*, vol. 410, 2001, pp. 63-64.
[2] A.Kabata-Pendias, H. Pendias: Biogeochemia pierwiastków śladowych *PWN* 1993 str. 168.

[3] J.Biernat, J. Pieczyńska: Rola boru w przemianach metabolicznych i żywieniu człowieka *Bromat.Chem.Toksykol. XXXIII*, 2000, 4, str. 289-294
[4] W. Seńczuk: Toksykologia 1990, 14.9, str. 557-558.
[5] W. Kostowski: Farmakologia 1998, str. 940-941.
[6] W.Rusiecki, P. Kubikowski: Toksykologia współczesna 1977 str. 313-314

***Authors**: dr inż. Jacek Rymaszewski, Politechnika Łódzka Instytut Elektrotechniki Teoretycznej, Metrologii i Materiałoznawstwa, Zakład Materiałoznawstwa i Elektrotechnologii 90-924 Łódź, ul. Stefanowskiego 18/22 E-mail: jacekrym@matel.p.lodz.pl, dr inż. Marcin Lebioda, Politechnika Łódzka Instytut Elektrotechniki Teoretycznej, Metrologii i Materiałoznawstwa, Zakład Materiałoznawstwa i Elektrotechnologii 90-924 Łódź, ul. Stefanowskiego 18/22 E-mail: marcleb@matel.p.lodz.pl, dr inż. Ewa Korzeniewska, Politechnika Łódzka Instytut Elektrotechniki Teoretycznej, Metrologii i Materiałoznawstwa, Zakład Materiałoznawstwa i Elektrotechnologii 90-924 Łódź, ul. Stefanowskiego 18/22 E-mail: ewakorz@matel.p.lodz.pl, mgr farm. Krzysztof Politowski, Pharm-Hand s.j. 93-166 Łódź, ul. Łączna 28 E-mail: k.politowski@magiczna.com*

The Correspondence address is:

e-mail: biuro@matel.p.lodz.pl